A NUMERICAL AND ANALYTICAL ANALYSIS OF THE PHYSICS OF PHASE-SEPARATION FRONTS

A Dissertation
Submitted to the Graduate Faculty
of the
North Dakota State University
of Agriculture and Applied Science

By

Eric Merlin Foard

In Partial Fulfillment
for the Degree of
DOCTOR OF PHILOSOPHY

Major Department:
Physics

March, 2012

Fargo, North Dakota

North Dakota State University

Graduate School

Title

A NUMERICAL AND ANALYTICAL ANALYSIS OF THE PHYSICS OF PHASE-SEPARATION FRONTS

By

Eric Merlin Foard

The Supervisory Committee certifies that this *disquisition* complies with North Dakota State University's regulations and meets the accepted standards for the degree of

DOCTOR OF PHILOSOPHY

SUPERVISORY COMMITTEE:

Alexander Wagner
Chair

Iskander Akhatov

Daniel Kroll

Sylvio May

Approved by Department Chair:

March 28, 2012 Daniel Kroll

ABSTRACT

My dissertation is an investigation into the basic Physics of phase separation fronts. Such phase-separation fronts occur in many practical applications, like the formation of immersion precipitation membranes, Temperature induced phase-separation of polymeric blends, or the formation of steel. Despite the fact that these phenomena are ubiquitous no generally applicable theory of phase-separation front exists. I believe the reason lies in the complexity of many of these material systems where a large number of physical effects (like phase-separation, crystallization, hydrodynamics, etc) cooperate to generate these structures.

As a Physicist, I was driven to develop an understanding of these systems, and we choose to start our investigation with the simplest system that would incorporate a phase-separation front. So we initially limited our study to systems with a purely diffusive dynamics. The phase-separation is induced by a control-parameter front that is a simple step function advancing with a prescribed velocity. We investigated these systems numerically using a lattice Boltzmann method and also investigated them analytically as much as possible. Starting from a one-dimensional front moving with a constant velocity we then extended the complexity of the systems by increasing the number of dimensions, examining a variable front velocity, and finally by including hydrodynamics.

ACKNOWLEDGMENTS

Many people have given me support, both great and small, throughout the many years leading up to the completion of my doctoral dissertation in Physics. To my family, friends, colleagues, and even some students, I offer you my sincerest thanks.

I am grateful for all the assistance and support from the faculty and staff of the Department of Physics at North Dakota State University. To my adviser Alexander Wagner, thank you for your patience and encouragement, and for all the hard work and extra time you took with me both on a professional and a personal level. To my supervisory committee members Sylvio May, Iskander Akhatov from the Department of Mechanical Engineering, Alexander Wagner, and Daniel Kroll, I express my great appreciation for your suggestions to improve this disquisition, and for your interesting thoughts on directions in which this research could be expanded. Thank you Patty Hartsoch for your help with finer points of academic bureaucracy, i.e. getting the impossible done. I am especially grateful to Goetz Kaehler, Stephan Loew, and Ben Lu who have been my fellow graduate students and colleagues during my graduate career at NDSU. Thank you for all the late night camaraderie which helped make the years tolerable. Thank you to my long time friend Paul Omernik, what a long strange trip it's been.

Very special thanks goes to my parents Merlin and Laureen for the science books, the graph paper, the Lego blocks, the math story problems on long drives, and all the other unusualness of my upbringing. To my sisters Meghan and Sonja and my brother Jason, thank you for being interesting people. I feel by trying to emulate your drive, passion, and sense of adventure that you have made me more interesting. Finally, to Anne, thank you for finding me interesting. I will always work to stay that way.

TABLE OF CONTENTS

LIST OF FIGURES

LIST OF APPENDIX TABLES

LIST OF APPENDIX FIGURES

CHAPTER 1. INTRODUCTION

In this dissertation I develop a minimal model for phase-separation fronts, and numerically and analytically examine the phase-separated morphologies left in their wake. Phase separation fronts determine morphology formation for a wide variety of important real world applications. The initial motivation for the research presented in this dissertation was provided by a desire to understand the formation of structures observed in the creation of immersion precipitation membranes. My adviser A. J. Wagner, developed the hypothesis that the dynamics of their formation was largely a front-driven phenomenon [1]. However, the process is fantastically complicated and it is extremely difficult to try to devise faithful models that cover the length-scale from initial phase-separation to final filter morphology. This lead to the desire to examine other systems where phase separation fronts were primarily responsible for structure formation in order to see if it were possible to identify some generic phenomena. Discussed below are some of these systems, such as the previously mentioned immersion precipitation membranes, and their relationship to this research. Inspired by the common elements of models of these physical systems, a simple model for phase separation fronts which could reproduce many of the observed structures was created in order to expand the analytical understanding of structure formation by phase separation fronts.

1.1. Examples of Phase Separation Fronts in Physical Systems

As previously mentioned, a wide variety of front-formed morphologies have been observed to form in many different phase separating systems. In the case of eutectoid alloys and immersion precipitation membranes, the resulting materials have incredibly important industrial applications [31, 12]. In contrast, the formation of Liesegang patterns does not yet have significant practical applications, despite a long, rich history of extensive research trying to elucidate its features [42, 53, 17]. Another system

in a relatively new field of study, which is anticipated to have useful applications in biotechnology and bioindustrial areas, is the formation of patterned lipid membranes.

Despite their wide differences, these systems have some commonalities. Foremost is they are examples of phase separation front induced pattern formation. Additionally, the phase separation dynamics of each system is believed to be dominated by diffusive dynamics. Therefore these systems are often modeled using a Cahn-Hilliard equation of motion. The Cahn-Hilliard equation is a diffusive equation of motion where the effective diffusion coefficient is positive (generating dissipation of excess material) or negative (generating accumulation of excess material) depending on the volume fraction of material [37]. This dissertation uses the Cahn-Hilliard equation to model the dynamics of front induced phase separation, and is discussed further in Section 1.2.4.

1.1.1. Lamella Formation in Eutectoid Alloys

Phase separation fronts are important in the creation of structure in some metal alloys. For instance, the pearlite phase of steel is formed by the slow cooling of certain iron and carbon alloys. The eutectoid point of iron and carbon occurs at a composition of 0.77 wt % C and temperature 727 °C. Iron and carbon alloys with this composition above this temperature are in the γ phase in which iron and carbon are miscible. When cooled below the eutectoid point, the γ phase is no longer stable, and the mixture phase separates into carbon-poor α-ferrite and carbon-rich β-ferrite regions [57, Ch. 12.2]. Cooling of the alloy is accomplished by contact with an external temperature reservoir held below the eutectoid temperature. Heat diffuses out of the alloy and a temperature gradient forms. Where the temperature crosses the eutectoid temperature phase separation ensues. This region moves as a front through the material. Phase separated structure formation is not unique to alloys of iron and carbon, and have been observed in many other eutectoid alloys. Pearlite is often

treated as a typical case, and other alloys which have undergone this type of phase separation transition are often referred to as pearlite.

The structure of pearlite is characterized by alternating lamellar domains of carbon-poor ferrite and carbon-rich austenite. The front's speed determines the lamellar spacing and the lamella orient along the direction of travel of the phase separation front [50]. Since thermal conductivity remains constant, this is equivalent to saying the temperature of the reservoir fixes the domain growth rate and the domain spacing [34]. Experiments by Faivre *et al.* [15] on tilt waves, which are defects in lamellar orientation that travel transverse to the front, show that their appearance provides a mechanism by which the proper domain spacing can be selected without destroying lamella or forming new lamella.

A composite material, pearlite posses bulk material properties which are not simply a mixture of ferrite and austenite properties, but are emergent from the structure itself. Measurements by Hyzak and Bernstein [31] show that hardness and yield strength of pearlite increase significantly with decreasing lamella spacing. Clayton and Danks [12] found corresponding increases in their measurements of hardness, and measured decreasing surface wear rates with decreasing lamella spacing. That is, the speed at which the phase-separation front moves through the steel alloy determines the bulk mechanical properties of the material.

As pearlite and other metallic alloy morphological phases are so useful in practical applications, there has been considerable effort to study their structure formation. A solid foundation for much of the subsequent theoretical research into eutectoid alloy structure formation was made by Jackson and Hunt [34] in their analysis of lamellar and rod formation in eutectoid mixtures where they modeled the phase separation front as a steady state diffusion process. Soon after, Verhoeven and Homer [56] included a convection layer ahead of the solidification front in order to more accurately

model the kind of solidification front following a phase separation front which occurs in many metallic alloys. This kind of refinement from the general to the specific is typical of the analytical work performed on structure formation by phase separation fronts in eutectoid alloys. However, even more complicated models retain the basic diffusive, Cahn-Hilliard like, phase separation dynamics.

1.1.2. Liesegang Patterns in Reaction Diffusion Systems

Seemingly entirely unrelated to eutectoid alloy pattern formation is the phenomenon of precipitate pattern formation in electrolyte impregnated gel solutions. However, despite the apparent differences, these two systems have much in common.

Similar to the pattern formation in immersion precipitation membranes which was inspiration for the research in this dissertation, it was the motivation of understanding pattern formation in simple systems which lead to the publication by R. E. Liesegang of his observations of highly ordered patterns of concentric rings. Published just over one hundred years ago, the pattern of concentric rings, later named Liesegang rings in his honor, formed around a drop of silver nitrate on a glass slide with a thin gel coating containing potassium dichromate [42]. General patterns which have similar structure and formation properties are known as Liesegang patterns.

Liesegang rings are thin and form close together near the center, increasing their width and spacing the further from the center they form. Since the first experiments by Liesegang, several alternatives to silver nitrate and potassium dichromate have been used in the production of Liesegang rings and patterns. In general, some electrolytes A and B combine to form an insoluble precipitate D which separates out, producing Liesegang patterns. Most recent publications use linear Liesegang patterns of bands and gaps which are produced by adding the A electrolyte to a test-tube containing the B electrolyte suspended in gel. Liesegang patterns have even been shown to occur in pure liquid systems where convective currents are suppressed by nar-

row channels, or even using gaseous electrolytes in a narrow tube which prevents non-diffusive flow [51]. Just as with pattern formation in eutectoid alloy systems, the dynamics which result in Liesegang patterns are diffusive, and the patterns are formed in a region which moves as a front through the system.

Early research characterized Liesegang patterns by a set of empirical laws, first presented by M. C. K. Jablczynski [33]. The "time law" ($x_n \propto \sqrt{t_n}$) relates the position of a ring n with the time of its appearance, the "spacing law" ($x_{n+1} \propto x_n$) relates the spacing between adjacent rings, and the "width law" ($x_n \propto w_n$) relates the width of a ring with its position relative to the center. The phenomenological Matalon-Packter law attempts to relate the initial concentrations of electrolytes with the proportionality constants in the Liesegang laws, but with limited success.

Despite the many attempts to forge a model which would explain the formation of Liesegang patterns and Liesegang-like patterns, currently none are completely successful. Janke and Kantelhardt [36] recently published a review and comparison of Liesegang pattern forming models. The review by Janke and Kantelhardt of the leading models included a theory of pattern formation by spinodal decomposition based on precipitation dynamics described by the Cahn-Hilliard equation. This was based on the models used by Antal *et al.* [2] and Rácz [49] where the production of the D precipitate is treated as a moving Gaussian source term in the Cahn-Hilliard equation, and a Liesegang band forms when precipitate concentrations reach the spinodal saturation point.

Other examples of numerical techniques and models of Liesegang pattern formation were presented and discussed by us (Foard and Wagner [19]), which is reproduced in this dissertation as Paper 2. In that paper we argue that the diffusion of the A electrolyte into the material containing B electrolyte, and the subsequent production of the precipitate D constitutes a moving front which induces phase separation. The

key difference between the models of Antal *et al.* [2] and Rácz [49], where phase separation is described by a Cahn-Hilliard equation, and the model used in this dissertation, where the same Cahn-Hilliard equation is used, is the nature of the moving front itself. In the model presented in this dissertation, the front is a moving change in the effective thermodynamic stability, and not a moving source. As will be shown in Paper 2, we were able to analytically determine all constants of proportionality in the Liesegang laws mentioned above. As far as we are aware, such a complete analysis has not been performed for other Liesegang pattern producing models.

1.1.3. Immersion Precipitation Membranes

Still another system which seems unrelated to the two previous systems, but yet is an example of phase separated structure formed by a moving front is the formation of immersion-precipitation membranes. A relatively new material, immersion precipitation membranes are already finding important uses in industrial applications as media for microfiltration, ultrafiltration, and reverse osmosis [64].

To create an immersion precipitation membrane, a thin coating of a polymer and solvent mixture is applied to a substrate. The substrate is then immersed in a bath of non-solvent. Solvent diffuses out of the polymer solvent layer into the immersion bath. At the same time, non-solvent diffuses into the polymer layer. Where the solvent concentration in the layer drops below a critical value the polymer and solvent spontaneously phase separate, leaving polymer domains with solvent and non-solvent domains. When the solvent and non-solvent fluid is removed, the result is a polymer membrane with interstitial voids. The voids form asymmetrically in the membrane: Small, roughly isotropic void formation occurs near the surface, changing over to larger, elongated voids forming deeper in the membrane [10].

In order to understand how immersion precipitation membrane structures are formed, Akthakul *et al.* [1] simulated the process using the lattice Boltzmann method

(LBM) in two dimensions. Their model consisted of a two component system with a Flory-Huggins free energy, and phase separation dynamics driven by the Cahn-Hillard equation coupled to the Navier-Stokes equation. They managed to capture some of the essential structural aspects of immersion precipitation membranes, such as the "selective skin layer" at the outer surface of the membrane and the increasing size of voids at increasing depth in the membrane. Soon after this, Zhou and Powell [64] simulated a three component model in two and three dimensions using a finite difference method (FDM) approach which lacked hydrodynamic effects. Their model also used a Cahn-Hillard equation of motion with an underlying Flory-Huggins free energy. They then reintroduced hydrodynamic effects in two dimensions using a finite element method (FEM) Navier-Stokes solver for incompressible flows. They conclude that hydrodynamics are essential for destabilizing the selective skin layer in order to allow for the production of voids which penetrate the selective skin layer, however this conclusion is not supported by the results of Akthakul *et al.* which did include hydrodynamics but did not produce voids in the selective skin layer. Subsequently, Wang *et al.* [63] simulated the effects of varying polymer chain length on the formation of immersion precipitation membranes in two dimensions using dissipative particle dynamics (DPD). They find the primary kinetics of structure formation is late-time domain coarsening following spinodal decomposition, which is consistent with the observations of simulations by Akthakul *et al.* and Zhou and Powell. What is remarkably different is that their DPD simulations were much more effective at forming small voids in the selective skin layer than the LBM or FDM with FEM calculations. The key difference is that the DPD method used by Wang *et al.* is inherently stochastic, whereas the Akthakul *et al.* and Zhou and Powell used mean-field numerical methods which only included fluctuations in the initial conditions.

The role of fluctuations in the formation of immersion precipitation membranes is explored further in Appendix D. There, evidence is given that supports the notion that initial fluctuations alone are insufficient to reproduce the kinds of structures observed in immersion precipitation membranes. Rather, it is necessary to include fluctuations during the phase separation process, similar to Wang *et al.* [63] with their DPD simulation method.

Results shown in Paper 3, previously published by Foard and Wagner [20], explain the transition from small voids near the surface to elongated voids deeper in the membrane which is responsible for the asymmetric structure of immersion precipitation membranes. It is shown that a phase separation front selects a preferred morphology which is dependent upon the speed of the front. Fast moving fronts produce lamella which form parallel to the front. Slow moving front produce lamella which form perpendicular to the front, and grow in the direction of motion of the front in a manner similar to lamella growth observed in eutectoid alloys discussed in Section 1.1.1 above.

1.1.4. Lipid Membranes

The final example of a physical system where phase separation fronts play a roll in structure formation is in the patterned deposition of a lipid layer onto a substrate. Experiments typically involve preparing an amphiphilic lipid monolayer on the surface of water in a Langmuir trough. A hydrophilic substrate is drawn out from the trough through the surface. A thin layer of water adheres to the substrate which draws the lipid layer up with the substrate. The transition to the thin layer of water on the substrate induced phase separation of the lipids into domains where lipids are in the condensed conformational state and other domains where lipids are in the expanded conformational state. The pattern of expanded and condensed domains formed through this process is typically highly regular stripes. The stripe orientation

and spacing are determined by the speed and direction of substrate extraction and the surface pressure [52, 23, 9]. Numerical simulations by Köpf *et al.* using a model based on a Cahn-Hilliard style of free energy closely match experimental results [40]. While research on lipid pattern formation is in a relatively early stage, the results are clearly similar to the results obtained from the front induced phase separation model shown in Paper 3 of this dissertation.

1.2. Phase Separation Front Model

The examples given above of physical systems which display pattern formation following a phase separation front, though vastly different in many details, are often modeled using the Cahn-Hilliard equation with a prescribed underlying free energy. Due to the flexibility of this approach, the model developed for this dissertation is also based on the Cahn-Hilliard equation. The model was introduced and discussed in detail in the first publication by Foard and Wagner, included as Paper 1 in this dissertation. The model is briefly presented here.

1.2.1. Free Energy

The model consists of an $\mathcal{A}$-type and $\mathcal{B}$-type material in a binary mixture. The total density of the mixture $\rho = \rho_{\mathcal{A}}(\boldsymbol{r}, t) + \rho_{\mathcal{B}}(\boldsymbol{r}, t)$ is a constant, i.e. the material is incompressible. The material order parameter is the relative concentration of the two material types:

$$\phi(\boldsymbol{r}, t) = \frac{\rho_{\mathcal{A}}(\boldsymbol{r}, t) - \rho_{\mathcal{B}}(\boldsymbol{r}, t)}{\rho} \,. \tag{1}$$

Miscibility of the two materials is described by an underlying Ginzburg-Landau free energy

$$F = \int \mathrm{d}\boldsymbol{r} \left\{ \psi(\boldsymbol{r}, t) + \frac{\kappa(\boldsymbol{r}, t)}{2} \left[\nabla\phi(\boldsymbol{r}, t)\right]^2 \right\} \,, \tag{2}$$

with a free energy density

$$\psi(\boldsymbol{r},t) = \frac{a(\boldsymbol{r},t)}{2}\phi(\boldsymbol{r},t)^2 + \frac{b(\boldsymbol{r},t)}{4}\phi(\boldsymbol{r},t)^4 + c(\boldsymbol{r},t)\phi(\boldsymbol{r},t)\ . \tag{3}$$

This Landau free energy is a mean-field, general expansion of a free energy near the critical temperature $a \propto T - T_c$ [30, Ch. 17]. Parameter b in part determines the equilibrium concentration of the phase separated material, the c parameter provides spatial variation of the chemical potential, and the κ parameter provides a surface tension between phase separated domains. The free energy density of Eq. (3) for different values of the effective temperature a is shown in Figure 1a. The phase diagram associated with this free energy is shown in Figure 1b.

The Landau free energy is a very simple model. It is not based on any underlying statistical mechanical pinnings, and has known shortcomings [6, Ch. 10-4]. However, the simplicity of the model is a great asset that will allow analytical treatment which would be difficult or perhaps impossible with more physical and more complex underlying free energy equations.

1.2.2. Equilibrium Concentration and the Common Tangent Construction

For non-conserved order parameters the equilibrium state is found at the free energy minimum, and there is no coexistence of phases. However, in this model the total concentration

$$\langle\phi\rangle = \frac{1}{V}\int \phi \,\mathrm{d}V \tag{4}$$

is conserved, and the total free energy density $\langle\psi\rangle$ is minimized with respect to this constraint. Here the minimization process is reviewed for the free energy given in Eq. (2). The common tangent construction, an important part of the analysis presented in Paper 1, is derived as a result of this process.

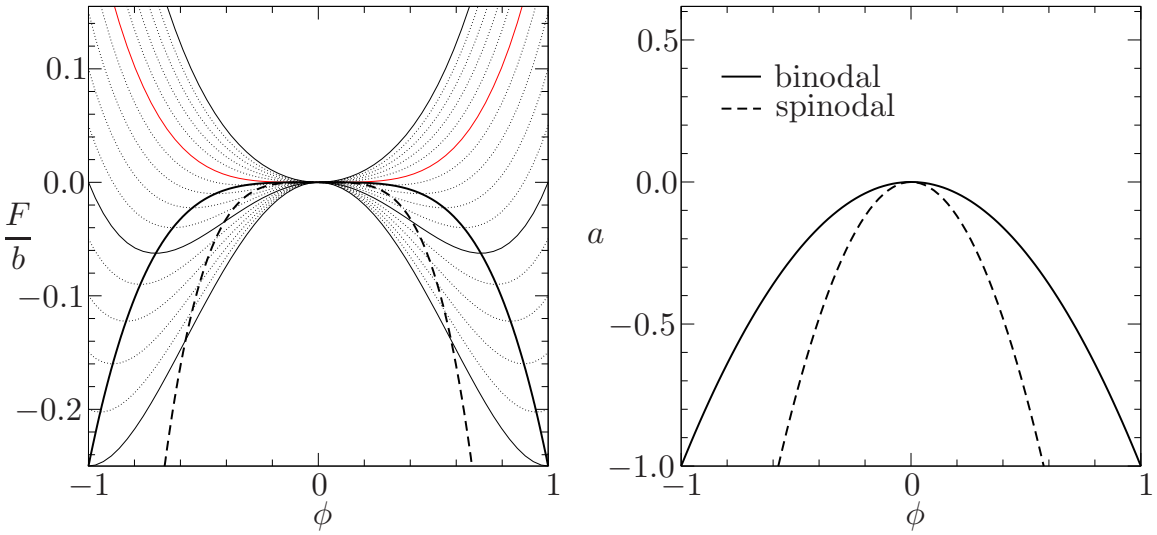

(a) (b)

Figure 1. (color online) Ginzburg-Landau free energy curves (a) and associated phase diagram (b) for the Ginzburg-Landau mixing free energy of Eq. (3) with $c = 0$, and $b = 1$. On the left, the free energy density divided by the quartic pre-factor is plotted for values of the reduced temperature $a = \{-1.0, -0.9, \ldots, 0.4, 0.5\}$, with thin solid curves for the values $a = \{-1.0, -0.5, 0.5\}$, and a thin red (online) curve for the critical value $a = 0$. In both plots heavy solid curves trace the energy minima which determines the equilibrium values, and heavy dashed curves are the upper bound for parts of the free energy curves with negative curvature $\partial^2\psi/\partial\phi^2 \leq 0$. In the phase diagram on the right the heavy solid coexistence curve (known as the binodal) is the upper bound for the region of instability, inside of which material will phase separate to the equilibrium values. In the phase diagram the heavy dashed curve (known as the spinodal) is an upper bound for the spinodal region, inside of which phase separation occurs through spinodal decomposition. Between the binodal and spinodal lines phase separation occurs through nucleation [37].

From Eq. (2) and (3), ignoring the gradient terms in Eq. (2), a volume V composed of two sub-volumes V_1 and V_2 of material with respective concentrations ϕ_1 and ϕ_2 has a total energy:

$$F = \int_V \psi(\phi)\, \mathrm{d}\boldsymbol{r} = V\langle\psi\rangle = V_1\psi(\phi_1) + V_2\psi(\phi_2) = V_1\psi_1 + V_2\psi_2\ . \tag{5}$$

Incompressibility and conservation of the order parameter and total volume require:

$$\left.\begin{aligned} V &= V_1 + V_2 \ , \\ V\langle\phi\rangle &= V_1\phi_1 + V_2\phi_2 \ , \end{aligned}\right\} \Rightarrow \begin{cases} V_1 = \dfrac{\phi_2 - \langle\phi\rangle}{\phi_2 - \phi_1} V \ , \\ V_2 = \dfrac{\langle\phi\rangle - \phi_1}{\phi_2 - \phi_1} V \ . \end{cases} \tag{6}$$

Combining Eq. (5) and (6) yields:

$$\langle\psi\rangle = \frac{\psi_2 - \psi_1}{\phi_2 - \phi_1} \left(\langle\phi\rangle - \phi_1\right) + \psi_1 \ . \tag{7}$$

This means the total free energy density $\langle\psi\rangle$ lies on line connecting the points (ϕ_1, ψ_1) and (ϕ_2, ψ_2) on the free energy density diagram.

The total free energy density $\langle\psi\rangle$ of the system described above in Eq. (7) is represented graphically in Figure 2 as an open circle on the thin solid line. It is clear from this graphical representation that the total free energy density is minimized (filled circle) when the line which connects the coexistence phases (heavy dashed line) is tangent to the free energy density curve at both coexisting phases ϕ^-_{eq} and ϕ^+_{eq}. This graphical means of determining the coexistence phases from an underlying free energy density curve is known as the common tangent construction.

The common tangent construction is represented by the conditions:

$$\left.\frac{\partial\psi}{\partial\phi}\right|_{\phi^-_{eq}} = \left.\frac{\partial\psi}{\partial\phi}\right|_{\phi^+_{eq}} \qquad \text{(equal bulk chemical potential)}, \tag{8}$$

$$\frac{\psi(\phi^+_{eq}) - \psi(\phi^-_{eq})}{\phi^+_{eq} - \phi^-_{eq}} = \left.\frac{\partial\psi}{\partial\phi}\right|_{\phi^+_{eq}} \qquad \text{(common tangent)}. \tag{9}$$

The term "bulk" refers to the fact that the common tangent construction beginning with Eq. (5) ignores the gradient terms in Eq. (2) which give rise to the interfacial free energy cost of having adjacent domains of differing phases.

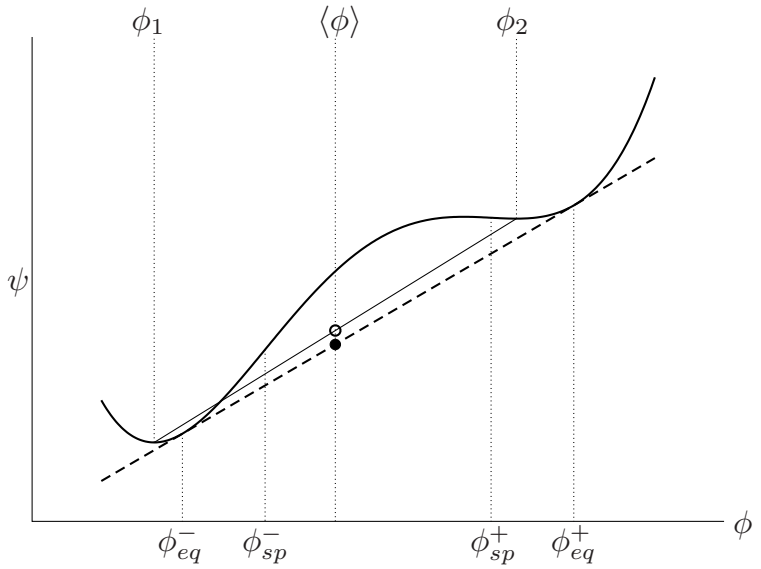

Figure 2. Example of the common tangent construction (heavy dashed line) on an isotherm for a given underlying free energy (heavy solid curve) for a conserved order parameter ϕ. This free energy isotherm has two stable coexistence values $\phi_{eq}^{\pm}$. The inflection points of the free energy isotherm determine the spinodal values $\phi_{sp}^{\pm}$ of the order parameter. The thin solid line represents a hypothetical, nonphysical isotherm which connects the two free energy minima. The open circle shows the total energy density of a system (see text for details) prepared with half its material at each of the two concentrations associated with the energy minima ($\int \phi \, \mathrm{d}\boldsymbol{r} = \langle\phi\rangle = 0.5\phi_1 + 0.5\phi_2$). The system can lower its total energy to that of the filled circle by changing the concentration of the phase separated material to the equilibrium concentrations, yet retain the same average concentration and therefore conserve the total order parameter ($\int \phi \, \mathrm{d}\boldsymbol{r} = \langle\phi\rangle = 0.61\phi_{eq}^- + 0.39\phi_{eq}^+$).

In this model, the chemical potential is defined from the free energy Eq. (5) as:

$$\mu = \frac{\delta F}{\delta \phi} = a\phi + b\phi^3 + c - \kappa\nabla^2\phi \; . \tag{10}$$

Therefore the bulk chemical potential is:

$$\mu_0(\phi) = \frac{\partial \psi}{\partial \phi} = a\phi + b\phi^3 + c \; . \tag{11}$$

Applying the conditions of Eq. (8) and (9), the equilibrium concentrations of the

coexistence phases are

$$\phi_{eq}^{\pm} = \pm\sqrt{\frac{-a}{b}}\,, \tag{12}$$

for temperatures below the critical temperature ($a < 0$). The equilibrium concentrations are shown as the heavy solid curve in Figure 1a, which for the case $c = 0$ shown in Figure 1a correspond to the energy minima. As the temperature approaches the critical temperature from below $a \to 0^-$ the energy minima coalesce, a characteristic of second order phase transitions. Above the critical temperature $a > 0$ the energy density has a single minimum, and the equilibrium state of the order parameter is single valued $\phi = 0$.

The common tangent construction concept will be revisited in Paper 1 in the analysis of the nucleation condition for domain formation following a phase separation front in one dimensional systems.

1.2.3. Phase Separation Front

As mentioned above, phase separation is induced in a region when the free energy density of Eq. (3) for that region changes from a state with a single stable concentration value to a state with two stable concentration values. This corresponds to the effective temperature changing in space from a positive mixing value $a = a_M > 0$ to a negative separating value $a = a_S < 0$. A phase separation front is generated when that transition moves progressively through the system.

The simplest possible transition for the effective temperature is an abrupt flat transition which moves at constant speed in a constant direction. To visualize this front in a three dimensional system imagine a surface plane moving at constant speed in the direction of the surface normal; ahead of the plane the effective temperature is a constant value greater than zero, behind the plane the effective temperature is a constant value less than zero. This simplest model of moving effective temperature

front is also applied to the other parameters in Eq. (2) and Eq. (3). A phase separation front which takes the free energy parameters from a single mixing value (denoted by subscript M) to a single separating value (denoted by subscripts S), starting at position $\boldsymbol{r}_0$ moving with constant velocity $\boldsymbol{u}$ is

$$a(\boldsymbol{r},t) = a_S + (a_M - a_S)\Theta\left[(\boldsymbol{r} + \boldsymbol{r}_0 + \boldsymbol{u}t)\cdot\hat{\boldsymbol{u}}\right] \ , \tag{13}$$

$$b(\boldsymbol{r},t) = b_S + (b_M - b_S)\Theta\left[(\boldsymbol{r} + \boldsymbol{r}_0 + \boldsymbol{u}t)\cdot\hat{\boldsymbol{u}}\right] \ , \tag{14}$$

$$c(\boldsymbol{r},t) = c_S + (c_M - c_S)\Theta\left[(\boldsymbol{r} + \boldsymbol{r}_0 + \boldsymbol{u}t)\cdot\hat{\boldsymbol{u}}\right] \ , \tag{15}$$

$$\kappa(\boldsymbol{r},t) = \kappa_S + (\kappa_M - \kappa_S)\Theta\left[(\boldsymbol{r} + \boldsymbol{r}_0 + \boldsymbol{u}t)\cdot\hat{\boldsymbol{u}}\right] \ , \tag{16}$$

where Θ is the Heaviside step function.

The straight, flat, abrupt front described by Eq. (13–16) may seem overly simplified. However, adding complexity to make the front appear more like the physical examples in Section 1.1 would reduce the general applicability of model. As can been seen from those examples of physical phase separation front systems, the specific properties of a phase separation front for two given systems can be widely different from another. Furthermore, maintaining simplicity of the model is essential to facilitate analytical understanding of how structures are formed by phase separation fronts. For example, without such simplicity the direct analysis of the dynamics of domain formation presented in Paper 1 might not have been possible.

The simplicity of the abrupt front in this model is advantageous for analysis. It is reasonable to be suspicious that an abrupt front may be an oversimplification, as the control parameter fronts which induce phase separation in real systems are spatially extended. However, as will be shown later in this dissertation, models of front induced phase separation similar to this one with extended fronts produce similar dynamics of phase separation and result in the same phase separated structures as this abrupt

front model. For comparison, some notable examples of phase separation induced by extended fronts are given in references [2, 21, 24, 25, 28] and described later.

1.2.4. Equation of Motion

The phase separation front and the thermodynamic instability which produces phase separation for the model of this dissertation are described above. Here the equation of motion which governs the dynamics of phase separation for the model is described.

In this model, material is neither created, destroyed, or changes species in the process of phase separation. The change in order parameter at a given location is due to rearrangement of material. The order parameter in a region increases when $\mathcal{A}$-type material flows in and $\mathcal{B}$-type material flows out. Likewise, the order parameter decreases when the flow is the reverse. In mathematical terms, the order parameter obeys the continuity equation

$$\partial_t \phi(\boldsymbol{r}, t) = -\boldsymbol{\nabla} \cdot \boldsymbol{j}(\boldsymbol{r}, t) \ , \tag{17}$$

where changes in the order parameter ϕ at position $\boldsymbol{r}$ are due to divergences in the current $\boldsymbol{j}$.

In equilibrium the chemical potential is constant. Therefore, in the absence of externally generated currents, gradients in the chemical potential are responsible for the generation of currents in the order parameter. For small deviations in the chemical potential, currents are assumed to be proportional to the chemical potential gradient:

$$\boldsymbol{j}(\boldsymbol{r}, t) = m \boldsymbol{\nabla} \mu(\boldsymbol{r}, t) \ . \tag{18}$$

Here, the constant of proportionality m is the diffusive mobility. Combining Eq. (17)

and (18) yields the equation of motion:

$$\partial_t \phi(\boldsymbol{r}, t) = -\boldsymbol{\nabla} \cdot [m \boldsymbol{\nabla} \mu(\boldsymbol{r}, t)] \ . \tag{19}$$

Using the definition in Eq. (10) of the chemical potential, and leaving the time and spatial dependence of the order parameter implied, the above equation becomes:

$$\partial_t \phi = -\boldsymbol{\nabla} \cdot \left\{ m \boldsymbol{\nabla} \left(a\phi + b\phi^3 + c - \kappa \nabla^2 \phi \right) \right\} \ . \tag{20}$$

This is a form of the Cahn-Hilliard equation. As mentioned previously, the Cahn-Hilliard equation is often used to model phase separation in binary materials.

The equation of motion shown in Eq. (20) introduces the diffusive mobility m. In the model used in this dissertation, the diffusive mobility is a parameter of the phase separation front:

$$m(\boldsymbol{r}, t) = m_S + (m_M - m_S) \Theta \left[(\boldsymbol{r} + \boldsymbol{r}_0 + \boldsymbol{u}t) \cdot \hat{\boldsymbol{u}} \right] \ . \tag{21}$$

As with the other parameters of the front given in Eq. (13–16), the diffusive mobility may take on a mixing value m_M ahead of the front which is different from the separating value m_S following the front. The total number of parameter of this model now stands at twelve (a_M, a_S, b_M, b_S, c_M, c_S, κ_M, κ_S, m_M, m_S, u, ϕ_{in}), where ϕ_{in} is the initial concentration of the mixed material into which the front is moving. However, the non-dimensionalization presented below will show that there are only seven independent parameters.

1.2.5. Non-dimensionalization

As previously mentioned, a reduction in the number of free parameters is typically done by rescaling the equation of motion Eq. (20) into a non-dimensional form.

The equation of motion is rescaled by the characteristic length and time scales of spinodal decomposition phase separation dynamics, and the equilibrium concentration of the coexisting phases of phases separated material given in Eq. (12). The details are provided here to show more easily the relationship of this model to other models based on Cahn-Hilliard like equations of motion.

Phase separation by spinodal decomposition occurs when material is in a state that has a concave underlying free energy density. In Figure 1 this corresponds to states which fall below the heavy dashed lines. For the isotherm shown in Figure 2, material concentrations between ϕ_{sp}^{-} and ϕ_{sp}^{+} will result in phase separation through spinodal decomposition. Phase separation by spinodal decomposition occurs due to the negative effective diffusion coefficient which results from a concave free energy density. With a negative effective diffusion coefficient, small concentration fluctuations are amplified. This is the reverse of the normal diffusion process where concentration fluctuations are are suppressed. The process of spinodal decomposition relies on the presence of initial concentration fluctuations, which are present in all real systems. However, spinodal decomposition is not driven by fluctuations or other stochastic processes [37, Ch. 3.3.2].

The characteristic length scale of spinodal decomposition λ_{sp} is the wavelength of initial concentration fluctuations which are most greatly amplified during phase separation by spinodal decomposition. The spinodal wavelength for a given equation of motion, such as Eq. (20), is determined by linearization of the equation of motion around the initial mixed concentration $\phi = \phi_{in}$, then performing a k-space Fourier transform of the linearized equation:

$$\partial_t \tilde{\phi}(\boldsymbol{k}) = -m \left[\left(a + 3b\phi_{in}^2 \right) k^2 + \kappa k^4 \right] \tilde{\phi}(\boldsymbol{k}) = R(k) \tilde{\phi}(\boldsymbol{k}) \, , \tag{22}$$

where $k = |\boldsymbol{k}|$. The solution to Eq. (22)

$$\tilde{\phi}(\boldsymbol{k}) = e^{R(k)t} \ , \tag{23}$$

shows that small fluctuations initially grow exponentially with a k-dependent growth rate $R(k)$. The highest growth rate occurs for wavevector magnitude:

$$k_{sp} = \sqrt{\frac{-(a + 3b\phi_{in}^2)}{2\kappa}} \ . \tag{24}$$

The highest growth rate wavevector k_{sp} corresponds to the wavelength of the fastest growing concentration fluctuation

$$\lambda_{sp} = \frac{2\pi}{k_{sp}} = 2\pi\sqrt{\frac{2\kappa}{-(a + 3b\phi_{in}^2)}} \ , \tag{25}$$

known as the spinodal wavelength. The growth rate of the fastest growing concentration fluctuation $R(k_{sp})$ corresponds to the characteristic time scale of spinodal decomposition:

$$t_{sp} = \frac{1}{R(k_{sp})} = \frac{4\kappa}{m(a + 3b\phi_{in}^2)^2} \ . \tag{26}$$

This is referred to as the spinodal time. The spinodal length and time are used to define the spinodal speed:

$$u_{sp} = \frac{\lambda_{sp}}{t_{sp}} = 2\pi m\sqrt{\frac{-(a + 3b\phi_{in}^2)^3}{8\kappa}} \ . \tag{27}$$

The values of the parameters for the spinodal length, time, and speed are the phase separating values found in the wake of the phase separation front of this model, denoted with subscript S as shown in Eq. (13–16) and (21). So that the non-dimensionalization does not depend on the mixed material concentration, the rescal-

ing is done using the spinodal length and time for a symmetric mixture $\phi_{in} = 0$. The resulting length, time, and concentration scales used for the non-dimensionalization are:

$$\lambda_{sp} = 2\pi\sqrt{\frac{2\kappa_S}{-a_S}}\,,\; t_{sp} = \frac{4\kappa_S}{m_S a_S^2}\,,\; \phi_{eq} = \sqrt{\frac{-a_S}{b_S}}\,. \tag{28}$$

These are used to define the following non-dimensional scales:

$$\boldsymbol{R} = \frac{\boldsymbol{r}}{\lambda_{sp}} = \frac{\boldsymbol{r}}{2\pi}\sqrt{\frac{-a_S}{2\kappa_S}}\,, T = \frac{t}{t_{sp}} = \frac{t m_S a_S^2}{4\kappa_S}\,, \Phi = \frac{\phi}{\phi_{eq}} = \phi\sqrt{\frac{b_S}{-a_S}}\,. \tag{29}$$

Applying the above non-dimensional scales to Eq. (20) results in

$$\partial_T \Phi = \frac{1}{2\pi^2}\boldsymbol{\nabla}_{\boldsymbol{R}} \cdot \left[\frac{m}{m_S}\boldsymbol{\nabla}_{\boldsymbol{R}}\left(\frac{-a}{a_S}\Phi + \frac{b}{b_S}\Phi^3 + \frac{c}{-a_S\phi_{eq}} - \frac{1}{8\pi^2}\frac{\kappa}{\kappa_S}\nabla^2_{\boldsymbol{R}}\Phi\right)\right]\,, \tag{30}$$

where the space and time dependence of the phase separation front parameters and the order parameter is implied. This equation suggests the use of the following non-dimensional parameters:

$$A = -\frac{a_M}{a_S}\,,\; B = \frac{b_M}{b_S}\,,\; C = \frac{c_M - c_S}{a_S\phi_{eq}}\,,\; M = \frac{m_M}{m_S}\,,\; K = \frac{\kappa_M}{\kappa_S}\,. \tag{31}$$

Additionally, the non-dimensional front speed

$$U = u\frac{t_{sp}}{\lambda_{sp}}\,, \tag{32}$$

and nondimensional initially mixed material concentration

$$\Phi_{in} = \frac{\phi_{in}}{\phi_{eq}}\,, \tag{33}$$

complete the set of seven independent parameters of the non-dimensionalized model.

This completes the definition of this model for phase separation in the wake of

a simple moving front. Analysis of this model presented in this dissertation will use the non-dimensional parameters. Numerical simulation of this model is performed using the lattice Boltzmann method, which is presented in the next section.

1.3. Model Implementation with Lattice Boltzmann

Outlined in this section is the numerical method for simulating the model of front induced phase separation introduced in Section 1.2. First the Lattice Boltzmann method (LBM) is briefly introduced. Following that, the equation of motion given as Eq. (30) is altered in order to be more effectively simulated with LBM. Then the specifics of matching LBM to this model of front induced phase separation is presented. Finally, details of implementation in one, two, and three dimensional systems are given.

1.3.1. About the Lattice Boltzmann Method

The lattice Boltzmann method (LBM) used in this dissertation solves the standard lattice Boltzmann equation (LBE) with Bhatnager-Gross-Krook (BGK) approximation

$$f_i(\boldsymbol{r}+\boldsymbol{v}_i, t+1) - f_i(\boldsymbol{r}, t) = \frac{1}{\tau(\boldsymbol{r}, t)}\left[f_i^0 - f_i(\boldsymbol{r}, t)\right] \ , \tag{34}$$

for the continuous functions f_i, on a discrete lattice $\boldsymbol{r}$, in discrete integer time, using a finite set of discrete velocities $\boldsymbol{v}_i$ defined such that, for every i, $\boldsymbol{r}$ and $\boldsymbol{r}+\boldsymbol{v}_i$ are on the lattice. The lattice Boltzmann equation with the Bhatnager-Gross-Krook approximation (LBE-BGK) is a discretized form of the Boltzmann transport equation which evolves the functions f_i toward the equilibrium functions f_i^0 with a characteristic time τ. The choice of equilibrium functions f_i^0 determine the equation of motion simulated by the LBE.

Once the equilibrium functions are defined the equation of motion simulated by the lattice Boltzmann equation (34) is determined. As is typically done, the

lattice Boltzmann equation is numerically implemented in two stages; a collision step followed by a streaming step. The collision step evolves the distribution functions at position $\boldsymbol{r}$ in time:

$$\tilde{f}_i(\boldsymbol{r}, t+1) = f_i(\boldsymbol{r}, t) + \frac{1}{\tau(\boldsymbol{r}, t)} \left[f_i^0 - f_i(\boldsymbol{r}, t) \right] \ . \tag{35}$$

The streaming step evolves the distribution functions in space according to the choice of discrete velocities:

$$f_i(\boldsymbol{r} + \boldsymbol{v}_i, t+1) = \tilde{f}_i(\boldsymbol{r}, t+1) \ . \tag{36}$$

These two steps perform the lattice Boltzmann iteration of Eq. (34) for given equilibrium functions f_i^0 and set of velocities $\boldsymbol{v}_i$. The set of velocities and the form of the equilibrium distributions is determined by the equation of motion to be simulated, the dimensionality of the system, and isotropy requirements of the discretized equation of motion.

1.3.2. Galilean Transformation for Comoving Fronts

Numerical simulations utilizing the lattice Boltzmann method function on a finite number of nodes. The number of lattice nodes, and therefore the size of the simulated material, are limited by the system memory and computational resources available. We desire to observe the dynamics of front induced phase separation for long periods of time. This means observing a front as it travels a long distance through a material. For technical reasons, a LBM simulation which could contain such a large amount of material is infeasible.

However, as will be shown later, nearly all the dynamics of phase separation induced by a moving front occurs in the vicinity of the front. Thus, in order to effectively simulate front induced phase separation dynamics using LBM, the Galilean transform $\boldsymbol{R} \to \boldsymbol{R} - \boldsymbol{U}$ into a reference frame comoving with the front is performed

on Eq. (30):

$$\partial_T \Phi + \boldsymbol{\nabla}_{\boldsymbol{R}} \cdot (\Phi \boldsymbol{U}) = \frac{1}{2\pi^2} \boldsymbol{\nabla}_{\boldsymbol{R}} \cdot \left[\mathcal{M} \boldsymbol{\nabla}_{\boldsymbol{R}} \left(\mathcal{A}\Phi + \mathcal{B}\Phi^3 + \mathcal{C} - \frac{\mathcal{K}}{8\pi^2} \nabla^2_{\boldsymbol{R}} \Phi \right) \right] . \tag{37}$$

Here the scripted letters are nondimensional, spatially (but no longer temporally) dependent parameters of the phase separation front. In this model the front moves in a constant direction, which we choose to align to the X-axis $\boldsymbol{U} = (U_X, 0)$. Therefore the phase separation front parameters in Eq. (37) are given in terms of the nondimensional parameters Eq. (31) for a stationary front at position $X = X_f$ as:

$$\{\mathcal{A}, \mathcal{B}, \mathcal{C}, \mathcal{K}, \mathcal{M}\} = \begin{cases} \{-1, 1, 0, 1, 1\}, & X < X_f \\ \{A, B, C, K, M\}, & X > X_f \end{cases} . \tag{38}$$

Due to numerical stability requirements [60] the following dimensional form of the equation will be used:

$$\partial_t \phi + \boldsymbol{\nabla} \cdot (\phi \boldsymbol{u}) = \boldsymbol{\nabla} \cdot (m \boldsymbol{\nabla} \mu) . \tag{39}$$

Recall that the chemical potential μ is defined by Eq. (10). The non-dimensionalization described in Section 1.2.5 allows LBM simulations of Eq. (39) to be compared to analysis of Eq. (37).

The lattice Boltzmann method will be used to simulate Eq. (39) in the comoving reference frame of the front. Mixed material flows into the simulation at the right hand boundary, and phase separated material flows out of the simulation at the left hand boundary. The trade-off for performing a LBM simulation in the comoving reference frame of the phase separation front is the increased complexity of inflow and outflow boundaries. An analysis of different inflow and outflow boundary conditions for this model is given in Appendix G.

1.3.3. Taylor Expansion of the LBE

The approach taken here to match the LBE with the desired equation of motion is to begin by performing a Taylor expansion of the time evolved distribution function in Eq. (34) to second order. This approach and result is well known, however what is different here is that the spatial and temporal dependence of the relaxation time τ is taken into account. The Taylor expansion of the lattice Boltzmann equation is:

$$f_i(\boldsymbol{r} + \boldsymbol{v}_i, t+1) = f_i(\boldsymbol{r}, t) + Df_i(\boldsymbol{r}, t) + \frac{1}{2}D^2 f_i(\boldsymbol{r}, t) + O(D^3) \; . \tag{40}$$

The material derivative operator D is defined

$$D \equiv \partial_t + v_{i\alpha} \cdot \nabla_\alpha \; , \tag{41}$$

where the subscript α indicates Einstein vector notation which will be used extensively in the context of the discrete spatial components of the lattice Boltzmann equation. Substitution of Eq. (40) into Eq. (34) gives:

$$Df_i(\boldsymbol{r}, t) + \frac{1}{2}D^2 f_i(\boldsymbol{r}, t) + O(D^3) = \frac{1}{\tau(\boldsymbol{r}, t)} \left[f_i^0(\boldsymbol{r}, t) - f_i(\boldsymbol{r}, t) \right] \; . \tag{42}$$

The previous equation is solved for the unknown function $f_i(\boldsymbol{r}, t)$ to first order, and substituted back into itself obtaining:

$$f_i(\boldsymbol{r}, t) = f_i^0(\boldsymbol{r}, t) - \tau D f_i(\boldsymbol{r}, t) + O(D^2) \tag{43}$$

$$= f_i^0(\boldsymbol{r}, t) - \tau D f_i^0(\boldsymbol{r}, t) + O(D^2) \; . \tag{44}$$

Substitution of Eq. (44) into left hand side of Eq. (42) gives:

$$D\left[f_i^0(\boldsymbol{r},t) - \tau(\boldsymbol{r},t)Df_i^0(\boldsymbol{r},t)\right] + \frac{1}{2}D^2\left[f_i^0(\boldsymbol{r},t)\right] + O(D^3)\ .$$

Therefore the Taylor expanded form of the lattice Boltzmann equation in terms of derivatives of the equilibrium distributions to third order is:

$$Df_i^0(\boldsymbol{r},t) - D\left[\tau(\boldsymbol{r},t) - \frac{1}{2}\right]Df_i^0(\boldsymbol{r},t) + O(D^3) = \frac{1}{\tau(\boldsymbol{r},t)}\left[f_i^0(\boldsymbol{r},t) - f_i(\boldsymbol{r},t)\right]\ . \quad (45)$$

The next step, detailed in the following section, is to show that this set of equations is equivalent to the equation of motion (39).

1.3.4. Equilibrium Moments and Hydrodynamic Equation of Motion

The zero order moment and equilibrium distribution moments must be chosen appropriately in order to make the summation of the Taylor expanded lattice Boltzmann equation (45) over the discrete velocity set i equivalent to Eq. (39) up to second order. The process of proving that a given set of moments result in the proper equation of motion is the same process by which the correct set of moments can be found without a priori knowledge that they are the correct moments. Therefore, this latter approach is the one presented here.

First the unknown moments are defined. The zero order moment is an unknown scalar:

$$\sum_i f_i(\boldsymbol{r},t) = \tilde{S}(\boldsymbol{r},t)\ . \quad (46)$$

The zero, first, and second order equilibrium moments are defined respectively as an

unknown scalar, vector, and tensor:

$$\sum_i f_i^0(\boldsymbol{r},t) = S(\boldsymbol{r},t)\,, \tag{47}$$

$$\sum_i f_i^0(\boldsymbol{r},t) v_{i\alpha} = V_\alpha(\boldsymbol{r},t)\,, \tag{48}$$

$$\sum_i f_i^0(\boldsymbol{r},t) v_{i\alpha} v_{i\beta} = T_{\alpha\beta}(\boldsymbol{r},t)\,. \tag{49}$$

As stated previously, the subscripts indicate Einstein notation. For brevity and clarity, from this point on spatial and temporal dependence will be implied unless necessary, i.e. $\tau(\boldsymbol{r},t)$ will be written as τ.

The right hand side of Eq. (45) contains no derivatives. However, Eq. (39) has no terms which are not the result of a spatial or temporal derivative. Therefore a summation of the right hand side of Eq. (45) must be zero:

$$\sum_i \frac{1}{\tau}\left(f_i^0 - f_i\right) = \frac{1}{\tau}\left(\sum_i f_i^0 - \sum_i f_i\right) = \frac{1}{\tau}\left(S - \tilde{S}\right) = 0\,. \tag{50}$$

Therefore $S = \tilde{S}$, and the zero order moment is the same as the zero order equilibrium moment.

Using the above result, the summation over the velocity set of Eq. (45) is rearranged so that first order derivative terms are on the left hand side with higher order terms on the right

$$\sum_i D f_i^0 = \sum_i D\left(\tau - \frac{1}{2}\right) D f_i^0 + O(D^3)\,. \tag{51}$$

This arrangement is similar to Eq. (39) which only has first order derivatives on the left hand side. Equating the left hand side of Eq. (51) with the left hand side of

Eq. (39) gives:

$$\sum_i Df_i^0 = \partial_t \sum_i f_i^0 + \nabla_\alpha \sum_i f_i^0 v_{i\alpha} = \partial_t S + \nabla_\alpha V_\alpha = \partial_t \phi + \nabla_\alpha \left(\phi u_\alpha\right) \ . \tag{52}$$

Equating like terms reveals $S = \phi$ and $V_\alpha = \phi u_\alpha$ as suitable choices.

A few identities will be useful shortly. The first comes directly from Eq. (51):

$$\sum_i Df_i^0 = \partial_t \phi + \nabla_\beta \left(\phi u_\beta\right) = O(\partial^2) \ . \tag{53}$$

The second comes from the constant velocity field $\boldsymbol{u} = (u_x, 0)$ for some constant u_x defined by the model:

$$D\boldsymbol{u} = \partial_t \boldsymbol{u} + \nabla_\alpha u_\alpha = 0 \ . \tag{54}$$

The right hand side of Eq. (51) is:

$$\sum_i D\left(\tau-\frac{1}{2}\right)Df_i^0+O(\partial^3) \tag{55}$$

$$=\partial_t\left(\tau-\frac{1}{2}\right)\underbrace{\sum_i Df_i^0}_{O(\partial^2),\text{ Eq. (53)}}+\nabla_\alpha\left(\tau-\frac{1}{2}\right)\sum_i Df_i^0+O(\partial^3) \tag{56}$$

$$=\nabla_\alpha\left(\tau-\frac{1}{2}\right)\left[\partial_t\sum_i f_i^0 v_{i\alpha}+\nabla_\beta\sum_i f_i^0 v_{i\alpha}v_{i\beta}\right]+O(\partial^3) \tag{57}$$

$$=\nabla_\alpha\left(\tau-\frac{1}{2}\right)\left[\partial_t\left(\phi u_\alpha\right)+\nabla_\beta T_{\alpha\beta}\right]+O(\partial^3) \tag{58}$$

$$=\nabla_\alpha\left(\tau-\frac{1}{2}\right)\left[\phi\partial_t u_\alpha+u_\alpha\partial_t\phi+\nabla_\beta T_{\alpha\beta}\right]+O(\partial^3) \tag{59}$$

$$\begin{aligned}=\nabla_\alpha\left(\tau-\frac{1}{2}\right)\Bigg[\phi\Bigg(&\underbrace{\partial_t u_\alpha+u_\beta\nabla_\beta u_\alpha}_{0,\text{ Eq. (54)}}-u_\beta\nabla_\beta u_\alpha\Bigg)\\&+u_\alpha\Bigg(\underbrace{\partial_t\phi+\nabla_\beta(\phi u_\beta)}_{O(\partial^2),\text{ Eq. (53)}}-\nabla_\beta(\phi u_\beta)\Bigg)+\nabla_\beta T_{\alpha\beta}\Bigg]+O(\partial^3)\end{aligned} \tag{60}$$

$$=\nabla_\alpha\left(\tau-\frac{1}{2}\right)\left[\nabla_\beta T_{\alpha\beta}\underbrace{-\phi u_\beta\nabla_\beta u_\alpha-u_\alpha\nabla_\beta(\phi u_\beta)}_{-\nabla_\beta(u_\alpha\phi u_\beta)}\right]+O(\partial^3) \tag{61}$$

$$=\nabla_\alpha\left(\tau-\frac{1}{2}\right)\left[\nabla_\beta T_{\alpha\beta}-\nabla_\beta(u_\alpha\phi u_\beta)\right]+O(\partial^3)=\underbrace{\nabla_\alpha m\nabla_\alpha\mu}_{Eq.\ (39)}\ . \tag{62}$$

Which reveals the correct second order equilibrium moment $T_{\alpha\beta}$. This also identifies the diffusive mobility as:

$$m=\tau-\frac{1}{2}\ . \tag{63}$$

From the above analysis, the equilibrium and zero order moments are:

$$\sum_i f_i(\boldsymbol{r},t) = \sum_i f_i^0(\boldsymbol{r},t) = \phi(\boldsymbol{r},t)\,, \tag{64}$$

$$\sum_i f_i^0(\boldsymbol{r},t) v_{i\alpha} = s u_\alpha \phi(\boldsymbol{r},t)\,, \tag{65}$$

$$\sum_i f_i^0(\boldsymbol{r},t) v_{i\alpha} v_{i\beta} = s\mu(\boldsymbol{r},t)\delta_{\alpha\beta} + s^2 u_\alpha u_\beta \phi(\boldsymbol{r},t)\ , \tag{66}$$

where $s = \Delta t$ is a time-scaling constant which provides a convenient dial for selecting the fastest stable simulation dynamics with a single parameter. The resulting equation of motion as simulated by the lattice Boltzmann method is:

$$\frac{1}{\Delta t}\partial_t \phi + \nabla_\alpha \left(\phi u_\alpha\right) = \nabla_\alpha \left(\tau - \frac{1}{2}\right) \nabla_\alpha \mu + O(\partial^3)\ . \tag{67}$$

The chemical potential defined in Eq. (10) at a given lattice Boltzmann node is calculated from the concentration field, which is itself the zero-order moment calculated from the non-equilibrium distributions. Note that the chemical potential depends on the concentration and the concentration Laplacian $\mu(\phi, \nabla^2\phi)$, and since the simulated concentration is defined on a discrete lattice, the simulation method requires a discrete Laplace operator for the lattice.

Typically a finite difference method is used, where a Laplacian operation on a node depends on the values at the surrounding nodes. A commonly used discrete Laplace operator applied at position x on a one dimensional lattice is $\nabla^2\phi(x) = \phi(x-1) - 2\phi(x) + \phi(x+1)$. Additional dimensions simply add additional terms. For example

$$\nabla^2\phi(x,y) = \phi(x-1,y) + \phi(x,y-1) - 4\phi(x,y) + \phi(x+1,y) + \phi(x,y+1) \tag{68}$$

is a common discrete Laplace operator in two dimensions. Discussion of the effects of different discrete Laplace operator for LBM simulations are given by Pooley in his PhD thesis [47], and by Wagner and Pooley [61].

1.3.5. Velocity Sets & Equilibrium Distribution Functions

The equilibrium moments given in Eq. (64–66) are a set of equations, the total number of which is determined by the dimensionality of the simulation and the number of discrete velocities used. The number of discrete velocities for a given dimensionality must be large enough to fully constrain the set of equilibrium moment equations. Additionally, the set of velocities must provide sufficient isotropy in the equilibrium distributions. Once these conditions are met, the set of equilibrium moment equations are used to find the equilibrium distribution functions f_i^0 required by the LBM scheme of Eq. (34) outlined in Section 1.3.1.

In one dimensional simulations, the set of equilibrium moments constitute three equations for the equilibrium distributions. Therefore, three discrete velocities are sufficient to completely constrain the system:

$$\boldsymbol{v}_i^{1\mathrm{D}} = \{0, -1, 1\} \ . \tag{69}$$

Simple symmetry is sufficient to demonstrate that isotropy holds for this set. This velocity set allows Eq. (64–66) to be written as the following system of equations:

$$f_0^0 + f_1^0 + f_2^0 = \phi \,, \tag{70}$$

$$-f_1^0 + f_2^0 = su\phi \,, \tag{71}$$

$$f_1^0 + f_2^0 = s\mu + s^2u^2\phi \,. \tag{72}$$

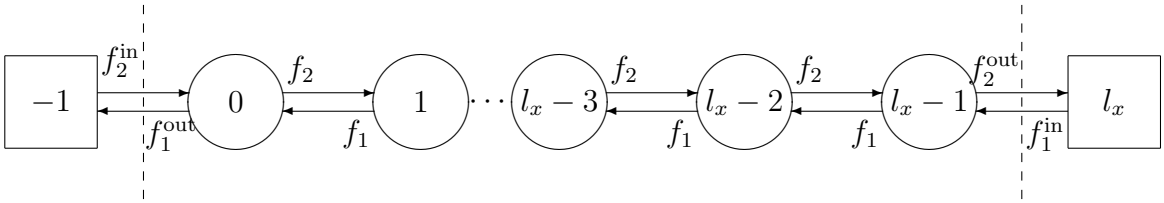

Figure 3. Illustration of a D1Q3 LBM implementation of l_x nodes with open boundaries. Circles represent simulation nodes, with the node's x-coordinate inside. Streaming between nodes is represented by arrows labeled f_1 and f_2. Squares represent off-lattice positions which take "out"-streaming distributions $[f_1^{\text{out}}(0)$, and $f_2^{\text{out}}(l_x - 1)]$ and provide "in"-streaming distributions $[f_1^{\text{in}}(l_x)$, and $f_2^{\text{in}}(-1)]$. The off-lattice positions are not simulated by LBM, but are part of the boundary condition. Boundary conditions are discussed further in Appendix G.

This system leads to the following set of equilibrium distributions:

$$\begin{aligned} f_0^0 &= \left(1 - s^2u^2\right)\phi - s\mu \ , \\ f_1^0 &= \frac{1}{2}\left[\left(s^2u^2 - su\right)\phi + s\mu\right] \ , \\ f_2^0 &= \frac{1}{2}\left[\left(s^2u^2 + su\right)\phi + s\mu\right] \ . \end{aligned} \tag{73}$$

In lattice Boltzmann terms, this is known as a D1Q3 implementation: D1 for one lattice dimension, and Q3 for three discrete lattice velocities. A schematic of the algorithm described in Section 1.3.1 for a D1Q3 implementation with open boundaries is shown in Figure 3

The situation becomes slightly more complicated in two dimensions. In situations where the flow field only has x-direction components, the velocity vector becomes:

$$\boldsymbol{u} = \begin{pmatrix} u_x \\ 0 \end{pmatrix} \ . \tag{74}$$

This is consistent with the above definition of this model for phase separation fronts, which describes a front moving through a material which experiences purely diffusive dynamics. In this case, the equilibrium moments produce a set of five equations. The

five discrete velocities

$$\boldsymbol{v}_i^{\mathrm{2D}} = \left\{ \begin{pmatrix} 0 \\ 0 \end{pmatrix}, \begin{pmatrix} -1 \\ 0 \end{pmatrix}, \begin{pmatrix} 1 \\ 0 \end{pmatrix}, \begin{pmatrix} 0 \\ -1 \end{pmatrix}, \begin{pmatrix} 0 \\ 1 \end{pmatrix} \right\} , \tag{75}$$

provide the sufficient isotropy and fully constrain the system of equations. Using this velocity set the equilibrium moments in Eq. (64–66) become the following set of equations:

$$f_0^0 + f_1^0 + f_2^0 + f_3^0 + f_4^0 = \phi , \tag{76}$$

$$-f_1^0 + f_2^0 = s u_x \phi , \tag{77}$$

$$-f_3^0 + f_4^0 = 0 , \tag{78}$$

$$f_1^0 + f_2^0 = s\mu + s^2 u_x^2 \phi , \tag{79}$$

$$f_3^0 + f_4^0 = s\mu , \tag{80}$$

which is solved for the equilibrium distributions:

$$f_0^0 = \left(1 - s^2 u_x^2\right) \phi - 2s\mu , \tag{81}$$

$$f_1^0 = \frac{1}{2} \left[\left(s^2 u_x^2 - s u_x\right) \phi + s\mu \right] , \tag{82}$$

$$f_2^0 = \frac{1}{2} \left[\left(s^2 u_x^2 + s u_x\right) \phi + s\mu \right] , \tag{83}$$

$$f_3^0 = \frac{1}{2} s\mu , \tag{84}$$

$$f_4^0 = \frac{1}{2} s\mu . \tag{85}$$

This is known as a D2Q5 LBM implementation. An illustration of this scheme with open boundaries on the x-axis is shown in Figure 4. An interesting feature of this D2Q5 implementation is that a simulation with one node in the y-direction and periodic boundaries on the y-axis is exactly equivalent to the D1Q3 implementation

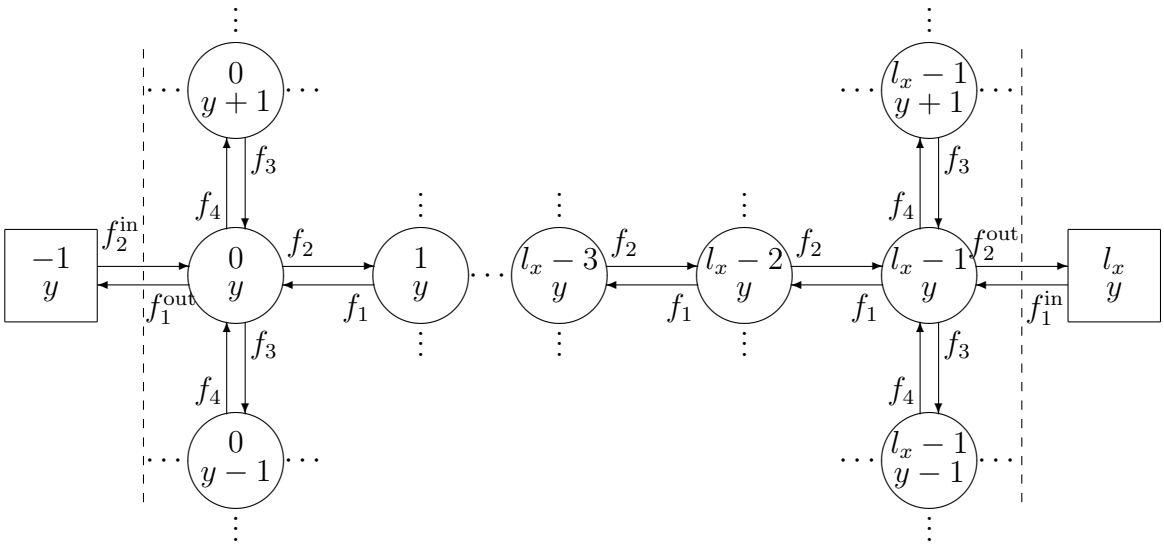

Figure 4. Illustration of a D2Q5 LBM implementation of size (l_x, l_y) with open boundaries on the x-axis. Nodes and streaming distributions are similar to the illustration in Figure 3, however here the node position is given as a column vector.

given above.

For materials which undergo fluid flow, the flow field $\boldsymbol{u}(\boldsymbol{r}, t)$ in the drift-diffusion equation (37) is coupled to the Navier-Stokes equation and the velocity field can no longer be assumed to be aligned with the x-axis. Therefore condition in Eq. (74) no longer applies. Phase separation fronts moving through two dimensional fluids is discussed further in Appendix F, and a LBM scheme is presented in Appendix E.

If the assertion in Eq. (74) of an x-axis aligned flow holds for the three dimensional system, the equilibrium moment definitions result in a set of seven equations. The following seven discrete velocities provide sufficient isotropy:

$$\boldsymbol{v}_i^{\mathrm{3D}} = \left\{ \begin{pmatrix} 0 \\ 0 \\ 0 \end{pmatrix}, \begin{pmatrix} -1 \\ 0 \\ 0 \end{pmatrix}, \begin{pmatrix} 1 \\ 0 \\ 0 \end{pmatrix}, \begin{pmatrix} 0 \\ -1 \\ 0 \end{pmatrix}, \begin{pmatrix} 0 \\ 1 \\ 0 \end{pmatrix}, \begin{pmatrix} 0 \\ 0 \\ -1 \end{pmatrix}, \begin{pmatrix} 0 \\ 0 \\ 1 \end{pmatrix} \right\} . \tag{86}$$

The equilibrium moment equations become

$$f_0^0 + f_1^0 + f_2^0 + f_3^0 + f_4^0 + f_5^0 + f_6^0 = \phi \ , \tag{87}$$

$$-f_1^0 + f_2^0 = s u_x \phi \ , \tag{88}$$

$$-f_3^0 + f_4^0 = 0 \ , \tag{89}$$

$$-f_5^0 + f_6^0 = 0 \ , \tag{90}$$

$$f_1^0 + f_2^0 = s\mu + s^2 u_x^2 \phi \ , \tag{91}$$

$$f_3^0 + f_4^0 = s\mu \ , \tag{92}$$

$$f_5^0 + f_6^0 = s\mu \ , \tag{93}$$

which is solved for the equilibrium distributions:

$$f_0^0 = \left(1 - s^2 u^2\right) \phi - 3 s\mu \ , \tag{94}$$

$$f_1^0 = \frac{1}{2} \left[\left(s^2 u_x^2 - s u_x \right) \phi + s\mu \right] \ , \tag{95}$$

$$f_2^0 = \frac{1}{2} \left[\left(s^2 u_x^2 + s u_x \right) \phi + s\mu \right] \ , \tag{96}$$

$$f_3^0 = \frac{1}{2} s\mu \ , \tag{97}$$

$$f_4^0 = \frac{1}{2} s\mu \ , \tag{98}$$

$$f_5^0 = \frac{1}{2} s\mu \ , \tag{99}$$

$$f_6^0 = \frac{1}{2} s\mu \ . \tag{100}$$

With the definition of the proper equilibrium moments, the lattice Boltzmann method described in Section 1.3.1 will simulate this model for front induced phase separation in the co-moving reference frame of the phase separation front moving through a diffusively dominated material.

1.3.6. Examples of Earlier Simulations of Phase Separation Fronts

The numerical method just described is not the first application of computer simulation to the study of front induced phase separation. Already mentioned in Section 1.1 were simulations of specific front induced phase separation systems. More general models of front induced phase separation have been developed and numerically analyzed, especially in more recent years as computing resources have grown. Background relevant to the particular subjects in Papers 1–3 is given in the appropriate introductions, however the following examples represent early fundamental work in the area and recent interesting results.

Ball and Essery developed one of the early numerical simulations of front induced phase separation in a general binary mixture. Their two-dimensional model used the same Ginzburg-Landau free energy as the one used here, however their front was designed to mimic heat diffusion, and therefore was diffuse and moved with a time dependent speed which was a function of the thermal conductivity. They observed the formation of irregular structures as well as stripe structures oriented parallel and orthogonal to the phase-separation front. The structure and stripe orientation was found to depend on the thermal conductivity and distance of travel of the front, however they did not analytically determine that dependence [4]. Early numerical simulations by Furukawa used a similar Ginzburg-Landau free energy and a constant speed front. By isolating the front speed from other parameters, Furukawa was able to show that parallel oriented lamella were formed by fast moving fronts, and orthogonal lamella were formed by slow moving fronts [21]. Much more recently, Hantz and Biró used a rotating source as a phase-separation front. They observed concentric stripe domains forming near the axis of rotation where the local front speed is slow, transitioning to radial stripe domains further out, then finally to a radius beyond which phase-separation began to lag further and further behind the front. They observed

that the concentric stripes were quite stable to coarsening, whereas the structures formed further out coarsened relatively quickly [28].

1.4. Outline

The phenomenon of pattern formation by phase separation fronts has been introduced in Section 1.1 by way of examples of physical systems which exhibit such pattern formation. The wide variety of physical systems presented motivates an approach to study pattern formation by phase separation fronts in a general way, rather than the many previous approaches which focused on specific systems. Presented in Section 1.2 is a simple model for phase separation following a moving front. The model consists of an underlying Ginzburg-Landau free energy of Eq. (2) which determines the phase stability of the material. The front as described in Section 1.2.3 is a constant speed, abrupt transition of parameters in the free energy density of Eq. (3) from single-phase stability to two-phase stability. The dynamics of phase separation are diffusive, and governed by the Cahn-Hilliard Equation (20) as described in Section 1.2.4. Like other models which use the Cahn-Hilliard Equation, this model is non-dimensionalized in Section 1.2.5, in order to enhance the generality of the results by elimination of interdependent variables. A technique for numerical simulation of this model using the lattice Boltzmann method (LBM) is presented in Section 1.3. This requires a Galilean transformation of the governing equations of the model into the co-moving reference frame of the phase separation front, resulting in the non-dimensional drift diffusion equation (37). Simulations of the model in the co-moving reference frame consist of a stationary front dividing the simulation space into two parts – a region "ahead" of the front where a single mixed phase is stable, and a region "behind" the front where two de-mixed phases are stable – with material being advected continuously across the front.

The following three papers are based on this simple model of phase separation

fronts and were previously published in peer reviewed journals. Paper 1 was published May 26, 2009 in the journal Physical Review E. This paper contains theoretical analysis and numerical simulation of front induced phase separation morphologies in one-dimensional systems for constant speed fronts, and an in-depth study of the effects of various parameters of the model is performed. A parameter-free analytical relationship between phase separation front speed and phase separated domain size is found. Results from this first paper are used extensively in the following two publications.

Paper 2 was published September 2, 2010 in the journal Communications in Computational Physics. This simple model is modified such that the front moves with diffusive speed $u \propto t^{-1/2}$. The model is analytically proven to produce Liesegang patterns for a critical range of model parameters, with all Liesegang pattern coefficients fully determined. Liesegang patterns, discussed in Section 1.1.2, are a specific type of phase separation morphology which are described by a set of Liesegang laws containing several coefficients. So far, no other models have been analytically proven to produce Liesegang patterns with parameter-free derivation of all coefficients.

The third paper was published January 5, 2012 in the journal Physical Review E. This paper contains a survey of morphologies formed by phase separation fronts in two dimensional systems. A family of different structures (an essentially one-dimensional structure of stripes oriented parallel to the front, stripes orthogonal to the front, and droplet arrays) are observed to form, depending on front speed, and mixed material volume fraction. Morphology formation was observed to experience strong hysteresis effects. To isolate the effect of hysteresis, an initial condition containing a variety of morphologies was used in order to determine the preferred morphology for a given front speed and volume fraction. An analysis of orthogonal stripe formation for symmetric volume fraction results in the discovery of a front speed dependent region

of stability and a prediction for transition from orthogonal to parallel stripes.

Orthogonal stripes formed from off-critical mixtures are observed in Paper 3 to pinch off, or reduce stripe width, at the phase separation front. This effect is explained in Appendix A as resulting from a preferred wetting angle. The wetting angle is analytically determined and compared to results from numerical simulation.

The analysis in Paper 3 of the region of stability is extended in Appendix B in order to generate predictable depth-dependent structure formation in two-dimensional systems by control of phase separation front speed. Numerical simulations with variable speed fronts in two dimensions using LBM demonstrate the effectiveness of controlled, predictable structure formation.

Additional front formed phase separation structures formed in three dimensional systems are discussed in Appendix C. This is followed by Appendix D which demonstrates depth dependent structure formation by variable speed fronts in three dimensional systems. Simulations demonstrate that morphologies similar to immersion precipitation membranes can be formed by this simple model with the inclusion of fluctuations.

The effects of hydrodynamics on the region of stability in two-dimensional systems are analyzed in Appendix F, showing that hydrodynamics introduces a cutoff of the region. The cutoff is a minimum speed, below which orthogonal stripe formation does not occur. A lattice Boltzmann method for coupling the drift-diffusion equation (37) with the Navier-Stokes equation (271) is shown in Appendix E. This allows numerical simulation of this model for phase separation fronts passing through fluids.

Open boundary conditions for two-dimensional lattice Boltzmann method simulations of moving phase separation fronts for diffusive materials are developed and analyzed in Appendix G. Open boundary conditions are needed in order to flow mixed material into, and phase separated material out of, the simulation. Several different

open boundary conditions are systematically proposed for use in lattice Boltzmann simulations of this front induced phase separation model. Boundary conditions for the inflow of mixed material have different requirements than boundary conditions for outflow of phase separated material. These requirements are discussed, and the proposed boundary conditions are tested for their ability to meet the different requirements of inflow and outflow boundaries. Unsurprisingly, it is found that the boundary condition which works best as an open inflow boundary is different than the one for the outflow.

PAPER 1. ENSLAVED PHASE-SEPARATION FRONTS IN ONE-DIMENSIONAL BINARY MIXTURES[1]

ABSTRACT: Phase-separation fronts leave in their wakes morphologies that are substantially different from the morphologies formed in homogeneous phase-separation. In this paper we focus on fronts in binary mixtures that are *enslaved phase-separation fronts*, *i.e.* fronts that follow in the wake of a control-parameter front. In the one-dimensional case, which is the focus of this paper, the formed morphology is deceptively simple: alternating domains of a regular size. However, determining the size of these domains as a function of the front speed and other system parameters is a non-trivial problem. We present an analytical solution for the case where no material is deposited ahead of the front and numerical solutions and scaling arguments for more general cases. Through these enslaved phase-separation fronts large domains can be formed that are practically unattainable in homogeneous one-dimensional phase-separation.

2.1. Introduction

Phase-separation fronts are critically important for the formation of phase-separation morphologies in many practical applications. Experiments in two-dimensional phase separation of eutectic mixtures using carefully controlled fronts have revealed a rich family of morphologies. Lamellar patterns may be formed parallel, perpendicular, or at some angle to the advancing front. Elongated stripes of droplets and highly ordered droplet lattices are just a few of the interesting minority component structures. The review by Flesselles *et al.* explain the appearance of tilt waves in eutectic

[1]Alexander Wagner (A. W.) provided the initial plan for the research presented in this paper. The model development and analysis were developed jointly by Eric Foard (E. F.) and A. W. Theoretical analysis, simulation development and execution, and analysis of results were performed by E. F. with guidance from A. W. The manuscript and figures were authored by E. F. with editorial input from A. W.

mixtures as a mechanism for the selection of the optimal, front-speed induced, stripe width [16]. This is of industrial relevance for steel production [50]. Here a binary iron-carbon alloy which is slowly cooled from one side of the sample below its critical temperature may form a structure of alternating carbon-rich and carbon-poor bands [35, 29]. More complicated mechanisms are relevant for he spontaneous pattern formation in crystal growth. These patterns can be understood as a result of a highly dynamic solidification front, as explained in an excellent review by Langer [41].

An industrial example from a very different research field is the formation of immersion-precipitation membranes [10, 1, 64]. Here a polymer-solvent mixture is immersed in a non-solvent. Phase-separation is induced as the solvent diffuses out of the mixture and is replaced by the non-solvent. Phase-separation starts at the initial interface. From there a phase-separation front advances into the mixture.

The examples above have in common that a space and time dependent parameter, *i.e.* the temperature in the binary alloy case and the solvent concentration in the immersion precipitation case, induce phase-separation. We call such a quantity a control parameter. The advance of the temperature or the solvent concentration then constitutes a control parameter front which is responsible for inducing phase-separation.

An example of essentially one dimensional patterns are Liesegang patterns. These are also believed to be an example of front-driven morphology formation. Liesegang patterns typically occur when one electrolyte diffuses into another electrolyte forming an ordered series of precipitation bands, though the exact mechanisms of band formation are still under investigation. Antal *et al.* map the ion-product supersaturation set of theories onto the same Model B equations used in this paper with the major difference of a moving source term acting as the phase-separation inducing front [2].

Despite its critical role in the formation of complex structures, only limited attention has been paid to phase-separation fronts in the soft-matter literature. In the context of phase-separation theory, the lamellar structure formation was rediscovered by Furukawa [21], who examined the phase-separation in two-dimensional binary mixtures following a sharp control parameter front. Furukawa noted that the morphology formed was strongly determined by the speed of the front, and that the morphology may change quite suddenly if the front speed is altered. Hantz and Biro [28] again noticed the front speed dependence of morphology using a novel rotating control parameter front where the front speed depends on distance from the axis of rotation. Dziarmaga and Sadzikowski [14] suggested a model that is very similar to the one presented in the current work as a model for phase-separation in the early universe, and found that for slow fronts the density of domain walls is linear with front speed, *i.e.* domain size is proportional to the inverse of front speed. More recently Gonnella *et al.* [24] considered the full dynamics of the temperature front formed in a system quenched by contact with external walls, finding that lamella form parallel to the temperature front, despite the tendency of the neutral wetting boundary condition to impose perpendicular lamella.

The dynamics of the front may in itself be a complex process. In some cases fronts are strongly influenced by the dynamics of the material they move through. As noted by Karma and Sarkissian in their analysis of banded structures which can form in some binary alloys, a planar front that induces solidification may undergo strong velocity oscillations induced by the latent heat of solidification [38]. By contrast the latent heat of phase-separation in binary mixtures is much smaller than the latent heat associated with solidification. It can typically be assumed that it has a negligible effect on the front itself.

In this paper we focus on the simplest situation of a one-dimensional binary

mixture. The phase-separation is induced by a sharp front moving with an imposed, constant velocity. When our control parameter front is not progressing too quickly a phase-separation front follows directly behind and therefore moves at the same speed. We call those fronts enslaved phase-separation fronts. In the opposite case, the phase-separation front will not keep up with the control parameter front. This then results in a free phase-separation front moving into an unstable medium. This special case has received a significant amount of attention and a good review is given by Saarloos [55].

Enslaved phase-separation fronts give rise to a host of complicated phenomena, as witnessed by the large variety of morphologies formed. For example, the previously mentioned immersion precipitation membranes [10] form very different morphologies as processing parameters are varied. In these systems the dependence is typically so strong that it becomes difficult to generate reproducible morphologies. This is why we initially focus on the simplest example of enslaved phase-separation fronts. Here we consider only one-dimensional sharp (*i.e.* not spatially extended) control parameter fronts in binary mixtures. This already gives rise to unexpected and non-trivial behavior as explained below. In particular it is noteworthy that large domains can be formed efficiently, even though such domain sizes are practically unobtainable through homogeneous phase-separation in one-dimensional systems.

In Section 2.2 we review the theory of spinodal decomposition, as it is relevant to the understanding of the dynamics of phase-separation at the front. We then define our model which consists of a Cahn-Hilliard equation with an underlying ϕ^4 free energy. The control parameter front enters though the time and space dependence of the parameters in the free energy. We expect the details of the phase-separation dynamics to depend strongly on the shape of the control parameter profile and its dynamics. To simplify our analysis in this paper we focus on the simplest case consisting

of a control parameter front which is a sharp step moving with a constant velocity. To numerically explore the dynamics of this model we developed a lattice Boltzmann method (LBM) simulation in Section 2.3. Generic results of these simulations shown in Section 2.5 elucidate the general behavior of an enslaved phase-separation front. As the control parameter front advances into the mixed region, phase-separation ensues. Excess material is then diffused both ahead of the front and through the forming domain into the next domain. This continues until switching occurs and a new domain of the opposite kind is formed. This is a regular process that repeats, resulting in regular domains after a few cycles.

To predict the morphology we only need to find the dependence of this one length-scale as a function of the nondimensional parameters of the equation of motion defined in Section 2.4. Despite its apparent simplicity this is still a non-trivial problem. We show in Section 2.6 that this can be done analytically in the case where the mobility ahead of the front is negligible and the front is moving very slowly. The main ingredients in the analytical solution are solving for the time dependence of the concentration right behind the front and the condition for the switching to a new domain. Together, those allow us to determine the switching time and hence the domain size.

Using the results from this special case as a foundation, in Section 2.7 we examine more general enslaved fronts. When we investigate the effect of non-zero mobility ahead of the front we observe in Figure 12 that domain-size has an unexpected non-monotonic dependence on mobility. We were able to qualitatively explain this behavior as a competition of the diffusive deposition of material ahead of the front and the switching condition.

With satisfactory results for this model in one dimension, we conclude with a discussion of possible extensions such as using the front speed to imprint a domain

pattern, and a road map of future research of enslaved front systems.

2.2. Phase-Separation and Fronts

As previously mentioned, phase-separation occurs after some physical control parameter, such as temperature, changes so that the system becomes thermodynamically unstable. The system forms two or more distinct coexisting phases, and the property which distinguishes the phases is called the order parameter. We are concerned with systems that transition from a one-phase state to a two-phase state as a control parameter is varied. Despite the fact that most theoretical work on phase-separation has focused on the homogeneous case, most practical cases exhibit phase-separation that does not occur everywhere-at-once, but starts at one or more initial points and spreads through the system. The boundary between phase separated and non phase separated material is called the phase-separation front. Likewise, when the control parameter changes in-homogeneously we refer to the boundary between the single phase and two-phase regions as the control parameter front. The correlation of the phase-separation front and the control parameter front depends on the exact nature of the dynamics of the control parameter.

Consider a binary mixture of $\mathcal{A}$-type and $\mathcal{B}$-type material described by the free energy:

$$F = \int dx \left[\frac{a}{2}\phi^2 + \frac{b}{4}\phi^4 + \frac{\kappa}{2}(\nabla\phi)^2 + c\phi \right] . \tag{101}$$

This is a general fourth-order expansion of more specific free energy expressions. The cubic term which would normally appear has been scaled away, without loss of generality, by choosing the critical concentration to be zero. The c parameter, which can be neglected for homogeneous control parameters, matters here because it may take different values on either side of the control parameter front. For one-dimensional binary systems the dynamics is diffusive and is described by the Cahn-

Hilliard equation

$$\partial_t \phi = \nabla(m \nabla \mu) \ , \tag{102}$$

where the chemical potential is derived from the free energy as

$$\mu = \frac{\delta F}{\delta \phi} = a\phi + b\phi^3 - \kappa \nabla^2 \phi + c \ . \tag{103}$$

Here a is the control parameter that determines the stability of the system; $a > 0$ corresponds to the one-phase region and $a < 0$ corresponds to the two-phase region. The order parameter $\phi = \rho_{\mathcal{A}} - \rho_{\mathcal{B}}$ is the concentration difference of the two components. For homogeneous parameters the linear c term can be neglected because it does not change the equilibrium properties or the dynamics of homogeneous systems. However, when $c = c(x)$ it will introduce chemical potential gradients between the material on either side of the control parameter front. Of the other parameters, m is the mobility, κ determines the interfacial energy cost, and the amplitude of the non-linear term b determines the equilibrium values of the order parameter:

$$\phi_{eq} = \pm \sqrt{\frac{-a}{b}} \ . \tag{104}$$

We now discuss different phase-separation mechanisms described by this model.

2.2.1. Homogeneous Control Parameter Change

If the control parameter does change rapidly everywhere at once—the well studied homogeneous quench—no control parameter front exists. If the system is also homogeneous in composition a phase-separation front will not form, in which case phase-separation occurs via spinodal decomposition or nucleation.

Another interesting situation occurs when the control parameter is changed

homogeneously but gradually. In such a situation, cascades of sequential phase-separation events are observed, as shown in the work of Vollmer *et al.* [58, 7]. Such phenomena are probably also exhibited for extremely extended enslaved control parameter fronts but are outside the scope of the current paper.

In the case of a homogeneous quench where the initial concentration is between the spinodal values

$$\phi_{sp} = \pm\sqrt{\frac{1}{3}}\phi_{eq} \ , \tag{105}$$

spinodal decomposition is typically observed. It manifests itself in an exponential change of the order parameter from initial fluctuations towards one of the two equilibrium values. The growth rate depends on the fluctuation's wavelength, and the fastest growing wavelength will outgrow the others and quickly dominate the morphology. This fastest growing wavelength is called the spinodal wavelength, denoted λ_{sp}. Though it is not often discussed in the analysis of homogeneous quenches, we refer to the reciprocal of the fastest growth rate as the spinodal time, denoted t_{sp}.

To derive the spinodal wavelength and time one performs a linear expansion of the Cahn-Hilliard equation (102) around the initial concentration ϕ_{in}, then Fourier transforms this linearized Cahn-Hilliard equation into k-space which results in the ODE:

$$\partial_t\tilde{\phi}(k) = -m\left[\left(a + 3b\phi_{in}^2\right)k^2 + \kappa k^4\right]\tilde{\phi}(k) = R(k)\tilde{\phi}(k) \ . \tag{106}$$

The solution of this equation is the exponential growth of fluctuations where the growth rate depends on the angular wavenumber k:

$$\tilde{\phi}(k) = e^{R(k)t} \ . \tag{107}$$

The angular wavenumber with the fastest growth rate corresponds to the spinodal

wavelength:

$$\lambda_{sp} = \frac{2\pi}{k_{sp}} = 2\pi\sqrt{\frac{2\kappa}{-(a+3b\phi_{in}^2)}} \ . \tag{108}$$

The fastest growth rate corresponds to the spinodal time:

$$t_{sp} = \frac{1}{R(k_{sp})} = \frac{4\kappa}{m(a+3b\phi_{in}^2)^2} \ . \tag{109}$$

Such a morphology, with an initial domain wavelength of λ_{sp}, will coarsen to larger length-scales, but the process is inefficient in one dimension since it obeys a logarithmic growth law $L \propto \ln(t)$ at late times [43]. Therefore it is hard to form large structures in a finite time.

From the spinodal wavelength and time we define a spinodal speed

$$u_{sp} = \frac{\lambda_{sp}}{t_{sp}} = \frac{\pi m}{\sqrt{2\kappa}}\left(-a-3b\phi_{in}^2\right)^{3/2} \ , \tag{110}$$

which can be thought of as a natural speed of phase-separation. This is important to our later analysis of the dynamics of enslaved phase-separation fronts because it allows us to define a non-dimensional front speed.

2.2.2. Free Propagation of a Phase-Separation Front

Phase-separation fronts can form if a system has become unstable due to a sudden homogeneous control parameter change and a front is nucleated. This can occur if a defect causes local phase-separation to occur much more rapidly than through spinodal decomposition. From this defect a front spreads through the system. Saarloos *et al.* performed an analysis of the speed of such fronts for many different types of systems. For a conserved order parameter system described by the Cahn-Hilliard equation (102) with $a = -1$ and $m = b = \kappa = 1$, the speed of the front,

which they call the linear spreading speed, is:

$$u^* = \sqrt{\frac{34 + 14\sqrt{7}}{27}} \left(1 - 3\phi_{in}^2\right)^{3/2} \approx 0.73 \; u_{sp} \; . \tag{111}$$

The initial domain wavelength is found to be smaller than the spinodal wavelength $\lambda^* \approx 0.35 \; \lambda_{sp}$ and the morphology then coarsens in time [55].

2.2.3. Enslaved Phase-Separation Fronts

Freely propagating phase-separation fronts can also form as a special case in a system with a control parameter front. If the control parameter front moves at a speed $u \geq u^*$, this can result in the suppression of spontaneous spinodal decomposition, yet not inhibit the advancement of a freely propagating phase-separation front. However, if the control-parameter is moving slower than the linear spreading speed $u < u^*$, the phase-separation front cannot propagate freely and becomes enslaved by the control parameter front.

The nature of a control parameter front highly depends on the particulars of the physical system. For instance, if temperature is the control parameter of a long binary metal alloy rod which is being cooled from one end, the control parameter front will resemble the familiar error-function solution of the heat-diffusion equation. However, if the same rod is being extruded from a hot oven into a cooling environment, the control parameter front will be a much sharper transition. The shape and speed of the control parameter front will have an impact on the morphology formed in the wake of the front. In this paper we focus on phase-separation fronts enslaved by a sharp control parameter front moving with a constant velocity. This sharp control parameter front will be represented by a step function for the parameters in the free energy and the mobility in the Cahn Hilliard equation.

We now introduce a lattice Boltzmann method to numerically investigate this

system. We will see that this control-parameter front induces phase-separation dynamics which is confined to a limited region around the front. Consequently we can reduce the computational cost by focusing on a narrow region around the front.

2.3. Lattice Boltzmann Method for Phase-Separation Fronts in 1D

As we mentioned above, the dynamically important region for this model is restricted to a narrow area around the front. So rather than simulate a stationary system with a front moving through it, we consider the equivalent case of material advected with velocity u past a stationary phase-separation front. This allows us to use a much smaller simulation size. This changes the diffusive equation of motion (102) to the advection-diffusion equation

$$\partial_t \phi + \nabla(u\phi) = \nabla(m\nabla\mu) \ , \tag{112}$$

where u was the constant phase-separation front speed, which now appears as the material advection speed. The parameters which define the sharp control parameter front are

$$\begin{aligned} a(x) &= a_S + (a_M - a_S)\Theta(x - x_0) \ , & (113)\\ b(x) &= b_S + (b_M - b_S)\Theta(x - x_0) \ , & (114)\\ m(x) &= m_S + (m_M - m_S)\Theta(x - x_0) \ , & (115)\\ \kappa(x) &= \kappa_S + (\kappa_M - \kappa_S)\Theta(x - x_0) \ , & (116) \end{aligned}$$

where $\Theta(x)$ is the Heaviside step function and x_0 is the position of the front. Our naming convention uses the subscript M to denote the mixing region ahead of the control parameter front, and the subscript S to denote the separating region behind the control parameter front.

This paper deals only with a one-dimensional system, and hydrodynamic effects are irrelevant for one-dimensional binary mixtures. We could therefore use one of many different methods to numerically simulate diffusive enslaved fronts, some of which are much simpler than the LBM. However, our initial interest in enslaved fronts was for higher dimensional systems where hydrodynamics may play a very important role, and we developed this LBM with those higher-dimensional simulations in mind.

The LBM implementation of the advection-diffusion equation is similar to that of the ordinary diffusion equation, however the key differences of an advecting material with spatially dependent parameters warrants further clarification. The standard lattice Boltzmann equation with the Bhatnager-Gross-Krook (BGK) approximation is

$$f_i(x + v_i, t + 1) - f_i(x, t) = \frac{1}{\tau(x, t)} \left[f_i^0 - f_i(x, t) \right] \ , \tag{117}$$

for discrete integer time, and a finite set of discrete velocities v_i defined such that x and $x + v_i$ are sites on the spatial lattice. In order to properly preserve the effect of mobility gradients in Eq. (112) we allow the relaxation time to retain position and time dependence $\tau \equiv \tau(x, t)$. To determine the macroscopic evolution equation for this model we define a continuous $f_i \equiv f_i(x, t)$, and expand the first term to second order in a Taylor series as

$$f_i(x + v_i, t + 1) = f_i + Df_i + \frac{1}{2} D^2 f_i + O(D^3) \ ,$$

where D is the total derivative operator:

$$D \equiv \partial_t + v_{i\alpha} \nabla_\alpha \ . \tag{118}$$

This allows us to rewrite Eq. (117) as

$$Df_i + \frac{1}{2}D^2 f_i + O(D^3) = \frac{1}{\tau}\left(f_i^0 - f_i\right) \ , \tag{119}$$

and to first order we obtain:

$$f_i = f_i^0 - \tau D f_i + O(D^2) \ . \tag{120}$$

With repeated use of Eq. (120) to replace f_i in Eq. (119) with the local equilibrium functions, the hydrodynamic limit of the lattice Boltzmann equation then becomes

$$Df_i^0 - D\left(\tau - \frac{1}{2}\right) Df_i^0 + O(D^3) = \frac{1}{\tau}\left(f_i^0 - f_i\right) \ . \tag{121}$$

We then define the equilibrium moments

$$\sum_i f_i = \sum_i f_i^0 = \phi \ , \tag{122}$$

$$\sum_i f_i^0 v_{i\alpha} = s u_\alpha \phi \ , \tag{123}$$

$$\sum_i f_i^0 v_{i\alpha} v_{i\beta} = s\mu + s^2 u_\alpha u_\beta \phi \ , \tag{124}$$

corresponding to a conserved order parameter and a current of $su\phi$. Summing up the Taylor expanded LBE (121) over i we obtain the equation of motion

$$s^{-1}\partial_t \phi + \nabla(u\phi) + O(\partial^3) = \nabla(m\nabla\mu) \ . \tag{125}$$

This is Eq. (112) to second order, with the addition of a parameter s which allows for rescaling simulation time. The ability to scale simulation time allows us to trade computational speed for enhanced numerical stability and improved local Galilean

invariance [60]. In this formulation the mobility m is given by:

$$m(x) = \tau(x) - \frac{1}{2} \, . \tag{126}$$

In one dimension we use three discrete velocities

$$v_i = \{0, -1, +1\} \, , \tag{127}$$

which define the set of equilibrium distributions

$$f_0^0 = (1 - s^2u^2)\phi - s\mu \, , \tag{128}$$

$$f_{-1}^0 = \frac{1}{2}\left((s^2u^2 - su)\phi + s\mu\right) \, , \tag{129}$$

$$f_{+1}^0 = \frac{1}{2}\left((s^2u^2 + su)\phi + s\mu\right) \, . \tag{130}$$

These equilibrium moments are then used with Eq. (117) to calculate the time evolution of the system.

We now have to pay the cost for smaller simulation size allowed by fixing the position of the front in terms of more complicated inflow and outflow boundary conditions. To represent a front moving in the positive x direction we define $u < 0$ which moves the material from right to left past the stationary front. This defines a fixed inflow boundary at $x = x_{max}$ and free outflow boundary at $x = 0$. Our inflow boundary condition is then given by

$$f_{-1}(x_{max}, t+1) = f_{+1}(x_{max}, t) + su\phi_{in} \, , \tag{131}$$

which ensures a constant material influx $j_{in} = u\phi_{in}$. On the other end of the simula-

tion we have a free advection outflow boundary condition

$$f_{+1}(0, t+1) = f_{-1}(0, t) - su\phi(0, t) \ , \tag{132}$$

ensuring an outflow of $j_{out} = u\phi(0)$. Both boundary conditions are implemented as the densities are advected. The boundary conditions are open and therefore the total integral of the order parameter is not conserved. To calculate the derivatives of the concentration required for the calculation of μ in Eq. (103) at the boundaries, we define the concentrations outside the lattice to be

$$\phi(x_{max} + 1, t) = \phi_{in} \ , \tag{133}$$

$$\phi(-1, t) = \phi(0, t) \ . \tag{134}$$

This fully defines our lattice Boltzmann method.

2.4. Dimensional Analysis

Our main purpose is to predict the final morphology formed by enslaved phase-separation fronts. In Figure 5 we show the evolution of the phase-separation front and we see that only regular alternating domains are formed. Thus, the final morphology is fully characterized by the length of the domains formed as a function of the parameters:

$$\lambda = \lambda(a_M, a_S, b_M, b_S, m_M, m_S, \kappa_M, \kappa_S, c_M, c_S, u, \phi_{in}) \ . \tag{135}$$

However, not all of these parameters are independent. To reduce the number of free

parameters we define the following non-dimensional scales:

$$X = \frac{x}{\lambda_{sp}} = \frac{x}{2\pi}\sqrt{\frac{-a_S}{2\kappa_S}}\,, \tag{136}$$

$$T = \frac{t}{t_{sp}} = \frac{t m_S a_S^2}{4\kappa_S}\,, \tag{137}$$

$$\Phi = \frac{\phi}{\phi_{eq}} = \phi\sqrt{\frac{b_S}{-a_S}}\,. \tag{138}$$

Here the length and time are scaled by their spinodal values, and the concentration is scaled by the positive equilibrium concentration of the separated material. In contrast with homogeneous quench spinodal decomposition and free-front propagation, the initial non-dimensional concentration (ϕ_{in}) does not play a meaningful role in the scaling of the dynamics of phase-separation for enslaved front systems. We therefore set $\phi_{in} = 0$ for the definition of spinodal wavelength in Eq. (108) and spinodal time in Eq. (109) used for non-dimensionalization.

When we apply these non-dimensionalizations to the equation of motion (112) we obtain:

$$\partial_T\Phi + \nabla_X\left(\frac{u}{u_{sp}}\Phi\right) = \frac{1}{2\pi^2}\nabla_X\left(\frac{m(x)}{m_S}\nabla_X \left(\frac{-a(x)}{a_S}\Phi + \frac{b(x)}{b_S}\Phi^3 - \frac{1}{8\pi^2}\frac{\kappa(x)}{\kappa_S}\nabla_X^2\Phi + \frac{c(x)}{-a_S\phi_{eq}}\right)\right)\,. \tag{139}$$

This leaves us with the following dimensionless parameters:

$$U = \frac{u}{u_{sp}} = \frac{u}{\pi m_S}\sqrt{\frac{2\kappa_S}{(-a_S)^3}}\,, \tag{140}$$

$$M = \frac{m_M}{m_S}\,,\; A = -\frac{a_M}{a_S}\,,\; B = \frac{b_M}{b_S}\,,$$

$$K = \frac{\kappa_M}{\kappa_S}\,,\; C = \frac{c_M - c_S}{a_S\phi_{eq}}\,. \tag{141}$$

In the mixed material region the free-energy is a convex function. We can therefore linearize the free-energy around the mean concentration. Formally this is equivalent to setting $b_M = 0$ and obtaining new a_M and c_M parameters. We therefore consider B an irrelevant non-dimensional parameter and choose it to be zero.

For equal concentrations and our symmetric free-energy the c_M parameter is always zero. For unequal concentrations and negligible mobility ahead of the front, the c_M parameter is irrelevant because there is no dynamics in the mixing region. For non-negligible mobility C is expected to be relevant and lead to a long-range diffusive profile in the mixed region. This effect, however, is outside the scope of this paper.

We do not expect there to be a strong dependence of interfacial free-energy on the control parameter, and thus little difference between κ_S and κ_M. Additionally, due to the large size of structures being formed, front induced phase separation should be insensitive to changes in interfacial free energy. We therefore set $K = 1$. This results in a non-dimensional domain wavelength which is a function of four non-dimensional parameters:

$$L = L(A, M, U, \Phi_{in}) \; . \tag{142}$$

To investigate the dependence of L on U we first turn to numerical simulations.

2.5. Simulation Results

Let us first consider a generic simulation to discuss the main features of morphology formation. The result of one simulation using this one-dimensional LBM implementation is shown in Figure 5 as a space-time plot of concentration and chemical potential. It is clear from this plot that the dynamics of phase-separation is limited to the region around the front, and the chemical potential away from the front is flat. This simulation started with equal parts $\mathcal{A}$-type and $\mathcal{B}$-type material in the mixed region, and the $\mathcal{A}$ and $\mathcal{B}$ domains formed after the front passed are therefore of equal

size.

We shall now examine the domain formation using the middle $\mathcal{A}$-type domain in Figure 5 as an example. Three key events in the formation of this domain are marked A, B, and C. At point A the domain is nucleated. The concentration plot shows a very narrow domain and the chemical potential plot shows the previous peak collapsing toward a flat profile. The domain there expands as it is pulled along with the front. To grow this domain, $\mathcal{B}$-type material must be transported away. From the gradient on the chemical potential we see that most of this material is pulled across and deposited on the back of the domain, which advances the back interface of the domain. Some of the rest is pushed ahead of the front, and a small amount builds up on the forming domain just behind the front. These last two depositions have the effect of making the forming domain increasingly unstable as the concentration at the front increasingly deviates from the equilibrium concentration. To maintain the currents of material away from the interface, the chemical potential gradients must be maintained. Therefore the trough in the chemical potential deepens.

At point B the $\mathcal{A}$-type domain has just detached from the front as a new $\mathcal{B}$-type domain has been nucleated. The chemical potential very quickly becomes flat across the newly detached $\mathcal{A}$-type domain as it fully separates to the positive equilibrium concentration. However, the formation of a $\mathcal{B}$-type domain at the front causes $\mathcal{A}$-type material to be deposited on the leading edge of the detached domain, thereby expanding it. The interface between the $\mathcal{A}$-type domain and the new $\mathcal{B}$-type gets pulled along by the front, but is moving with about half the front's speed. The rate of deposition of material on this moving interface is nearly constant as revealed by the almost constant linear slope of the chemical potential.

Point C marks the end of the formation of the domain by the enslaved phase-separation front as yet another domain is nucleated. The chemical potential curve

has become flat immediately adjacent to the domain, and all material currents to the interfaces have stopped. The domain is now completely stationary. Because the domains are highly ordered and much larger than the interface width, they do not evolve further at any appreciable rate [43].

We now qualitatively understand how the morphology is formed by a one-dimensional enslaved front. To make quantitative statements we need to measure the relevant quantities from the LBM simulations of our model.

2.5.1. Measurement Methods

The sizes of domains formed are found numerically by determining the length between zero-crossings of the concentration. To find the zero-crossing point to sub-lattice precision we linearly interpolate between the two lattice sites on either side of the crossing. The first two domains after the control parameter front are still forming and expanding, therefore domain length measurements begin at the third zero-crossing behind the front and is an average of two or more domains. To ensure that there are enough fully-formed domains, we dynamically grow the simulation to always keep the number of interfaces behind the front greater than those used to calculate a meaningful average. The measurement is recorded once the uncertainty in the domain length is both less than one lattice spacing, and less than one thousandth the domain length itself. To more directly compare our enslaved front system to previous work, we double the domain size to find the domain wavelength. For asymmetric ($\phi_{in} \neq 0$) the domain size is multi-valued and may lead to some confusion. In this paper, however, we only present domain wavelength measurements for symmetrically mixed material.

In addition to the sizes of domains formed, we need to know the time-dependent concentration of the partially phase-separated material near the front. We cannot simply measure the concentration at the front, as it would always be near zero due

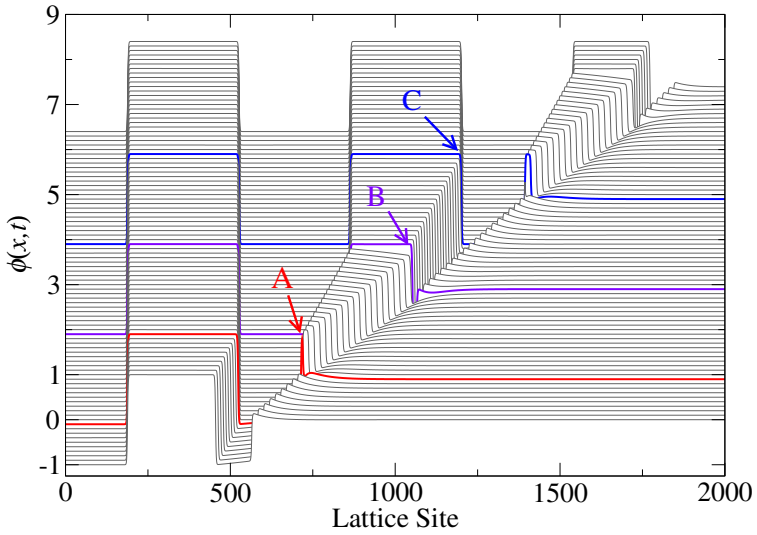

(a) Concentration $\phi(x,t)$

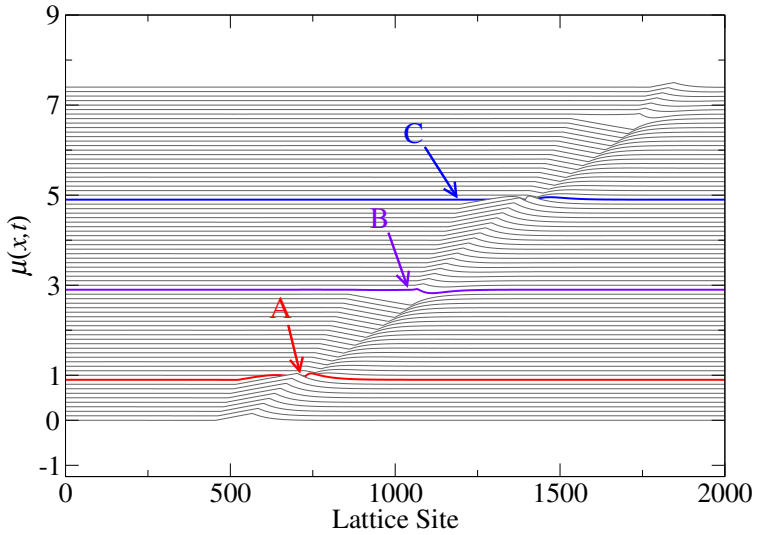

(b) Chemical Potential $\mu(x,t)$

Figure 5. (color online) Timelapse plots for an enslaved phase-separation front moving from left to right at constant speed $U = 0.001$ leaving regular alternating domains in its wake. The first recorded profile is at the bottom of the graph with subsequent profiles shifted in the positive y-axis. Each profile is separated by 200,000 iterations, or a non-dimensional time difference $\Delta T = 12{,}500$. The x-axis scale is in lattice sites. The upper graph shows the concentration profile over nearly two cycles of domain formation. The concentration ahead of the front can be seen to increase over time as the width of the two domains behind the front increases, until a new domain is nucleated. The lower graph is the total chemical potential for this system, showing that the gradient of the chemical potential is flat except for just ahead of the front and across the first domain behind the front. Simulation parameters $A = 1$, $M = 0.1$, $\kappa = 2$, $\phi_{in} = 0$, and $s = 0.1$ were chosen primarily for display purposes, and similar patterns will be produced for other parameters.

to the interface there. However, since the chemical potential is continuous across the front we can invert the bulk chemical potential (defined as Eq. (103) for $\kappa = 0$) to find the relevant concentration. As shown in the time-lapse plots of Figure 5, the chemical potential has a local extremum at the location of the control parameter front. The chemical potential value we use to find the near-front concentration is the inter-lattice extremum value of a polynomial fitted to the three most-extreme values near the front.

2.5.2. Domain Size as a Function of Front Speed

Since it is the speed of the control parameter front that determines whether the phase-separation front is enslaved, and for many physical systems the front speed may vary over time, it seems natural to first observe how the front speed determines the size of domains. In addition, the interfacial free energy cost κ plays an important role in determining homogeneous and free-front length scales. Therefore its effect on domain size will also be investigated.

As shown in Figure 6a, domains get larger the slower the front becomes. Also evident is that the larger the domains become the smaller the effect from the interfacial free energy, and that for slow enough front speeds the effect would become negligible. However, we know from our non-dimensionalization of the equation of motion that all dependence on the interfacial energy cost should scale away completely, but only if the simulation is capable of faithfully reproducing the equation of motion. In Figure 6b the non-dimensional rescaling of the top plot is shown, revealing an impressive data collapse onto a single curve.

The data collapse provided by the non-dimensionalization, though not unexpected, is very encouraging. We can be confident that the appropriate parameters for continued investigation of this model are those revealed in Eq. (141) by the non-dimensionalization procedure. In the remainder of this paper, we investigate the

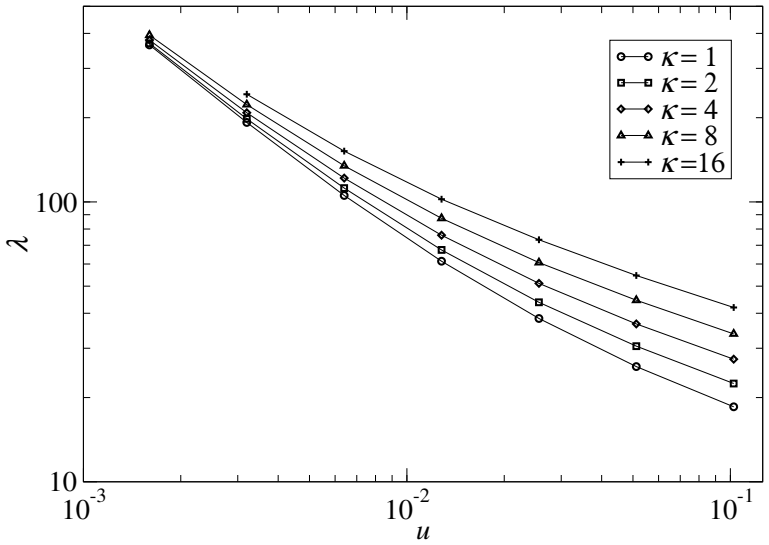

(a) Domain sizes as a function of u and κ.

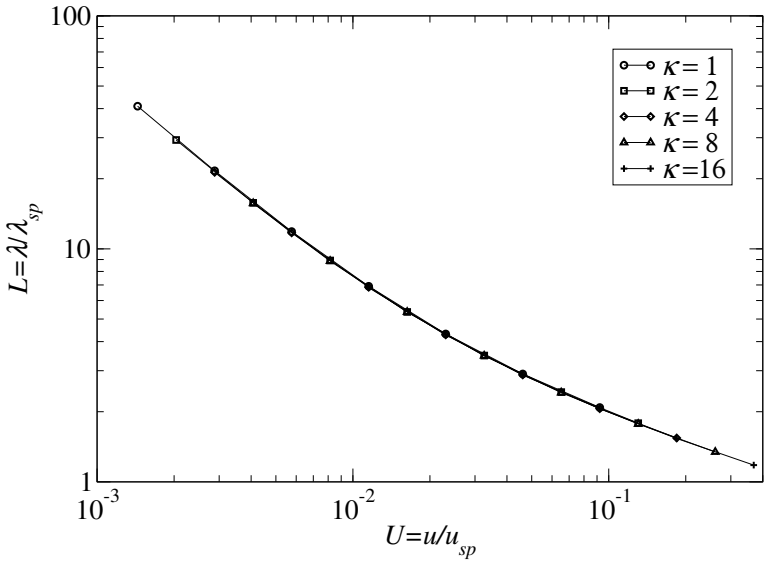

(b) Nondimensionalized domain wavelengths.

Figure 6. Simulation results for domain wavelength λ as a function of phase-separation front speed u for various interfacial energy costs. Results are shown for raw data (top) and after rescaling to non-dimensional lengths and speeds (bottom). A single constant value of mobility $m_M = m_S = 1/2$ was used for these simulations.

dependence of the domain wavelength on the non-dimensional parameters given in Eq. (142). We now analytically investigate a situation where the non-dimensional front speed U is the only relevant non-dimensional parameter.

2.6. Analytical Solution for Zero Mixed Phase Mobility $M = 0$

To develop an analytical theory of domain formation we focus on the special case of $M = 0$, where there is no dynamics in the mixed material ahead of the front. This reduces the relevant parameters to just the enslaved front speed U. All other dimensionless parameters are irrelevant since there is no dynamics ahead of the front. Due to its simplicity, this system lends itself especially well to an analytical approach. We will predict the resultant morphology (domain wavelengths) by explicitly solving the dynamics of phase-separation at the front. We accomplish this in two parts: determine the time-dependence of the concentration just behind the front, and find the concentration at which a new domain will nucleate. By combining these two results we find the switching time t_{sw}, and thus the domain wavelength:

$$\lambda = 2ut_{sw} \ . \tag{143}$$

To numerically verify our analytical results we cannot simply set the mobility of the mixed region to zero. This would require that $\tau_M = 1/2$, which would lead to an unstable simulation [8]. Instead, the $M = 0$ case is implemented by placing the control parameter front at the positive boundary, and defining the off-lattice concentration as ϕ_{in}.

2.6.1. Concentration at the Front

To determine the time evolution of the concentration at the phase-separation front we examine the current of material into and out of the domain interface formed at the front. We first assume the interface to be sharp by comparison to the size of the domain forming at the phase-separation front. From the definition of the non-dimensional speed U in Eq. (140) we can see that $U \propto \sqrt{\kappa}$. Thus a vanishing cost of interfacial free energy ($\kappa \to 0$) is equivalent to assuming the front speed is much

slower than the spinodal velocity, *i.e.* $U \ll 1$. This assumption of a slow front speed is not especially limiting to our analysis as we are primarily interested in the formation of large stable structures; unlike those found for front speeds approaching the free-front speed u^* which are small and rapidly coarsen [55].

The buildup rate of material in a region is

$$J = \int \partial_t \phi \, dx = \int \nabla \cdot \mathbf{j} \, dx \, , \tag{144}$$

where the current $\mathbf{j}$ at a point is determined by the gradient of the chemical potential:

$$\mathbf{j}(t) = -m \nabla \mu(t) \, . \tag{145}$$

We're interested in the region of the interface forming directly behind the front at position $x = x_0$. Since that region is vanishingly small, the rate of material deposited there can be written as a difference of the chemical potential gradients on either side of the front

$$\begin{aligned} J &= \int (m_M \nabla \mu_M - m_S \nabla \mu_S) \delta(x - x_0) \, dx \\ &= m_M \nabla \mu_M - m_S \nabla \mu_S \, . \end{aligned} \tag{146}$$

Since the mobility ahead of the front is zero, the time dependent rate of deposition for the interface forming at the front is:

$$J(t) = -m_S \nabla \mu(t) \, . \tag{147}$$

The gradient of the chemical potential across the entire forming domain is nearly constant, as can be seen in Figure 5. This means that material pulled behind the front is transported all the way across the forming domain and deposited on the

second domain. Any deviation from a linear profile of the chemical potential is of order $\partial_t \phi$, as can be seen from the Cahn-Hilliard equation (102) and the fact that $\phi(x,t)$ is nearly stationary inside the forming domain.

The value of the chemical potential at the phase-separation front μ_0 changes with time, but the chemical potential at the other end of the domain is zero. We can therefore write the chemical potential gradient as

$$\nabla\mu(t) = \frac{\mu_0(t)}{\ell(t)} \ , \tag{148}$$

where ℓ is the width of the domain forming at the phase-separation front.

The interface at the phase-separation front moves with the front, expanding the domain forming behind it. This requires that the rate of material deposited into the phase-separation front interface be equal to the difference in concentration across the interface times the front speed

$$J(t) = u\left[\phi_0(t) - \phi_{in}\right] \ , \tag{149}$$

where u is the (dimensional) front speed, $\phi_0(t)$ is the concentration at the phase-separation front, and ϕ_{in} is the mixed-material concentration.

The $M = 0$ condition means that none of the wrong-type material can be pushed ahead of the phase-separation front; instead it must be transfered across and deposited behind the forming domain. This results in the expansion of the second domain by moving the interface at a speed $u_I \leq u$ which trails the phase-separation front. Taking this into account, and using an argument similar to the one used to derive Eq. (149), we can write another expression for the rate of material deposition behind the front in terms of material removed and transported to the second interface.

We obtain

$$-J(t) = (u - u_I(t))2\phi_{eq} \ , \tag{150}$$

where $2\phi_{eq}$ is the change in concentration across the fully formed interface, and ϕ_{eq} is the equilibrium concentration given by Eq. (104). For now we'll continue to write ϕ_{eq}, and eliminate the variable later through non-dimensionalization.

The width of the first domain is found by integrating over time the relative speeds of the interfaces at both ends of the domain

$$\ell(t) = \int_0^t u_I(t)\, dt = u \int_0^t \left(1 + \frac{\phi_0(t) - \phi_{in}}{2\phi_{eq}}\right) dt \ , \tag{151}$$

where we eliminated u_I by combining Eq. (149) and Eq. (150). We then combine Eq. (147) with Eq. (149), use the definition of $\nabla\mu(t)$ from Eq. (148), then substitute the definition of the chemical potential for our model, to find the following alternative expression for the forming domain's width:

$$\ell(t) = -\frac{m_S}{u}\frac{\mu_0(t)}{\phi_0(t) - \phi_{in}} = -\frac{m_S}{u}\frac{a_S\phi_0(t) + b_S\phi_0^3(t)}{\phi_0(t) - \phi_{in}} \ . \tag{152}$$

Equating Eq. (151) with Eq. (152) we find the integral equation

$$\int_0^t \left(1 + \frac{\phi_0(t) - \phi_{in}}{2\phi_{eq}}\right) dt = -\frac{m_S}{u^2}\frac{a_S\phi_0(t) + b_S\phi_0^3(t)}{\phi_0(t) - \phi_{in}} \ , \tag{153}$$

for the concentration at the phase-separation front as a function of time. Differentiation of Eq. (153) with respect to time yields

$$1 + \frac{\phi_0 - \phi_{in}}{2\phi_{eq}} = -\frac{m_S}{u^2}\left(\frac{b_S\phi_0^2\left(2\phi_0 - 3\phi_{in}\right) - a_S\phi_{in}}{\left(\phi_0 - \phi_{in}\right)^2}\right)\partial_t\phi_0 \ . \tag{154}$$

Therefore

$$\partial_t \phi_0 = \frac{-u^2(\phi_0 - \phi_{in})^2(2\phi_{eq} + \phi_0 - \phi_{in})}{2m_S\phi_{eq}\left(b_S\phi_0^2\left(2\phi_0 - 3\phi_{in}\right) - a_S\phi_{in}\right)} \,, \tag{155}$$

where the time dependence of ϕ_0 is implied. We non-dimensionalize this using Eqs. (136-138), and obtain

$$\partial_T \Phi_0 = \pi^2 U^2 \frac{(\Phi_0 - \Phi_{in})^2(2 + \Phi_0 - \Phi_{in})(3\Phi_{in}^2 - 1)}{2\Phi_0^3 - 3\Phi_0^2\Phi_{in} - \Phi_{in}} \,, \tag{156}$$

which, for general U and Φ_{in}, can be solved numerically.

For the $\Phi_{in} = 0$ case of symmetric inflow concentration, Eq. (156) simplifies to

$$\partial_T \Phi_0 = -\pi^2 U^2 \left(\frac{1}{\Phi_0} + \frac{1}{2}\right) \,. \tag{157}$$

The initial concentration must be at equilibrium ($\Phi_0(0) = 1$), allowing us to find the analytical solution

$$\Phi_0(T) = 2 + 2W\left(-\frac{1}{2}\exp\left(\frac{1}{4}\pi^2 U^2 T - \frac{1}{2}\right)\right) \,, \tag{158}$$

where W is the principal branch of the Lambert W function. The Lambert W function is the solution to the equation $x = W(x)\exp(W(x))$ for complex x and has infinitely many branches. The principal real branch used for this solution is plotted in Figure 7, and more information on the Lambert W function can be found in [13].

As explained earlier, our simulations are able to track and record the concentration at the front by inverting the chemical potential. In Figure 8 we show that the analytic solution is in excellent agreement with our simulation results for slow phase-separation front speeds. For faster fronts there is a deviation which is consistent with our assumption of small U.

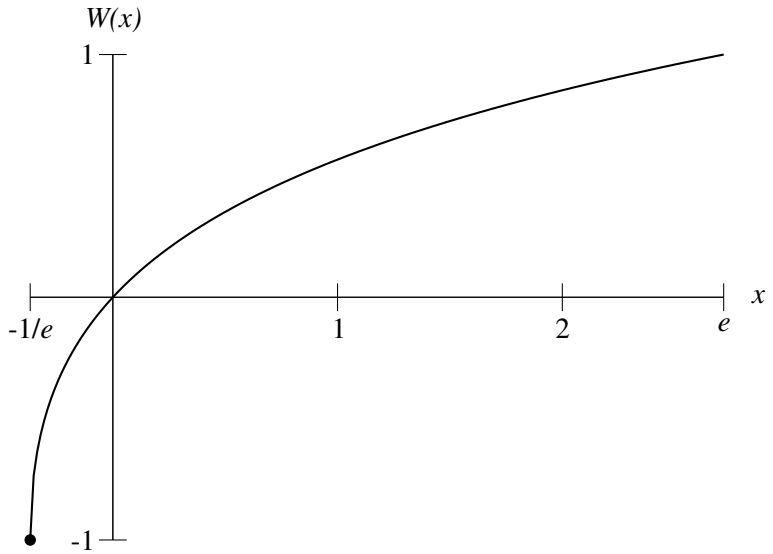

Figure 7. Real principal branch of the Lambert W function for $1/e \leq x \leq e$ [13]. The Lambert W function appears in the solution for an enslaved front with $M = \Phi_{in} = 0$ for $U \ll 1$.

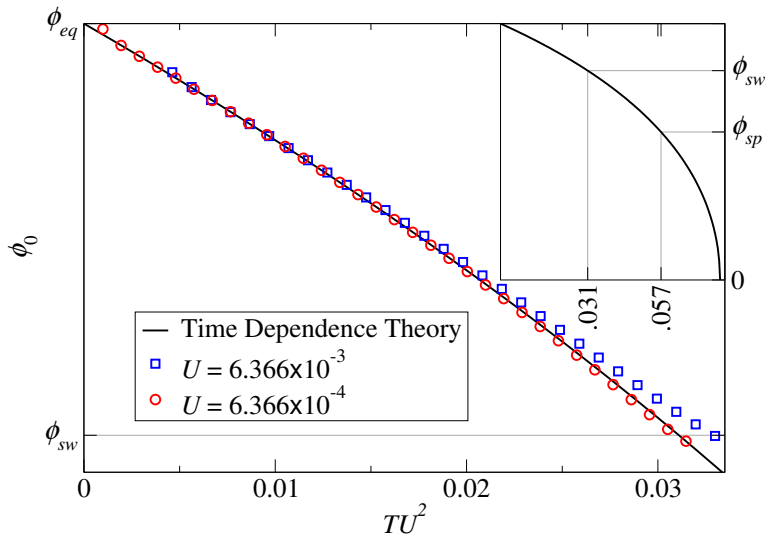

Figure 8. (color online) Comparison of the simulation results for the time evolution of the concentration at the phase-separation front for fast and slow front speed with $\phi_{in} = 0$. Note that the fast phase-separation front speed simulation shows marked deviation from the theoretical curve, as expected. Also note that the concentration at which the domain switches (ϕ_{sw}) does not seem to depend on front speed. Inset shows the full theoretical curve, though concentration should never go below ϕ_{sp} as that is unconditionally unstable and would immediately undergo spinodal decomposition. While not essential to this analysis, zero concentration occurs for $TU^2 = (\ln(16) - 2)/\pi^2 \approx 0.078$.

2.6.2. Switching Condition

We will now need to determine when a new domain will be formed. At first glance one might expect that the system will switch when the concentration reaches its spinodal value. As we saw in Figure 8, however, the switch typically occurs much earlier. Consider an $\mathcal{A}$-rich domain forming behind the front. Overtaken material can either extend the existing domain by transporting away excess $\mathcal{B}$-type material, or nucleate a new $\mathcal{B}$-rich domain; we will see that the system will choose the option that most rapidly minimizes the total free energy. We now observe that there is already an interface between the domain forming behind the front and the material the front is overtaking. Because the interface required to nucleate a new domain is already in place, we only need to consider the bulk free energy for the switching mechanism. The inflowing material will nucleate a new domain, even without fluctuations, when such a domain formation continuously minimizes the bulk free energy.

This argument is sketched in Figure 9. The concentration of the potential nucleus of $\mathcal{B}$-type material forms one point on the free energy curve. The other point on the free energy curve is the concentration of phase-separated $\mathcal{A}$ material just behind the front. If the line-segment intersects the free energy curve at some other point, the free energy can be lowered by dissolving the potential type-$\mathcal{B}$ nucleus, thus diluting the domain of type-$\mathcal{A}$ material. Nucleation will occur if the line-segment connecting these two points on the free energy curve is below the free energy curve. Thus the system will always switch before the spinodal concentration is reached.

In our case the mixed material ahead of the control-parameter front has a vanishingly small mobility ($M = 0$), so the effective concentration of material ahead of the front is simply ϕ_{in} the concentration of the overtaken mixed material. With that point firmly fixed on the free energy curve, we can predict the critical concentration at which domain switching will occur.

We denote the switching concentration—the concentration at which domain switching due to nucleation occurs—as ϕ_{sw}. We just need to find the line which lies tangent to ϕ_{sw} on the free energy curve and crosses the nucleation kernel concentration ϕ_{in}. The slope of this line is the slope of the bulk free energy curve evaluated at the switching concentration. This is also the definition of the chemical potential at the switching concentration.

$$\frac{F(\phi_{sw}) - F(\phi_{in})}{\phi_{sw} - \phi_{in}} = \left.\frac{dF}{d\phi}\right|_{F(\phi_{sw})} = \mu(\phi_{sw}) \ . \tag{159}$$

This construction is illustrated in Figure 9, and results in the closed-form solution for the switching concentration:

$$\phi_{sw} = -\frac{\phi_{in}}{3} \pm \sqrt{\frac{2}{3}\phi_{eq}^2 - \frac{2}{9}\phi_{in}^2} \ . \tag{160}$$

We verified Eq. (160) using our LBM simulations by tracking the peak of the chemical potential near the front during a complete half-cycle and recording the maximum value of the peak for different inflow concentrations ϕ_{in}. This is then inverted to find the concentration as a function of the chemical potential. The concentration at the maximum value of the chemical potential peak is the switching concentration. The results of this test are shown in Figure 10, and demonstrate excellent agreement with the theoretical prediction in the range of $-\phi_{sp} < \phi_{in} < \phi_{sp}$. Outside this range the system is meta-stable and we do not find alternating domains since we do not consider fluctuations required to induce nucleation.

2.6.3. Domain Size

The expression for the switching concentration in Eq. (160) is trivially non-

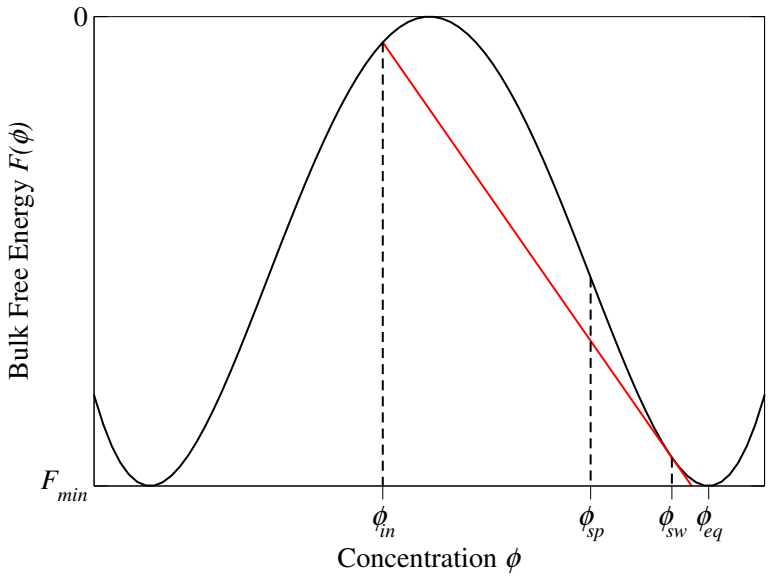

Figure 9. (color online) Free energy tangent construction for the switching condition for an enslaved phase-separation front. The nucleation kernel has concentration ϕ_{in} and domain type switching will occur when the concentration just behind the front reaches ϕ_{sw}. Also marked are the equilibrium (ϕ_{eq}) and spinodal (ϕ_{sp}) concentrations.

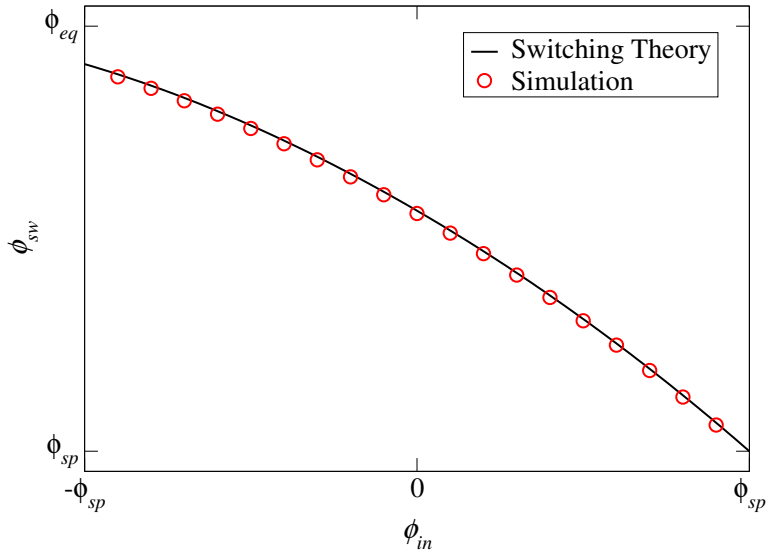

Figure 10. (color online) Verification of the switching condition for various mixed material concentrations. The solid line shows the analytic solution for the value of ϕ behind the front at which switching occurs. The circles are switching concentrations recorded from LBM simulations. The simulation parameters were $M = 0$, and $U = 6.366 \times 10^{-3}$.

dimensionalized

$$\Phi_{sw} = -\frac{\Phi_{in}}{3} \pm \sqrt{\frac{2}{3} - \frac{2}{9}\Phi_{in}^2} \,, \tag{161}$$

as is the expected domain wavelength

$$L = 2UT_{sw} \,. \tag{162}$$

Here T_{sw} is the non-dimensional switching time defined as the time when the concentration at the front reaches the switching concentration. Plugging the switching concentration of Eq. (161) for symmetric mixed material inflow ($\Phi_{in} = 0$) into the solution of the differential equation for the concentration at the front, presented in Eq. (158), yields

$$\Phi_{sw} = \sqrt{\frac{2}{3}} = 2 + 2W\left(-\frac{1}{2}\exp\left(\frac{1}{4}\pi^2 U^2 T_{sw} - \frac{1}{2}\right)\right) \,, \tag{163}$$

which can be inverted to solve for the switching time:

$$T_{sw} = \frac{2\left(\sqrt{6} + 6\ln\left(2 - \sqrt{2/3}\right) - 3\right)}{3\pi^2 U^2} \,. \tag{164}$$

With this value for the switching time we can, at long last, explicitly solve for the domain wavelength

$$L(U) = \frac{4\left(\sqrt{6} + 6\ln\left(2 - \sqrt{2/3}\right) - 3\right)}{3\pi^2 U} \,, \tag{165}$$

as a function of phase-separation front speed for symmetric inflow ($\phi_{in} = 0$). This solution contains no free parameters and only relies on the front speed being much smaller than the spinodal speed.

We verify Eq. (165) by comparing it to data taken from the LBM simulations.

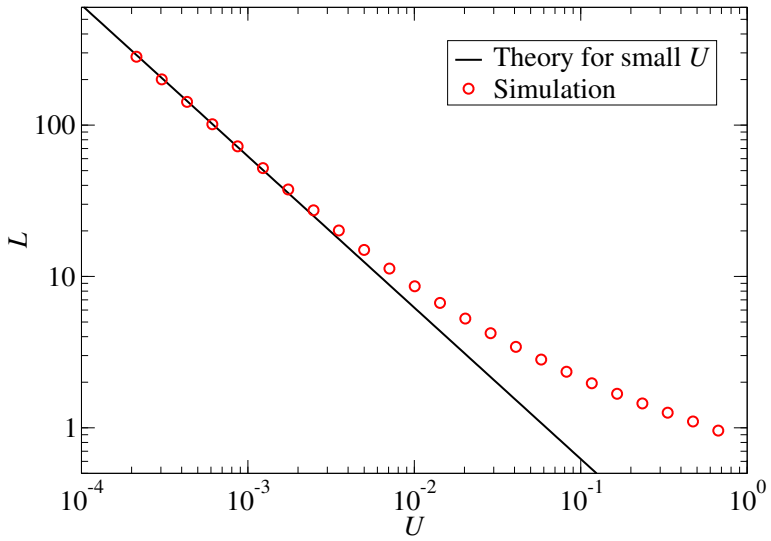

Figure 11. (color online) Analytical and numerical domain wavelength as a function of phase-separation front speed. Non-dimensional domain wavelengths L for zero mixed material mobility $M = 0$ from lattice Boltzmann method simulations agree very well with the analytical prediction for slow speed $U < 10^{-3}$ phase-separation non-dimensional fronts. Note that the theory contains no adjustable parameters.

The results are shown in Figure 11. We see that the simulation results are in excellent agreement with our theoretical parameter-free prediction for non-dimensional phase-separation front speeds slower than $U \sim 10^{-3}$.

The domain wavelengths for asymmetric inflow ($\Phi_{in} \neq 0$) can similarly be obtained by numerically solving Eq. (156) for the switching time as a function of ϕ_{in}.

2.7. Some Properties of More General Cases

We have successfully developed an analytical expression for the morphology formed by an enslaved phase-separation front in the special case where there is no mixed material dynamics and the mixed material is symmetrically composed. We accomplished this by constructing a differential equation from the analysis of currents which drive the dynamics of phase-separation at the front. We could only solve this differential equation analytically after the simplification allowed by assuming symmetric mixed material, however the more general case can be tackled numerically. Along

these same lines, one should be able to construct an even more general differential equation which includes dynamics ahead of the control-parameter front. However, even without such an in-depth analysis we can, at least qualitatively, understand the effects of mixed material mobility on domain formation.

We "turn-on" the dynamics ahead of the control parameter front by setting the non-dimensional mobility M to some positive value. This results in a family of curves in the L vs. U plane, each of which are similar in shape to Figure 6(b). To see how this affects the size of domains formed we can choose some slow front speed and perform a series of simulations with varying M. The results of such a series of simulations is shown in Figure 12. We observe a rapid but continuous reduction in domain wavelength as the non-dimensional mobility is increased from zero, until it reaches a minimum. We should mention that data of two different kinds of simulation are shown in the graph. The simulation for $M = 0$ where the front is at the inflow boundary, and $M > 0$ where the front is firmly inside the lattice. There is excellent agreement between the methods.

After the sharp reduction levels off, L increases with M and eventually results in the formation of very large domains. This non-monotonic behavior is discussed below, followed by an explanation of the effects of the final free non-dimensional parameter A.

2.7.1. Small Mixed Mobility ($M \ll 1$)

If the dynamics of material ahead of the front are very slow by comparison to the separated region, the currents are almost identical to the case of no mixed-material dynamics. Such a case could be physically realized for a system where the mobility strongly increases with temperature and we have a lower critical point. In this case, very little material is allowed to build up ahead of the front. Currents ahead of the front are then vanishingly small. What does change, due to this small buildup ahead of

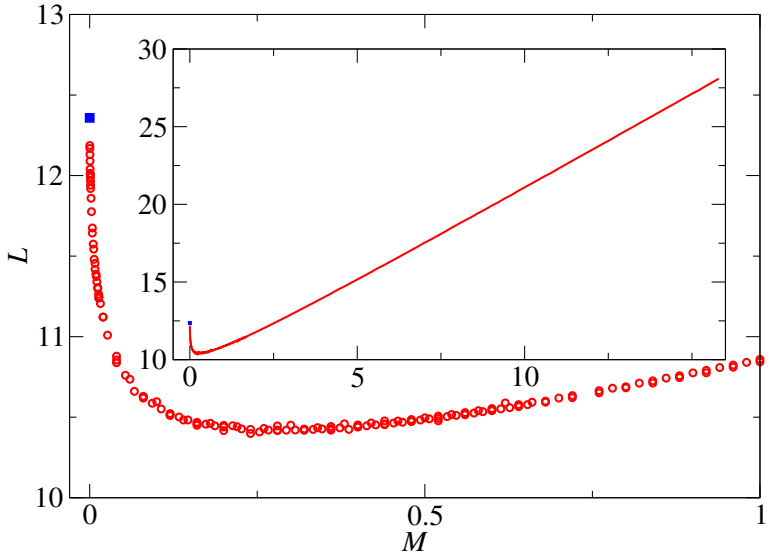

Figure 12. (color online) Dimensionless domain wavelength L as a function of mobility ratio M obtained from LBM simulations. The inset plot shows the same data over larger mobility ratio range. This shows how the family of curves found in the L vs. U plane depends on M. For the red (online) circles, the phase-separation front speed was kept a constant at $U = 6.366 \times 10^{-3}$, while κ, m_S and m_M were varied. The blue (online) square is from a simulation of the special case $M = 0$ at the same non-dimensional speed. Note this curve is not monotonic.

the front, is that the front is now overtaking a slightly larger nucleus of material. This slightly larger nucleus will make domain type switching more energetically favorable.

We can see the effect a small increase in nucleus volume has on the switching condition by re-examination of Figure 9. A slightly larger nucleation kernel has the effect of shifting ϕ_{in} towards the opposite material type. This results in a shallower tangent line construction which contacts the free energy curve closer to the equilibrium concentration. This means that the concentration of material just behind the front cannot be diluted as much before domain type switching occurs, and earlier domain type switching results in smaller domains.

2.7.2. Large Mixed Mobility ($M \gg 1$)

This is a case that is easily realizable in real systems. For strongly phase-separated regions the mobility can become very small compared to the mixed material.

As we saw from the results of the simulations shown in the inset of Figure 12, for large M the domain wavelengths become very large. This happens because diffusion is rapid in the mixed material region, and large amounts of material can build up ahead of the front. When the domain at the front switches type, this buildup floods into the new domain, thereby making it very large. In the limit of large M, the domain is predominantly formed from this material. Since this is effectively the same as halting the dynamics behind the front, we can understand this further by examining just the mixed material dynamics ahead of the front.

In the reference frame of the front, material pushed ahead of the front is governed by the drift-diffusion equation

$$\partial_t \phi + \nabla(u\phi) = \nabla m \nabla \phi \,, \tag{166}$$

which is defined for $x > x_0$. Here we have neglected the interfacial term and absorbed the a parameter into the mobility. Recall that the b parameter does not appear here due to our earlier decision to set the non-dimensional $B = 0$. The boundary condition at the front at $x = x_0$ is

$$J(t) = u[\phi(x_0, t) - \phi_{eq}] \,, \tag{167}$$

which is the current of material rejected by the forming domain, analogous to the result of Eq. (149). This boundary condition results in a buildup of material which will eventually lead to switching. These two equations are sufficient to define the material dynamics ahead of the front. We now non-dimensionalize these equations to recover their parameterless versions.

We introduce the general length and time scales

$$x = \mathcal{X}\hat{\boldsymbol{x}} \text{ , and } t = \mathcal{T}\hat{\boldsymbol{t}} \,. \tag{168}$$

It should be noted that $\mathcal{X}$ and $\mathcal{T}$ are not the same as the spinodal wavelength and time we used in the earlier non-dimensionalization. The drift diffusion equation then becomes

$$\frac{1}{\mathcal{T}}\partial_{\hat{t}}\phi + \frac{1}{\mathcal{X}}\widehat{\nabla}\left(\frac{\mathcal{X}}{\mathcal{T}}\hat{\boldsymbol{u}}\phi\right) = \frac{1}{\mathcal{X}}\widehat{\nabla}\left(m\frac{1}{\mathcal{X}}\widehat{\nabla}\phi\right) \ , \tag{169}$$

which we rewrite as

$$\partial_{\hat{t}}\phi + \widehat{\nabla}(\hat{\boldsymbol{u}}\phi) = \widehat{\nabla}\left(\frac{m\mathcal{T}}{\mathcal{X}^2}\widehat{\nabla}\phi\right) \ . \tag{170}$$

For the boundary condition

$$J(t) = \frac{\mathcal{X}}{\mathcal{T}}\hat{\boldsymbol{u}}(\phi(x_0,t) - \phi_{eq}) \ , \tag{171}$$

we obtain the non-dimensionalized boundary current:

$$\hat{\boldsymbol{J}}(\hat{\boldsymbol{t}}) = \hat{\boldsymbol{u}}(\phi(x_0,t) - \phi_{eq}) \ . \tag{172}$$

We now choose the length and time scales such that

$$1 \equiv \hat{\boldsymbol{u}} = \frac{\mathcal{T}}{\mathcal{X}}u \text{ , and } 1 \equiv m\frac{\mathcal{T}}{\mathcal{X}^2} \ . \tag{173}$$

This results in the 1D parameterless equation of motion

$$\partial_{\hat{t}}\phi + \widehat{\nabla}\phi = \widehat{\nabla}^2\phi \ , \tag{174}$$

and boundary condition

$$\hat{\boldsymbol{J}} = (\phi(x_0,t) - \phi_{eq}) \ . \tag{175}$$

While we do not have the analytical solution of this differential equation, we know that the solution exists and will result in a non-dimensional switching time $\hat{\boldsymbol{t}}_{sw}$.

We use this to replace the dimensional switching time appearing in Eq. (143), which gives the domain wavelength

$$\lambda = 2u\mathcal{T}\hat{\boldsymbol{t}}_{sw} \; . \tag{176}$$

We now evaluate $\mathcal{T}$ in terms of m and u from Eq. (173):

$$\mathcal{T} = \frac{m}{u^2} \; . \tag{177}$$

This uncovers the expected domain wavelength

$$\lambda = 2\frac{m}{u}\hat{\boldsymbol{t}}_{sw} \propto \frac{m}{u} \; . \tag{178}$$

We can re-express this result in terms of the earlier non-dimensionalization of Eqs. (136-138) as

$$L \propto \frac{M}{U} \; . \tag{179}$$

Thus we uncover the expected scaling behavior of the domain wavelength for the simultaneous limit of small U and large M.

Interestingly, the scaling behavior of 1D coarsening of a homogeneous quench is logarithmic in time, therefore enslaved phase-separation fronts can build large domains much more effectively than the phase-ordering which follows spinodal decomposition. In principle, the speed of the front can be controlled, and thus the production of highly ordered, position-dependent structures becomes possible.

We have already seen from the analytical result for $M = 0$ in the limit as $U \to 0$ that the domain wavelength is proportional to the inverse of the front speed ($L \propto U^{-1}$) which matches the previous scaling argument for the opposite case of $M \to \infty$. The scaling argument reveals that LU vs M will result in universal scaling in the limit of very slow fronts. We test this by performing simulations on a selected

range of sufficiently slow front speeds $U \leq 10^{-3}$, and a range of mobilities. The results of these simulations are shown in Figure 13 revealing the large difference in domain wavelengths in the U vs M plot which then collapse reasonably well in the LU vs M plot.

To improve the collapse, even slower simulations would be required, however this becomes too computationally expensive. For the measurements presented here we required simulations of more than 10^5 lattice sites simulated for more than 10^8 iterations. Such simulations take about one week on a Xeon powered Linux workstation.

2.7.3. A and M at the Front Boundary

The relative quench depth A is the last relevant parameter which needs to be considered in determining morphology formed by slow enslaved phase-separation fronts in 1D. The control parameter in either a purely mixed (a_M) or purely separating (a_S) system is usually not a function of position and can be absorbed into the mobility. In fact, if we were to consider the mixing region ahead of the front as being entirely detached from the separating region behind the front, we would be able to completely non-dimensionalize away all free parameters, resulting in separate scale-invariant equations of motion. However, due to the shared boundary at the front linking the two regions, the change of the control parameter $a(x)$ across the front cannot be ignored. This means that changing the control parameter ratio A has different consequences for the resulting morphology than does changing the mobility ratio M.

The first consequence of changing the order parameter A has for the dynamics of phase-separation is for the material which gets pushed ahead of the control parameter front. Recall that the chemical potential is continuous across the front ($\mu_S = \mu_M$). Ignoring for the moment the interfacial contribution to the chemical potential, we

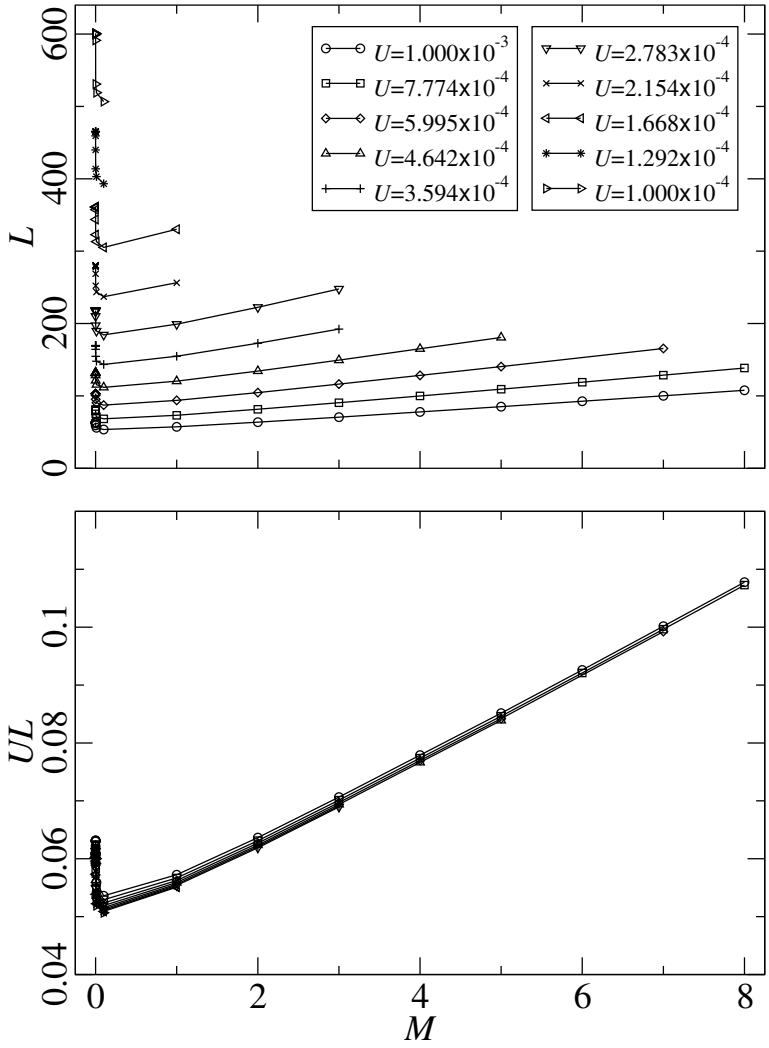

Figure 13. Universality in scaling of domain length L in terms of front speed U and mobility ratio M in the slow front speed limit. The upper graph shows that the non-dimensional domain wavelengths L and front speed U both vary by an order of magnitude, yet retain similar curve shapes.

can write the continuity of the chemical potential as

$$\begin{aligned} \phi_S^3 - \phi_S &= A\phi_M \ , \\ \Rightarrow \phi_M &= \frac{1}{A}\left(\phi_S^3 - \phi_S\right) \ . \end{aligned} \tag{180}$$

This means that the concentration just ahead of the front and the concentration just behind the front are tied together. This is important because the switching condition,

even for very large M, is partly dependent on the concentration of material just ahead of the front. For $A \ll 1$, the concentration ahead of the front becomes larger, causing the switching concentration to approach the equilibrium concentration, resulting in very early switching. On the other hand, for $A \gg 1$ the concentration ahead of the front becomes close to the symmetrically mixed concentration, resulting in switching taking longer to occur.

If we simply use ϕ_M in Eq. (180) as an effective ϕ_{in} in the earlier derived switching condition of Eq. (160), we discover a new switching condition for large M which is dependent only on A. This predicted switching concentration is plotted as the solid line in Figure 14, along with switching concentrations measured from our LBM simulations. Since the switching condition assumed no dynamics ahead of the front it is not surprising that this prediction is inadequate for the opposite scenario. If we take into account the additional current j across the front due to the dynamics ahead of the front, and account for this in the effective ϕ_{in} in the switching condition

$$\phi_{in}^{eff} = \frac{1}{A}\left(\phi_S^3 - \phi_S - j\right) \ , \tag{181}$$

we can measure this current at one value of A and use it to fit the rest of the curve. This new prediction is the dashed line in Figure 14, with the $A = 1$ switching concentration used as the fitting value. This new prediction agrees well, although not perfectly, with the simulated values, showing that the current across the front at switching seems to scale as the inverse of A.

2.8. Summary and Outlook

Phase-separation front driven morphology is a rich and complex subject which has significant potential for new research and applications. In this paper we focused on the simplest case: a one-dimensional binary mixture. For abruptly changing control-

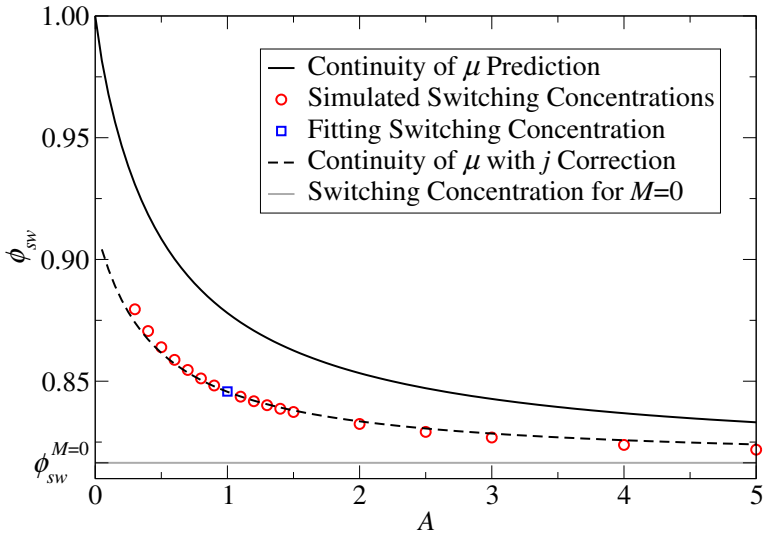

Figure 14. (color online) Switching concentration for large non-dimensional mobility ratio M as a function of control parameter ratio A. The predicted curves are calculated by assuming perfect continuity of the chemical potential across the front, and using this to predict the size of the nucleation kernel in the switching condition. The dashed line includes the addition of a current j which is caused by the dynamics ahead of the front, and is zero in the $M = 0$ case. The simulation used a non-dimensional mobility ratio $M = 5$, and front speed $U = 10^{-4}$.

parameters we found that a regular alternating morphology is formed. We have shown that, complex though the subject may be, certain important aspects of enslaved phase-separation fronts can be understood well enough to theoretically predict the morphology.

Using our model of a binary mixture with an sharp control parameter front, we were able to determine the effect of all relevant free parameters on the size of domains formed in a 1D system. We verified our predictions by comparing them to LBM simulations of our model.

We were able to reduce the number of relevant parameters from twelve to four. We achieved this by rescaling length and time with the spinodal wavelength and time and the concentration by the equilibrium value of the order parameter, and by making some simple physical assumptions, such as: near homogeneous mixing ahead of the front ($B = 0$), lack of an over-all chemical potential gradient ($C = A\Phi_{in}$), and a

negligible change in interfacial free-energy across the front ($K = 1$).

Analytical solutions are few and far between for the theory of morphology formation. Choosing the non-dimensional front speed as the primary parameter of interest, we consider the radical simplification of a front moving into material which has no mixed-material dynamics. This fixes the other free parameters and allows us to analytically determine the dynamics of phase-separation induced by a slow front.

We first find the time-dependence of the concentration at the front. We then determine the mechanism for domain switching. While typical nucleation arguments are heavily dependent on the interfacial free energy our switching condition was found to depend purely on the bulk free energy.

This gives us an analytical prediction of the formed morphology which is in remarkable agreement with the numerical results. Additionally, this solution functioned as a stepping stone for understanding the effects of the remaining parameters.

By allowing dynamics in the material ahead of the front we discovered a non-monotonic dependence of the domain wavelength on the non-dimensional mobility. Allowing a small amount of material to be pushed ahead of the front actually decreased domain wavelength, whereas allowing a large buildup of material ahead of the front resulted in huge increases in domain wavelength. The former is understood by an extension of the switching condition, and the latter is explained by a simple scaling argument; when the mobility in the mixing region is much greater than in the separating region, the domain wavelength formed by the front should scale with the same dependence as the length scale in the mixing region. This argument resulted in the discovery that, for very slow front speeds, there is a single universal scaling curve of the non-dimensional domain wavelength as a function of the non-dimensional mobility and front speed.

Domain type switching is very well understood for the case of no mixed material

dynamics, and we've explained the effect of very small mixed material mobility. The effect of large mixed material mobility on the switching condition is uncovered in the analysis of the quench depth A of the enslaved front. Modification of the switching condition is accomplished by including the continuity of the chemical potential, and a current j which is inversely proportional to A.

The effect on one-dimensional morphology formation of three of the relevant non-dimensional parameters is now well understood. We now briefly mention several research avenues that lead on from the results presented in this paper.

We are currently examining higher-dimensional enslaved control parameter fronts. Two-dimensional fronts open the possibility for the formation of stripe morphologies which are perpendicular or at an angle to the control parameter front. Additionally we find other exotic morphologies like polka-dot lattices and ovoid domains. Also, dimensionalities of two and higher allow hydrodynamics to play a role in the phase-separation dynamics. In three-dimensions, enslaved fronts can induce a rich family of morphologies depending on the properties of the material and the front. Perhaps the most intriguing possibility is to be able to control the material and front well enough to reliably switch morphologies during front traversal, resulting in highly-ordered, highly-inhomogeneous composite materials.

What also remains is to examine more general enslaved fronts. The most straightforward extension is to attempt to develop an analytical solution to the sharp one-dimensional enslaved front for all three free parameters U, A, and M. A careful accounting of the additional currents caused by dynamics ahead of the front should allow an extension of the differential equation describing the dynamics at the front, presented in Eq. (156), for this more general sharp one-dimensional enslaved front.

Then we will relax the condition of an sharp control parameter front to obtain an extended front. We expect that there will be little change while the width of an

extended control parameter front is on the order of the interface width, but extended fronts which approach the size of the forming domain may result in new and interesting phase-separation dynamics, even in 1D.

PAPER 2. ENSLAVED PHASE-SEPARATION FRONTS AND LIESEGANG PATTERN FORMATION[2]

ABSTRACT: We show that an enslaved phase-separation front moving with diffusive speeds $U = C/\sqrt{T}$ can leave alternating domains of increasing size in their wake. We find the size and spacing of these domains is identical to Liesegang patterns. For equal composition of the components we are able to predict the exact form of the pattern analytically. To our knowledge this is the first fully analytical derivation of the Liesegang laws. We also show that there is a critical value for C below which only two domains are formed. Our analytical predictions are verified by numerical simulations using a lattice Boltzmann method.

3.1. Introduction to Liesegang Patterns

The formation of highly ordered patterns in naturally occurring biological, chemical, and mineralogical systems has long been a subject of intense interest. The study of such pattern formation can sometimes allow deep insight into their underlying natural phenomena. In a previous paper we analyzed the dynamics of pattern formation behind a one-dimensional, slow moving (enslaved), phase-separation front. Our analysis concerned fronts moving with constant speed, and the pattern formed was a series of alternating bands of regular width and spacing [17]. We show here that a front moving with diffusive speed will form a more complex Liesegang pattern.

It was with the motivation of understanding pattern formation in simple systems that, just over one hundred years ago, R. E. Liesegang observed a highly ordered pattern of concentric rings precipitating around a drop of silver nitrate on a glass slide with a thin gel coating containing potassium dichromate [42]. These concentric rings

[2]Eric Foard (E. F.) developed the idea for the research presented in this paper. Alexander Wagner (A. W.) and E. F. worked jointly on the theoretical analysis. Simulation development, numerical simulation, and numerical analysis were performed by E. F. The manuscript and figures were authored by E. F. with editorial input from A. W.

are now known as Liesegang rings. The radial width and spacing of the rings increases with increasing distance from the center. Rings close to the center are narrow and tightly packed. Rings far from the center are wide and far apart. The pattern forms from the center outwards, and is stationary once visible. Several alternatives to silver nitrate and potassium dichromate in the production of Liesegang rings have been used in the literature. In general, some electrolytes A and B combine to form an insoluble precipitate D which then produces Liesegang patterns. Most recent publications use linear Liesegang patterns of bands and gaps which are produced by adding the A electrolyte to a test-tube containing the B electrolyte suspended in gel [49].

To characterize Liesegang bands or rings, they are typically numbered from the first formed to the last formed, the nth appearing at time t_n at position x_n with a width w_n. Repeated careful measurements of Liesegang patterns revealed that discrete, defect-free bands could be characterized by a set of empirical laws [33]. They are

$$\text{Time Law} \qquad x_n \propto \sqrt{t_n}\ , \tag{182}$$

$$\text{Spacing Law} \qquad x_{n+1}/x_n = 1 + p\ , \tag{183}$$

$$\text{Width Law} \qquad x_n \propto w_n\ . \tag{184}$$

The *time law* relates the position of the nth band with the time of its appearance. The location of subsequent bands is given by the *spacing law*, where $p > 0$ is the spacing coefficient. The *width law* states that the band width is proportional to the position of the band, which is a natural result of the *spacing law* with the assumptions of mass conservation and uniform concentration of precipitate bands [36]. These laws are only considered valid for *large* n. Much attention has been paid to the phenomenological Matalon-Packter law $p = F(B_0) + G(B_0)/A_0$, which relates p to

the initial concentrations A_0 and B_0 of the A and B electrolytes [3]. $F(B_0)$ and $G(B_0)$ are known to be decreasing functions of B_0, though not much else about them is known. Antal *et al.* [3] show that the Matalon-Packter law can be derived in limiting cases from more general expressions.

Soon after their characterization, study into the nature and cause of Liesegang patterns was prolific. For instance, a paper by Stern in 1954 makes mention of more than six hundred papers having been published on the subject by that time [53]. There were many early attempts to develop a comprehensive model of Liesegang pattern formation. However, it proved difficult to account for the wide variety and complexity of possible patterns, and many early models were eliminated by additional experiments. The complexity of Liesegang pattern formation thwarted theoretical understanding, and progress slowed. More than a century later there is currently still no generally accepted comprehensive mechanism for Liesegang pattern formation.

Current dominating theories of Liesegang pattern formation can be categorized as either an *ion-product supersaturation* theory where electrolytes combine directly into the precipitate ($A + B \rightarrow D$), or a *nucleation and growth* theory where one or more intermediate compounds form before final precipitation ($A + B \rightarrow C \rightarrow D$). A brief discussion of these models is given in the recent paper by Jahnke and Kantelhardt [36].

For either of these theories, precipitation occurs behind a reaction front formed by the A electrolyte diffusing into the B electrolyte. Since the initial concentration (A_0) of A in the drop is typically an order of magnitude higher than the concentration (B_0) of B in the gel, the time dependent concentration profile $A(x,t)$ of A electrolyte in the gel forms a reaction front which resembles the familiar heat-diffusion profile moving with speed $u_r \propto t^{-1/2}$ [3]. Coincident with, or trailing behind this reaction front is a precipitation front, moving at a speed $u_p \propto t^{-1/2}$, which produces the

banded pattern. The precise relationship of the precipitation front to the reaction front depends on the specific chemical and physical mechanism of Liesegang pattern formation which are still not entirely understood.

The recent trend for publications on Liesegang patterns shows a re-surging interest. A search of the ISI Web of Science Internet database for publications on the topic "Liesegang" shows an increase in papers since a fall in the early second half of the 20th century. We found only 8 papers from 1970 to 1979, 35 from 1980 to 1989, 107 from 1990 to 1999, and 196 since 2000. Much of the recent research into Liesegang pattern formation has focused on the moving front by employing a variety of numerical techniques to simulate models of precipitation fronts. Some examples are the reaction-diffusion cellular automata simulations by Chopard *et al.* [11], direct simulation of a model-B system with a chemical reaction like source term by Antal *et al.* [2] and Rácz [49], the discrete stochastic simulation which used random walkers to model the diffusion front by Izsák and Lagzi [32], as well as the lattice gas simulation by Jahnke and Kantelhardt [36].

In this paper we show that patterns identical to Liesegang patterns can be formed in a much simpler physical system. We consider a binary mixture that can phase-separate if a control parameter crosses a critical value. In this system an enslaved phase-separation front moves at a speed of $u = ct^{-1/2}$. An example of such a system would be a binary mixture that is cooled below its critical temperature from one end. This situation is somewhat similar to that of the electrolytes, where material is formed at the front and will subsequently phase separate. However the details are quite different, most notably in the nucleation conditions.

It should be noted that this model is somewhat similar to the Model-B precipitation front proposed by Antal *et al.* [2], but there are several key differences. Their model has a moving, Gaussian shaped source of $\mathcal{A}$-type material designed to mimic

the product of a chemical reaction front. Their source moves through a region which is phase-separated into an equilibrium $\mathcal{B}$-type. When the concentration of $\mathcal{A}$-type material in a given area reaches the spinodal value, an $\mathcal{A}$-type domain nucleates and depletes the surrounding region of its $\mathcal{A}$-type material. The source moves on, leaving stable domains. The speed, width, and concentration of their source are free parameters of their model. Our model has an abrupt control parameter front which induces phase-separation as it passes through a mixed material, the mechanism for nucleation of new domains is quite different. Notably switching does not occur at the spinodal value for reasons explained in [17]. Also the analysis of Antal *et al.* is numerical in nature. Our model has only one parameter and can be solved analytically.

To allow for an analytical treatment we make the simplifying assumption of an abrupt front. We expect that the results will be qualitatively similar to those for an extended control parameter front. In practice, an abrupt front could be experimentally achieved by immersing a thin sample into a temperature bath at a prescribed speed $u \propto t^{-1/2}$.

The key result is that we are able to analytically determine the resulting patterns and we show that they obey the Liesegang laws given by Equations (182), (183), and (184). We derive an analytical expression for the spacing coefficient p in terms of the free parameters of this model. We verify these theoretical predictions by direct numerical simulations using a lattice Boltzmann method.

3.2. A Model for Liesegang Patterns Formed by Enslaved Phase Separation Fronts

We consider two materials, an $\mathcal{A}$-type and a $\mathcal{B}$-type, in an incompressible mixture such that the total density $\rho = \rho_{\mathcal{A}}(x,t) + \rho_{\mathcal{B}}(x,t)$ remains constant. The relevant variable is then the relative concentration of $\mathcal{A}$ to $\mathcal{B}$-type material defined as

$$\phi(x,t) = \frac{\rho_{\mathcal{A}}(x,t) - \rho_{\mathcal{B}}(x,t)}{\rho} \ . \tag{185}$$

From here on the time and position dependence of the concentration will be implied. For simplicity we assume that the two materials have the mixing free energy described by a ϕ^4 law

$$F = \int dx \left[\frac{a(x,t)}{2}\phi^2 + \frac{b(x,t)}{4}\phi^4 + \frac{\kappa(x,t)}{2}(\nabla\phi)^2 \right] . \tag{186}$$

The time and position dependence of the control parameters (a, b, and κ) are such that they constitute a spatially abrupt transition from the mixing region to the phase-separating region of the phase diagram. For example:

$$a(x,t) = a_S + (a_M - a_S)\Theta\left(\int u\, dt + x_0 \right) , \tag{187}$$

where Θ is the Heaviside step function, and the transition takes the form of a front moving with velocity $u(t)$. The free energy of Eq. (186) has a single minimum for $a > 0$, resulting in material *mixing*. When $a < 0$ there are two minima, resulting in the *separating* of material. The control parameters for the *mixing* and *separating* regions are denoted by subscripts M and S respectively. The other parameters are defined similarly.

Since we assume incompressibility and a one-dimensional geometry of the system, hydrodynamics can be neglected here, and the dynamics is therefore purely diffusive

$$\partial_t \phi = \nabla \left[m(x,t) \nabla \mu(x,t) \right] . \tag{188}$$

The chemical potential is derived from the free energy as,

$$\mu(x,t) = \frac{\delta F}{\delta \phi} = a(x,t)\phi + b(x,t)\phi^3 - \kappa(x,t)\nabla^2\phi , \tag{189}$$

and the diffusive mobility m is one of the control parameters which can vary across the front similarly to (187). Aside from time and space dependence of the control

parameters, this is the familiar Model-B.

This model for a moving front has many parameters which can affect the dynamics of phase separation, however not all of these parameters are independent. As we elaborate on in our previous paper, introduction of appropriate time, space, and concentration scaling can non-dimensionalize the equations of motion [17]. For the remainder of this paper we will work entirely in the non-dimensional scales

$$T = \frac{t}{t_{sp}} \ , \quad X = \frac{x}{\lambda_{sp}} \ , \quad \Phi = \frac{\phi}{\phi_{eq}} \ . \tag{190}$$

Here $t_{sp} = 4\kappa/ma^2$ and $\lambda_{sp} = 2\pi\sqrt{-2\kappa/a}$ are the characteristic time and length scales of spinodal decomposition, and $\phi_{eq} = \sqrt{-a/b}$ is the positive equilibrium concentration of the phase-separated material. Non-dimensional quantities will be denoted by capital letters.

Non-dimensionalization reduces the free parameters to an independent set of four parameters: $U = u/u_{sp}$ is the speed of the front scaled by the natural speed of spinodal decomposition $u_{sp} = \lambda_{sp}/t_{sp}$, $M = m_M/m_S$ is the ratio of the diffusive mobility ahead of the front to behind the front, $A = -a_M/a_S$ is the depth of the quench into the unstable region of the phase diagram, and $\Phi_{in} = \phi_{in}/\phi_{eq}$ is the non-dimensional initial concentration of the mixed material. As we have previously shown, the dynamics becomes particularly simple if we let the diffusive mobility ahead of the front be negligible $m_M \to 0$. In this case the dynamics ahead of the front, represented by Eq. (188), is halted. This makes the A parameter unnecessary. This is not a particularly physical assumption, but it does only cause a small quantitative change in the pattern formation as compared to $M = 1$, as we have previously shown [17]. The existence of analytical solutions, however, makes $M = 0$ an attractive choice. If we then assume that the front moves into material which has an equally mixed initial concentration, the morphology of domains formed depends only on the non-

dimensional front speed (U). Interestingly, an analytical expression can be found for the non-dimensional domain wavelength (L) when U is small and constant:

$$L(U) = \frac{4\left(\sqrt{6} + 6\ln\left(2 - \sqrt{2/3}\right) - 3\right)}{3\pi^2 U} = \frac{\Psi_0}{U} \,. \tag{191}$$

The derivation of this law is given in [17]. Because it is convenient to work with this analytical solution, we will focus on the condition where the initial mixed material contains equal parts of $\mathcal{A}$-type and $\mathcal{B}$-type material.

To complete our model we require that the front moves with a time dependent speed

$$U(T) = \frac{C}{\sqrt{T}} \,, \tag{192}$$

appropriate for a diffusive velocity. The parameter C now becomes the only free parameter in this model. This parameter will therefore determine the spacing and width of the resulting domains.

3.3. Derivation of Liesegang Laws

We will now show that for certain parameter choices the model presented in the previous chapter will result in the formation of Liesegang patterns. We will do this by deriving the Liesegang laws of Equations (182), (183), and (184) directly from the model. We will conclude this section by deriving a Matalon-Packter like analytical expression for the spacing coefficient.

We first recognize that domain production at any point in space can only occur after the phase-separation front has passed. From our previous paper we observe that once an enslaved front has passed a point, domain growth or nucleation occurs very rapidly [17]. That is, domains form and grow near the front. The position of the

front at time T is found by integrating the front-speed:

$$X(T) = \int_0^T U(T)\, dT = \int_0^T \frac{C}{\sqrt{T}}\, dT = 2C\sqrt{T} = \alpha\sqrt{T}\ . \tag{193}$$

From this we see that if domains are formed, then the nth domain will be formed at time T_n at position X_n which is proportional to $\sqrt{T_n}$ in agreement with the time law of (182). This is simply a result of the imposed front speed.

Deriving the width and spacing laws is more interesting. As we found in our previous paper [17] and reproduced in Eq. (191), a front moving at constant speed produces domains of a predictable wavelength. In the process of deriving Eq. (191), we discovered domain growth has two distinct stages: first is a formation stage where a domain nucleates at the front and grows as it is pulled along with the front until a new domain nucleates; second is an expansion stage where the just detached domain grows due to deposition of material excluded from the newly forming, opposite type domain. For a constant speed front moving into material which is initially symmetrically mixed and of negligible mobility, each stage accounts for growing half of the domain's final width. In essence, it takes two domain-type switching cycles to completely form a stable domain, and the domain width grows at half the front speed.

The width of a domain as it detaches from a constant speed front is half of its final width, which is then a quarter of the constant speed domain wavelength for a front at that speed. If the front speed is changing, the width at detachment W^{det} is one quarter the domain wavelength predicted in Eq. (191) for a front moving with instantaneous speed U at detachment. This statement implies the assumption that our nucleation theory that was derived for constant U can also be applied for time-dependent U. This is a non-trivial assumption but it is justified by the excellent agreement of our theory with direct numerical simulations of the full PDE. Using Eq. (192) to replace the front speed dependence with time, then using Eq. (193) to

replace the time dependence with position, we can predict the width W^{det} of a domain as it detaches from a front when this front is at position X:

$$W^{det} = \frac{1}{4}L(U) = \frac{\Psi_0}{4U} = \frac{\Psi_0\sqrt{T}}{4C} = \frac{\Psi_0}{8C^2}X = \beta X \ . \tag{194}$$

Note that this already resembles the Liesegang width law, but does not relate the final domain width to the domain position. For that we must consider the growth of the domain after it detaches from the front. The information presented in this section thus far is graphically shown in Figure 15 which represents the growth and final morphology of Liesegang pattern formation.

To derive the width law, recall the formation and expansion stages of domain growth mentioned previously. A domain forming at the front increases its width at half the front speed. Due to mass conservation, the detached domain directly behind it increases its width at the same rate. The width of domains at detachment is predicted by Eq. (194). The final width of domain n is then its detachment width, plus the detachment width of the next domain of opposite material, which we count as $n + 1/2$. From this we get:

$$W_n = W_n^{det} + W_{n+1/2}^{det} = \beta X_n^{det} + \beta X_{n+1/2}^{det} \ . \tag{195}$$

The position of the first interface X_n^0 of domain n can be easily found from the detachment position X_n^{det} by subtracting the width W_n^{det} of the domain at detachment:

$$X_n^0 = X_n^{det} - W_n^{det} = (1-\beta)\, X_n^{det} \ . \tag{196}$$

As evident in Figure 15, the position $X_{n+1/2}^0$ of the first interface of the next domain, which will be of opposite composition, is simply the position of the current

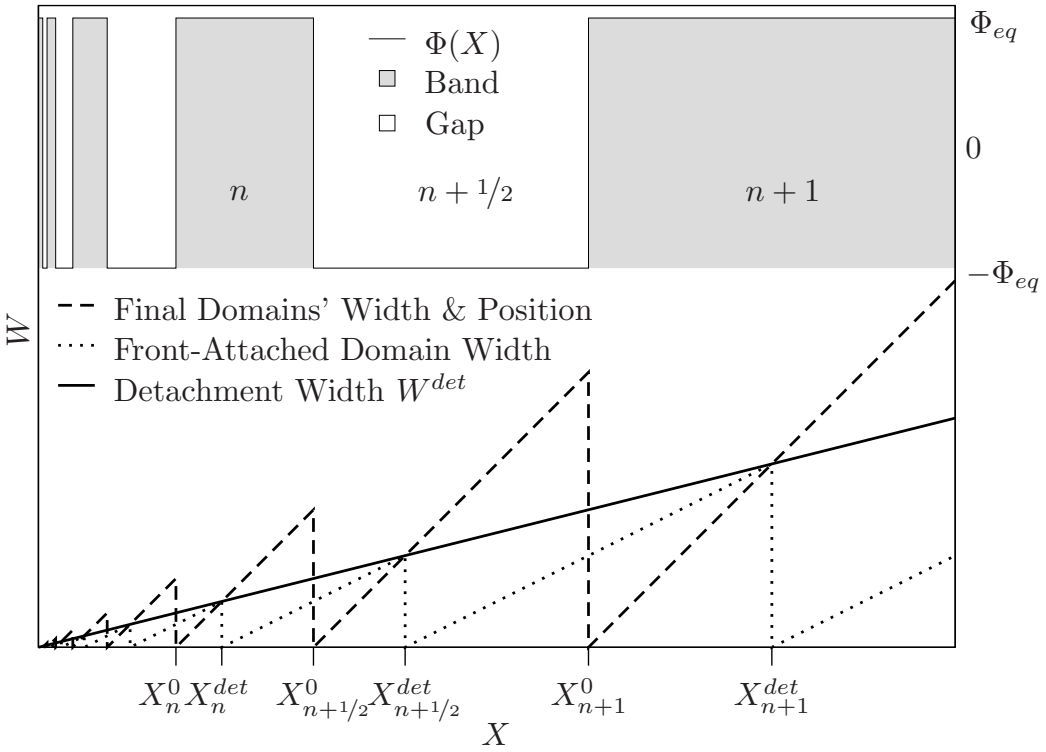

Figure 15. Illustration of domain formation in a Liesegang pattern. The top of the figure is a concentration profile in a Liesegang pattern where positive equilibrium concentration domains are considered bands and negative equilibrium concentration domains are gaps. The bottom of the figure shows three important aspects of Liesegang pattern formation corresponding to the concentration profile at the top. The dashed line represents the distance from the previous domain in the final morphology. We label the position of the first interface of a domain n as X_n^0. Therefore the height of the dashed line is $X - X_n^0$ where n is the domain that exists at position X. The dashed line has slope 1 because the W and X axes have the same scale. The dotted line represents the width W of the front-attached domain as a function of the front position X. The slope 1/2 is explained in the text and in our previous paper on enslaved front phase-separation [17]. The solid line represents the maximum front-attached domain width of Eq. (194) for the position X of the front. When a domain forming at the front reaches $W^{det}(X)$, it detaches from the front, and a new domain is nucleated at the front. The dotted, dashed, and solid lines all intersect at the points where domain type switching occurs at the front. Note that when a domain n becomes detached from the front its first interface becomes stationary at X_n^0.

domain's second interface, and is found by adding the current domain's width to its first interface position:

$$X^0_{n+1/2} = X^0_n + W_n \ . \tag{197}$$

Combining Equations (195), (196), and (197), we recover the Liesegang width law:

$$W_n = \frac{1}{1/2\beta - 1} X^0_n = \frac{1}{4C^2/\Psi_0 - 1} X^0_n = \gamma X^0_n \ . \tag{198}$$

We now derive the spacing law. As seen from Eq. (197), the position of the first interface of the subsequent domain scales by a constant factor:

$$X^0_{n+1/2} = X^0_n + W_n = (1+\gamma) X^0_n \ . \tag{199}$$

Two subsequent domains increase the index n by one, and their positions scale by that same factor squared:

$$X^0_{n+1} = (1+\gamma) X^0_{n+1/2} = (1+\gamma)^2 X^0_n \ . \tag{200}$$

This gives the Liesegang spacing law

$$\frac{X^0_{n+1}}{X^0_n} = (1+\gamma)^2 = \frac{1}{(2\beta - 1)^2} = \frac{1}{(\Psi_0/4C^2 - 1)^2} \ . \tag{201}$$

The position of the band is taken as the boundary between the band and the previous gap. Due to experimental reasons, the location of a Liesegang band is often considered to be at the center of the band, *i.e.* $X_n = X^0_n + W_n/2$. Our derivation of the Liesegang time, spacing, and width laws uses the fact that there is some freedom in measuring the positions of the domains X_n, as long as all domains are measured consistently. It is clear that the scaling law holds whether one measures the position

on the leading or trailing edge of the domain edge. Note that if one definition of the position given by

$$X_n = X_n^0 + \nu W_n \ , \tag{202}$$

obeys the Liesegang laws, then all these definitions of the position will still fulfill the Liesegang spacing laws because:

$$\frac{X_{n+1}}{X_n} = \frac{X_{n+1}^0 + \nu W_{n+1}}{X_n^0 + \nu W_n} = \frac{(1+\gamma\nu)\, X_{n+1}^0}{(1+\gamma\nu)\, X_n^0} = \frac{X_{n+1}^0}{X_n^0} \ . \tag{203}$$

From Eq. (201), we determine that the Liesegang spacing coefficient for this model is:

$$p = \frac{1}{\left(\Psi_0/4C^2 - 1\right)^2} - 1 \ . \tag{204}$$

Note that this expression replaces the Matalon-Packter law, but bears no apparent resemblance to this phenomenological law. For values of $C > \sqrt{\Psi_0}/2$, the Liesegang spacing coefficient p is greater than zero, and many domains will form, generating a Liesegang pattern. For C below the critical value $C^{cr} = \sqrt{\Psi_0}/2 \approx 0.1247$, no Liesegang patterns will be formed. Instead only two domains continue to grow and no nucleation of new domains occurs. A graphical representation of Eq. (204) is shown in Figure 17. The authors are not aware of any previous purely analytical expressions that accurately predict the spacing coefficient for any Liesegang pattern producing models.

We have now derived all of the laws for Liesegang patterns. Surprisingly there are no free parameters and our analytical expressions completely determine the patterns. It remains to be shown that the approximations made in this analytical derivation do not significantly alter the results. To do this we compare our analytical results to direct numerical simulations of our model.

3.4. Numerical Method and Results

In our previous paper we presented a one-dimensional lattice Boltzmann method (LBM) simulation of our model for enslaved phase-separation fronts moving with constant speed. We did this by creating a lattice with spatially dependent control parameters, where the parameters change abruptly at the location of the front. We then advect the material at speed u across this stationary front, using carefully constructed inflow and outflow boundary conditions. A Galilean transformation $x' \to x - ut$ of this simulation returns the original model. The simulation was designed this way, because a slow moving abrupt front on a discrete spatial lattice would be stationary for long periods followed by an instantaneous change of position. On the other hand, since the current of material in a LBM simulation is represented by continuous distribution functions, a constant drift speed u in the drift diffusion of material can be made arbitrarily small. For details on the development of the LBM simulations for enslaved fronts please refer to our previous paper [17]. Here we will only discuss the changes required to implement this method for fronts moving with a non-constant speed.

3.4.1. Changes for Diffusive Fronts and Details of Implementation

The method we presented was designed with constant speed fronts in mind, but there was no requirement made that the front speed, and therefore the material advection speed in the LBM simulation, be constant. To implement our model for the diffusive speed front of Eq. (192) we make two changes. First, the simulation is started at time $T = T_0 > 0$ to ensure that the advection speed is finite. Second, the advection speed is recalculated according to Eq. (192) at every iteration. To ensure the analytical solution of Eq. (191) is applicable, we must use front speeds that are much slower than the speed of a free front. The numerical verification of Eq. (191)

is given in [17, Fig. 7] and shows that fronts moving at non-dimensional speed of $U \leq 0.001$ produce domain sizes that agree very well with the prediction. This being the case, we begin our simulation so that the initial front speed is $U_0 = 0.001$, by setting our simulation start time $T_0 = (C/U_0)^2$.

The simulation is initialized with random concentration fluctuations around the symmetrically mixed concentration value of $\Phi_{in} = 0$. This results in spinodal decomposition in the region behind the front. These small domains serve to buffer the domains formed by the enslaved front from being adversely effected by any anomalies due to the outflow boundary condition. To increase simulation performance the number of lattice sites is initially rather small, and is dynamically grown to maintain a buffer of small domains.

3.4.2. Measurements and Calculations

Our goal with these simulations is to verify our analytical predictions of Equations (198) and (201) for the Liesegang laws. We accomplish this by performing simulations with different values of C, measuring the width W_n of the nth domain formed, and performing a numerical fitting to the equation

$$W_n = W_0 + Q\,(1+p)^n \ , \tag{205}$$

where W_0, Q, and p are the fitting parameters. This is an alternative form of Eq. (183) with a substitution provided by Eq. (184).

The domain widths are measured by interpolating the sub-lattice position of the zero-crossing of the concentration at an interface, and determining the distance to the sub-lattice position of the next interface. To ensure that there are sufficient domains to perform meaningful fitting to Eq. (205) we track the number of switching events; after 19 switching events have occurred the domain widths and other data,

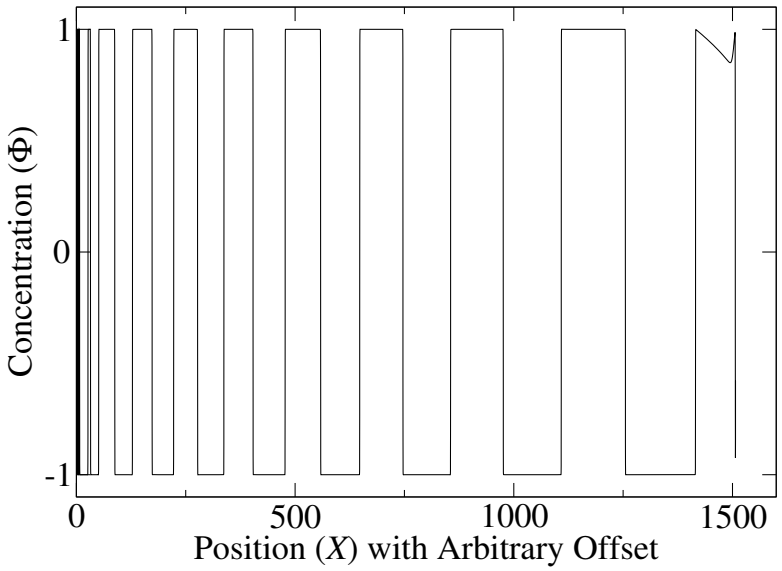

(a)

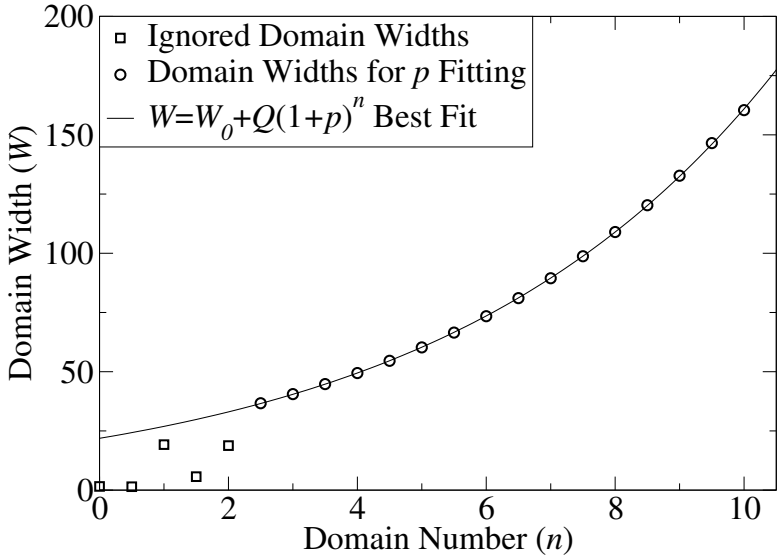

(b)

Figure 16. LBM simulation results showing concentration and domain widths of a Liesegang pattern. The front speed parameter for this example is $C = 0.4$. Subfigure (a) shows an example concentration profile of Liesegang pattern morphology at simulation completion. The offset is due to requiring an initial finite speed and dynamic growing of the simulation. Subfigure (b) shows the fitting of domains widths found in (a) to determine $p(C)$. Some domains are ignored because they are not formed by the front, but are instead artifacts of the simulation procedure. The width W_n of domain n is fitted to the equation $W_n = W_0 + Q(1 + p)^n$ to find an experimental value of p to compare to the theoretical prediction of Eq. (204). For these data the fitting values are $W_0 = -1.92468$, $Q = 23.7999$, and $p = 0.212093$.

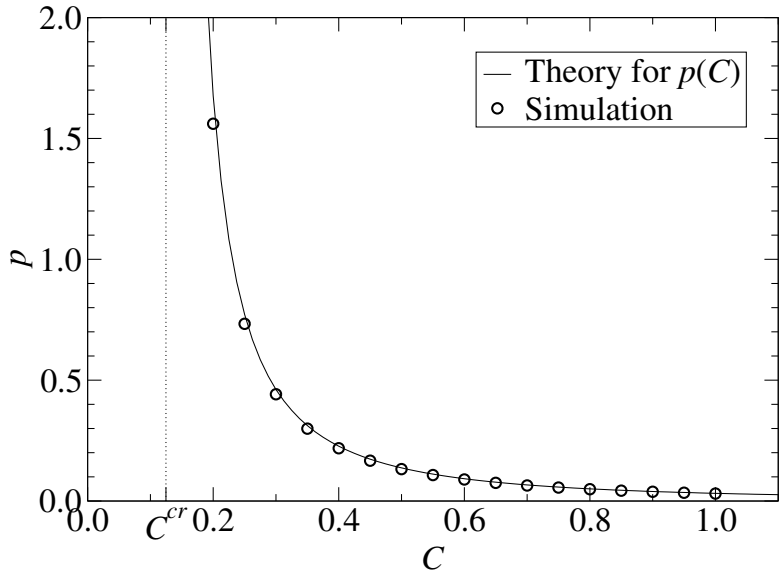

Figure 17. Comparison of the analytical prediction for the Liesegang scaling coefficient p as a function of the front speed parameter C. The analytical prediction is shown in Eq. (204). This expression replaces the Matalon-Packter law for this model. The results show excellent agreement of the simulation results with the assumptions made in the derivation of the Liesegang scaling laws for this model. For $C < C^{cr}$ no new domains were nucleated. These data were taken from a series of simulations, the details of which are explained in the text.

such as the concentration profile, are written out to disk. As explained in the previous section, the two domains directly behind the front are not completely formed, and are not used to find the experimental p value. The first domain formed by the front may also be ignored as it can sometimes be induced by the very strong dynamics of spinodal decomposition. This typically leaves 16 alternating domains of $\mathcal{A}$ and $\mathcal{B}$-type material which can be used for fitting to Eq. (205). Example simulation data and p fitting are shown in Figure 16 for the $C = 0.4$ data point shown in Figure 17. The concentration profile is shown in Figure 16a, and the width fitting is shown in Figure 16b.

One additional note: the concentration profile of Figure 16a seems to show a very sharp interface. The actual interface width covers approximately ten lattice sites, and is in agreement with the bulk stability requirements outlined by Wagner and

Pooley in [61]. The use of the minimum stable interface width increases simulation spatial efficiency. Additionally, the use of smaller interface widths allows a larger time scaling factor s to be used which further increases simulation efficiency by calculating a larger time step each iteration [17].

Numerous simulations of the type shown in Figure 16 were performed for different values of C and the corresponding p values were measured and compared to the theoretical prediction of Eq. (204). These results are shown in Figure 17 and show excellent agreement. This remarkable agreement suggests that approximations made in the derivation of the analytical results have negligible effect on the final results. This is notable, as no other Liesegang pattern forming model has an accurate analytical prediction of the Liesegang scaling laws.

3.5. Outlook

In this paper we have shown that a model for an enslaved phase separation front which moves at diffusive speed $U = C/\sqrt{T}$ can be used to produce Liesegang patterns. We have done this by deriving the Liesegang time, width and spacing laws from the model. Our analysis includes the determination of the Liesegang spacing coefficient p as a function of the front speed parameter C. In doing so we determined the values of C where Liesegang patterns are produced, and verified this with direct numerical simulations of the model.

For this paper we have chosen the initial material composition to be symmetrically mixed. This corresponds to $\Phi_{in} = 0$ and allows us to use the analytical result in Eq. (191) to determine the Liesegang laws and their constants of proportionality. This model, however, can generate Liesegang patterns for the range of initial concentrations between the spinodal concentrations. An example is shown in Figure 18 of a Liesegang pattern for asymmetrically mixed initial material generated by this model. The parameters used in this simulation were $C = 0.5$ and $\Phi_{in} = -0.3$. We expect

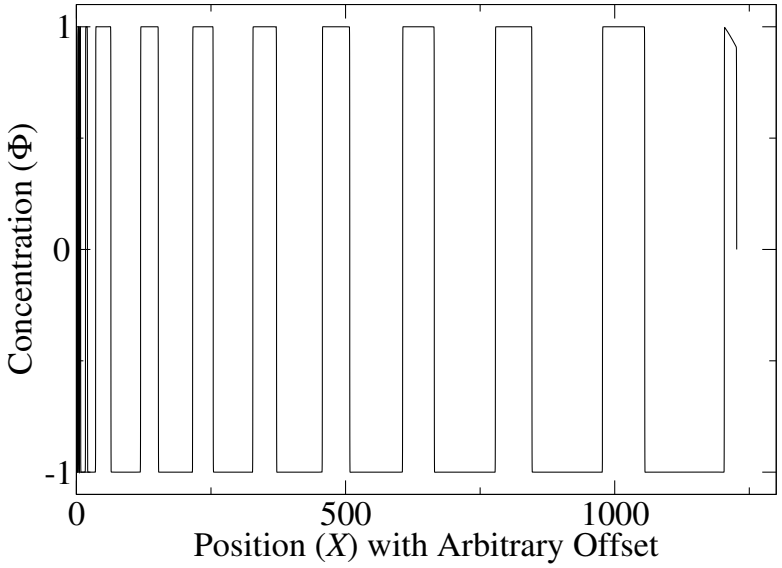

(a)

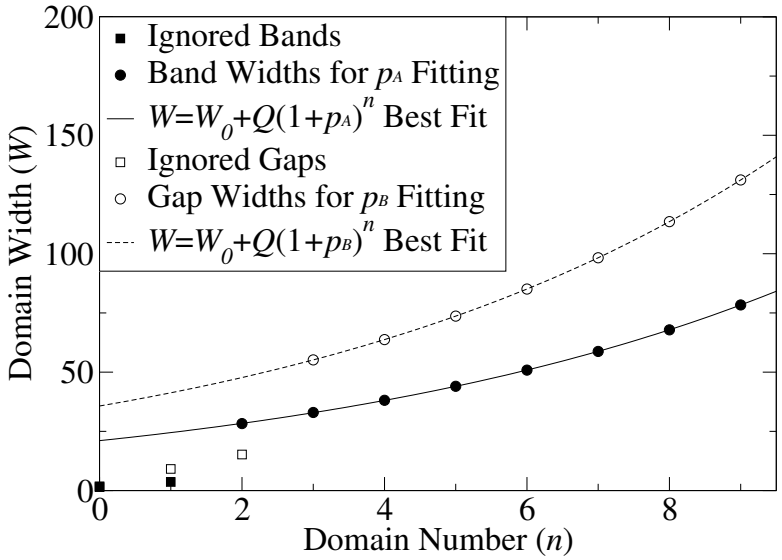

(b)

Figure 18. LBM simulation results showing concentration and domain widths of a Liesegang pattern for unequal mixed material volume fractions. In this example the initial mixed material concentration is $\Phi_{in} = -0.3$, and the front speed scaling constant is $C = 0.5$. The profile is shown in sub-figure (a) at simulation completion. Sub-figure (b) shows fitting the band ($\mathcal{A}$-type) and gap ($\mathcal{B}$-type) widths separately to find $p(C)$ for initial material consisting of a majority $\mathcal{B}$-type. Fitting parameters for the bands are $W_0 = -1.41736$, $Q = 22.4956$, and $p_{\mathcal{A}} = 0.151002$. Fitting parameters for the gaps are $W_0 = -0.449771$, $Q = 36.1552$, and $p_{\mathcal{B}} = 0.15435$. This spacing coefficient is higher than for material which is initially equally mixed $\Phi_{in} = 0$. As can be seen in Figure 17, the spacing coefficient for $C = 0.5$ is $p \approx 0.12$ in the case where $\Phi_{in} = 0$.

that it will be possible to determine a spacing law for off-critical mixtures, but that is outside the scope of this paper. Additionally, the production of Liesegang patterns by enslaved fronts which move into material with non-zero mixed mobility should be considered. We expect the results to be qualitatively similar, but we are not sure than this case will be amenable to an analytical treatment.

PAPER 3. SURVEY OF MORPHOLOGIES FORMED IN THE WAKE OF AN ENSLAVED PHASE-SEPARATION FRONT IN TWO DIMENSIONS[3]

ABSTRACT: A phase-separation front will leave in its wake a phase-separated morphology that differs markedly from homogeneous phase-separation morphologies. For a purely diffusive system such a front, moving with constant velocity, will generate very regular, non-equilibrium structures. We present here a numerical study of these fronts using a lattice Boltzmann method. In two dimensions these structures are regular stripes or droplet arrays. In general the kind and orientation of the selected morphology and the size of the domains depends on the speed of the front as well as the composition of the material overtaken by the phase-separation front. We present a survey of morphologies as a function of these two parameters. We show that the resulting morphologies are initial condition dependent. We then examine which of the potential morphologies is the most stable. An analytical analysis for symmetrical compositions predicts the transition point from orthogonal to parallel stripes.

4.1. Introduction

Phase-separation is a ubiquitous phenomenon observed in a wide variety of systems. The theoretical analysis of phase-separation has mostly focused on the case where the system is homogeneously quenched, i.e. moved instantaneously and uniformly from a mixed state to a state where the system will separate into different phases. A good overview of this theoretical work is provided in the book by Onuki [45].

[3]Eric Foard (E. F.) developed the idea of a survey of morphologies. E. F. wrote the numerical simulations and analysis tools for the survey, and performed the analysis of the survey results. E. F. with guidance from Alexander Wagner (A. W.) performed the theoretical analysis for stripe formation. Numerical stripe stability analysis was designed jointly by E. F. and A. W. Simulations and numerical analysis were performed by E. F. Manuscript and figures were authored by E. F. with editorial input from A. W.

In many practically occurring systems phase-separation does not occur everywhere at once, but rather starts in a specific region and from this place successively invades the system. We refer to the surface of transition between the mixed and the separated regions as the phase-separation front. The resulting morphologies formed in the wake of a phase-separation front can differ significantly from the structures resulting from homogeneous phase-separation.

Our interest in phase-separation fronts arose from an investigation of immersion precipitation membranes [1]. In these systems a polymer-solvent mixture, applied thinly to a substrate, is immersed in water. As solvent leaks into the water and as water enters the polymer-solvent mixture phase-separation is induced. It starts from the water–polymer/solvent interface until all the solvent migrated into the water bath and a porous, asymmetric, polymer structure is formed. This structure shows a thin initial layer of polymer on the surface that will, ideally, show small holes. Below this layer one typically finds much larger structures. To understand why such structures are formed Akthakul et al. simulated immersion precipitation membrane formation in a lattice Boltzmann framework [1]. Shortly thereafter Zhou and Powell examined the same system using a finite difference approach [64]. More recently Wang et al. used a dissipative particle dynamics method to simulate a the effects of varying polymer chain length on the formation of immersion precipitation membranes [63]. However, the system proved much too complicated to allow the simulations to generate significant insight into the main phenomena governing the membrane formation.

The simulations by Akthakul et al. suggested to us the possibility that the main factor controlling the structure formation was the dynamics of the phase-separation front. However, we found that the dynamics of phase-separation fronts in polymer systems was poorly studied. This inspired us to investigate the simplest possible

model for a phase-separation front, i.e. a phase-separation front induced by sharp front of a control parameter (solvent concentration in the immersion precipitation example) moving with a prescribed speed.

Phase-separation fronts are also of paramount importance in many eutectic alloys, where the physics of the front is responsible for the formation and orientation of ordered structures, and phase-separation goes hand in hand with a solidification problem. Jackson and Hunt analyzed the formation of the lamellar (essentially two-dimensional) and rod structures sometimes formed in eutectics. They modeled the dynamics as a steady-state diffusion driven phase-separation which occurs directly ahead of the solidification front [34]. They confirmed the earlier observed relation between the solidification front speed and the lamellar spacing, and in doing so refined some of the earlier theoretical findings. Much of the work on eutectic solidification fronts following Jackson and Hunt involved adding refinements to their model, increasing complexity to make it more like the real alloys under investigation. For instance, the inclusion of a convection layer just ahead of the solidification front by Verhoeven and Homer [56].

Other researchers took an opposite approach; developing simple models that could be simulated with numerical methods. Early work by Ball and Essery simulating front-induced phase-separation of a binary mixture noted the remarkable difference between phase-separation structures formed by fronts and those formed by homogeneous phase separation [4]. Their model consists of an underlying Ginzburg-Landau free energy, similar to our model in this paper. However, their control parameter is designed to mimic a heat-diffusion process, in analogy to the temperature front in eutectic solidification. For slow thermal diffusion they observed the lamellar structure familiar to eutecticts researchers, in addition to a lamellar structure oriented orthogonally to the motion of the temperature front when thermal diffusion was fast.

More recently, realistic phase separation fronts induced by a control-parameter with its own dynamics, have also been studied by Gonnella *et al.* [24, 25]. They examined a binary fluid where a phase-separation is induced by temperature change at the walls. The temperature then diffuses into the finite system, inducing a phase-separation front. In this systems the shape and speed of the control parameter (in this case the temperature) are space and time dependent, complicating the analysis of the resulting structures.

Another example of a realistic modeling of a phase-separation front is given by Köpf *et al.* who examined pattern formation in monolayer transfer for systems with substrate mediated condensation [40]. Here the similar patterns to the ones predicted in this paper are observed in a more complicated system were additional hydrodynamic effects lead to a condensation of surfactants in the deposition layer. In this case the surfactant concentration in the deposited later differs substantially from the lipid concentration in the free film so that the concentration is now dependent on the speed with which the phase-separation front advances.

Hantz and Biró developed a further simplified model of a phase-separation front as a moving Gaussian source in a diffusive system [28]. By decoupling phase separation from a dynamic control parameter, they are able to control the phase separation front more directly. In particular, Hantz and Biró assembled a rotating front, where the front speed is a function of distance from the axis, and the direction of motion of the front changes as it sweeps across the material. They found, in addition to the expected perpendicular and parallel lamella structures at the respective slow and fast front speeds, that the lamellar structures could bend to continue growing perpendicular to the front. They also observed that the parallel lamella formed with width and spacing dependent on the speed of the front, and they noted that this was consistent with experimental observations of Liesegang patterns. Liesegang patterns

are highly ordered structures formed in the wake of an electrolyte reaction front in a gel [42]. Antal *et al.* had earlier used a similar Gaussian source front to produce patterns with position and spacing laws consistent with Liesegang patterns [2]. In an earlier paper of ours, we prove analytically that Liesegang patterns are reproducible by a similar model [19]. Refer to the citations contained in that earlier paper for other models which have been demonstrated to produce Liesegang patterns under the proper conditions.

An even simpler model of a moving phase separation front was used by Furukawa for simulating the formation of phase separation induced morphologies [21]. The front in his model is an abrupt change in the control parameter moving at a constant average speed. Similar to Ball and Essery, Furukawa used a Ginzburg-Landau free energy. The model by Furukawa is very similar to the one used here, with a few minor differences. The implementation of our model in numerical simulation, however, is quite different as we will show in Section 4.3.

In this paper we focus on the simplest possible case: we consider a purely diffusive system, as hydrodynamics adds additional complexity to this problem. We consider fronts moving with a constant speed, since this allows us to separate transient phenomena from generic phenomena, simply by observing the front after a sufficiently long time. Furthermore we consider a sharp front, so we do not have to consider the effects of the shape of the front. For this paper we will focus on two-dimensional systems. Despite its simplicity such fronts still exhibit a rich collection of behaviors, as we will show in this paper.

This work is an extension of our work on phase separation fronts in one-dimensions. In the one dimensional case phase-separation fronts will leave in their wake alternating domains, and the only remaining question is the size of these domains [19, 17]. We were able to show that this problem could be solved analytically,

at least in the limit of small velocities. For two-dimensional systems one possible solution are stripes oriented in parallel with the front, which are essentially the same as the one-dimensional systems observed earlier.

4.2. Model

The model we use is essentially the same as the one we presented in our earlier paper [17] extended to two dimensions. We therefore give the most important aspects in short here:

To construct a model for phase separation fronts in two dimensions we consider a mixture of two materials, an $\mathcal{A}$-type and a $\mathcal{B}$-type, in an incompressible mixture such that the total density $\rho = \rho_{\mathcal{A}}(\boldsymbol{r}, t) + \rho_{\mathcal{B}}(\boldsymbol{r}, t)$ is a constant. In this paper the position vector $\boldsymbol{r} = (x, y)$ is two-dimensional. The order parameter for this system is the relative concentration:

$$\phi(\boldsymbol{r}, t) = \frac{\rho_{\mathcal{A}}(\boldsymbol{r}, t) - \rho_{\mathcal{B}}(\boldsymbol{r}, t)}{\rho} \,. \tag{206}$$

For simplicity of the model, we choose a ϕ^4-type mixing free energy [22]:

$$F = \int dx \quad \left[\frac{a(\boldsymbol{r}, t)}{2} \phi(\boldsymbol{r}, t)^2 + \frac{b(\boldsymbol{r}, t)}{4} \phi(\boldsymbol{r}, t)^4 + c(\boldsymbol{r}, t)\phi(\boldsymbol{r}, t) + \frac{\kappa(\boldsymbol{r}, t)}{2} (\nabla \phi(\boldsymbol{r}, t))^2 \right] . \tag{207}$$

The c term, linear in the order parameter, adds a constant to the chemical potential for spatially homogeneous systems. However, in the equation of motion only gradients of the chemical potential enter the dynamics, so that a constant added to the chemical potential does not alter the dynamics of the order parameter. It is included here, however, since we will consider different values of c across the front, which does influence the dynamics.

A phase separation front constitutes a spatio-temporal change in the control parameter $a(\boldsymbol{r},t)$ such that the free energy at a given location transitions from a mixing state ($a>0$) with a single minimum, to a separating state ($a<0$) with two minima. Again for simplicity, we choose the transition to be an abrupt jump from a single positive mixing value $a_M>0$ to a single negative separating value $a_S<0$. The transition moves with constant velocity $\boldsymbol{u}$, and is flat perpendicular to $\boldsymbol{u}$. The other control parameters are similarly two-valued, with an abrupt transition at the front:

$$\begin{aligned} a(\boldsymbol{r},t) &= a_S + (a_M - a_S)\Theta\left[(\boldsymbol{r}+\boldsymbol{r}_0+\boldsymbol{u}t)\cdot\hat{\boldsymbol{u}}\right] , \\ b(\boldsymbol{r},t) &= b_S + (b_M - b_S)\Theta\left[(\boldsymbol{r}+\boldsymbol{r}_0+\boldsymbol{u}t)\cdot\hat{\boldsymbol{u}}\right] , \\ c(\boldsymbol{r},t) &= c_S + (c_M - c_S)\Theta\left[(\boldsymbol{r}+\boldsymbol{r}_0+\boldsymbol{u}t)\cdot\hat{\boldsymbol{u}}\right] , \\ \kappa(\boldsymbol{r},t) &= \kappa_S + (\kappa_M - \kappa_S)\Theta\left[(\boldsymbol{r}+\boldsymbol{r}_0+\boldsymbol{u}t)\cdot\hat{\boldsymbol{u}}\right] . \end{aligned} \tag{208}$$

The *mixing* and *separating* values are denoted by subscripts M and S respectively, and Θ is the Heaviside step function.

For our diffusive system the equation of motion is

$$\partial_t\phi(\boldsymbol{r},t) = \nabla\cdot\left[m(\boldsymbol{r},t)\nabla\mu(\boldsymbol{r},t)\right] , \tag{209}$$

where m is the diffusive mobility and μ is the chemical potential. The chemical potential is derived from the free energy:

$$\begin{aligned} \mu(\boldsymbol{r},t) = \frac{\delta F}{\delta\phi} &= a(\boldsymbol{r},t)\phi(\boldsymbol{r},t) + b(\boldsymbol{r},t)\phi(\boldsymbol{r},t)^3 \\ &\quad + c(\boldsymbol{r},t) - \kappa(\boldsymbol{r},t)\nabla^2\phi(\boldsymbol{r},t) . \end{aligned} \tag{210}$$

The equation of motion only considers gradients of the full chemical potential. Since μ is itself continuous [17, Fig. 1(b)], we need not be concerned with the computational

messiness of delta functions which result from gradients of the Heaviside function present in the parameters of Eq. (208). For this model the diffusive mobility can take different values across the front:

$$m(\boldsymbol{r},t) = m_S + (m_M - m_S)\Theta\left[(\boldsymbol{r} + \boldsymbol{r}_0 + \boldsymbol{u}t)\cdot\hat{\boldsymbol{u}}\right] . \tag{211}$$

For the remainder of this paper, space and time dependence will not be written explicitly, except where needed to avoid ambiguity.

Since we intend to simulate our system with a numerical method, we will only be able to examine a finite system. The way the system is described above, this would limit our analysis to times $t = l_x/u$, where l_x is the length of the simulation in the direction of travel of the front. This was a limitation of an earlier, similar model by Furukawa [21]. In turn, this would make it costly to investigate the system for large times. To effectively look at large times we employ a transformation here (as we did in our earlier work [17]), where we keep the position of the front stationary in our simulation domain and move the sample with a constant speed u. This transformation changes the diffusive equation of motion Eq. (209) to a drift-diffusion equation of motion:

$$\partial_t\phi(\boldsymbol{r},t) = \nabla\cdot\left[-\phi(\boldsymbol{r},t)\boldsymbol{u} + m(\boldsymbol{r})\nabla\mu(\boldsymbol{r},t)\right] . \tag{212}$$

Mathematically these two approaches are entirely equivalent, but for simulation purposes the latter approach has the great advantage of allowing us to examine the front for long times.

We rewrite this model in a dimensionless form by considering the length, time, and concentration scales of spinodal decomposition for a symmetrical system ($\phi_{in} = 0$) [17]. The spinodal length is the wavelength of the concentration fluctuation that is most unstable, i.e. phase-separating the most rapidly after homogeneous phase

separation is induced by the quenching a material into the spinodal region of the phase diagram. The spinodal time is the inverse of the growth rate of those spinodal wavelength fluctuations. These are, respectively:

$$\lambda_{sp} = 2\pi\sqrt{\frac{2\kappa_S}{-a_S}}\,,\; t_{sp} = \frac{4\kappa_S}{m_S a_S^2}\,,\; \phi_{eq} = \sqrt{\frac{-a_S}{b_S}}\,. \tag{213}$$

One of the benefits of this non-dimensionalization is a reduction in the number of free parameters of this model to the seven following non-dimensional quantities:

$$\begin{aligned} &A = -\frac{a_M}{a_S}\,,\; B = \frac{b_M}{b_S}\,,\; C = \frac{c_M - c_S}{a_S\phi_{eq}}\,, \\ &M = \frac{m_M}{m_S}\,,\; K = \frac{\kappa_M}{\kappa_S}\,,\; \Phi_{in} = \frac{\phi_{in}}{\phi_{eq}}\,,\; U = u\frac{t_{sp}}{\lambda_{sp}}\,. \end{aligned} \tag{214}$$

The non-dimensional equation of motion then becomes:

$$\begin{aligned} &\partial_T\Phi + \nabla_{\boldsymbol{R}}\cdot(\Phi\boldsymbol{U}) \\ &= \frac{1}{2\pi^2}\nabla_{\boldsymbol{R}}\cdot\mathcal{M}\nabla_{\boldsymbol{R}}\left(\mathcal{A}\Phi + \mathcal{B}\Phi^3 + \mathcal{C} - \frac{\mathcal{K}}{8\pi^2}\nabla^2_{\boldsymbol{R}}\Phi\right)\,, \end{aligned} \tag{215}$$

where $\boldsymbol{R} = \boldsymbol{r}/\lambda_{sp}$ and $T = t/t_{sp}$ are the discrete non-dimensionalized length and time coordinates. The capital script letters are spatially dependent functions of the non-dimensional parameters:

$$\{\mathcal{A},\mathcal{B},\mathcal{C},\mathcal{K},\mathcal{M}\} = \begin{cases} \{-1,1,0,1,1\}\,, & X < X_f \\ \{A,B,C,K,M\}\,, & X > X_f \end{cases}. \tag{216}$$

The parameters A, B, M, K are chosen as $A = M = K = 1$ and $B = 0$. The choice of $B = 0$ is unconventional. Its justification is as follows: Since $\phi \approx \phi_{in}$ in the mixing region, we can re-expand the free energy around $\phi = \phi_{in}$, retaining only terms to

second order. This reduces the number of free parameters. As in our previous paper [17], we will restrict ourselves here to the case where $\mu_S(\pm\phi_{eq}) = \mu_M(\phi_{in})$, so that there are no long-range diffusion dynamics ahead of the front. Relaxing this restriction will alter the effective ϕ_{in} at the front and the details of the domain switching. Our choice corresponds to $C = -A\Phi_{in}$.

This leaves as the only remaining free parameters: the initial concentration of the mixed material Φ_{in}, and the speed of the advancing front U. Details of the effect of changing some of the other non-dimensional parameters can be found in our previous work [17].

4.3. Simulation method

To simulate the drift diffusion equation (212) we use a lattice Boltzmann (LB) method, mostly because we intend to extend our analysis to hydrodynamic systems where lattice Boltzmann methods have been shown to perform particularly well. Lattice Boltzmann uses a discretized form of the Boltzmann transport equation [48]:

$$f_i(\boldsymbol{r} + \boldsymbol{v}_i, t+1) - f_i(\boldsymbol{r}, t) = \frac{1}{\tau(\boldsymbol{r}, t)} \left[f_i^0 - f_i(\boldsymbol{r}, t) \right] . \tag{217}$$

Time advances in discrete steps ($\Delta t = 1$ is implied above), and space is divided into regular cells which tile the simulation space. The density distribution functions for individual particles are replaced by a discrete set of distribution functions $f_i(\boldsymbol{r}, t)$ that represent the density of particles at position $\boldsymbol{r}$ and time t moving with velocity $\boldsymbol{v}_i$. The velocity vectors are restricted such that from any given lattice site $\boldsymbol{r}$, the transformation $\boldsymbol{r} \to \boldsymbol{r} + \boldsymbol{v}_i$, for every index i, always results in a $\boldsymbol{r}$ which lies on a lattice site or a boundary site. Following C programming language conventions, the lattice sites are numbered from 0 to $l_x - 1$ in the x direction.

The zero-order velocity moment of the non-equilibrium distribution functions is

the order parameter:

$$\sum_i f_i(\boldsymbol{r},t) = \phi(\boldsymbol{r},t)\,. \tag{218}$$

The choice of the equilibrium moment distributions determines the equation of motion to be simulated. For a drift-diffusion equation, we chose:

$$\begin{aligned}
\sum_i f_i^0(\boldsymbol{r},t) &= \phi(\boldsymbol{r},t)\,, \\
\sum_i f_i^0(\boldsymbol{r},t) v_{i\alpha} &= s u_\alpha \phi(\boldsymbol{r},t)\,, \\
\sum_i f_i^0(\boldsymbol{r},t) v_{i\alpha} v_{i\beta} &= s\mu(\boldsymbol{r},t) + s^2 u_\alpha u_\beta \phi(\boldsymbol{r},t)\delta_{\alpha\beta}\,.
\end{aligned} \tag{219}$$

The subscripts α and β are indices for the spatial dimensions x and y; for instance u_α represents the magnitude of the vector $\boldsymbol{u}$ in the α direction. The time-scaling parameter s introduced here could easily be absorbed into the other parameters, but it provides us with a convenient dial to select the fastest stable simulation parameters.

In this transformed reference frame, the control parameter front that induces phase-separation is stationary, and the material is advected across the front. We choose to align the advection velocity with the x-axis: $\boldsymbol{u} = (u_x, 0)$. The control parameter front is then implemented by setting the parameters for $x < x_f$ to their separating values, and setting the parameters for $x \geq x_f$ to their mixing values. For example, the model parameter $a(\boldsymbol{r},t)$ from Eq. (208) implies the simulation parameter:

$$a(\boldsymbol{r}) = \begin{cases} a_S\,, & x < x_f \\ a_M\,, & x \geq x_f \end{cases}\,. \tag{220}$$

Derivation of the equation of motion from these moments can be accomplished by a Taylor expansion of the lattice Boltzmann equation (217) with repeated substitution of the unknown functions f_i with first order approximations in terms of the

known equilibrium f_i^0. This is shown in more detail in our previous paper for the one-dimensional system [17], and the analysis in higher dimensions remains essentially the same. In terms of the simulation parameters, the equation of motion becomes:

$$\frac{1}{s}\partial_t\phi - \nabla\cdot(\boldsymbol{u}\phi) + O\left(\partial^3\right) = \nabla\cdot(\tau - 1/2)\,\nabla\mu\,. \tag{221}$$

So we have to identify the mobility m with $m = \tau - 1/2$. It turns out that this method does not show numerical artifacts for rapidly changing mobilities. This suitability for simulating abrupt changes in τ was previously used to simulate abrupt changes in dielectric properties of a medium [62].

To fulfill Galilean invariance and isotropy requirements on a square lattice, implied by our choice of moment distributions Eqs. (219) for an arbitrary advection velocity $\boldsymbol{u}(\boldsymbol{r},t)$–as would be the case were this simulation coupled to a hydrodynamic flow–would require the use of nine (or seven on a hexagonal lattice) velocity vectors in two dimensions. However, because $\boldsymbol{u} = u_x$ is fixed and aligned to the x-axis we require only five velocities in two dimensions:

$$\boldsymbol{v}_i = \left\{ \begin{pmatrix} 0 \\ 0 \end{pmatrix}, \begin{pmatrix} -1 \\ 0 \end{pmatrix}, \begin{pmatrix} 1 \\ 0 \end{pmatrix}, \begin{pmatrix} 0 \\ -1 \end{pmatrix}, \begin{pmatrix} 0 \\ 1 \end{pmatrix} \right\} \tag{222}$$

a so-called D2Q5 LB implementation. For this velocity set we use the equilibrium distributions:

$$\begin{aligned} f_0^0 &= \left(1 - u_x^2 s^2\right)\phi - 2\mu s\,, \\ f_1^0 &= \frac{1}{2}\left(u_x^2 s^2 - u_x s\right)\phi + \mu s/2\,, \\ f_2^0 &= \frac{1}{2}\left(u_x^2 s^2 + u_x s\right)\phi + \mu s/2\,, \\ f_3^0 &= f_4^0 = \mu s/2\,. \end{aligned} \tag{223}$$

In lattice Boltzmann units the material velocity is $-u_x s$, and can be made arbitrarily small by adjusting s.

The equilibrium distributions contain the chemical potential μ given by Eq. (210). The chemical potential contains a Laplacian which is evaluated on the discrete lattice as

$$\nabla^2\phi(x,y) = \sum_{i,j=-1}^{1} w_{ij}\phi(x+i, y+j)\,, \tag{224}$$

where the weights w_{ij} are the elements of the stencil matrix

$$\boldsymbol{w} = \frac{1}{4}\begin{pmatrix} 1 & 2 & 1 \\ 2 & -12 & 2 \\ 1 & 2 & 1 \end{pmatrix}\,, \tag{225}$$

where the row and columns are numbered $\{-1, 0, 1\}$. This choice of discrete Laplacian with $(x \pm 1, y \pm 1)$ terms is less susceptible to certain instabilities than those which have only $(x \pm 1, y)$, and $(x, y \pm 1)$ terms, allowing us to use an almost twice as large an effective time step [47] at very small computational cost.

We still need to define the boundary conditions. The y-dimension boundary conditions are periodic. The inflow boundary condition at $x = l_x$ is straightforward with homogeneous material advancing with a constant prescribed flux:

$$f_1(x = l_x - 1, y, t+1) = f_2(x = l_x - 1, y, t) + u_x s\phi_{in}\,. \tag{226}$$

To calculate the Laplacian on this boundary we simply set $\phi(l_x, y) = \phi_{in}$.

The outflow boundary condition is somewhat more complicated, since we now have phase-separated material that is advected out and we need information about ϕ and μ from lattice sites that are not part of the simulation space. We define our outflow boundary condition with the understanding that it should be neutral wetting to all concentration values, should not introduce gradients on the chemical potential,

and any effect on the morphology should be short ranged compared to the simulation size. This is accomplished by simply bouncing back the outflow density distribution after subtracting the material advected out of the simulation:

$$f_2(x=0,y,t+1) = f_1(x=0,y,t) - u_x s\phi(x=0,y,t)\,. \tag{227}$$

For the purpose of calculating the Laplacian at the outflow boundary we set off-lattice concentrations to be the same as the boundary $\phi(-1,y) = \phi(0,y)$. The effect of the outflow boundary condition on the bulk of the simulation can be ascertained by observing a normally stationary morphology as it is advected out of the simulation. One choice is a single large circular region of $\mathcal{B}$-type material suspended in a bulk which is otherwise entirely $\mathcal{A}$-type. Tests such as these (not shown) verify that this boundary condition has a very small effect, and is acceptable for this model. Further evidence can be found by comparing phase-separation structures in Figure 19a and Figure 20b which are nearly identical, as discussed later.

This fully describes our method which allows us to simulate the dynamics of structure generation by phase separation fronts. As a final note: while simulations will show material moving past a stationary front, in our discussion of these simulation results we will always refer to the front as moving and the bulk of the material as stationary.

4.4. First Survey

Using our lattice Boltzmann method we now investigate how the phase separation front will influence the formation of structure. To do this we set up a medium size simulation of $x = 512$ by $y = 1024$ lattice points. We put the position of the front at $x_f = 384$ (in lattice units). The region from $x = 0$ to $x = x_f$ undergoes homogeneous phase-separation. We use the initial condition $\Phi(\boldsymbol{r}) = \Phi_{in} + 0.01\xi$,

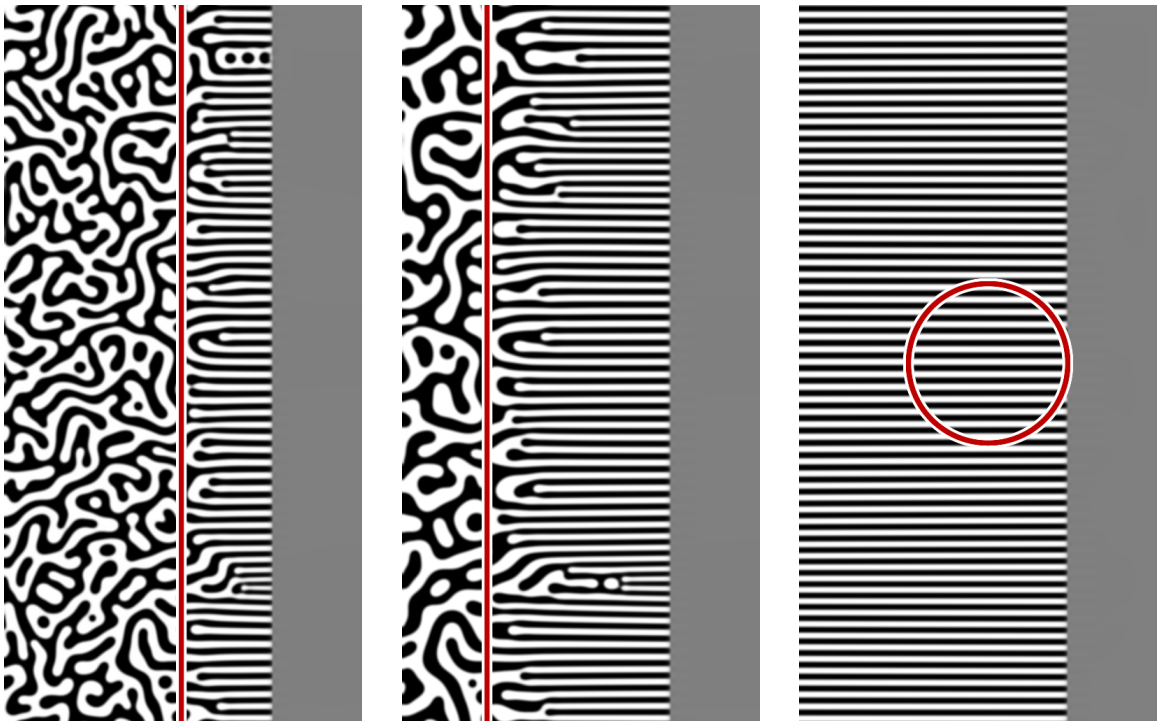

(a) $T = 82$, $UT = 10.5$ (b) $T = 164$, $UT = 20.9$ (c) $T = 966$, $UT = 123.6$

Figure 19. (Color online) Stripe formation in the wake of a phase separation front as seen in an LBM simulation at $U = 0.128$ and symmetric mixed material concentration $\Phi = 0$. The starting location of the front is marked as a vertical stripe. The rightmost image is the final structure observed after the front has moved far into the material. A sample of the final morphology, noted by the circled region, will be compared to samples from other simulations performed with different parameter values.

where ξ is random noise uniformly distributed in the range $[-1, 1]$, as is typically done for homogeneous phase-separation simulations. The other simulation parameters are: $a_M = 1$, $a_S = -1$, $b_M = 0$, $b_S = 1$, $c_M = -\phi_{in}$, $c_S = 0$, $m_M = m_S = 1/2$, and $\kappa_M = \kappa_S = 2$, consistent with the choice of non-dimensional parameters made at the end of Section 4.2. The time scaling parameter $s = 0.026$ is chosen as a maximum numerically stable effective time step for these parameters [61].

Such a simulation for $U = 0.128$ is shown in Figure 19. The current position of the front at any time is easily visible as the transition between the black-and-white phase-separated region and the gray mixed region. In Figure 19a the front has moved only a short distance of $x = 132 = 10.5\,\lambda_{sp}$ (in units of the spinodal wavelength).

The position where the front started is marked by a vertical stripe. The area to the left of the initial location of the front has undergone normal spinodal decomposition generating a phase-separation morphology typical of homogeneous phase-separation. As the front moves on, new material phase-separates, but we see immediately that the structure of these newly formed domains is quite different from the domains formed through homogeneous phase-separation. In the region between the initial front position and the current front position we observe a different kind of morphology: the domains are oriented orthogonally to the front, and show a variety of widths. In Figure 19b the front has advanced a distance $x = 263 = 20.9\,\lambda_{sp}$. The region of homogeneous phase-separation has noticeably coarsened and the newly overtaken material continues to phase-separate into a striped morphology. The striped structure, however, is not homogeneous. Particularly where the stripes are thin, defects can be seen to traverse into the striped domains. In Figure 19c the front has traveled a distance $x = 1553 = 123.6\,\lambda_{sp}$. Now all the defects have been advected out of the system and the stripes are taking on a uniform thickness. This is a stationary solution that will persist indefinitely. Note that there is no evidence of any further coarsening at the position of the front.

To examine the effect of front speed we now perform a simulation for $U = 0.256$. The results of this simulation are shown in Figure 20. This time the morphology formation at the front is qualitatively different. Again a regular striped morphology is formed, but it is now oriented parallel to the front in agreement with previous results[21, 28]. In Figure 20a the front has traveled a short distance of $x = 105 = 8.4\,\lambda_{sp}$. We observe typical homogeneous phase-separation morphology behind the original front location, however, where the front has traversed there are stripes of somewhat regular widths oriented roughly parallel to the front. While the stripe widths are fairly uniform, there are still a large number of bends in these stripes. In

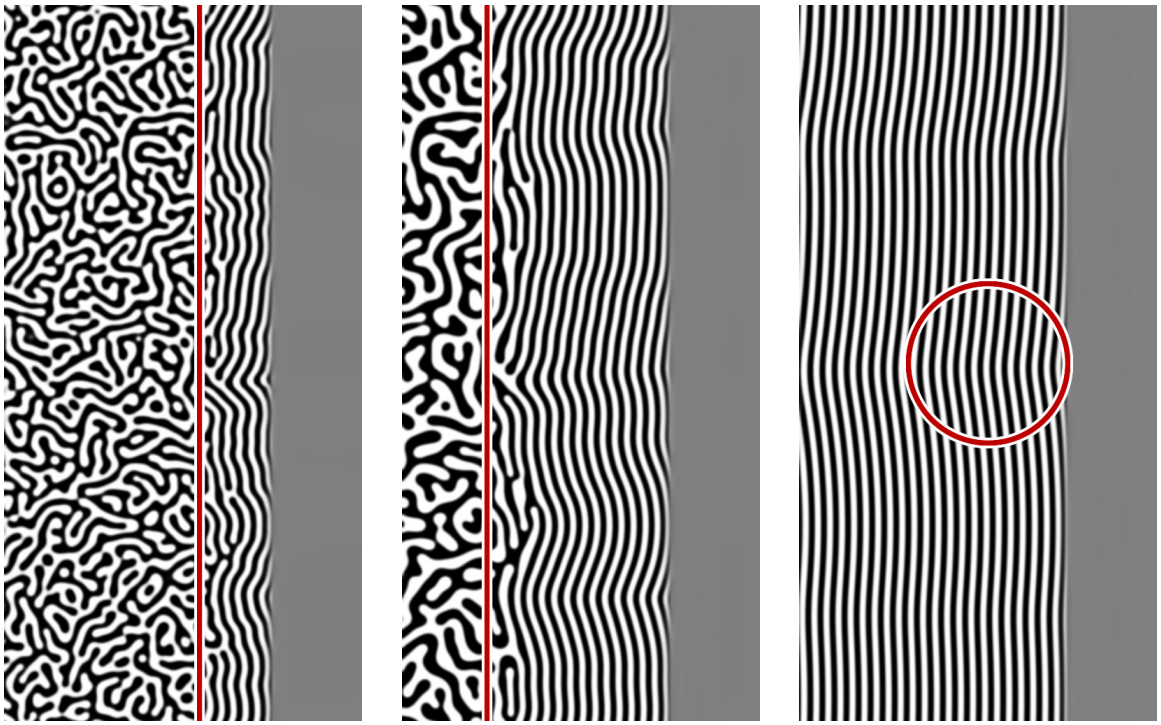

(a) $T = 33$, $UT = 8.4$ (b) $T = 82$, $UT = 20.9$ (c) $T = 491$, $UT = 125.7$

Figure 20. (Color online) Stripe formation in the wake of a phase separation front as seen in an LBM simulation at $U = 0.256$ and symmetric mixed material concentration $\Phi = 0$, similar to Figure 19. At this faster speed the stripes formed by the front are oriented parallel to the front.

Figure 20b we see that as time progresses new stripes form with fewer sharp bends, but the stripe widths do not appreciably change.

Note that the region of homogeneous phase-separation corresponds to the homogeneous phase-separation in Figure 20a at the same non-dimensional time. The initial noise on the order parameter was identical for both simulations and closer examination shows that the resulting phase-separation morphologies are nearly identical. This shows that there is little interaction between the regions of striped morphology and the homogeneous region. It also shows that neither the outflow boundary condition nor the advection speed significantly influence the simulations. This indicates that the coarsening of the region which separated under homogeneous conditions only slightly affects the striped morphology.

The width of stripes oriented parallel to the front can be understood by considering this as a quasi one-dimensional system. We analyzed this situation in an earlier paper [17] and found that the wavelength of the parallel stripes follows from the front speed as

$$L(U) = \frac{8 \ln \left(2 - \sqrt{2/3}\right) + 4\sqrt{2/3} - 4}{\pi^2 U}, \tag{228}$$

for very slow fronts ($U < 0.001$) moving into material that has vanishingly low diffusive mobility ahead of the front ($M \to 0$). For faster speeds this relation breaks down, and this theoretical prediction is inappropriate for the front speed of $U = 0.256$ in the example simulation shown in Figure 20. However, the observed wavelength of these quasi-one-dimensional stripes $L_{\parallel 2\mathrm{D}} = 1.39$ with $M = 1$ compares favorably with the measured stripe wavelength $L_{1\mathrm{D}} = 1.36$ from the $M = 0$ simulation results in our earlier paper on phase separation fronts in one-dimensional systems [17].

These two qualitatively different morphologies were first described by Furukawa [21]. They were later rediscovered by Hantz and Biró [28] and appear also to be related to structures formed from eutectic mixtures, although typically a phase-field formalism is used to describe these structures.

The fact that simply changing the velocity leads to a change in orientation of the domains raises the question as to where this transition happens, and surprisingly there appears to be no numerical value for the speed at which this transitions happens in the literature. Also if we change the input composition, we will have to obtain stripes that have different width depending on the composition. This more systematic investigation constitutes the main contribution of this paper. Next we obtain a state-diagram from simulations such as the simulations as shown above. We pick a sample of the morphologies–shown as a circle in Figure 19c and Figure 20c–and place these sample morphologies in a diagram at a position corresponding to Φ_{in} and U. We then performed simulations for a set of different values of Φ_{in} and U, but with all

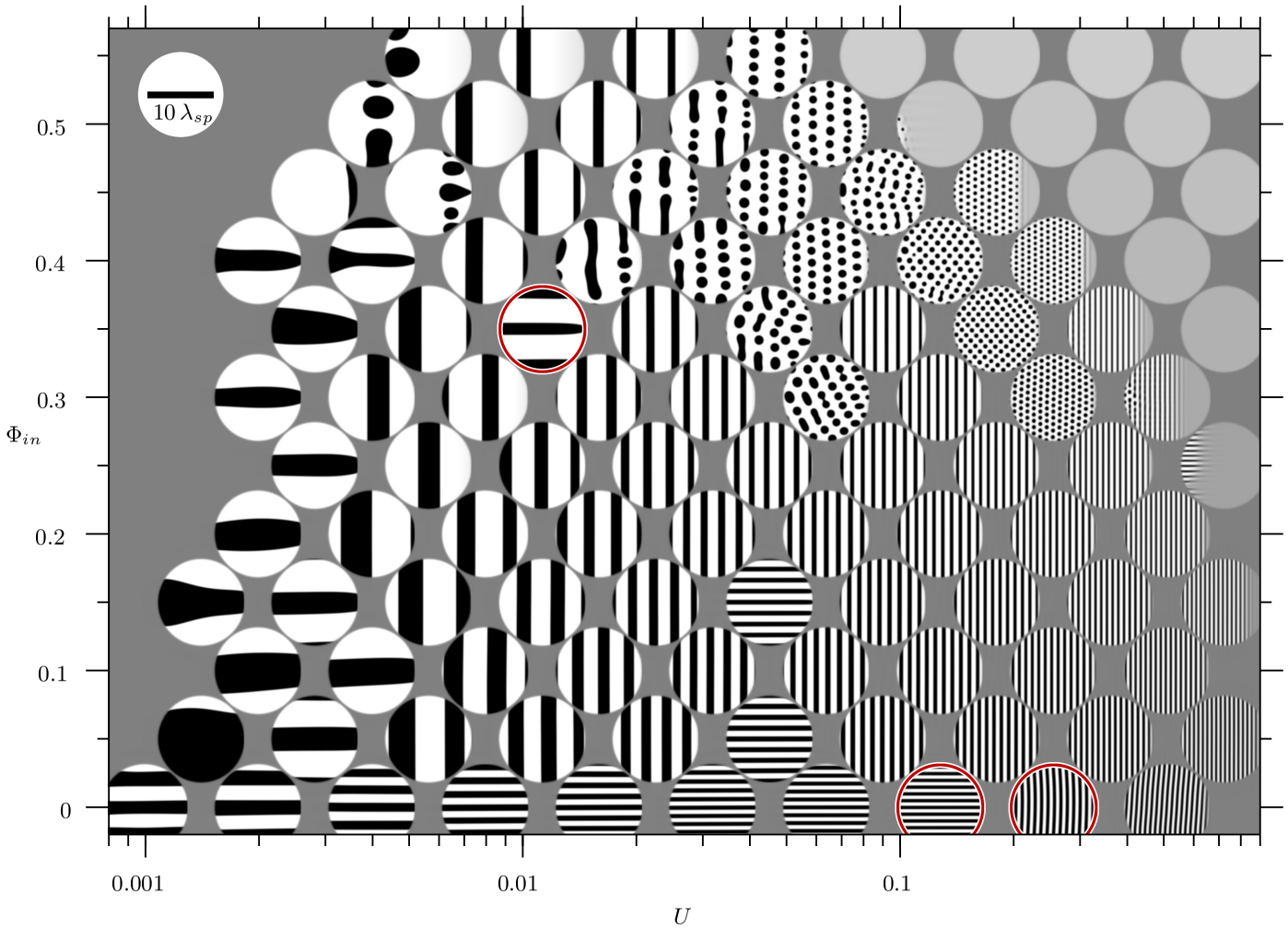

Figure 21. (Color online) Morphology phase diagram as a function of front speed U and material volume fraction Φ_{in} measured with random initial morphologies. Examples from this map are shown in Figure 19, 20, and 22. The bar in the upper left corner provides scale. The lack of an apparent pattern in the morphology grouping is due to the strong hysteresis of morphologies. Further explanation is given in Figure 22 and the text.

other parameters kept constant. We ran each of these simulations until the front had moved approximately 1500 lattice sites, or about 4 times the distance from outflow boundary at $x = 0$ to the front position at $x_f = 384$. We again use a circular section near the front, as indicated in Figure 19c and Figure 20c, and put them in a Φ_{in}/U graph at the appropriate position. This survey of resulting morphologies is shown in Figure 21.

The result of the survey is initially surprising: while there is a clear transition from parallel to orthogonal stripes for $\Phi_{in} = 0$ at around $U \approx 0.2$, orthogonal domains appear to be an anomaly only observed for exactly symmetric domains. However, there appears to be another transition between orientations of asymmetric domains at around a hundredth of this speed at $U \approx 0.003$. The state diagram shows one additional boundary between regions of stripes and droplets for more off-critical mixtures. These droplet structures appear to be preferred for larger speeds. For even larger speeds and more off-critical mixtures we see only mixed material, visible as gray disks. This means that the speed of a phase-separation front moving with constant speed into the mixture is smaller than the imposed speed of our front, and phase-separation is unable to keep up with our front. The transition to a free front, to the accuracy of this survey, is unaffected by the initial conditions. For the parallel stripes the free front speed is given by [55]

$$U_{\text{free}}(\Phi_{in}) = \frac{1}{27\pi}\sqrt{2\left(34 + 14\sqrt{7}\right)\left(3 - 9\Phi_{in}^2\right)^3}\,. \tag{229}$$

Closer examination of this state-diagram reveals more unexpected results. There are three examples of orthogonal stripes formed in a sea of parallel stripes at (U, Φ_{in}) values of (0.045, 0.05), (0.045, 0.15), and (0.01, 0.35). These structures appear to break the prevalent trend of their neighbors and it is worth while to consider these simulations in some more detail. We will focus here on the simulation for ($U =$

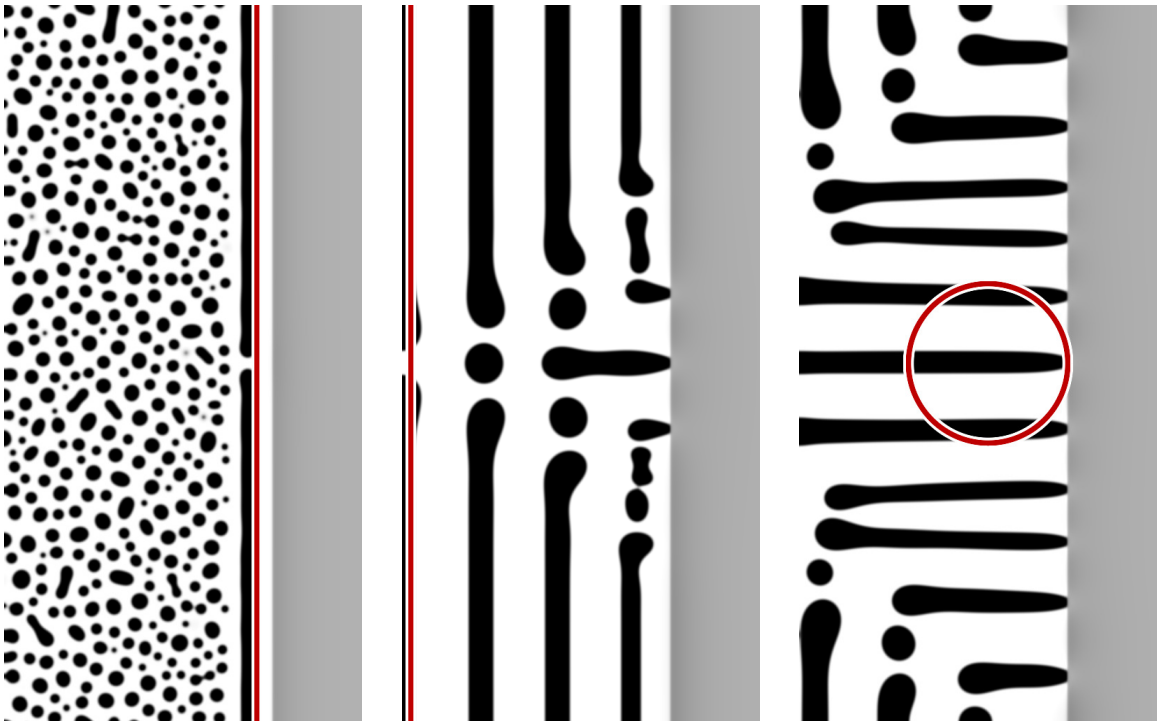

(a) $T = 164$, $UT = 1.8$ (b) $T = 2619$, $UT = 29.6$ (c) $T = 5565$, $UT = 62.9$

Figure 22. (Color online) LBM simulation results showing strong depletion effects following a phase separation front for asymmetric mixed material volume fraction. The moving front suddenly appears in a mixed material with volume fraction $\Phi_{in} = 0.35$ containing small variations. Shown in (a), the region far behind the front undergoes spinodal decomposition and droplet growth as in a homogeneous quench. Near the front the formation of a depletion zone induces domains oriented parallel to the front. By chance a defect in this domain facilitates a transition (b) to the favored orthogonal stripe morphology shown in (c). The circle in (c) shows the region sampled for use in Figure 21. The front speed is $U = 0.0113$ for this example.

0.01, $\Phi_{in} = 0.35$). Three snapshots of this simulation are shown in Figure 22. The homogeneous spinodal morphology are droplets. However at the front a depletion zone favoring white material is formed.

The reason for this depletion layer is as follows: we chose to set the C-parameter in the mixing region such that $\mu(\Phi_{in}) = 0$ in the mixing region. After phase-separation we have $\mu(\Phi = \pm 1) = 0$ in the separated region and there will be no long range chemical potential gradient leading to extended diffusion of material into or out of the mixing region. Before the initial phase-separation in the separating region the

order parameter is nearly uniformly Φ_{in} and $\mu(\Phi_{in}) \neq 0$. Therefore we get some diffusion into and out of the mixing region leading, in this example, to a depletion of black material near the front. Once the phase-separation is complete, there is no longer a difference in the chemical potential far away from the front.

After the initial phase-separation with the creation of the depletion zone we then observe the nucleation of a first parallel black domain, as can be seen in Figure 22a. So far this scenario is generic, but this simulation is special in that the formation of the first parallel stripe is not perfect, but a single defect was created. This defect now has a profound effect on the further evolution of the morphology formation. The next black domain that is formed has two defects with an interspersed drop. The following generation of parallel stripes has three drops, but the middle drop now maintains contact with the front, forming the first orthogonal stripe. The defect invades the formation of parallel domains leading to a wedge of orthogonal stripes that replace the parallel stripes. After a sufficiently long time we are left with a purely orthogonal morphology.

This suggests that instead of our state-diagram as shown in Figure 22 we should associate the orientation of the domains with a probability, since the selection is apparently probabilistic, depending on the details of the homogeneous phase-separation, which in turn depends on the initial noise. However, since the appearance of a single defect can be sufficient to switch the orientation (as shown in Figure 22) we expect the probability of finding a certain morphology to also depend on the system size, since it is more likely to develop such a defect in a larger system. In the limit of a macroscopic system, we would expect that the probability of finding a defect would increase significantly, so that it becomes more interesting to examine which morphology is the preferred morphology.

To find out what is the preferred morphology we choose an initial condition which contains stripes of both parallel and orthogonal orientation and is consistent with the overall composition Φ_{in}. Parallel stripes are generated through a nucleation process and such a stripe selects its preferred length. For the formation of orthogonal strips no nucleation occurs and it is more difficult for such stripes to select a preferred length scale. Here we design our initial condition with a range of stripe widths to allow for easy selection of the preferred width. We show this initial condition in Figure 23a.

We construct the initial conditions by selecting a square region of the simulation with side length l that is half the simulation height. Assuming this region has an origin in the lower left, the concentration in the region is given by:

$$\Phi(x,y) = \text{signum}\left[\sin\left(\frac{2\pi l y}{al-(a+b)y}\right) + \sin\left(\frac{\pi\Phi_{in}}{2}\right)\right] , \tag{230}$$

where $a = \lambda_{sp}$ and $b = 4\,\lambda_{sp}$ are, respectively, the smallest and largest stripe wavelengths initially generated. The region described is the lower-center of Figure 23a. The upper-center region is constructed similarly, although with a $\pi/2$ rotation to favor formation of parallel oriented stripes. To avoid the possibility of the outflow boundary condition interfering with stripe selection dynamics, we disconnect the initially phase separated regions from the boundary with a region of mixed material at the initial volume fraction containing small fluctuations similar to the region ahead of the front.

In Figure 23b we see that only one of these initial stripes is selected to form the first orthogonal stripe. For this example the orthogonal stripes are again the preferred morphology (Figure 23b) and the orthogonal stripes eventually replace the

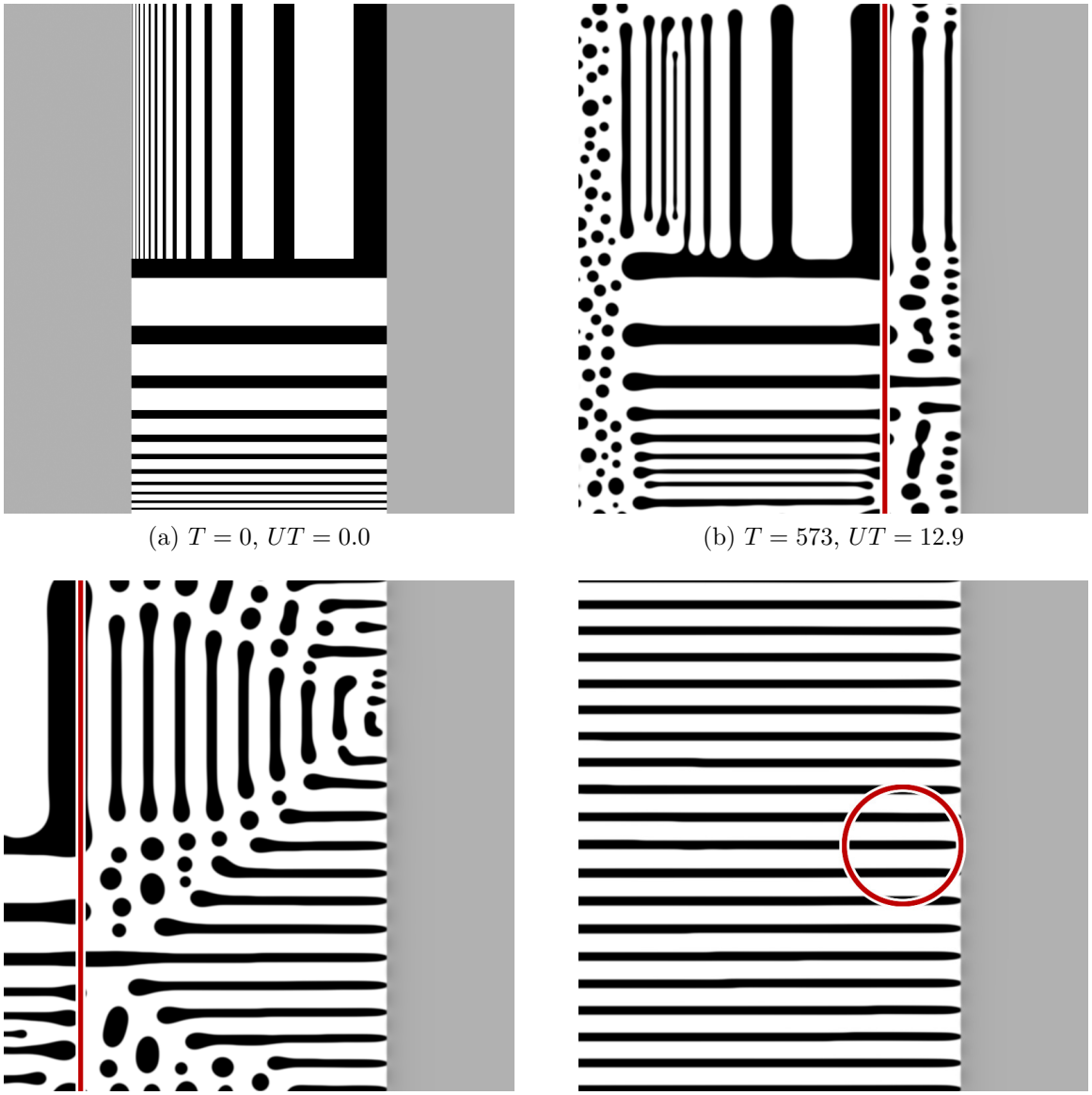

(a) $T = 0$, $UT = 0.0$

(b) $T = 573$, $UT = 12.9$

(c) $T = 2292$, $UT = 51.9$

(d) $T = 9739$, $UT = 220.4$

Figure 23. (Color online) LBM simulation results showing favored morphology selection from an initial morphology mixture. Here the imposed front speed is $U = 0.0226$ and initial concentration is $\Phi_{in} = 0.35$. These parameters have a favored morphology of stationary stripes, but is close in parameter space to the droplet morphology region. The initial phase separation configuration (a) allows for the selection of the favored morphology without the strong depletion effects observed in Figure 22a which sometimes occur after spinodal decomposition near a front. The stability of the periodic stripes is evident in (c). The final configuration in (d) shows the stable stationary stripe morphology, and a circle which outlines the region sampled for use in Figure 24.

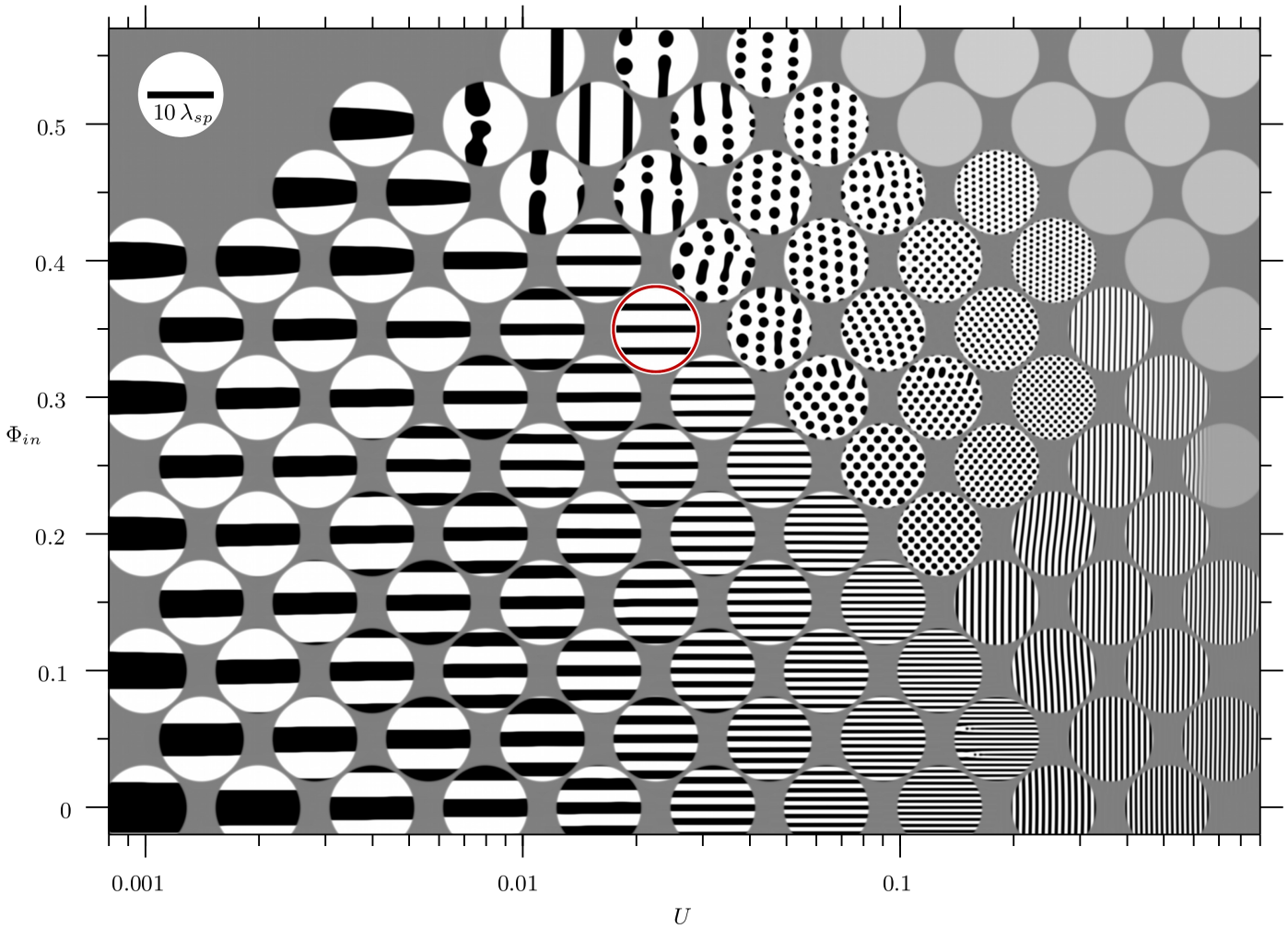

Figure 24. (Color online) Morphology phase diagram as a function of front speed U and material volume fraction Φ_{in} measured after initialization with morphologies containing parallel and orthogonal stripes. The initial stripe wavelengths range from one to ten spinodal wavelengths. Behind the initial stripes is a region of mixed material with small fluctuations near the outflow boundary. An example of the initial condition and final morphology selection is shown in Figure 23.

parallel stripes (Figure 23c). Depending on the volume fraction and the front speed either orthogonal stripes (as shown here), parallel stripes, or droplets may turn out to be the preferred morphologies.

With this new initial condition we may now calculate a new state diagram. The simulations used in this survey use the same non-dimensional parameters as the first survey. Here the simulation size has been changed to $x = 768$ by $y = 1024$; widened to accommodate the new initial conditions. To compensate for the increased computational cost of a larger simulation we chose to use a smaller value for the interfacial free energy cost $\kappa = 1$, which increases the effective simulation speed by allowing a larger effective time step $s = 0.079$ [47]. This new state diagram is shown in Figure 24. As expected we find that for the preferred morphologies there is now a much larger range of parameter values for which we find orthogonal stripes. For symmetric mixtures the transition between orthogonal and parallel stripes appears unchanged up to the accuracy of this survey. As we change the Φ_{in} from symmetrical ($\Phi_{in} = 0$) to asymmetrical ($\Phi_{in} \neq 0$) compositions we now observe a continuous transition in morphologies. This is because we start with a phase-separated morphology in the separating region, and we no longer form a depletion layer. Thus parallel or orthogonal stripes are not *a priori* favored. We see that increasing the volume fraction still lowers the speed for which we see a transition between orthogonal and parallel stripes, albeit in a much less drastic fashion.

We also find a larger parameter range for which we find droplet arrays, particularly for larger speeds and more symmetrical volume fractions. We can now write a schematic state diagram for the preferred morphologies. This is shown in Figure 25. The region labeled "free front (periodic)" is where phase separation lags behind the control parameter front. The "free front (single domain)" regions are where initially undifferentiated material will not spontaneously demix without fluctuations to induce

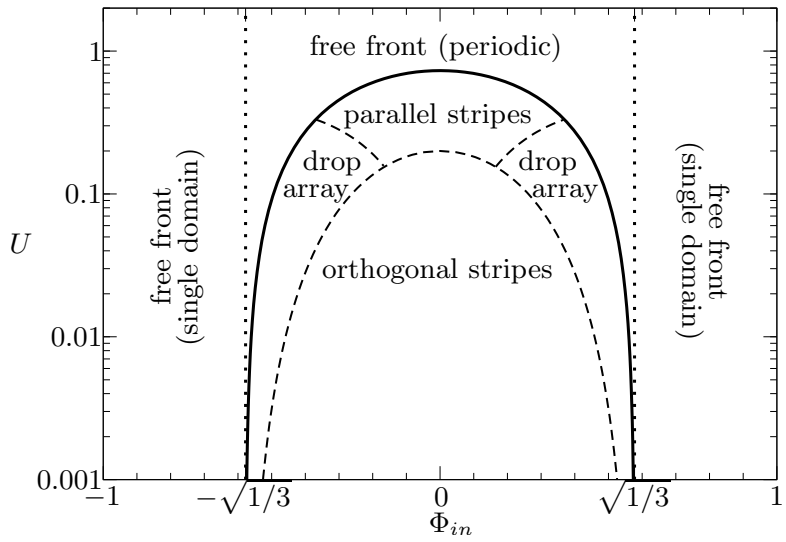

Figure 25. Morphology phase diagram of front induced phase separation generated structures in two dimensions. See text at the end of Section 4.5 for a detailed description of the regions and boundaries.

nucleation. Without fluctuations, instead of new domain formation, any existing domains of phase-separated material will slowly grow into the mixed material. How structures which may form in these regions are effected by the passage of a control parameter front is beyond the scope of this paper. The regions under the solid curve are based on observations of the preferred morphology evidenced in Figs. 21 and 24. Apart from the free front region we also show the regions where we observe parallel stripes, orthogonal stripes, and droplet arrays. The former two we have covered in previous sections, but the later requires more discussion. The droplet structure is observed to initially form near the front with little long-range order. As the front progresses, the position of the newly forming droplets is influenced by the depletion of material caused by the formation of the previous drops. The larger the drop formed, the more it depletes the surrounding region, and the further away the next droplets will form. This mechanism causes reordering and elimination of small droplets in favor of larger droplets. A nucleation condition imposes a maximum droplet size for a given front speed and mixed material concentration. The result is a droplet structure which

converges towards a highly ordered array of homogeneous size droplets. Whether the droplet array has a preferred orientation, or if it is periodic in the reference frame of the front, are open questions.

4.6. Analysis of Results for Critical Concentrations

We have observed in the surveys that a phase separation front moving into material that is at the critical concentration $\Phi_{in} = 0$ will form a striped morphology that is oriented either parallel or orthogonal to the front. The parallel stripes are an essentially one-dimensional morphology, and have been discussed in our previous paper [17]. As mentioned in Section 4.4, the key property of parallel stripes is that for a given set of parameters there is a unique stripe wavelength, and the wavelength scales $L_{\|} \propto 1/\sqrt{U}$. By contrast, orthogonally oriented stripes may form with a wide range of wavelengths for a given parameter set. In this section we analytically determine the stable wavelengths for orthogonal stripes as a function of the enslaved front speed. We accomplish this in two stages. We first determine the maximum wavelength of a stripe before a new stripe nucleates in its center, splitting it. We next find that there is a metastable minimum stripe width, below which coarsening dynamics can result in stripes which disappear into the front. The result is a region of stability for the orthogonal stripe morphology, outside of which we predict the favored morphology is parallel stripes or droplets.

4.6.1. Maximum Orthogonal Stripe Size

The mechanism responsible for limiting the maximum stripe wavelength is the nucleation of an opposite-type stripe at its center. This can occur, even without fluctuations, due to the build-up of a nucleation kernel ahead of the enslaved front, similar to what happens in the one-dimensional case [17].

Formation of stable orthogonal stripes by a moving front results in a chemical potential profile that is stationary in the reference frame of the font. We analytically determine this profile directly from the stationary solution ($\partial_T \Phi \to 0$) to the equation of motion:

$$0 = \frac{1}{2\pi^2} \nabla^2_{\boldsymbol{R}} \mu - \nabla_{\boldsymbol{R}} \cdot (\Phi \boldsymbol{U}) \ . \tag{231}$$

The morphology under consideration is an array of highly ordered orthogonal stripes of wavelength $L_\perp$ with an $\mathcal{A}$-type stripe centered on the X-axis and the phase separation front on the Y-axis. The front velocity $\boldsymbol{U} = (U, 0)$ is entirely in the X-direction and constant, simplifying the gradient term to a derivative of the concentration Φ in the X-direction which is highly dominated by the concentration gradient at the front. We approximated this term as an abrupt step which we expect to become exact in the limit of large stripes and slow fronts. We focus on critical mixtures here, since additional complications occur for off-critical situations, as mentioned below. For critical mixtures, the gradient term then simplifies to

$$\boldsymbol{\nabla}_{\boldsymbol{R}} \cdot (\boldsymbol{U}\Phi) = U \frac{d}{dX} \Phi \approx U \delta(X) \, \mathrm{Sqr}(Y/L_\perp) \ , \tag{232}$$

where $\mathrm{Sqr}(x) \equiv \mathrm{signum}[\cos(2\pi x)]$ is the square-wave function. This is the only approximation made in our calculation.

An alternate form of the square-wave function is as an infinite series of delta function convolutions. To make the series converge faster, each term of the series is centered on a crest and extends to include half of each adjacent trough:

$$Sq(x) = \sum_{n=-\infty}^{\infty} \left(2 \int_{n-1/4}^{n+1/4} \delta(\widetilde{x} - x) \, d\widetilde{x} - \int_{n-1/2}^{n+1/2} \delta(\widetilde{x} - x) \, d\widetilde{x} \right) \ . \tag{233}$$

Combined with the delta function property $\delta(x/\alpha) = |\alpha| \, \delta(x)$ and the n-dimensional

vector delta function identity $\delta_n(\boldsymbol{r}) \equiv \delta(x_1)\delta(x_2)\cdots\delta(x_n)$, this alternate form allows Eq. (231) to be rewritten

$$\boldsymbol{\nabla}^2_{\boldsymbol{R}}\mu = 2\pi^2 U L_\perp \sum_{n=-\infty}^{\infty} \left(2\int_{n-1/4}^{n+1/4} \delta_2(L_\perp \widetilde{Y}\boldsymbol{e}_Y - \boldsymbol{R})\, d\widetilde{Y} - \int_{n-1/2}^{n+1/2} \delta_2(L_\perp \widetilde{Y}\boldsymbol{e}_Y - \boldsymbol{R})\, d\widetilde{Y} \right) , \tag{234}$$

where $\boldsymbol{e}_Y$ is the Y-axis unit vector. The boundary condition for this morphology is a vanishing chemical potential far ahead and behind the front: $\mu(X \to \pm\infty) = 0$. The Poisson equation $\nabla^2 f(\boldsymbol{r}, \boldsymbol{r}_0) = \delta_2(\boldsymbol{r}_0 - \boldsymbol{r})$ has the fundamental solution $f(\boldsymbol{r}, \boldsymbol{r}_0) = \frac{1}{2\pi} \ln|\boldsymbol{r}_0 - \boldsymbol{r}|$. This can be directly applied to the above equation to arrive at an infinite series integral solution for the chemical potential profile:

$$\mu(L_\perp \boldsymbol{R}) = \pi U L_\perp \sum_{n=-\infty}^{\infty} \left(2\int_{n-1/4}^{n+1/4} \ln\sqrt{X^2 + (\widetilde{Y} - Y)^2}\, d\widetilde{Y} - \int_{n-1/2}^{n+1/2} \ln\sqrt{X^2 + (\widetilde{Y} - Y)^2}\, d\widetilde{Y} \right) , \tag{235}$$

It is easily seen that, by symmetry, this solution satisfies the chemical potential boundary condition. The integrals are straightforward, however the result is some-

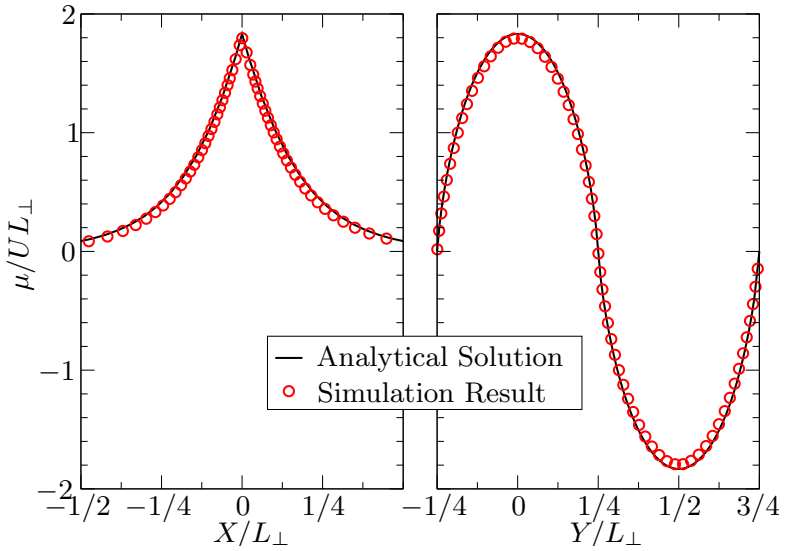

Figure 26. (Color online) Comparison of the analytical chemical potential profile of Eq. (236) (line) with LBM simulation results (circles) for large stripes $L_\perp = 70$ formed by a slow $U = 0.00235$ front. The left figure shows μ along the centerline of a stripe of $\mathcal{B}$-type material. The right figure shows μ at the position of the front ahead of two adjacent stripes. The profile in each figure intersect at $X/L_\perp = Y/L_\perp = 0$.

what lengthy:

$$\begin{aligned}\mu(L_\perp \boldsymbol{R}) = \pi U L_\perp \sum_{n=-\infty}^{\infty} \Bigg\{ & (n-Y)\left[2\,\mathrm{arctanh}\left(\frac{(n-Y)/2}{X^2+(n-Y)^2+1/16}\right)\right. \\ & \left. -\,\mathrm{arctanh}\left(\frac{n-Y}{X^2+(n-Y)^2+1/4}\right)\right] \\ & + X\left[2\,\mathrm{arccot}\left(\frac{X}{n+1/4-Y}\right) - 2\,\mathrm{arccot}\left(\frac{X}{n-1/4-Y}\right)\right. \\ & \left. -\,\mathrm{arccot}\left(\frac{X}{n+1/2-Y}\right) + \mathrm{arccot}\left(\frac{X}{n-1/4-Y}\right)\right] \\ & + \frac{1}{2}\ln\left(\frac{[X^2+(n+1/4-Y)^2]\,[X^2+(n-1/4-Y)^2]}{16\,[X^2+(n+1/2-Y)^2]\,[X^2+(n-1/2-Y)^2]}\right)\Bigg\}. \end{aligned} \tag{236}$$

We verify the analytical chemical potential in Eq. (236) by comparison to the chemical potential measured from a LBM simulation of a stripe pair with a large

stripe wavelength $L_\perp = 70$ and slow front speed $U = 0.00235$. The result of this comparison is shown in Figure 26, and demonstrates excellent agreement for large stripes and slow fronts. The assumption of Eq. (232) is invalid for fast fronts, and the $X/L_\perp$ profile becomes asymmetric (depressed on the leading edge, and bulging on the trailing edge) and both profiles show an overall suppression of the chemical potential from the analytical prediction. These additional profiles are not shown here.

However, to predict the values of L and U where nucleation occurs we only need the extremum value of the chemical potential. This occurs in the center of a stripe at the front and is given by

$$\mu(\boldsymbol{R} = \mathbf{0}) = \pi U L_\perp \sum_{n=-\infty}^{\infty} \left[\frac{1}{2} \ln \left(\frac{16n^2 - 1}{16n^2 - 4} \right) + n \ln \left(\frac{32n^3 - 6n - 1}{32n^3 - 6n + 1} \right) \right] = -2UL_\perp \mathcal{C} = \mu^{\text{peak}} \,. \tag{237}$$

Here $\mathcal{C} = 0.9159\ldots$ is a constant known as Catalan's constant. Nucleation of a new stripe will occur when the chemical potential peak reaches the nucleation chemical potential $\mu^{\text{peak}} = \mu^{\text{nucl}}$.

Due to the symmetry at the center of the stripe, the nucleation chemical potential for a two-dimensional stripe is the same as the one-dimensional switching condition. In a previous paper [17] we presented an analytical expression for the switching concentration for the special case $M = 0$ where there is negligible diffusive mobility ahead of the front. In that case an analytical expression for the switching chemical potential can be found. However, a nonzero M induces earlier switching due to the presence of a nucleation kernel ahead of the front [17]. With the same method we used to verify the switching condition in our previous paper, we have measured the one-dimensional switching chemical potential $\mu^{\text{nucl}} \approx 0.24$ for the non-dimensional parameters used in this two-dimensional system. Thus we find that the maximum

orthogonal stripe wavelength as a function of front speed is:

$$L_{\perp}^{\max} \approx \frac{0.24}{2\mathcal{C}U} \approx \frac{0.131}{U} \ . \tag{238}$$

It is interesting to note that the analytical composition profile ahead of a solidification front for lamellar morphologies of eutectic mixtures presented by Jackson and Hunt is also a solution to the full chemical potential profile, although in a very different form [34, Eqn. (3)]. By using the substitutions $C \to \mu$, $S_\alpha = S_\beta \to L_\perp/4$, $C_0^\alpha = C_0^\beta \to 1/2$, $v \to U$, $d \to 1/2\pi^2$, $x \to Y$, and $z \to |X|$, their solution can be written:

$$\mu(L_\perp \boldsymbol{R}) = 2UL_\perp \sum_{n=1}^{\infty} \frac{1}{n^2} \sin\left(\frac{n\pi}{2}\right) \cos\left(2n\pi Y\right) e^{-2n\pi|X|} \ , \tag{239}$$

which is, at least in a preliminary numerical evaluation, equivalent to our solution, although we have not yet shown this analytically. For off-critical situations a complication occurs: the inflow material induces a non-neutral wetting condition for the orthogonal stripes. This can be clearly seen in Figure 22. This situation requires additional considerations that will be discussed elsewhere.

4.6.2. Minimum Orthogonal Stripe Size

The minimum stripe width is limited by the width of stripes which, if a defect occurs, coarsen more quickly towards the front than the front moves away. A simple qualitative argument for the defect speed can be obtained from the dynamical scaling laws [5]. This law describes the time evolution of a morphology by stating that at later times the structure is statistically similar to that of earlier times when scaled with the typical length scale

$$L_{\mathrm{C}} = \mathrm{C}T^{1/3} \ . \tag{240}$$

The constant C is expected to depend on the parameters of the system and the details

of the morphology. From Eq. (240) we can define a coarsening speed which provides an estimate of how quickly the end of a finger of wavelength L_{C} will recede:

$$U_{\mathrm{C}} = \frac{d}{dT} L_{\mathrm{C}} = \frac{1}{3} \mathrm{C} T^{-2/3} = \frac{1}{3} \mathrm{C}^3 L_{\mathrm{C}}^{-2} \, . \tag{241}$$

If a finger protrudes from the front into the phase separating region, it will coarsen in the same direction as the front. If the coarsening speed is faster than the front $U_{\mathrm{C}} > U$, the finger will eventually coarsen away completely into the mixed material domain. According to Eq. (241) smaller fingers coarsen at a greater speed, and this sets a minimum wavelength for orthogonal stripes generated by a moving front:

$$L_{\perp}^{\min} \geq L_{\mathrm{C}}(U) = 2\sqrt{\frac{\mathrm{C}^3}{3U}} \, . \tag{242}$$

Unfortunately, numerical values of C for different situations are hard to come by in the literature. However, it is easy to obtain C by measurement during phase ordering of a homogeneous quench. We did this for a symmetric system (i.e. $\Phi(T = 0) \approx 0$) and obtained a value of $\mathrm{C} \approx 0.555$; for details please refer to Figure 27.

We expect this coarsening speed to be on the order of, but not exactly equal to, the speed with which a single finger coarsens. To obtain a better estimate of the coarsening speed of a finger we can measure the speed in a simulation. To do that we set up a proto-stripe similar to what is shown in Figure 28.

We then measure the position of the tip of the finger as the first zero-crossing of ϕ at the original y position of the center of the finger. We then vary the front speed slowly (once every $4l_x$ iterations) to stabilize the position of the finger tip. Once the velocity has reached a stationary state (determined by the tip speed and the average of the last 100 tip speed measurements being less than $U/10^6$) we find the coarsening speed of the finger. The results of those measurements are shown in Figure 29 and,

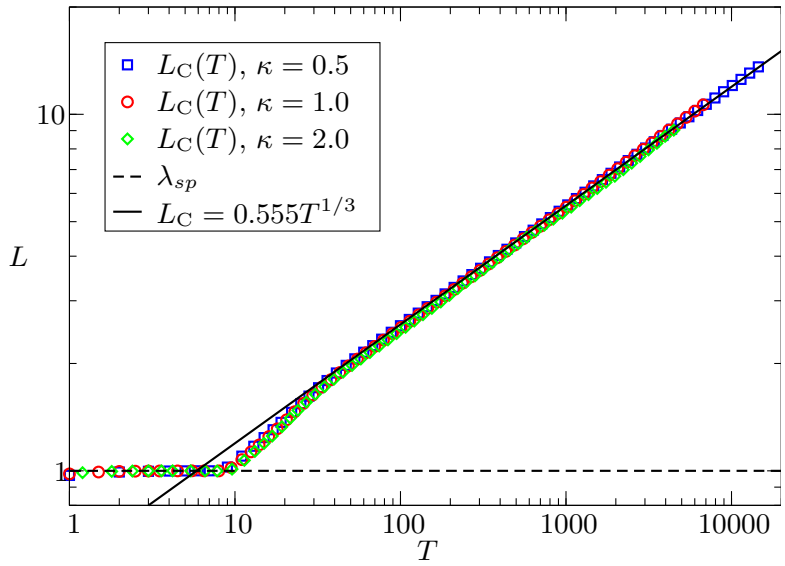

Figure 27. (Color online) Measurement of the dynamical scaling constant C in Eq. (240) using LBM simulations. Simulation size is 4096^2 lattice sites except for $\kappa = 2.0$ which is 1024^2. The numerical method is similar to that which is outlined in Section 4.3 for $u_x = 0$, except with fully periodic boundaries and no front. Characteristic length scale was measured by dividing the system area by the length of the $\Phi = 0$ interface, then non-dimensionalized by multiplication with a scaling factor $(2.27/\lambda_{sp})$ such that $L_C = 1$ is the length scale of spinodal decomposition.

as expected, the stripe speed is well approximated by $U = 4C^3/3L_\perp^2$, with C = 0.29. This is approximately a factor of 2 smaller than the dynamical scaling constant found in Figure 27.

4.6.3. Region of Stability

We now have a theoretical prediction for the minimum and maximum orthogonal stripe wavelength as a function of front speed. These boundaries describe region of stability for orthogonal stripes. Fronts moving faster than the speed at which the minimum and maximum stripes intersect $U_\perp^{\max} = 0.52$ will not form orthogonal stripes, although orthogonal stripe may be formed by other influences after the front passes: for example the presence of external walls, etc. as in [25].

We observe that the orthogonal stripes formed by a front in the simulation results shown so far fall in the region of stability, however we can test the bounds

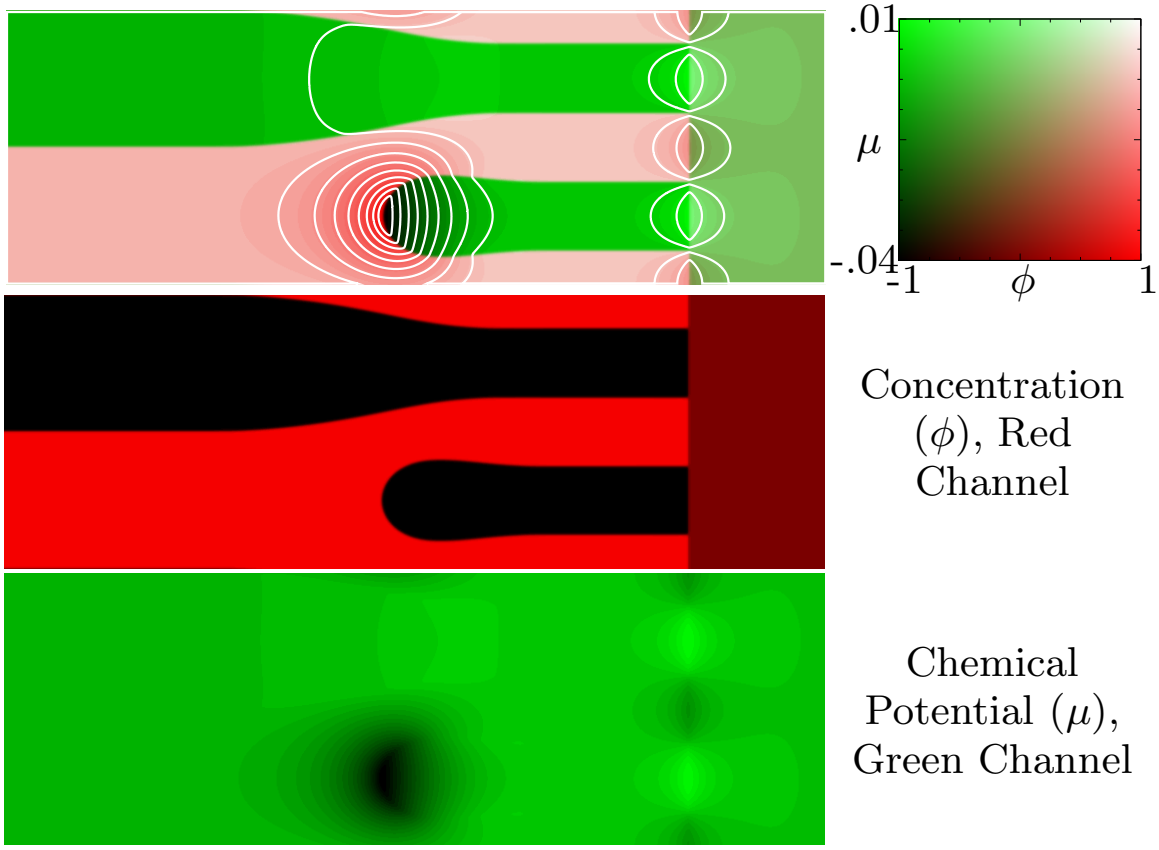

Figure 28. (Color online) Example of a proto-stripe stabilized by regulation of front speed. For the color version of this plot the range of values are shaded—in the additive RGB color model—red=$(\mu - \mu_{min})/(\mu_{max} - \mu_{min})$, green=$(\phi - \phi_{min})/(\phi_{max} - \phi_{min})$, and blue=red×green. A legend is shown at the right of the figure, and the extracted red and green color channels are shown below. Equi-chemical potential lines are superimposed. The front speed is increased when the stripe shrinks and decreased when the stripe grows until a stationary system is found; see text for methodology. Initial conditions are similar to the final state (shown), with an initial front speed $U = (0.2L_\perp)^2$ although the final U was found to be insensitive to the initial value. The result of several such simulations with varying initial $L_\perp$ are shown in Figure 29. Each simulation used $\kappa = \pi^2/8 \approx 1.23$ (so that $u_x = U$) as the interfacial free energy parameter, though system size varies as a function of $L_\perp$. The parameters for this simulation were $l_x = 312$, $l_y = 104$ ($L = 5.2687$), and $x_f = 260$. The final front speed was $U = 0.00113$ giving a scaling constant $C = 0.17746$.

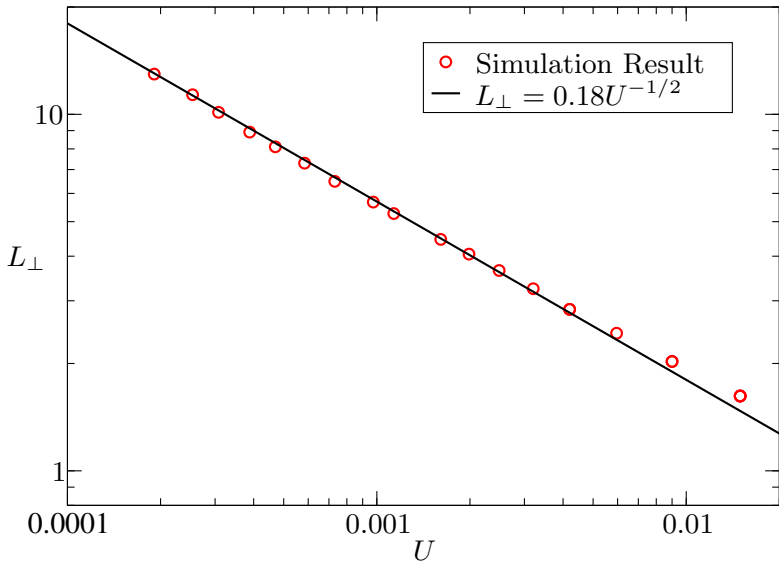

Figure 29. (color online) Measurement of the scaling constant C for the finger morphology shown in Figure 28. A proto-stripe morphology of wavelength $L_\perp$ is stabilized in a LBM simulation by adjusting the front speed U until a stationary profile is achieved. The fitted line gives an estimate of the minimum orthogonal stripe wavelength $L_\perp^{\min}$ for a given front speed U.

of the region more systematically. We do this by testing points in the $L_\perp$ vs. U parameter space for the formation of a stable stripe from the initial proto-stripe configuration shown in Figure 30a.

If the point is inside the region of stability, the proto-stripe grows as shown in the time-lapse overlay image in Figure 30b. If the point is below or above the region, the proto-stripe will respectively merge or split; examples of which are shown in (c) and (d) of Figure 30. If the point is to the right of the region, splitting and merging is followed by addition morphology changes until the stripes can reorient to become parallel to the front, however the simulation is classified and halted at the first morphology change. The final results of this series of simulations is shown in Figure 31.

These simulations confirm the predicted region of stability for orthogonal stripes for symmetrically mixed ($\Phi_{in} = 0$) initial concentration. Since our analytical predictions did not take into account the finite interface width we expect there will be devia-

(a) Initial configuration (b) Stable stripe

(c) Merged via coarsening (d) Split via nucleation

Figure 30. Examples of simulations performed to determine the stability of orthogonal stripes of a given size formed by a front moving at a prescribed speed in order to map the region of stable stripe formation shown in Figure 31. The initial configuration (a) is similar to the one used to predict the lower bound of the stability region (see Figure 28), and those observed in Figs. 19, 22, and 23. The simulation is run until the number of $\mathcal{A}$-to-$\mathcal{B}$-type interfaces intersecting the front and the outflow boundary changes, then the simulation is halted and classified. If the number of interfaces at the front decreases, the simulation is classified as having merged (c) and the point in Figure 31 gets a $\triangle$ symbol. If this number increases the simulation is classified as split (d) and gets a $\triangledown$ symbol. If the number of interfaces at the outflow boundary becomes 4 the simulation is classified stable (b) and the symbol is a circle with the radius proportional to the extremum value of the chemical potential at the front.

tion at small stripe widths and fast fronts. We see that the prediction for $U_{\perp}^{\max} = 0.52$ is close to the maximum front speed capable of forming orthogonal stripes observed as $U_{\perp}^{\text{obv}} \approx 0.3$ in Figure 31 or $U_{\perp}^{\text{obv}} \approx 0.2$ in Figure 24. The predicted allowed stripes widths for slow moving fronts agrees very well with simulation results. However, a careful observer will notice that there is a slight discrepancy and our proto-stripe seem to allow for slightly smaller front speeds. We attribute this detail to the shape of the persistent stripe, which is different for both kinds of simulations (see Figs. 28 & 30). The curvature in Figure 28 will allow for a slightly faster coarsening of the stripe tip.

We have now determined the characteristics of the ordered two-dimensional morphologies observed to be formed by phase separation fronts moving into mixtures of critical concentration: the orthogonal stripe morphology just presented, and the par-

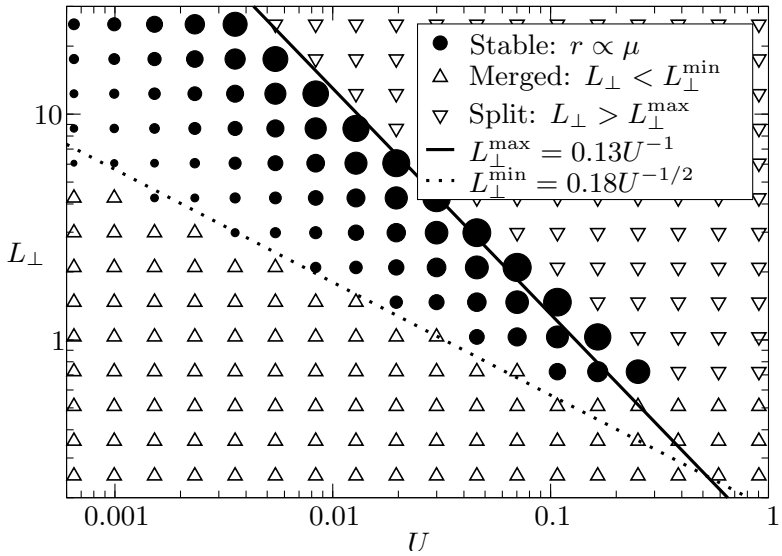

Figure 31. Stability of orthogonal stripes as function of front speed U and stripe wavelength L for symmetric mixed material $\phi_{in} = 0$. Filled circles are at points where simulations demonstrated stable stripe formation. Triangles are at points where stripe formation was unstable in the simulation. See Figure 30 for a description of how the simulation results were obtained. The predicted stable region is above the minimum (dashed) and below the maximum (solid) lines, and corresponds well with the field of filled circles. See text for further discussion.

allel stripe morphology–an essentially one-dimensional structure which we described and analyzed in previous work [17, 19]. The other ordered morphology we observed was an ordered droplet structure which was not observed to occur for fronts moving into critical mixtures.

4.7. Outlook

In this paper we presented a survey of the morphologies formed in the wake of a sharp phase-separation front. The resulting morphologies could be characterized as lamella in a parallel orientation with respect to the front, lamella in an orthogonal orientation and droplet arrays. We found that the selected morphology depended on the front speed, the volume fraction of the overtaken material, but also on the history of the system. If the front emerges from a homogeneous quench a depletion layer is typically formed and this will lead to the preferred formation of lamella

oriented parallel to the front. We saw, however, that sometimes defects will form and two systems under the same conditions–where the only difference lies in the random initial conditions for the homogeneous phase-separation–can instead form orthogonal lamella. By providing an unbiased initial condition we were able to determine the "preferred", i.e. most stable morphology. Using these results we were then able to present a state diagram as a function of the front speed and the volume fraction. We then examined in detail the formation of the orthogonal lamella for fronts moving into critical mixtures. We determined the range of allowed lamella sizes for a given front speed by analytically predicting the minimum and maximum lamella which can be stably formed. This gave a prediction for the transition between orthogonal and parallel lamella for critical mixtures which was within a factor of 3 of the observed transition point.

The next step in this analysis will be to determine the allowed stripe widths for fronts moving into mixtures with a minority and a majority phase in an effort to predict the boundary of the "orthogonal stripes" region in Figure 25–now marked with an observed dashed line. This will require additional research, such as: Determining how dynamical coarsening of stripe morphologies is changed by having off-critical mixtures; this subject is not well studied as dynamical scaling is typically studied in the context of homogeneous quench, which for off-critical mixtures results in droplet morphologies that coarsen due to Ostwald ripening [5]. Determining what effect off-critical mixtures ahead of the front will have on the nucleation of new stripe domains. Determining how the stripe morphology itself is altered by having an off-critical mixture. This last point may seem trivial at first glance, as conservation of the order parameter requires for stable stripes to form, the final width of the minority and majority stripes are a simple function of the mixed material concentration. We observe this to be true in our simulations for some distance away from the front, but

this is not the case directly at the front where the dynamics of morphology selection occur. As shown most readily in Figure 22, but also elsewhere in this paper, there is a pinching off of the minority phase due to the presence of a preferred contact angle induced by the control parameter front. These considerations will be published in future work.

This paper raises a number of interesting issues. Firstly, can one predict *a priori*, which morphology is most stable, and thereby provide analytical predictions for the state diagram? Secondly, what are the limits of metastability, i.e. what is the fastest orthogonal lamella structure that can be formed and what is the slowest parallel lamella morphology that can be formed and how far can either encroach on the droplet states and vice versa? Thirdly, what is the region of stability for orthogonal lamella formed in off-critical mixtures, and by determining this region can we predict the boundary between orthogonal lamella droplet morphologies? Additionally, it would be very useful to more accurately determine where in the parameter space of this, and perhaps other similar models, is the transition from parallel to orthogonal stripe morphologies. This transition has been noted several times, but a systematic study has not been done.

So far we have been able to successfully analytically predict the size of parallel lamella structures. In future work we will refine our prediction for the extent of the orthogonal stripe region in the morphology diagram by considering the effect of the non-neutral wetting condition at the front for off-critical volume fractions. Another natural extension is to consider the system in three dimensions. In a future paper we will present an analogous study which shows a slightly richer state diagram which includes cylinder arrays as well as three dimensional droplet lattices. Lastly this paper only considered diffusive dynamics. For many practical application it is important to include hydrodynamics effects, which can alter domain formation considerably.

CHAPTER 5. SUMMARY AND OUTLOOK

A number of interesting examples of physical pattern forming systems were given in the introduction. Though different in many details, these systems had the common property that their patterns were the result of a moving phase-separation front. This motivated the model for front induced phase-separation of a binary mixture which is analyzed in this dissertation. In order to facilitate development of analytical analysis, the model was made as simple as possible. A Ginzburg-Landau free-energy describes the thermodynamic miscibility of the binary phases. The front is an abrupt spatial transition of the effective temperature which moves at constant speed through a diffusive material. A lattice Boltzmann method simulation of the model was created so that numerical analysis could be used to validate the analytical results. These analytical and numerical analyses were published as three papers in peer review journals.

The first paper was an in-depth study of the model for one-dimensional systems. Owing to the simplicity of the model, the complete dynamics of phase-separation induced by a front moving with constant speed was analytically solved. From this analysis, the exact, closed-form relationship between domain size and front speed was determined. Numerical analysis confirmed the validity of the analytical result, and no fitting parameters were required. A solution in differential form included the effects of the mixed material volume fraction on the relationship between front speed a domain size. The remaining parameters of the phase separation front model were analyzed numerically and analytically, and found to have comparatively little effect.

The second paper extended the analytical findings in the first paper to phase-separation fronts moving at decreasing speed through one-dimensional systems. The form of the decreasing speed of the front matched the diffusive motion of an electrolyte moving from a high concentration bath through a gel, modeling the motion of the

phase-separation front which is responsible for forming Liesegang patterns. From the analytical relationship between phase-separation front speed and domain size found in the first paper, a complete theoretical description of Liesegang pattern formation for this model was derived. Numerical analysis confirmed the analytical results, and since the analysis was exact, there were no free parameters which could provide for fitting to the numerical results. To our knowledge this is the only model which has been analytically and numerically shown to produce Liesegang patterns with no free parameters.

The third paper began with an extensive numerical survey of phase-separated structures formed by fronts moving through two-dimensional systems. A phase diagram of morphologies formed as a function of front speed and mixed material volume fraction was generated from this survey. Matching the results found in other models, the stripes formed parallel to the front at high front speeds, and orthogonal to the front at low front speeds. An analytical analysis of the formation of orthogonal stripes predicted a range of stripe widths as a function of the front speed. The maximum size was found to be determined by a nucleation condition similar to the nucleation condition which governs domain formation in one-dimensional systems and the equivalent parallel stripe morphology. The minimum size was found to be determined by the faster coarsening of smaller stripes causing them to be re-absorbed into the front before it can move away. This analysis predicted that the range between minimum and maximum stripe width would decreased to zero at a maximum speed for orthogonal stripe formation, providing an analytical basis for the appearance of parallel stripes at higher front speeds. From numerical analysis it was found that our approximate theory for the maximum speed for orthogonal stripe formation was correct to within a factor of three.

The many analytical predictions made possible by the simplicity of the model

have been verified by the numerical results from simulation. Additionally, the numerical lattice Boltzmann method simulations of the model have guided and inspired analytical understanding of the formation of phase-separated structures formed in the wake of phase-separation fronts. As with any complicated system, understanding part of it leads to more questions. Some of the appropriate subjects which should be considered for further study are included in the appendices with preliminary results and discussion.

An observation in the third paper of the effects of off-critical volume fractions on the shape of orthogonal stripes near the phase separation front leads to the analysis of the wetting angle of a phase-separation front in Appendix A. The analysis of a maximum size in the range of orthogonal stripes widths is exploited in Appendix B to successfully generate controlled, depth dependent two-dimensional structure which is formed in situ. In Appendix C a preliminary morphology phase diagram for three-dimensional systems is constructed. Appendix D demonstrates the production of an immersion precipitation membrane like structure based on the morphology phase diagram in Appendix C and inspired by the controlled depth-dependent structure formation in Appendix B. The numerical method is expanded to include hydrodynamic transport in Appendix E in order to model phase-separation fronts traveling through binary fluid mixtures. Preliminary analysis on the effects of including hydrodynamics is presented in Appendix F along with some early numerical results. Development and evaluation of open boundary conditions for lattice Boltzmann method simulations of this model for phase-separation fronts moving through diffusive materials is given in Appendix G

[1] A. Akthakul, C. E. Scott, A. M. Mayes, and A. J. Wagner, *Lattice Boltzmann simulation of asymmetric membrane formation by immersion precipitation*, J. Memb. Sci. **249** (2005), no. 1–2, 213–226.

[2] T. Antal, M. Droz, J. Magnin, and Z. Rácz, *Formation of Liesegang patterns: A spinodal decomposition scenario*, Phys. Rev. Lett. **83** (1999), no. 15, 2880–2883.

[3] T. Antal, M. Droz, J. Magnin, Z. Rácz, and M. Zrinyi, *Derivation of the Matalon-Packter law for Liesegang patterns*, J. Chem. Phys. **109** (1998), 9479–9486.

[4] R. C. Ball and R. L. H. Essery, *Spinodal decomposition and pattern-formation near surfaces*, J. Phys.: Condens. Matter **2** (1990), no. 51, 10303–10320.

[5] A. J. Bray, *Theory of phase ordering kinetics*, Adv. Phys. **43** (1994), 357.

[6] H. B. Callen, *Thermodynamics and an introduction to thermostatistics*, Wiley, 1985.

[7] M. E. Cates, J. Vollmer, A. J. Wagner, and D. Vollmer, *Phase separation in binary fluid mixtures with continuously ramped temperature*, Phil. Trans. R. Soc. Lond. A **361** (2003), 793.

[8] S. Chen and G. D. Doolen, *Lattice Boltzmann method for fluid flows*, Annu. Rev. Fluid Mech. **30** (1998), 329–364.

[9] Xiaodong Chen, Steven Lenhert, Micheal Hirtz, Nan Lu, Harald Fuchs, and Lifeng Chi, *Langmuir-blodgett patterning: A bottom-up way to build mesostructures over large areas*, Accounts Chem. Res. **40** (2007), no. 6, 393–401.

[10] L. P. Cheng, D. J. Lin, C. H. Shih, A. H. Dwan, and C. C. Gryte, *PVDF membrane formation by diffusion-induced phase separation-morphology prediction based on phase behavior and mass transfer modeling*, J. Polym. Sci. **37** (1999), no. 16, 2079–2092.

[11] B. Chopard, P. Luthi, and M. Droz, *Reaction-diffusion cellular-automata model for the formation of Liesegang patterns*, Phys. Rev. Lett. **72** (1994), no. 9, 1384–1387.

[12] P. Clayton and D. Danks, *Effect of interlamellar spacing on the wear-resistance of eutectoid steels under rolling sliding conditions*, Wear **135** (1990), no. 2, 369–389 (English), International Conference on Wear of Materials, Denver CO, April 08–14 (1989).

[13] R. M. Corless, G. H. Gonnet, D. E. G. Hare, D. J. Jeffrey, and D. E. Knuth, *On the Lambert W function*, Adv. Comp. Math **5** (1996), 329.

[14] J. Dziarmaga and M. Sadzikowski, *Domain wall formation in the Cahn-Hilliard-Cook equation*, Phys. Rev. E **63** (2001), 036112.

[15] G. Faivre, S. de Cheveigne, C. Guthmann, and P. Kurowski, *Solitary tilt waves in thin lamellar eutectics*, Eurrophys. Lett. **9** (1989), no. 8, 779.

[16] J. M. Flesselles, A. J. Simon, and A. J. Libchaber, *Dynamics of one-dimensional interfaces: An experimentalist's view*, Adv. Phys. **40** (1991), 1–51.

[17] E. M. Foard and A. J. Wagner, *Enslaved phase-separation fronts in one-dimensional binary mixtures*, Phys. Rev. E **79** (2009), no. 5, 056710.

[18] ———, *Fluid dynamics video of domains with spiral dislocations formed in the wake of an enslaved phase-separation front*, `http://arxiv.org/abs/0910.3232v1`, 2009.

[19] ———, *Enslaved phase-separation fronts and Liesegang pattern formation*, Commun. Comput. Phys. **9** (2011), no. 5, 1081–1093.

[20] ———, *Survey of morphologies formed in the wake of an enslaved phase-separation front in two dimensions*, Phys. Rev. E **85** (2012), 011501.

[21] H. Furukawa, *Formation, dynamics, and statistics of patterns*, vol. 2, pp. 266–308, World Scientific, 1990.

[22] V. L. Ginzburg and L. D. Landau, Zh. Eksp. Teor. Fiz. **20** (1950), 1064.

[23] M. Gleiche, L. F. Chi, and H. Fuchs, *Nanoscopic channel lattices with controlled anisotropic wetting*, Nature **403** (2000), no. 6766, 173–175 (English).

[24] G. Gonnella, A. Lamura, and A. Piscitelli, *Dynamics of binary mixtures in inhomogeneous temperatures*, J. Phys. A: Math. Theor **41** (2008), no. 10, 105001.

[25] G. Gonnella, A. Lamura, A. Piscitelli, and A. Tiribocchi, *Phase separation of binary fluids with dynamic temperature*, Phys. Rev. E **82** (2010), no. 4, 046302.

[26] M. Gross, R. Adhikari, M. E. Cates, and F. Varnik, *Thermal fluctuations in the lattice Boltzmann method for nonideal fluids*, Phys. Rev. E **82** (2010), 056714.

[27] M. Gross, M. E. Cates, F. Varnik, and R. Adhikari, *Langevin theory of fluctuations in the discrete Boltzmann equation*, J. Stat. Mech.: Theory Exp. **03** (2011).

[28] P. Hantz and I. Biró, *Phase separation in the wake of moving fronts*, Phys. Rev. Lett. **96** (2006), no. 8, 088305.

[29] C.-J. Huang, D. J. Browne, and S. McFadden, *A phase-field simulation of austenite to ferrite transformation kinetics in low carbon steels*, Acta Materialia **54** (2006), 11–21.

[30] K. Huang, *Statistical mechanics*, Wiley, 1987.

[31] J. Hyzak and I. Bernstein, *The role of microstructure on the strength and toughness of fully pearlitic steels*, Metall. Mater. Trans. A **7** (1976), 1217–1224, 10.1007/BF02656606.

[32] F. Izsak and I. Lagzi, *Simulation of Liesegang pattern formation using a discrete stochastic model*, Chem. Phys. Lett. **371** (2003), no. 3-4, 321–326.

[33] K. Jablczynski, *La formation rythmique des pecipites: Les anneaux de Liesegang*, Bull. Soc. Chim. Fr. **33** (1923), 1592.

[34] K. A. Jackson and J. D. Hunt, *Lamellar and rod eutectic growth*, Trans. Metall. Soc. AIME **236** (1966), no. 8, 1129–1142.

[35] A. Jacot, M. Rappaz, and R. C. Reed, *Modelling of reaustenitization from the pearlite structure in steel*, Acta Materialia **46** (1998), 3949–3962.

[36] L. Jahnke and J. W. Kantelhardt, *Comparison of models and lattice-gas simulations for Liesegang patterns*, Eur. Phys. J. Special Topics **161** (2008), 121–141.

[37] R. A. L. Jones, *Soft condensed matter*, Oxford master series in condensed matter physics, Oxford University Press, 2002.

[38] A. Karma and A. Sarkissian, *Dynamics of banded structure formation in rapid solidification*, Phys. Rev. Lett. **68** (1992), no. 17, 2616–2619.

[39] Arie Kaufman, Zhe Fan, and Kaloian Petkov, *Implementing the lattice Boltzmann model on commodity graphics hardware*, J. Stat. Mech.: Theory Exp. **2009** (2009), no. 06, P06016.

[40] Michael H. Köpf, Svetlana V. Gurevich, Rudolf Friedrich, and Lifeng Chi, *Pattern formation in monolayer transfer systems with substrate-mediated condensation*, Langmuir **26** (2010), no. 13, 10444–10447.

[41] J. S. Langer, *Instabilities and pattern formation in crystal growth*, Rev. Mod. Phys. **52** (1980), no. 1, 1–28.

[42] R. E. Liesegang, *Über einige Eigenschaften von Gallerten*, Naturwissenschaftliche Wochenschrift **11** (1896), no. 30, 353–362.

[43] T. Nagai and K. Kawasaki, *Statistical dynamics of interacting kinks II*, Physica A **134** (1986), 483–521.

[44] S. T. T. Ollila, C. Denniston, M. Karttunen, and T. Ala-Nissila, *Fluctuating lattice-Boltzmann model for complex fluids*, J. Chem. Phys. **134** (2011), no. 6, 064902.

[45] A. Onuki, *Phase transition dynamics*, Cambridge University Press, 2002.

[46] E. Orlandini, M. R. Swift, and J. M. Yeomans, *A lattice Boltzmann model of binary-fluid mixtures*, Eurrophys. Lett. **32** (1995), no. 6, 463.

[47] C. M. Pooley, *Mesoscopic modelling techniques for complex fluids*, Ph.D. thesis, University of Oxford, 2003.

[48] Y. H. Qian, D. D'Humires, and P. Lallemand, *Lattice BGK models for Navier-Stokes equation*, Eurrophys. Lett. **17** (1992), no. 6, 479.

[49] Z. Racz, *Formation of Liesegang patterns*, Physica A **274** (1999), no. 1-2, 50–59.

[50] J. P. Schaffer, A. Saxena, T. H. Sanders Jr., S. D. Antolovich, and S. B. Warner, *Science and design of engineering materials*, second ed., McGraw-Hill, 2000.

[51] Ellen L. Spotz and Joseph O. Hirschfelder, *Liesegang ring formation arising from diffusion of Ammonia and Hydrogen Chlorine gases through air*, J. Chem. Phys. **19** (1951), no. 9, 1215–1215.

[52] K. Spratte, Li F. Chi, and H. Riegler, *Physisorption instabilities during dynamic Langmuir wetting*, Eurrophys. Lett. **25** (1994), no. 3, 211.

[53] K. H. Stern, *The Liesegang phenomenon*, Chemical Reviews **54** (1954), 79–99.

[54] S. Succi, *The lattice Boltzmann equation for fluid dynamics and beyond*, Clarendon Press, 2001.

[55] W. van Saarloos, *Front propagation into unstable states*, Phys. Rep. **386** (2003), 29.

[56] J. Verhoeven and R. Homer, *The growth of off-eutectic composites from stirred melts*, Metall. Mater. Trans. B **1** (1970), 3437–3441, 10.1007/BF03037876.

[57] J. D. Verhoeven, *Fundamentals of physical metallurgy*, Wiley, 1975.

[58] J. Vollmer, G. K. Auernhammer, and D. Vollmer, *Minimal model for phase separation under slow cooling*, Phys. Rev. Lett. **98** (2007), no. 11, 115701.

[59] A. J. Wagner, *Theory and application of the lattice boltzmann method*, Ph.D. thesis, University of Oxford, 1997.

[60] A. J. Wagner and Q. Li, *Investigation of Galilean invariance of multi-phase lattice Boltzmann methods*, Physica A **362** (2006), no. 1, 105–110.

[61] A. J. Wagner and C. M. Pooley, *Interface width and bulk stability: Requirements for the simulation of deeply quenched liquid-gas systems*, Phys. Rev. E **76** (2007), no. 4, 045702.

[62] Alexander J. Wagner and Sylvio May, *Electrostatic interactions across a charged lipid bilayer*, Eur. Biophys. J. **36** (2007), 293–303.

[63] Xiao-Lin Wang, Hu-Jun Qian, Li-Jun Chen, Zhong-Yuan Lu, and Ze-Sheng Li, *Dissipative particle dynamics simulation on the polymer membrane formation by immersion precipitation*, J. Membr. Sci. **311** (2008), no. 1-2, 251 – 258.

[64] B. Zhou and A. C. Powell, *Phase field simulations of early stage structure formation during immersion precipitation of polymeric membranes in 2D and 3D*, J. Memb. Sci. **268** (2006), no. 2, 150–164.

APPENDIX A. WETTING ANGLE ANALYSIS

In interesting result from the simulations of orthogonal stripe formation presented in Paper 3 is the observation that orthogonal stripes formed from off-critical mixtures have widths which vary as a function of distance from the front. Far behind the front the ratio of the $\mathcal{A}$-type stripe width ($w_{\mathcal{A}}$) to the $\mathcal{B}$-type stripe width ($w_{\mathcal{B}}$) is determined by simple conservation of the mixed material:

$$\frac{w_{\mathcal{A}}}{w_{\mathcal{B}}} = 1 - \frac{\phi_{in}}{\phi_{eq}} \; . \tag{243}$$

However, as shown in Figures 22 & 23, stripe width is reduced at the front for stripes composed of minority phase material, and increased for majority phase material, such that there is an overabundance of majority phase material present at the phase separation front. We propose that this phenomenon is due to a preferred contact angle between phase-separated domains in the phase-separating region behind the front and the mixed material in the phase mixing region ahead of the front. The following analysis is strictly true only in non-advecting stationary state, i.e. $u = 0$. However, for slow velocities these solutions are going to be a good approximation even for our non-equilibrium situation. This can be seen from the non-dimensional drift-diffusion equation 37 in the stationary limit

$$\partial_T \Phi \to 0 = \boldsymbol{\nabla}_{\boldsymbol{R}} \cdot \left(M \boldsymbol{\nabla}_{\boldsymbol{R}} \mu(\Phi, \boldsymbol{R}) - \Phi \boldsymbol{U} \right) \; , \tag{244}$$

assuming $\Phi \boldsymbol{U}$ is small so that $\boldsymbol{\nabla}_{\boldsymbol{R}} \cdot \Phi \boldsymbol{U} \approx \boldsymbol{C}$ is constant:

$$M \boldsymbol{\nabla}_{\boldsymbol{R}} \mu(\Phi, \boldsymbol{R}) = \boldsymbol{C} \quad \Rightarrow \quad \mu(\Phi, \boldsymbol{R}) = 0 \; . \tag{245}$$

The preferred contact angle for domains which are attached to an abrupt phase

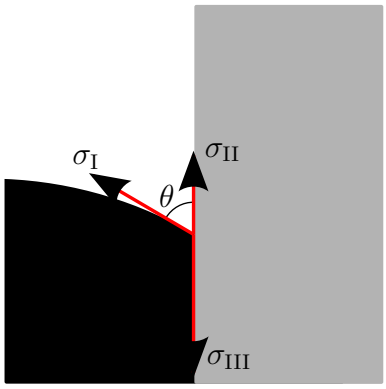

Figure A.1: (Color online) Illustration of line tension forces on the contact point between phase-separated domains and the mixed material at the phase separation front. In this figure, the line tension between the white phase-separated material and the gray mixed material is less than the line tension between the black phase-separated material and the mixed material $\sigma_{\mathrm{II}} < \sigma_{\mathrm{III}}$, therefore the front preferentially wets the white material. Derived in the text, balance of line tension forces longitudinal to the front reveal the contact angle θ.

separation front is calculated by balancing the line tension forces acting on the interface of the three domains ($\mathcal{A}$-type phase-separated domain, $\mathcal{B}$-type phase-separated domain, and the mixed material domain). An illustration of this principle is shown in Figure A.1, where the line tension σ_{II} between the $\mathcal{A}$-type material and the mixed material with non-dimensional order parameter Φ_{in} is less than the line tension σ_{III} between the $\mathcal{B}$-type material and the mixed material. Since the interface point between the three domains is constrained to lay on the phase separation front, balancing line tension forces along the front yields the Young-Laplace law:

$$\sigma_{\mathrm{I}} \cos\theta + \sigma_{\mathrm{II}} = \sigma_{\mathrm{III}} \, . \tag{246}$$

Determination of the line tension between the three domain types for different mixed material concentrations gives the contact angle θ.

A.1. Line Tension and Interface Profiles

The line tension along a straight interface between two domains is the line

integral across the interface normal of the square of the order parameter gradient. For simplicity, all calculations will be performed in non-dimensional quantities, and the interface is aligned to the Y-axis. Thus, the equation for line tension is:

$$\sigma = \int_{-\infty}^{\infty} (\nabla\Phi)^2 \, \mathrm{d}X \ . \tag{247}$$

The profile Φ for the interface between domains is all that is required.

A.1.1. Interface Profile Between Phase-Separated Domains

The profile for a stationary interface located at $X = X_0$ separating $\mathcal{A}$-type material on the left from $\mathcal{B}$-type material on the right is well-known:

$$\Phi_S(X) = -\tanh\left[2\pi(X - X_0)\right] \ . \tag{248}$$

The boundary conditions for this solution are $\Phi(-\infty) = 1$ and $\Phi(\infty) = -1$. This profile is a solution to the stationary state ($\partial_t\Phi \to 0$) of the non-dimensional equation of motion in the phase-separating region:

$$0 = \Phi^3 - \Phi - \frac{1}{8\pi^2}\nabla^2\Phi \ . \tag{249}$$

The profile is shown as the solid curve in Figure A.2. The solution of Eq. (248) can be adapted for negative-type material on the left and positive-type material on the right by simple negation.

A.1.2. Interface Profile in the Mixing Region

The interface profile for material in the mixing region must be a stationary state solution to the equation of motion in the phase-mixing region:

$$0 = \Phi - \Phi_{in} - \frac{1}{8\pi^2}\nabla^2\Phi \ . \tag{250}$$

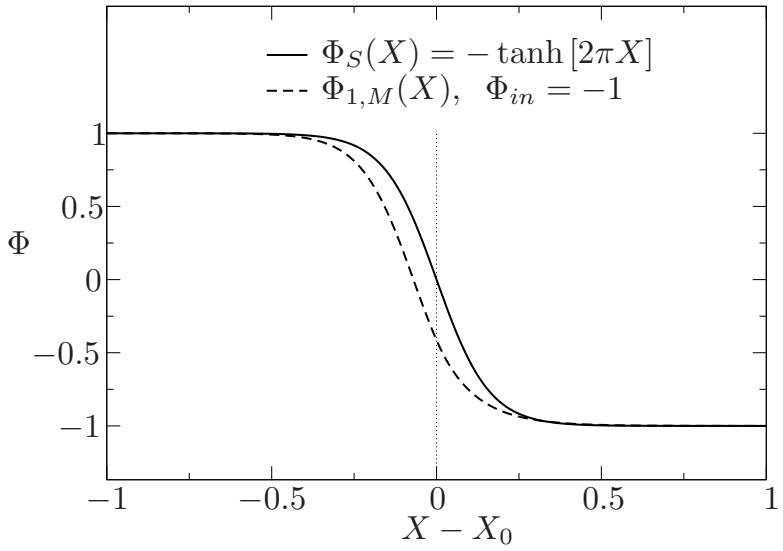

Figure A.2: Concentration profile of an interface between phase separated domains compared to an interface across phase-separation front. Both interfaces have boundary conditions $\Phi(-\infty) = 1$, and $\Phi(\infty) = -1$. The solid curve is the interface between two phase-separated domains. For comparison, the dashed curve is the interface between phase-separated material on the left ($X < X_0$) and mixed material at concentration $\Phi_{in} = -1$ on the right ($X > X_0$), and is the solution given in Eq. (253) The dashed curve helps illustrates why the front is not fully wetting to the majority phase for $\Phi_{in} = -1$, as discussed in Section A.4.

The boundary condition at infinity is $\Phi(X \to \infty) = \Phi_{in}$. The boundary condition at the phase separation front is an unknown concentration $\Phi(X = 0) = \Phi_0$, which is determined by matching the solution from the phase separating region as discussed below. The solution

$$\Phi_M(X) = \begin{cases} \Phi_{in} - e^{-\sqrt{8}\pi(X - X_0)}\ , & \Phi_0 < \Phi_{in} \\ \Phi_{in} + e^{-\sqrt{8}\pi(X - X_0)}\ , & \Phi_0 > \Phi_{in} \end{cases}\ , \tag{251}$$

can be matched to any $\Phi_0 \neq \Phi_{in}$ with suitable choice of X_0.

A.1.3. Interface Profile across a Phase Separation Front

It is clear that that the interface profile across a phase-separation front at $X = 0$ must be a solution to the respective equations of motion in the stationary limit:

Eq. (249) for $X < 0$, and Eq. (250) for $X > 0$. Furthermore, the profile and the gradient of the interface must be continuous between the solutions:

$$\Phi_S(0) = \Phi_M(0) \, , \nabla\Phi_S(0) = \nabla\Phi_M(0) \, . \tag{252}$$

As mentioned above, these conditions are met by choice of appropriate (possibly different) choice of X_0 in Eq. (248) and Eq. (253), where X_0 depends on the mixed material concentration Φ_{in}.

There are two solutions, one for each choice of boundary condition for Eq. (248). The solution for $\Phi(-\infty) = 1$ is:

$$\Phi_{1,M}(X) = \begin{cases} -\tanh\left[2\pi X + \frac{1}{2}\ln\left(\frac{1-\Phi_{in}}{\sqrt{2}+\Phi_{in}+\sqrt{3+\sqrt{8}\Phi_{in}}}\right)\right] & , X < 0 \\ \Phi_{in} + \left(\frac{\sqrt{3+\sqrt{8}\Phi_{in}}-1}{\sqrt{2}} - \Phi_{in}\right) e^{-\sqrt{8}\pi(X-X_0)} & , X > 0 \end{cases} . \tag{253}$$

The solution for $\Phi(-\infty) = -1$ is:

$$\Phi_{-1,M}(X) = \begin{cases} \tanh\left[2\pi X + \frac{1}{2}\ln\left(\frac{1+\Phi_{in}}{\sqrt{2}-\Phi_{in}+\sqrt{3-\sqrt{8}\Phi_{in}}}\right)\right] & , X < 0 \\ \Phi_{in} - \left(\frac{\sqrt{3-\sqrt{8}\Phi_{in}}-1}{\sqrt{2}} + \Phi_{in}\right) e^{-\sqrt{8}\pi(X-X_0)} & , X > 0 \end{cases} . \tag{254}$$

These solutions are illustrated in Figure A.3.

A.1.4. Line Tension between Phase-Separated Domains

The integration Eq. (247) of Eq. (248) is straightforward, and gives the line tension for a straight interface between two phase-separated domains as:

$$\sigma_I = \frac{8}{3}\pi \, . \tag{255}$$

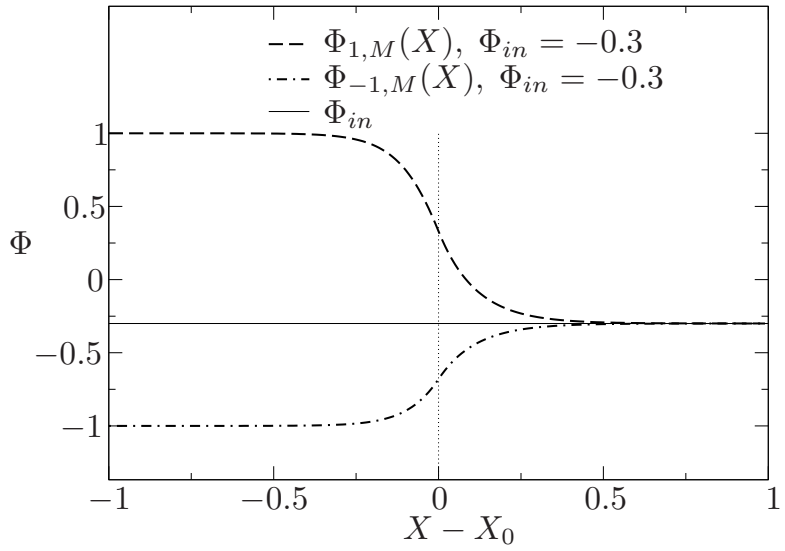

Figure A.3: Concentration profiles between phase separated domains and mixed material. The boundary conditions are $\Phi(-\infty) = \pm 1$ for the phase separated material on the left, and $\Phi(\infty) = 0.3$ for the mixed material across the phase-separation front at X_0. The dashed curve is the interface between a phase-separated domain of positive-type material behind the front and mixed material ahead of the front, as given by Eq. (253). The dash-dotted curve is the interface between a phase-separated domain of negative-type material behind the front and mixed material ahead of the front, as given by Eq. (254)

A.1.5. Line Tension across a Phase Separation Front

The integration Eq. (247) of the piecewise functions Eq. (253) and Eq. (253) to calculate the line tension for an interface between a phase-separated domain and mixed material is performed in two parts. The resulting line tension between positive type phase-separated material and mixed material, from Eq. (253), is:

$$\sigma_{II} = \frac{1}{3}\pi \left[4\sqrt{2} + 4 - 3\sqrt{6 + 4\sqrt{2}\Phi_{in}} + \Phi_{in} \left(3\sqrt{2} + 6 - 4\sqrt{3 + 2\sqrt{2}\Phi_{in}} \right) \right] \ . \quad (256)$$

Line tension for negative type phase-separated material, calculated from Eq. (254), is similar:

$$\sigma_{III} = \frac{1}{3}\pi \left[4\sqrt{2} + 4 - 3\sqrt{6 - 4\sqrt{2}\Phi_{in}} + \Phi_{in} \left(3\sqrt{2} - 6 + 4\sqrt{3 - 2\sqrt{2}\Phi_{in}} \right) \right] \ . \quad (257)$$

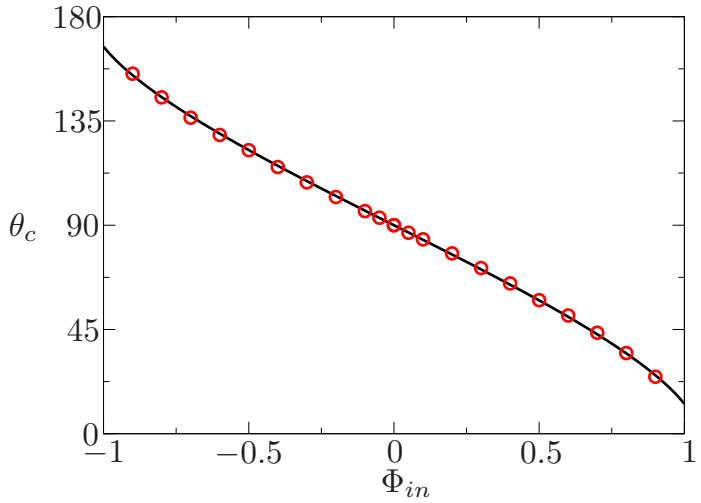

Figure A.4: (Color online) Analytical and numerical preferred contact angle for domains which are in contact with the phase separation front. The analytical prediction is shown as a solid line, with numerical results from LBM simulations shown as circles. An example numerical simulation is shown in Figure A.5.

A.2. Contact Angle of Phase-Separated Domains at an Abrupt Front

Combined with Eq. (246), the line tension between the three domains given by Eq. (255–257) gives the contact angle:

$$\cos\theta = \frac{1}{2}\sqrt{3+2\sqrt{2}\Phi_{in}}\left(\Phi_{in}+\frac{3\sqrt{2}}{4}\right)+\frac{1}{2}\sqrt{3-2\sqrt{2}\Phi_{in}}\left(\Phi_{in}-\frac{3\sqrt{2}}{4}\right)-\frac{3}{2}\Phi_{in}\ . \tag{258}$$

This is plotted as the solid curve in Figure A.4.

A.3. Numerical Verification

Lattice Boltzmann method simulations were used to test the validity of Eq. (258). This was done by placing a minority phase droplet in a finite phase-separating region between phase mixing regions, with zero advective flow. The minority phase droplet is allowed to rearrange into a stationary state.

An example stationary configuration is shown in Figure A.5, with additional simulation details. Once a stationary state is found, the minority phase will have

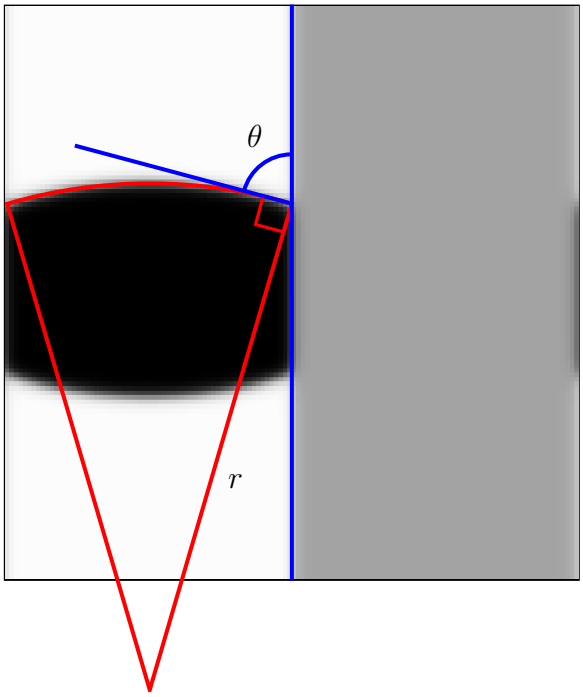

Figure A.5: (Color online) Example LBM simulation measurement for finding the preferred contact angle shown in Figure A.4. When the system has reached a stationary state, the position of the interface between the negative-type material (shaded black) and the positive type material (shaded white) is numerically measured across the length of the phase-separating region. From this, the curvature of the interface is determined, followed by the radius r, and finally the contact angle θ.

formed into a spherical lens shape. Knowing the length of the phase separating region and measuring the radius of curvature gives the contact angle. This procedure was performed for a number of different mixed-material concentration values, and the resulting contact angles are plotted as circles in Figure A.4 with the theoretical curve of Eq. (258). As shown, the measured contact angles match the theoretical predictions.

A.4. Observations and Outlook

The contact angle for domains which are in contact with a phase-separation front were analytically determined by careful consideration of the balance of line tension forces on the triple interface between mixed material ahead of the front, and the

phase-separated domains behind the front. The analytically predicted contact angles matched results from numerical simulations with zero imposed material advection.

One interesting prediction from the analytical result is that phase-separated positive-type material in the phase-separating region does not fully wet mixed material of the same concentration. This can be seen in Figure A.4 by the solid theoretical curve not reaching 0° at $\Phi_{in} = 1$, and not reaching 180° at $\Phi_{in} = -1$. This occurs for the following reason that, although the line tension between the phase-separated domain at $\Phi = 1$ and the mixed material at $\Phi_{in} = 1$ is zero, the line tension between the two phase-separated domains ($\Phi = -1$ and $\Phi = 1$) is $8\pi/3 \approx 8.38$ is greater than the line tension between the minority negative-phase material and the mixed positive material ($\Phi = -1$ and $\Phi_{in} = 1$) at $2\pi(7\sqrt{2} - 6)/3 \approx 8.17$. Therefore, overall energy due to line tension is minimized when some of the $\Phi = 1$ to $\Phi = -1$ interface is shared by the phase-separation front.

The analysis presented here should be extended to include the effects of an overall advection of material. That is, how does the motion of the phase-separation front alter the contact angle? Once this is determined, a better understanding of the pinching off effect, such as that observed in Figure 23 of Paper 1, can be used to analytically predict the morphology phase transition from orthogonal stripes to droplet arrays shown in Figure 25

APPENDIX B. CONTROLLED STRUCTURE FORMATION BY ACCELERATED PHASE-SEPARATION FRONT IN 2D

One motivation for studying the dynamics of structure formation by phase separation fronts was to gain enough understanding to facilitate controlled structure creation. Results from Papers 1-3 show that morphologies formed by front induced phase separation are principally determined by mixed material volume fraction and phase separation front speed. This latter property will be exploited to generate varying phase separated structures in situ by varying the speed of the phase separation front.

B.1. Using Orthogonal Stripe Nucleation to Change Morphology

In Paper 3 the formation of orthogonal stripe structures was found to be stable for a range of stripe widths. The range of stable widths depends on the phase-separation front speed. For equal volume fractions of mixed material $\Phi_{in} = 0$, the range of stable orthogonal stripe widths is shown in Figure 31. A smaller portion of Figure 31 is reproduced in Figure B.1 below. The upper stripe width (shown as a thick solid line in the figures) for a given speed is found to be due to a nucleation condition that, if exceeded, would result in the splitting of stripes into smaller stripes. This phenomenon can be exploited to generate controlled, depth-dependent structure.

Outlined here is an example procedure for generating depth-dependent stripe morphology by front-speed controlled nucleation. Beginning with a stripe morphology with width $w = 32\lambda_{sp}$, stripes of width $w/3$ are formed by increasing the speed of the phase separation front until the upper stripe width boundary for the front speed is exceeded. Note that this result is a special case for symmetric stripes where the nucleation in both domains occurs at exactly the same time. The more general case

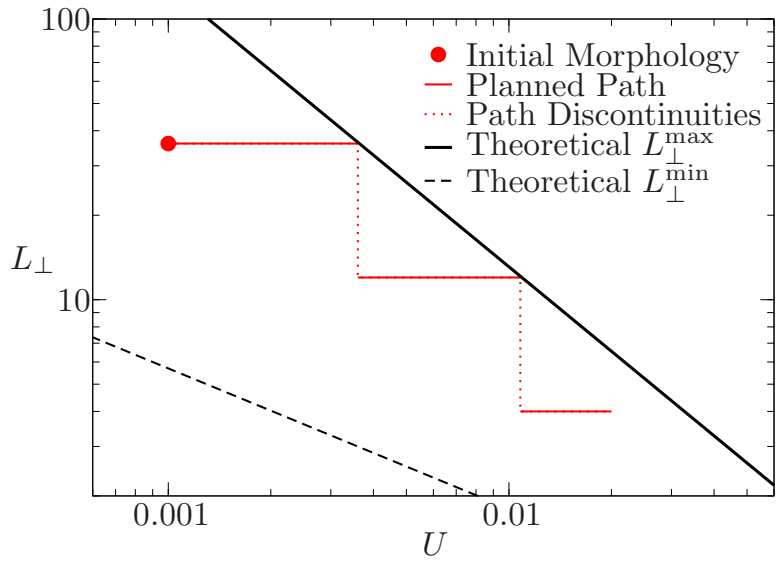

Figure B.1: (Color online) Illustration of controlled structure formation as a path through the region of stability.

of asymmetric stripes will lead to the nucleation of only one domain and a final width $w/2$. This more generic case will be easy to study, but the equivalent of Figures 31 and B.1 for asymmetric mixtures has not been developed yet. The front speed is increased further until these smaller stripes are too large to be formed by this faster moving front, and even smaller $w/9$ stripes form. This procedure is represented as a path through the region of stability in Figure B.1 by the thin (red online) line leading from the filled circle. This procedure is demonstrated using numerical simulation, with results shown in Figure B.2 and discussed below.

B.2. Simulation of In-Situ Controlled Structure Formation

The procedure represented by Figure B.1 and described above is implemented using lattice Boltzmann method simulations. The LBM implementation for the model is described in Section 1.3, however in this simulation the font speed is increased with time. For an example where the speed is decreased see Appendix D. The simulation size is $l_x = 512$ by $l_y = 256$ in lattice units, or $L_x = 64$ by $L_y = 32$ in non-dimensional units. The phase-separation front is at $X_f = 48$, and initially there are

two equal width phase-separated stripes of wavelength $L_\perp = 32$ behind the front, and mixed material of equal volume fraction ahead of the front. The initial front speed is $U_0 = 0.001$, and is increased exponentially to a final maximum value of $U_f = 0.2$.

The simulation was designed to produce 60 seconds of video at 30 frames per second with 2000 LBM iterations per frame. The video is available at `http://earth.physics.ndsu.nodak.edu/thesis/2012/foard/variable-speed-2D.mp4`. For this reason, the front acceleration $U = U_0 \exp(mI)$ is a bit unusual, where I is the current LBM iteration, and $m = \ln(U_f/U_0)/I_f$ is the scaling constant, where $I_f = 45 \times 30 \times 2000$ is the LBM iteration at which the front reaches maximum velocity. This produces 45 seconds of video of an accelerating front, and 15 seconds of video of a stationary front, showing the coarsening dynamics of orthogonal stripes. There remains a unknown parameter needed to reproduce this video exactly, and that is the time scaling constant, which is either $s = 0.056$, $s = 0.090$, or possibly something else. Exact reproduction is not all that important, as several videos with widely different parameters produced acceptable demonstration of in-situ depth-dependent structure formation. This one was specifically chosen above the others to also demonstrate stripe coarsening. More information on stripe coarsening is found in Section 4.6.2, and the subject reappears in Appendix F, and is responsible for some remarkable effects shown in Section F.5.

A time sequence of results from the simulation are shown in Figure B.2. Above each image in the sequence are two graphs. The left graph indicated (filled circle) the current position along the planned path (blue online) through the region of stability. The upper boundary of the region is indicated by the solid line. The planned path in these figures is the same as the one shown in Figure B.1. The right graph indicates the current front speed and time (filled circle), with the front speed dependence on time shown as the (blue online) curve. Figure B.2a shows the initial state of the

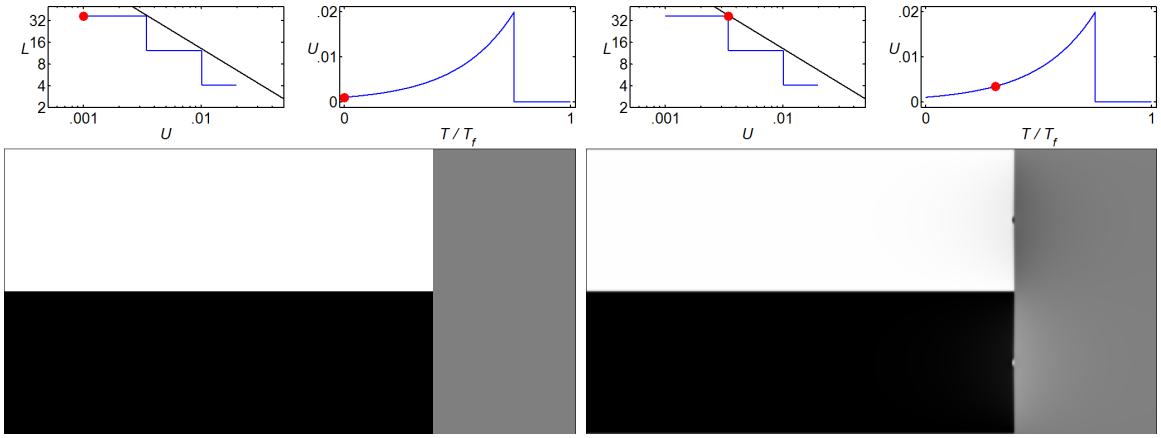

(a) Initial Condition

(b) Onset of First Nucleation

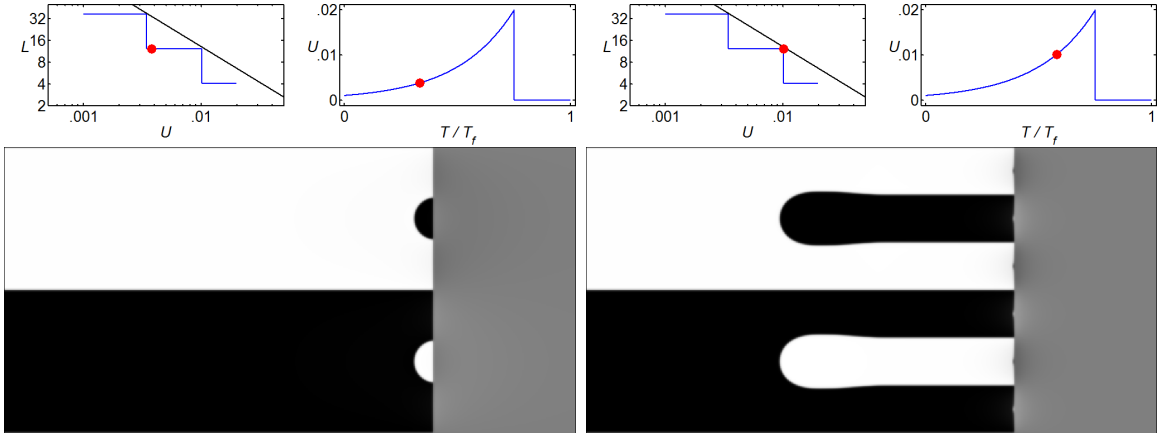

(c) Nucleation Induced Stripe Splitting

(d) Onset of Second Nucleation

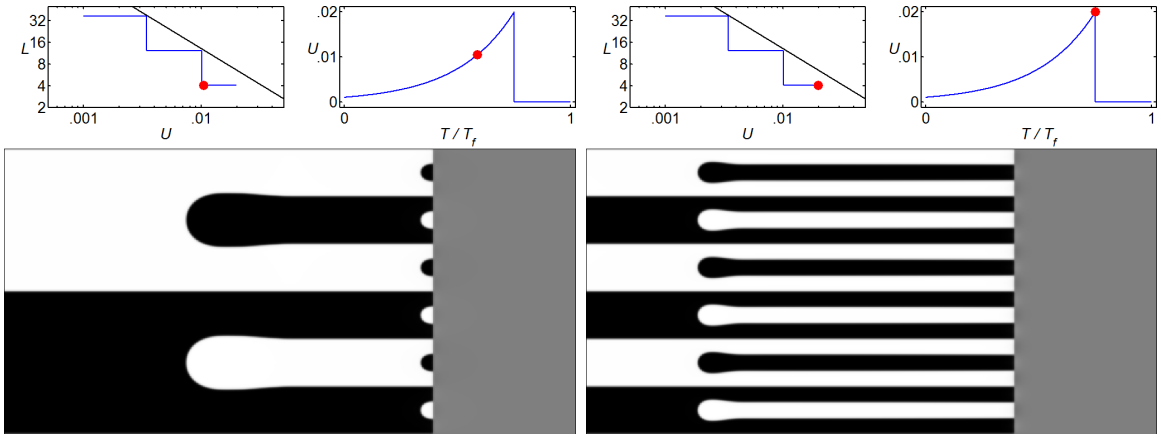

(e) Second Stripe Splitting

(f) Resulting Ordered Stripe Morphology

Figure B.2: (Color online) Simulation of controlled pattern formation. Simulation details and description in text.

simulation. In Figure B.2b the front speed has increased such that the initial stripe width just exceeds the maximum $L_\perp > L_\perp^{\max}$, and the nucleation of new domains at the center of the stripes occurs. Figure B.2c shows that the nucleated domain has split the original stripes, and the new stripe wavelength is $L_\perp = 10.7$ in non-dimensional units. In Figure B.2d the front speed has again increased enough that $L_\perp > L_\perp^{\max}$, and nucleation is beginning. Figure B.2e again shows the splitting of stripes after domain nucleation, and the stripe wavelength is now $L_\perp = 3.6$. In the final image, Figure B.2f, the phase separation front speed is at a maximum $U = 0.2$, and a highly ordered, depth-dependent structure has been formed in the material. A full video of the time sequence shown in Figure B.2 is available at `http://earth.physics.ndsu.nodak.edu/thesis/2012/foard/variable-speed-2D.mp4`.

B.3. Outlook

The principle of controlled phase-separated structure formation by phase-separation fronts in two dimensional materials has been demonstrated. This is a proof-of-concept made possible by understanding the dynamics of how a phase-separation front determines morphology. Splitting of stripes by nucleation from accelerating fronts is just one kind of morphology transition made possible by this analysis. Another possibility for accelerating fronts in 2D is the previously mentioned stripe doubling for asymmetric stripes. We expect that 3D, an accelerating front will be able to generate a tube morphology by nucleation of small stationary cylinders inside larger cylinders—see Figure C.2. The results in Paper 3 suggest the possibility of generating materials which contain structures from throughout the morphology phase diagram (Figure 25) by the relatively simple means of controlling the phase separation front speed and volume fraction of the mixed material.

As shown in Appendix C, there are more structures which may be formed by phase-separation fronts moving through three-dimensional systems. For parallel

morphologies a decrease in speed will lead to Liesegang patterns, as shown in Paper 2. For three dimensional systems with a significant amount of noise, morphologies reminiscent of immersion precipitations membranes are generated, as shown in Appendix D. These initial results for depth-dependent structure formation in three dimensional systems appear promising. Additional analysis will be required to generate similarly complex structure in bulk materials in a highly controlled way.

APPENDIX C. MORPHOLOGIES IN THREE DIMENSIONS

In three dimensional systems, additional structures other than those observed in Paper 3 are possible. Presented here are results from LBM simulations of a phase separation front moving at a variety of constant speeds through a material for a variety of inital mixed volume fractions. A snapshot of the simulated morphology is presented on a front speed U versus initial volume fraction Φ_{in} scale, similar to the morphology phase diagram of Figure 24.

C.1. Simulation Parameters

The size of each simulation was $l_x = 256$ by $l_y = 384$ by $l_z = 384$ lattice units, with the front at $x_f = 192$. The mixed material ahead of the front was initialized with random fluctuations around the specified volume fraction $\Phi = \Phi_{in} + \zeta_\phi$, where ζ_ϕ is a uniformly distributed random number between $\pm 10^{-6}$. In order to minimize the effects of the depletion layer observed in Paper 3 and shown in Figure 22, the mixed material behind the front was initialized with small random fluctuations around an equally mixed volume fraction $\Phi = 0 + \zeta_\phi$. The simulations were run until the type of morphology being formed by the front visually appeared to stabilize, although not necessarily until the morphology itself had stopped evolving. A schematic of the simulation space is presented in Figure C.1

Due to the technical limitations of performing three-dimensional simulations, it is currently infeasible to perform an extensive survey like the one for two-dimensional systems shown in Figure 24. Rather, a much smaller number of simulations were used to map out the approximate morphology phase space. To help guide the selection of appropriate parameters, it is useful to attempt to determine, by extension from earlier analysis, what kinds of structures which will form, and their approximate positions in the parameter space.

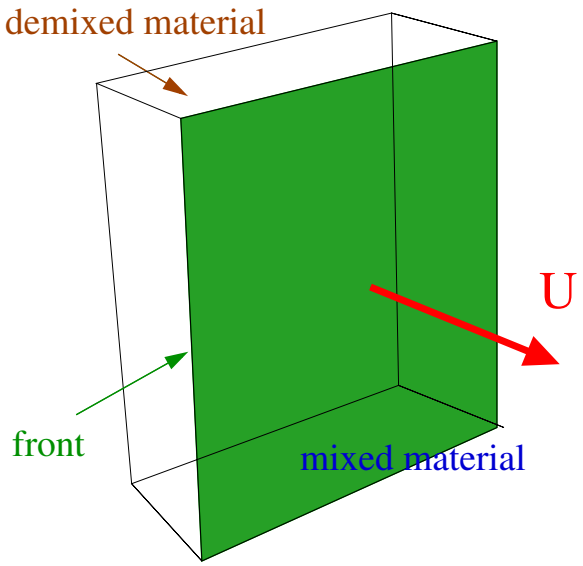

Figure C.1: (Color online) Illustration of the LBM simulation space for phase separation fronts moving though three dimensional systems. The simulation results shown in Figure C.3 are presented in the same orientation as this illustration. From this perspective the front moving down, right, and toward the observer.

C.2. Morphology Predictions

The results from the one dimensional and two dimensional analysis offers some insight as to the kinds of structures which can be formed by phase separation fronts in three dimensional systems, in analogy to block-copolymer and surfactant structures formed in equilibrium conditions. These predictions are shown in Figure C.2.

Some of the structures will be essentially unchanged, merely extending into an extra dimension. For example, the symmetric alternating domains for $\Phi_{in} = 0$ from the one-dimensional system, becoming parallel stripes in two-dimensions, appears as periodic lamella in three dimensions. Formed at higher front speeds, the two-dimensional structure of orthogonal stripes at $\Phi_{in} = 0$ become orthogonal lamella in three dimensions. This is a morphology which is stationary in the reference frame of the moving front. The extension of the two-dimensional droplet phase, which occurs for relatively fast fronts moving through material with sufficiently unequal volume fractions, appears either as arrays of cylinders oriented parallel to the front or as

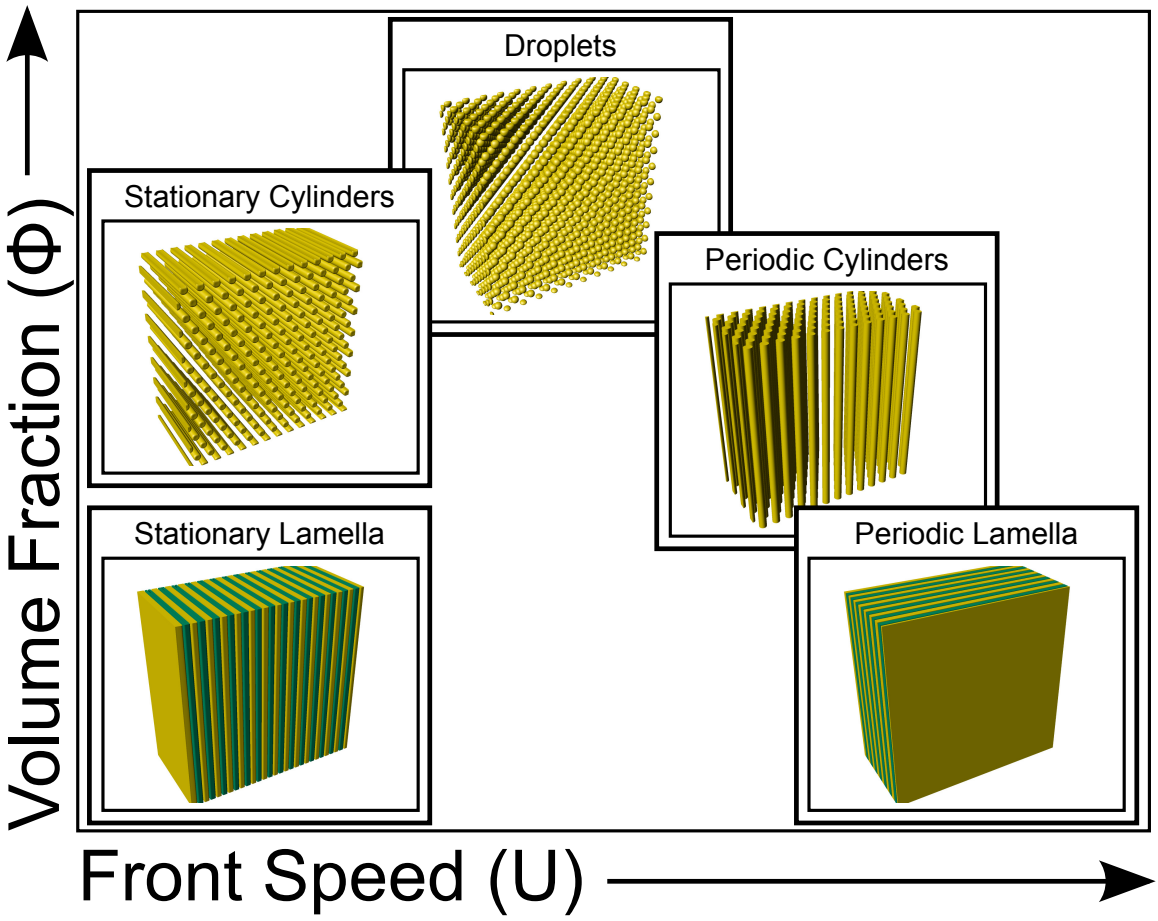

Figure C.2: (Color online) Idealized representations of expected structures formed by phase-separation front moving through three-dimensional material. Images of structure types are placed at the approximate expected location in the front speed versus volume fraction parameter space. Predictions and descriptions of the structures are in the text.

three dimensional arrays of drops.

Starting from the above four structures, new structures can be anticipated. Just as the periodic lamella have stationary lamella as a slow front speed counterpart, a stationary cylinder structure should appear as the slow front speed counterpart to periodic cylinders for asymmetric mixtures. For highly unequal volume fractions the Laplace pressure inside columnar structures become large, and Plateau-Rayleigh instability will result in columnar structures breaking up into droplets. These structures are very similar to block-copolymer systems and surfactant emulsion structures.

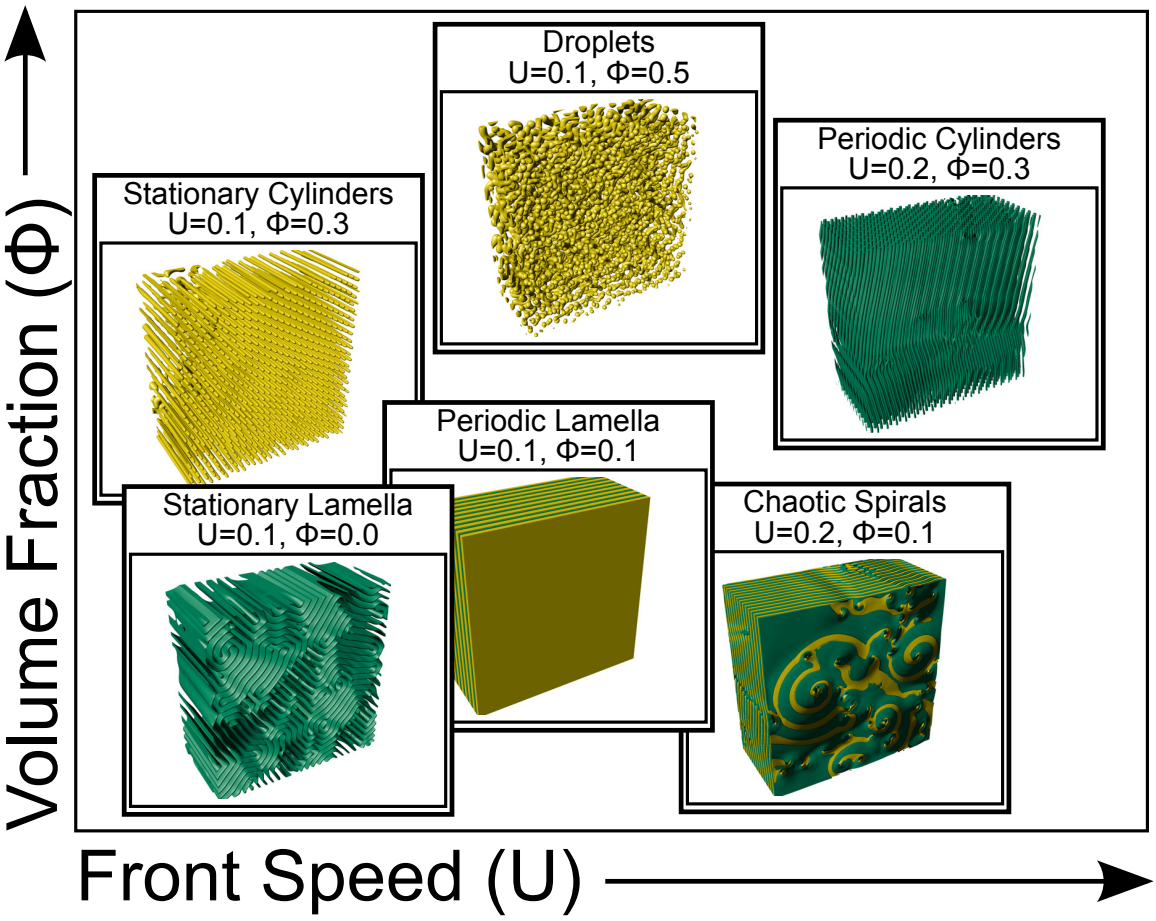

Figure C.3: (Color online) Resulting morphologies from LBM simulations of moving phase-separation fronts in three dimensions. The images of the resulting morphologies are placed on a front speed versus volume fraction space which approximately correspond to the simulation parameters. A brief description of the morphology and the simulation parameters accompany each image. Further simulation details and descriptions can be found in the text.

To locate these morphologies in the parameter space, and show they exists as phase-separation front-formed structures, a large number of very small simulations were performed. A graphical user interface for the simulations was useful here to readily scan through parameter values. These results allowed for informed parameter choices for large simulations to analyze their formation and defects.

C.3. Simulation Results

The parameters suggested by the predicted morphology above was largely successful

in producing the anticipated structures. An interesting exception was the appearance of periodic lamella with spiral dislocations, discussed below.

The simulation results for larger systems with the select parameter set are shown in Figure C.3. The surface of the phase-separated domains are rendered, and shaded differently (yellow or green online) for different material types. Particular shading was chosen to most easily show structure of a particular morphology, and does not indicate the material type. In order to readily illustrate domain structure, some of the images only render one of the material types.

The appearance of the droplet, periodic cylinder, and stationary cylinder structures appeared at the expected relative front speeds and volume fractions. However, the formation of periodic lamellar structures did not occur as expected. Instead, a quasi-lamellar structure formed, where domain layers were interconnected by a series of spiral dislocations. During phase separation, these spiral dislocations were observed to interact in non-trivial ways; sometimes attracting other spirals and mutually annihilating by merging, sometimes attraction was followed by repulsion, some dislocations would exclude other dislocations from their vicinity and appear to expand. The long-term dynamics of the spiral dislocations served to straighten out the lamella, and reorient them to be more parallel to the front. This suggests that their appearance is likely limited to a small transition region in the morphology phase space. A video showing the formation and interaction of spiral dislocations appears in the American Physical Society Division of Fluid Dynamics video gallery [18], and is also available at `http://earth.physics.ndsu.nodak.edu/thesis/2012/foard/spiral.mp4`.

Another interesting result is the production of a periodic lamella structure at the same slow speed, but with slightly unequal volume fraction, as the simulation which generated the stationary lamella structure with equal volume fractions of mixed material. In two dimensions, unequal volume fractions slightly favor the production

of parallel stripes over orthogonal stripes, as shown in Figure 24. This suggests that the transition between parallel and orthogonal lamella occurs at a front speed near $U = 0.1$, consistent with the results in Paper 3 for two-dimensional systems.

C.4. Outlook

With the development of powerful highly parallel computing systems, the simulation of large three-dimensional systems with the lattice Boltzmann method is becoming feasible [39]. This will allow more detailed analysis of structure formation and morphology transition for front induced phase-separated structures in bulk materials. Early results of a structure which shows morphology transition from periodic lamella (oriented parallel to the front) to stationary lamella (oriented orthogonal to the front) is shown in Appendix D.

APPENDIX D. IMMERSION PRECIPITATION MEMBRANES AND VARIABLE VELOCITY FRONTS IN THREE DIMENSIONS

The results from Appendix C, although still preliminary, can be used to plan the formation of phase-separated structures in bulk materials. For instance, a phase separation front which begins moving quickly through a material but then slows should result in a transition from a parallel (periodic in the co-moving reference frame of the front) lamella to orthogonal (stationary) lamella. An example of an immersion precipitation produced experimentally by Cheng *et al.* [10] is shown in Figure D.1a, and possesses a similar transition. As described in Section 1.1.3, during the formation of immersion precipitation membranes, the solvent leaves the polymer-solvent mixture as diffusion process, moving with an approximate speed $u \propto 1/\sqrt{t}$. This is the motivation for imposing a diffusive velocity $u = a/\sqrt{t}$ on the phase separation front.

It turns out that generating such a transition, and generating it in the proper place is tricky. Presented here is the result of a LBM simulation of a phase-separation front moving through three dimensions which generates a phase-separated structure which strongly resembles real immersion precipitation membranes produced experimentally. Perhaps just as interesting as the successful result are the unsuccessful attempts, also discussed below.

D.1. Numerical Method Outline

As discussed in the introductory material in Section 1.1.3, an immersion precipitation membrane is a phase-separation front formed structure. The general procedure for producing an immersion precipitation membrane in a laboratory is as follows: A substrate is coated with a thin layer of a polymer and solvent mixture. The substrate is then immersed in a bath of non-solvent liquid, typically water. Non-solvent diffuses into the mixture, as solvent diffuses out. When a region of the mixture is sufficiently

depleted of solvent, the polymer and solvent phase separate and the polymer solidifies. Phase-separation moves as a front into the layer from the outer surface [10].

Since the amount of non-solvent available in the bath is large compared to the polymer or solvent in the layer, to first approximation a given concentration of solvent can be assumed to progress through the layer at a diffusive speed $u \propto t^{-1/2}$, and solvent motion independent of the non-solvent is neglected, thus phase-separation is induced at a critical non-solvent concentration which moves as a front through the layer with speed $u \propto t^{-1/2}$.

To apply this model for front-induced phase-separation to the process of immersion precipitation membrane formation, the non-solvent is modeled as the temperature control-parameter, and the polymer and solvent are the $\mathcal{A}$-type and $\mathcal{B}$-type mixture components respectively. The phase-separation front is started at the edge of mixed material of equal volume fraction containing small fluctuations $\Phi(\boldsymbol{r}) = 0 + \zeta_\phi$ where ζ_ϕ is a uniformly distributed random number between $\pm\zeta_\phi^{\max}$. Behind the front, the phase-separated region is initialized with single pure domain of $\mathcal{B}$-type "solvent" $\Phi = -1$, thus creating an "immersion" effect. The (non-dimensional) front speed as a function of time is

$$U_x(T) = \frac{U_0}{\sqrt{1 + CT}} \,, \tag{259}$$

where U_0 is the initial front speed, $T = sI/t_{sp}$ is time since the start of the simulation (where t_{sp} is the spinodal time, I is the number of LBM iterations and s is the time scaling factor—see Section 1.3 for details), and C is a constant which determines the deceleration rate of the front. The offset of 1 for the time is for regulating the front speed since the numerical method has a limit on the velocity which can be imposed.

D.2. Early Trials

The method outlined above does not produce structures similar to immersion

precipitation membranes. The only structure it produces are Liesegang patterns—see Section 1.1.2 and Paper 2 for more information of Liesegang patterns. The reason is that the fully phase-separated $\mathcal{B}$-type domain behind the initial position of the front induced a depletion layer. As shown in Paper 3, the presence of a depletion layer will result in the production of parallel lamella, unless there is a sufficiently large defect in lamella. The same effect is visible in Figure C.3 for the off-critical systems $\Phi_{in} = 0.1$, $U = 0.1$. Even unrealistically large initial fluctuations $\zeta_{\phi}^{\max} = 10$ would not produce a defect sufficient to break the symmetry of the parallel lamella. The problem, of course, is that diffusive dynamics smooth out the irregularities much faster than the nucleation dynamics can produce a defect from those irregularities.

D.3. Fluctuating Lattice Boltzmann

The problem of initial fluctuation smoothing by diffusive dynamics has an obvious solution: add fluctuations to the dynamics. Adding fluctuations to LBM for a non-ideal multiphase system in a thermodynamically consistent way is an unresolved current issue in the research of lattice Boltzmann method development [44, 26, 27]. Therefore, fluctuations are added without regard to their thermodynamic correctness.

Fluctuations are added to the simulation by introducing fluctuations to the

distributions in the collision step just before streaming:

$$f_0(x, y, z, t+1) = f_0(x, y, z, t) \tag{260}$$

$$f_1(x-1, y, z, t+1) = f_1(x, y, z, t) - \zeta_x \tag{261}$$

$$f_2(x+1, y, z, t+1) = f_2(x, y, z, t) + \zeta_x \tag{262}$$

$$f_3(x, y-1, z, t+1) = f_3(x, y, z, t) - \zeta_y \tag{263}$$

$$f_4(x, y+1, z, t+1) = f_4(x, y, z, t) + \zeta_y \tag{264}$$

$$f_5(x, y, z-1, t+1) = f_5(x, y, z, t) - \zeta_z \tag{265}$$

$$f_6(x, y, z+1, t+1) = f_6(x, y, z, t) + \zeta_z \ , \tag{266}$$

where ζ_i is a uniformly distributed random number between $\pm\zeta^{\max}$. Note that no noise is added to the f_0 distribution, and that all other noise is added symmetrically. This ensures that the zero order moment, which is the conserved order parameter

$$\sum_i f_i(\boldsymbol{r}, t) = \phi(\boldsymbol{r}, t) \, , \tag{267}$$

stay conserved throughout the collision step.

D.4. Trials with Fluctuations

A number of simulations were run with varying noise amplitudes. It was found that $\zeta^{\max} = 0.08$ was sufficient to fairly reliably produce defects in the first parallel lamellar structure, whereas $\zeta^{\max} = 0.05$ was usually not a sufficient noise amplitude. With a reasonably reliable noise amplitude determined, the initial front speed was selected as $U_0 = 0.54$. As discussed in Section C, this high initial speed assured that the preferred morphology was firmly in the parallel lamella region of the morphology phase diagram. The first deceleration constant tried was $C = 0.024$, but the orthogonal lamella pattern did not appear at a short enough depth for the

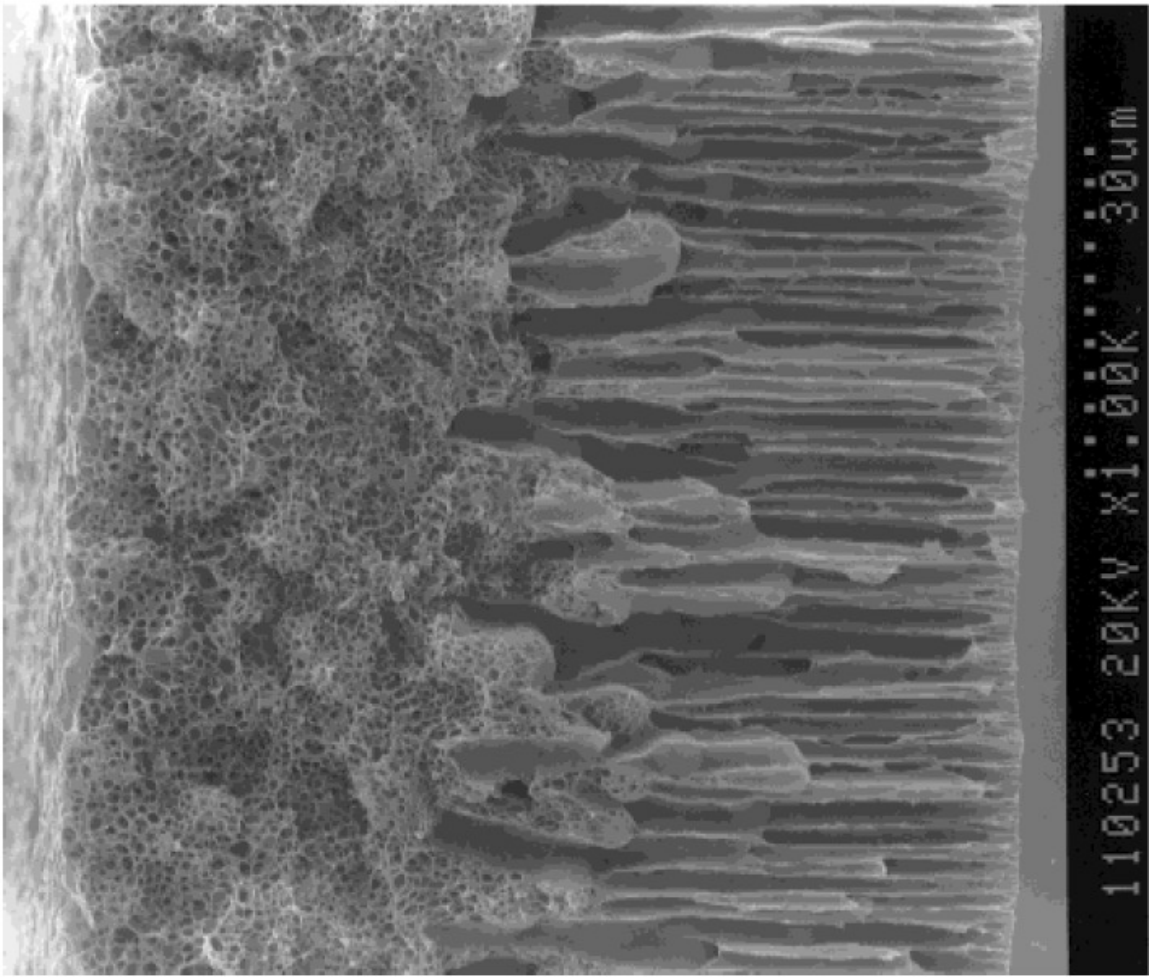

(a) Immersion precipitation membrane produced by Cheng *et al.*

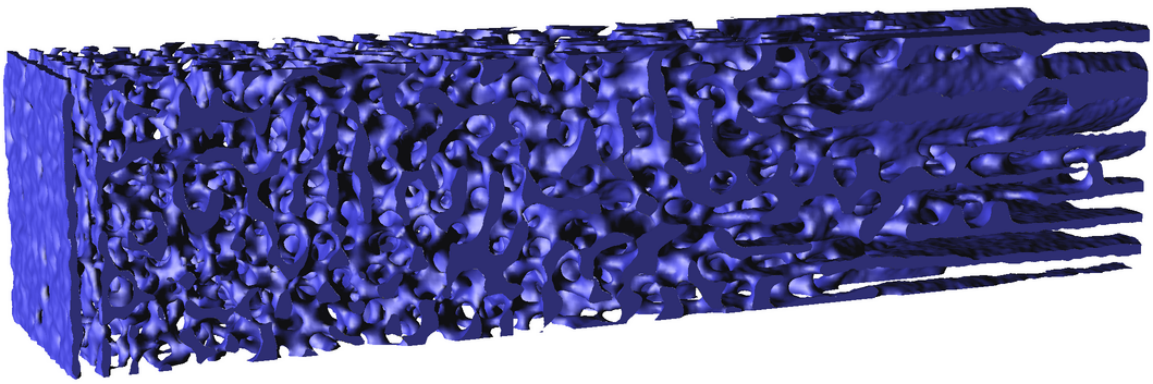

(b) LBM simulated phase-separated structure resembling an immersion precipitation membrane.

Figure D.1: (Color online) Comparison of a 3D front-induced phase-separated structure from a LBM simulation with an experimentally produced immersion precipitation membrane. The upper figure is from [10, Fig. 4a]. The production of the lower image is described in the text.

resulting structure to look similar to the desired experimental immersion precipitation membrane structure produced by Cheng *et al.* shown in Figure D.1a.

The next trial at $U_0 = 0.54$ and $C = 0.072$, produced the structure shown in Figure D.1, which strongly resembles the physical immersion precipitation membrane. The image is of an iso-surface around the $\mathcal{A}$-type material used to model the phase-separated polymer. The simulated length and time scales are $\lambda_{sp} = \pi\sqrt{8}$, and $t_{sp} = 24$, corresponding to $\kappa = 1$, $s = 0.023$, $\tau = 1$, $a_M = 1$, $b_M = 0$, $a_S = -1$, $b_S = 1$, $\phi_{in} = 0$. The simulation cell was $l_x = 64$ by $l_y = l_z = 128$ lattice units, with the front at $x_f = 48$. This is not large enough to produce the image in Figure D.1, which is $l_x = 801$ by $l_y = l_z = 128$ lattice units. A simulation as large as the final structure would take a prohibitively long time to produce results. However, since most of the phase-separation dynamics occur very near the phase separation front, the morphology changes very little once it is far enough away from the front. Fluctuations introduce additional dynamics everywhere, including far from the front. However, a video hosted at `http://earth.physics.ndsu.nodak.edu/thesis/2012/foard/variable-speed-3D.mp4` of the forming structure shows that the phase-separated domains, although the interfaces appear noisy, do not appreciably change once left behind by the front. Therefore, the structure that passes $x = 16$ is accumulated in a static array and saved to disc.

The transition in the generated structure occurs about 3/4 of the way into the membrane. The distance for the transition is $x_{\Vdash} = 600$ lattice units, or $X_{\Vdash} = 67$. Integrating the speed to get the transition time $T_{\Vdash}$ then reveals the transition speed:

$$X(T_{\Vdash}) = \int_0^{T_{\Vdash}} U(T_{\Vdash})\,\mathrm{d}T = 2U_0\sqrt{\frac{T_{\Vdash}}{C}} \quad \Rightarrow \quad U_{\Vdash} = \frac{2U_0^2}{CX_{\Vdash}} = \frac{2 \times 0.52^2}{0.072 \times 67} = 0.11\ , \quad (268)$$

which is in remarkable agreement with the transition speed $U \approx 0.2$ shown in Figure 24 for two dimensional systems.

A proper fluctuating LBM scheme for binary mixtures needs to be devised. Realistic values for fluctuations could then be introduced into the simulations to better compare the results to experimentally produced immersion precipitation membranes. Fluctuation wavelength and amplitude measurements by spectral microscopy from experiments may possibly be used to verify proper fluctuation parameters. Even without a thermodynamically correct fluctuation scheme, spectral microscopy measurements can be simulated for the lattice Boltzmann numerical implementation to determine if the fluctuations match those in experiments.

APPENDIX E. LBM FOR PHASE-SEPARATION FRONTS IN FLUIDS

A lattice Boltzmann method for the simulation of this model for phase separation fronts in the co-moving reference frame of the front is presented in Section 1.3. The appropriate equation of motion is the drift-diffusion equation first given as Eq. (39). The derivation of the simulated equation of motion, given as Eq. (67), relied on the velocity field being constant and homogeneous $\boldsymbol{u}(\boldsymbol{r}, t) = \boldsymbol{u}$. This is an appropriate assumption for diffusive materials, but does not hold for hydrodynamic materials. Here, this assumption is dropped, and a LBM implementation for this model of phase separation fronts moving through hydrodynamic materials is introduced.

E.1. Lattice Boltzmann Method for a Binary Fluid

The LBM for a binary fluid is covered in more detail in the references [46, 59, 54]. Presented here is a brief review.

The standard way to implement a lattice Boltzmann method for a binary fluid is to perform two LBM simulations simultaneously:

$$f_i(\boldsymbol{r} + \boldsymbol{v}_i, t+1) - f_i(\boldsymbol{r}, t) = \frac{1}{\tau_f(\boldsymbol{r}, t)} \left[f_i^0 - f_i(\boldsymbol{r}, t) \right] \ , \tag{269}$$

$$g_i(\boldsymbol{r} + \boldsymbol{v}_i, t+1) - g_i(\boldsymbol{r}, t) = \frac{1}{\tau_g(\boldsymbol{r}, t)} \left[g_i^0 - g_i(\boldsymbol{r}, t) \right] \ . \tag{270}$$

One simulation, operating on the g_i distributions, solves the isothermal Navier-Stokes equation for a non-ideal fluid, which calculates the velocity field of the fluid flow. The other simulation, operating on the f_i distributions, solves the drift-diffusion equation, which calculates the dynamics of phase separation of the two fluid components, and provides the non-ideal pressure contribution to the Navier-Stokes equation.

E.1.1. Navier-Stokes

The Navier-Stokes equation for a non-ideal fluid is:

$$\rho\left(\partial_t u_\alpha + u_\beta \nabla_\beta u_\alpha\right) = -\nabla_\beta p_{\alpha\beta} + \nabla_\beta \sigma_{\alpha\beta} \ . \tag{271}$$

The viscous stress tensor is:

$$\sigma_{\alpha\beta} = \eta[\nabla_\alpha u_\beta + \nabla_\beta u_\alpha] + \nu \nabla_\gamma u_\gamma \delta_{\alpha\beta} \ . \tag{272}$$

The non-ideal pressure tensor gradient

$$\nabla_\beta p_{\alpha\beta} = \rho \nabla_\beta \frac{\delta F}{\delta \rho} + \phi \nabla_\beta \frac{\delta F}{\delta \phi} = \rho \nabla_\beta \mu_\rho + \phi \nabla_\beta \mu \ , \tag{273}$$

is a function of the chemical potentials, which are calculated from the free energy

$$F = \int \mathrm{d}\boldsymbol{r} \left\{ \psi(\boldsymbol{r}, t) + \frac{\kappa(\boldsymbol{r}, t)}{2} \left[\nabla \phi(\boldsymbol{r}, t)\right]^2 \right\} \ , \tag{274}$$

which was first given as Eq. (2). The free-energy density $\psi(\boldsymbol{r}, t)$, first given as Eq. (3), now includes a term for the underlying free energy of an ideal gas:

$$\psi(\boldsymbol{r}, t) = \theta \rho(\boldsymbol{r}, t) \ln\left[\rho(\boldsymbol{r}, t)\right] + \gamma \left(\frac{a(\boldsymbol{r}, t)}{2} \phi(\boldsymbol{r}, t)^2 + \frac{b(\boldsymbol{r}, t)}{4} \phi(\boldsymbol{r}, t)^4 + c(\boldsymbol{r}, t) \phi(\boldsymbol{r}, t) \right) \ . \tag{275}$$

The mixing chemical potential μ is numerically calculated from the LBM simulation of the drift-diffusion equation (the other of the two coupled LBM simulations). The density chemical potential is $\mu_\rho = \theta + \theta \ln \rho$, where $\theta = 1/3$ is the temperature. The temperature is fixed by the LBM implementation of the isothermal Navier-Stokes equation [54]. Applying the product rule to the gradient of the density chemical

potential, the non-ideal pressure tensor gradient given as Eq. (273) becomes:

$$\nabla_\beta p_{\alpha\beta} = \nabla_\beta \left(\theta\rho\right) + \phi\nabla_\beta\mu \ . \tag{276}$$

A definition for the pressure tensor

$$p_{\alpha\beta} = \left(\rho\frac{\delta F}{\delta\rho} + \phi\frac{\delta F}{\delta\phi} - \psi\right)\delta_{\alpha\beta} + \gamma\kappa\left(\nabla_\alpha\phi\nabla_\beta\phi - \frac{1}{2}\nabla_\gamma\phi\nabla_\gamma\phi\delta_{\alpha\beta} - \phi\nabla_\gamma\nabla_\gamma\phi\right) \tag{277}$$

$$= \theta\rho\delta_{\alpha\beta} + \gamma\left(\frac{1}{2}a\phi^2 + \frac{3}{4}b\phi^4 - \frac{1}{2}\nabla_\gamma\phi\nabla_\gamma\phi - \phi\nabla_\gamma\nabla_\gamma\phi\right)\delta_{\alpha\beta} + \gamma\kappa\nabla_\alpha\phi\nabla_\beta\phi \tag{278}$$

satisfies the relation Eq. (273) [59].

The γ prefactor in the free energy is non-standard for the Navier-Stokes equation, but is very useful for LBM numerical simulations where it can be used to change the relative strength of the driving term $\phi\nabla_\beta\mu$ to the viscous term $\nu\nabla_\gamma u_\gamma\delta_{\alpha\beta}$. The standard definition of viscosity is $\eta = 2\rho\theta(\tau_g - 1/2)/D$, where D is the dimensionality. The conventional way to implement $\eta \to \infty$ is for $\tau_g \to \infty$, however in that limit the lattice Boltzmann method becomes collision-less, corresponding to a plasma. With γ in the free energy, changing the ratio m/γ has the same effect on the Navier-Stokes as changing η. The purpose of wanting to realize very large viscosities is to shift the the crossover from the diffusive to viscous hydrodynamic scaling regimes [5]. The relevance of the scaling regimes is discussed further in Appendix F.

The Navier-Stokes equation is implemented in LBM with the following moment

definitions :

$$\sum_i g_i = \sum_i f_i^0 = \rho \,, \tag{279}$$

$$\sum_i g_i^0 v_{i\alpha} = \rho u_\alpha \,, \tag{280}$$

$$\sum_i g_i^0 v_{i\alpha} v_{i\beta} = \rho u_\alpha u_\beta + \gamma p_{\alpha\beta} \,, \tag{281}$$

$$\sum_i g_i^0 v_{i\alpha} v_{i\beta} v_{i\gamma} = \theta\rho \left(u_\alpha \delta_{\beta\gamma} + u_\beta \delta_{\alpha\gamma} + u_\gamma \delta_{\alpha\beta}\right) \,. \tag{282}$$

E.1.2. Drift-Diffusion

As commented on previously, the use of LBM to solve the coupled Navier-Stokes and drift-diffusion equations to describe binary fluid mixtures is not new. What makes this implementation different from most previous ones is that the diffusive mobility is allowed to be spatially dependent. This is a minor point which does not change the final implementation, but it is good to shown this explicitly.

Recall the drift-diffusion equation

$$\partial_t \phi + \boldsymbol{\nabla} \cdot (\phi \boldsymbol{u}) = \boldsymbol{\nabla} \cdot (m \boldsymbol{\nabla} \mu) \,, \tag{283}$$

first given as Eq. (39). For a fluid, the velocity field is coupled to the Navier-Stokes equation. As discussed in Section 1.3, in order to show that the lattice Boltzmann method simulates Eq. (283), the lattice Boltzmann equation

$$f_i(\boldsymbol{r} + \boldsymbol{v}_i, t+1) - f_i(\boldsymbol{r}, t) = \frac{1}{\tau_f(\boldsymbol{r}, t)} \left[f_i^0 - f_i(\boldsymbol{r}, t)\right] \,, \tag{284}$$

is shown to recover Eq. (283) to second order. Since the only thing that is different is that the velocity field is no longer assumed to be constant, the derivation up to

Eq. (59) is unchanged. Up to that point, the LBE had been rewritten as:

$$\partial_t \phi + \nabla_\beta \left(\phi u_\beta\right) = \nabla_\alpha \left(\tau_f - \frac{1}{2}\right) \left[\phi \partial_t u_\alpha + u_\alpha \partial_t \phi + \nabla_\beta T_{\alpha\beta}\right] + O(\partial^3) \,, \tag{285}$$

and the zero order non-equilibrium and first two equilibrium moments were defined:

$$\sum_i f_i(\boldsymbol{r}, t) = \sum_i f_i^0(\boldsymbol{r}, t) = \phi(\boldsymbol{r}, t) \,, \tag{286}$$

$$\sum_i f_i^0(\boldsymbol{r}, t) v_{i\alpha} = u_\alpha \phi(\boldsymbol{r}, t) \,. \tag{287}$$

Remaining to be defined was the second order equilibrium moment $T_{\alpha\beta}$ which would make the right-hand-size of Eq. (285) match the right hand side of Eq. (283) to second order.

As before in Section 1.3, two useful identities will be needed in order to rewrite mixed spatial and temporal derivatives terms $\nabla_\alpha \partial_t$ as derivatives of space only $\nabla_\alpha \nabla_\beta$ in order to find the proper canceling terms in the second rank tensor. The first identity is the same as Eq. (53), and comes directly from Eq. (51):

$$\sum_i D f_i^0 = \partial_t \phi + \nabla_\beta \left(\phi u_\beta\right) = O(\partial^2) \,. \tag{288}$$

The second comes from the Navier-Stokes equation for a non-ideal fluid, given above as Eq. (271). The viscous stress tensor $\sigma_{\alpha\beta} = O(\partial)$ is first order in gradients of the velocity field, and the gradient of the stress tensor is second order $\nabla_\beta \sigma_{\alpha\beta} = O(\partial^2)$. The Navier-Stokes equation can be rewritten

$$\partial_t u_\alpha + u_\beta \nabla_\beta u_\alpha + \frac{\phi}{\rho} \nabla_\beta \mu = \frac{1}{\rho} \nabla_\beta \sigma_{\alpha\beta} = O(\partial^2) \,, \tag{289}$$

by use of the continuity equation $\partial_t \rho + \nabla_\alpha (\rho u_\alpha) = 0$. This is the second identity used

below.

Taking up the process at Eq. (59) before the assumption of constant u_α:

$$
\begin{aligned}
&\partial_t \phi + \nabla_\beta \left(\phi u_\beta\right) \\
&= \nabla_\alpha \left(\tau_f - \frac{1}{2}\right) \left[\phi \partial_t u_\alpha + u_\alpha \partial_t \phi + \nabla_\beta T_{\alpha\beta}\right] + O(\partial^3) && (290) \\
&= \nabla_\alpha \left(\tau_f - \frac{1}{2}\right) \left[\phi \Bigg(\underbrace{\partial_t u_\alpha + u_\beta \nabla_\beta u_\alpha + \frac{\phi}{\rho} \nabla_\beta \mu}_{O(\partial^2),\ \text{Eq. (289)}} - u_\beta \nabla_\beta u_\alpha - \frac{\phi}{\rho} \nabla_\beta \mu \Bigg) \right. \\
&\quad \left. + u_\alpha \Bigg(\underbrace{\partial_t \phi + \nabla_\beta (\phi u_\beta)}_{O(\partial^2),\ \text{Eq. (288)}} - \nabla_\beta (\phi u_\beta) \Bigg) + \nabla_\beta T_{\alpha\beta} \right] + O(\partial^3) && (291) \\
&= \nabla_\alpha \left(\tau_f - \frac{1}{2}\right) \left[\nabla_\beta T_{\alpha\beta} \underbrace{- \phi u_\beta \nabla_\beta u_\alpha - u_\alpha \nabla_\beta (\phi u_\beta)}_{-\nabla_\beta (u_\alpha \phi u_\beta)} - \frac{\phi^2}{\rho} \nabla_\beta \mu \right] + O(\partial^3) && (292) \\
&= \nabla_\alpha \left(\tau_f - \frac{1}{2}\right) \left[\nabla_\beta T_{\alpha\beta} - \nabla_\beta (u_\alpha \phi u_\beta) - \frac{\phi^2}{\rho} \nabla_\beta \mu \right] + O(\partial^3) \ . && (293)
\end{aligned}
$$

Using the second order moment definition

$$
\sum_i f_i^0(\boldsymbol{r}, t) v_{i\alpha} v_{i\beta} = T_{\alpha\beta} = \mu(\boldsymbol{r}, t) \delta_{\alpha\beta} + u_\alpha u_\beta \phi(\boldsymbol{r}, t) \ , \tag{294}
$$

to replace the second rank tensor in Eq. (293), the resulting equation of motion as simulated by the lattice Boltzmann method is:

$$
\partial_t \phi + \nabla_\alpha \left(\phi u_\alpha\right) = \nabla_\alpha \left(\tau_f - \frac{1}{2}\right) \left(1 - \frac{\phi^2}{\rho}\right) \nabla_\alpha \mu + O(\partial^3) \ . \tag{295}
$$

The dependence of the simulated effective diffusive mobility on the order parameter and density is an unresolved issue, and is typically ignored:

$$
m^{\text{eff}} = \left(\tau_f - \frac{1}{2}\right) \left(1 - \frac{\phi^2}{\rho}\right) \approx \left(\tau_f - \frac{1}{2}\right) = m \ . \tag{296}
$$

The drift diffusion equation is implemented in LBM with the following moment definitions :

$$\sum_i f_i = \sum_i f_i^0 = \phi \,, \tag{297}$$

$$\sum_i f_i^0 v_{i\alpha} = \phi u_\alpha \,, \tag{298}$$

$$\sum_i f_i^0 v_{i\alpha} v_{i\beta} = \phi u_\alpha u_\beta + \mu \delta_{\alpha\beta} \,. \tag{299}$$

E.2. Two Dimensional Drift-Diffusion Implementation

Note the second order moment for the drift-diffusion is no longer diagonal for an arbitrary velocity field u_α. Therefore a set of nine velocities are required in two dimensions on a square lattice:

$$\boldsymbol{v}_i^{\mathrm{D2Q9}} = \left\{ \begin{pmatrix} 0 \\ 0 \end{pmatrix}, \begin{pmatrix} -1 \\ 0 \end{pmatrix}, \begin{pmatrix} 1 \\ 0 \end{pmatrix}, \begin{pmatrix} 0 \\ -1 \end{pmatrix}, \begin{pmatrix} 0 \\ 1 \end{pmatrix}, \begin{pmatrix} -1 \\ -1 \end{pmatrix}, \begin{pmatrix} 1 \\ 1 \end{pmatrix}, \begin{pmatrix} -1 \\ 1 \end{pmatrix}, \begin{pmatrix} 1 \\ -1 \end{pmatrix} \right\} . \tag{300}$$

This is the same velocity set required to fulfill the LBM moment equations for the Navier-Stokes equation implementation. On this D2Q9 lattice, the moments given in Eq. (297–299) are:

$$f_0^0 + f_1^0 + f_2^0 + f_3^0 + f_4^0 + f_5^0 + f_6^0 + f_7^0 + f_8^0 = \phi \,, \tag{301}$$

$$-f_1^0 + f_2^0 - f_5^0 + f_6^0 - f_7^0 + f_8^0 = s u_x \phi \,, \tag{302}$$

$$-f_3^0 + f_4^0 - f_5^0 + f_6^0 + f_7^0 - f_8^0 = s u_y \phi \,, \tag{303}$$

$$f_1^0 + f_2^0 + f_5^0 + f_6^0 + f_7^0 + f_8^0 = s\mu + s^2 u_x^2 \phi \,, \tag{304}$$

$$f_5^0 + f_6^0 - f_7^0 - f_8^0 = s^2 u_x u_y \phi \,, \tag{305}$$

$$f_3^0 + f_4^0 + f_5^0 + f_6^0 + f_7^0 + f_8^0 = s\mu + s^2 u_y^2 \phi \,. \tag{306}$$

The above equations insufficiently constrain the nine equilibrium distributions.

An elegant choice for the equilibrium distributions is:

$$f_0^0 = \left[1 - \left(u_x^2 + u_y^2\right)\right]\phi - 2\mu \ , \tag{307}$$

$$f_1^0 = \frac{1}{2}\left[\left(u_x^2 - u_x\right)\phi + \mu\right] \ , \tag{308}$$

$$f_2^0 = \frac{1}{2}\left[\left(u_x^2 + u_x\right)\phi + \mu\right] \ , \tag{309}$$

$$f_3^0 = \frac{1}{2}\left[\left(u_y^2 - u_y\right)\phi + \mu\right] \ , \tag{310}$$

$$f_4^0 = \frac{1}{2}\left[\left(u_y^2 + u_y\right)\phi + \mu\right] \ , \tag{311}$$

$$f_5^0 = \frac{1}{2}s^2 u_x u_y \ , \tag{312}$$

$$f_6^0 = \frac{1}{2}s^2 u_x u_y \ , \tag{313}$$

$$f_7^0 = -\frac{1}{2}s^2 u_x u_y \ , \tag{314}$$

$$f_8^0 = -\frac{1}{2}s^2 u_x u_y \ . \tag{315}$$

This has a similar form to the D2Q5 LBM implementation of front-induced phase separation in a diffusive material. In the case where $\gamma = 0$, the drift diffusion is no longer coupled to the driving term in the Navier-Stokes equation. If the underlying fluid also in a stationary state where $u_y = 0$ and u_x is spatially constant, the first five D2Q9 distributions exactly match the D2Q5 distributions, and the last four D2Q9 distributions are zero.

E.3. Boundary Conditions

In order to complete the implementation of the lattice Boltzmann method for front-driven phase-separation in binary fluid, open boundary conditions for both the drift-diffusion equation and Navier-Stokes equations simulations must be formulated. An in-depth analysis of open boundary conditions for LBM simulations of phase-separation fronts moving through diffusive materials is given in Appendix G. The

results there suggest an impost conserved current method on the inflow, and non-current-conserving method on the outflow. The chosen boundary conditions for the LBM simulation of binary fluid are J1 for the inflow

$$f_1^{\text{in}} + f_7^{\text{in}} + f_5^{\text{in}} = f_2^{\text{out}} + f_6^{\text{out}} + f_8^{\text{out}} - u_x^{\text{front}} \phi_{in} \, , \tag{316}$$

$$g_1^{\text{in}} + g_7^{\text{in}} + g_5^{\text{in}} = g_2^{\text{out}} + g_6^{\text{out}} + g_8^{\text{out}} - u_x^{\text{front}} \rho_{in} \, , \tag{317}$$

and J3 on the outflow

$$f_2^{\text{in}} + f_6^{\text{in}} + f_8^{\text{in}} = f_1^{\text{out}} + f_5^{\text{out}} + f_7^{\text{out}} - u_x \phi \, , \tag{318}$$

$$g_2^{\text{in}} + g_6^{\text{in}} + g_8^{\text{in}} = g_1^{\text{out}} + g_5^{\text{out}} + g_7^{\text{out}} - u_x \rho \, . \tag{319}$$

Here u_x^{front} is the speed of the phase separation front, ϕ_{in} is the initial mixed material order parameter, ρ_{in} is the average density, and u_x, ϕ, and ρ are respectively the local velocity, concentration, and density. These boundary conditions prescribe a constant inflow current for both the order parameter and the density. Both boundaries are no-slip in the y-direction.

APPENDIX F. EFFECTS OF HYDRODYNAMICS ON PARALLEL LAMELLA FORMATION BY FRONT-INDUCED PHASE-SEPARATION

One of the effects of hydrodynamics is to change the ordering dynamics (coarsening) of phase-separated domains. As discussed in Section 4.6.2 in Paper 3, there is relationship between the typical length scale ℓ of a phase separated material and the elapsed time t. This dynamical scaling law states for phase ordering of connected domains following homogeneous phase separation, the typical length scale follows a power law relationship to elapsed time $\ell \propto t^{\alpha}$. The exponent α of the dynamical scaling depends on the type of dynamics which dominate the material motion:

$$\ell(t) \propto \begin{cases} \left(\frac{m}{\gamma}\sigma t\right)^{1/3} & , \ \ell \ll \left(\frac{m}{\gamma}\eta\right)^{1/2} & , \text{diffusive} \\ \frac{\sigma t}{\eta} & , \ \left(\frac{m}{\gamma}\eta\right)^{1/2} \ll \ell \ll \frac{\eta^2}{\rho\sigma} & , \text{viscous hydrodynamic} \\ \left(\sqrt{\frac{\sigma}{\rho}}t\right)^{2/3} & , \ \ell \gg \frac{\eta^2}{\rho\sigma} & , \text{inertial hydrodynamic.} \end{cases} \tag{320}$$

Here, σ is the surface tension of the interface between the phase-separated domains, m is the diffusive mobility, η is the viscosity, and ρ is the fluid density. The scaling exponents and scaling regimes in Eq. (320) are derived from dimensional analysis of the coupled drift-diffusion and Navier-Stokes equations of motion. Bray gives an excellent review on phase-ordering kinetics, and shown the origins of the dominate length scales given above [5].

As it turns out, the coarsening dynamics of phase-separated material is relevant in the formation of phase-separated structures in the wake of a moving phase-separation front, despite the twp systems being quite different in appearance.

F.1. Review of the Diffusive Case

Recall from Section 4.6.2 that the dynamical scaling law Eq. (240) (more generally

Eq. (320) above) was used to define a speed of dynamic coarsening

$$u_c = \frac{\mathrm{d}\ell}{\mathrm{d}t} = a\frac{\mathrm{d}t^\alpha}{\mathrm{d}t} = a\alpha t^{\alpha-1} = a\alpha\left(\frac{\ell}{\alpha}\right)^{1-1/\alpha} , \tag{321}$$

for some scaling constant a. When the speed of coarsening is larger than the speed of the phase separation front $u_c(\ell) > u$, structures forming at the front smaller than ℓ will coarsen into the front faster than the front is receding. For a phase separation front moving through a diffusive mixture, the exponent $\alpha = 1/3$, and the coarsening speed and length scale relationship is $u_c^{\mathrm{diff}} = a_{\mathrm{diff}}\ell^{-2}$, for some constant a_{diff}. This analysis explained the appearance of a front speed dependent minimum stripe width $\ell_{\perp,\mathrm{diff}}^{\mathrm{min}} \propto u^{-1/2}$ for the orthogonal stripe morphology. These results are explained in more detail in Section 4.6.3, and a figure showing the range of simulated orthogonal stripe widths with the theoretical minimum and maximum is shown in Section 31. For completeness, the analysis given in Section 4.6 predicts a maximum front-speed dependent orthogonal stripe width $\ell_{\perp}^{\mathrm{max}} \propto u^{-1}$ which, as it is derived from a nucleation standpoint, is independent of the bulk material kinetics which govern phase-ordering. The minimum and maximum orthogonal stripe widths are shown in Figure F.1 respectively as the black dashed and solid lines.

F.2. The Speed of Hydrodynamic Coarsening

The speed of coarsening in the viscous regime is a constant $u_c^{\mathrm{hyd}} = a_{\mathrm{hyd}}$, as given by Eq. (321) for $\alpha = 1$. This predicts that as structures become large enough to be dominated by viscous hydrodynamics, they will all coarsen at the same speed. This implies that the minimum length scale diverges $\ell_{\perp,\mathrm{hyd}}^{\mathrm{min}} \to \infty$ for structures (such as orthogonal lamella) attached to the phase separation front.

F.3. Hydrodynamic Crossover and Parallel Lamella Width

As evident from Eq. (320) there is a cross-over of the dominant kinetics from

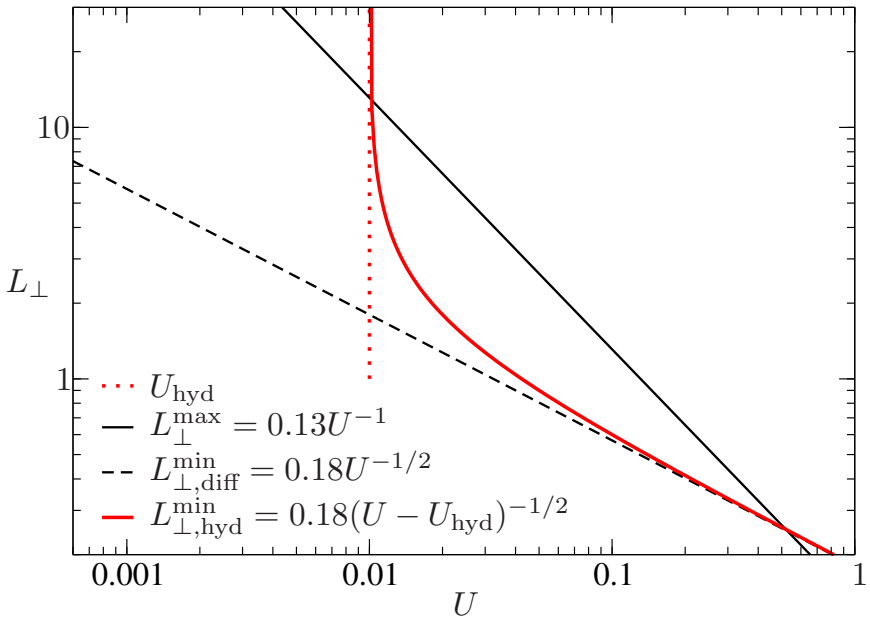

Figure F.1: (Color online) Minimum and maximum orthogonal stripe wavelengths formed by phase-separation fronts moving through viscous hydrodynamic materials. See Figure 31 for a comparison to purely diffusive materials. The maximum stripe width (solid black line) is the same for both diffusive and hydrodynamic materials. The striped black line is the diffusive minimum. The diffusive case is discussed in the text and in detail in Section 4.6. Orthogonal stripe formation by phase separation fronts can occur for stripe wavelengths $L_\perp$ and front speed U between the minimum and maximum. The speed of hydrodynamic coarsening (dotted line) presents a cutoff caused by the constant speed pf hydrodynamic coarsening. Fronts moving through viscous materials slower than the cutoff $U < U_{\rm hyd}$ do not produce orthogonal stripes. The solid curve (red online) gives a prediction for the minimum stripe wavelength formed by a front moving through a viscous material faster than the cutoff speed. More details are given in the text.

diffusive at small length scales to viscous hydrodynamic at larger lengths scales. At even larger length-scales there is another transition from viscous hydrodynamics to inertial hydrodynamics, however that effect will be ignored for now.

In the crossover between diffusive and viscous regimes, to first approximation the speed of coarsening is assumed to be a linear combination of the separate diffusive and viscous coarsening speeds:

$$u_c \approx u_c^{\rm diff}(\ell) + u_c^{\rm hyd} = a_{\rm diff}\ell^{-2} + u_c^{\rm hyd} \ . \tag{322}$$

Similar to the purely diffusive case described above, when the phase-separation front speed is slower than the combination of hydrodynamic and diffusive coarsening speeds $u < u_c$, any front-attached structures smaller than ℓ will coarsen into the front faster than the front recedes. Therefore the minimum length scale for phase-separated structures formed by a front moving through a mixed material with competing diffusive dynamics and viscous hydrodynamics is:

$$\ell_{\perp}^{\min} = \sqrt{\frac{a_{\text{diff}}}{u - u_c^{\text{hyd}}}} \tag{323}$$

This scaling behavior for competing dynamics is shown in Figure F.1 along with the results from purely diffusive dynamics.

F.4. Combined Coarsening Speed

To test the assumption that the combined coarsening speed is a linear combination of the diffusive and hydrodynamic speeds, as stated in Eq. (322), the speed of coarsening of a test morphology was measured for varying levels of hydrodynamics. The degree of hydrodynamics was dialed in by increasing the γ parameter. The initial morphology was set as an elongated finger domain of phase separated material suspended in a larger simulation of opposite type material. The interface of the coarsened reference finger is given in Figure F.2a. The other images in Figure F.2 show interfaces for fingers coarsened using γ values at order of magnitude intervals.

The simulations were $l_x = 384$ by $l_y = 256$ lattice sites, used periodic boundaries on all axes, had phase-separation parameters $-a = b = \kappa = 0.05$, and relaxation times $\tau_f = \tau_g = 1$ with corresponding diffusive mobility $m = 1/2$ and viscosity $\eta = 1/6$. The spinodal length and time were $\lambda_{sp} = 8.9$ and $t_{sp} = 160$. A number of simulations at different values of γ were allowed to coarsen from the same initial condition for 5000 LBM iterations. After this, the length of the finger $w(\gamma, t)$ was measured, and

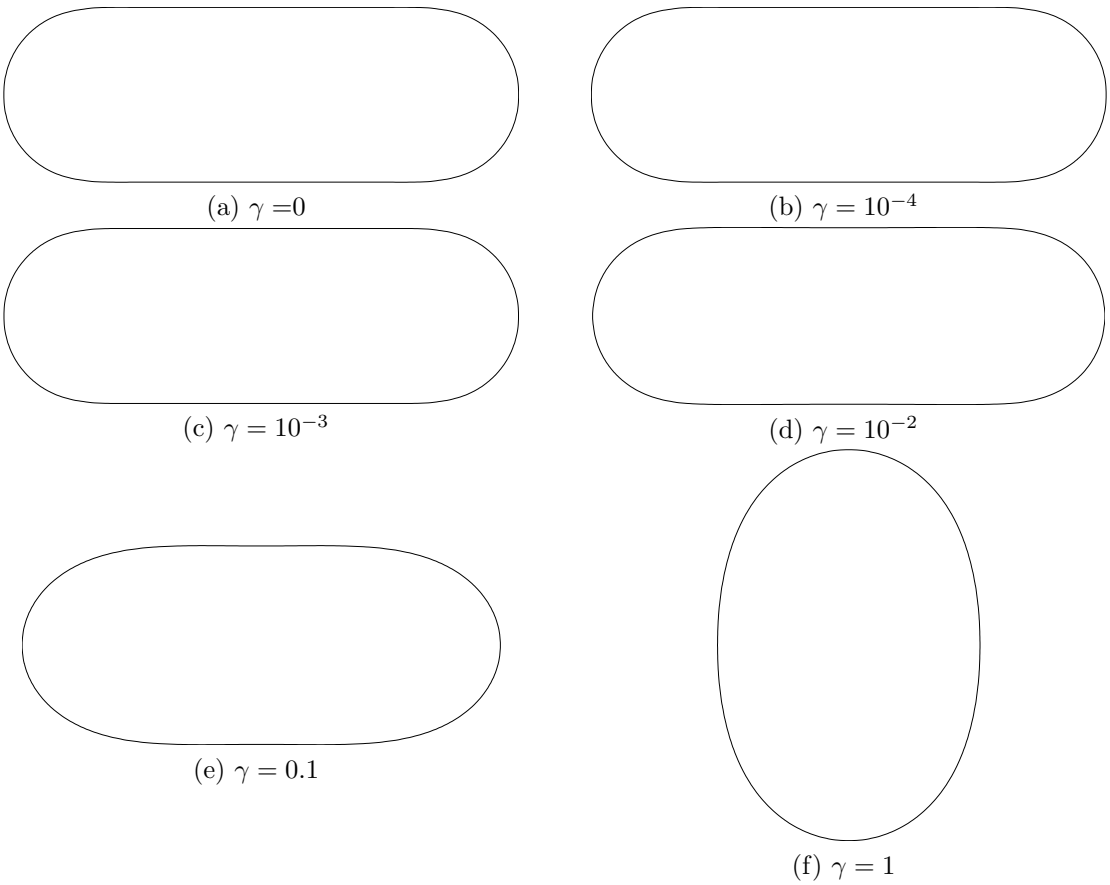

Figure F.2: Simulation results showing coarsening of finger morphologies for varying levels of hydrodynamics. The initial finger morphology is similar to the purely diffusive case shown in (a). The other cases demonstrate the effects of increasing the hydrodynamic driving parameter γ on the coarsening dynamics and speed.

that value was subtracted from the length $w(0,t)$ of the reference finger for $\gamma = 0$ where the coarsening dynamics were entirely diffusive.

Each final width in this set of simulations is proportional the negative coarsening speed for the appropriate dynamics. That is $w(0,t) \propto u_c^{\text{diff}}$, and in general $w(\gamma,t) \propto u_c$. The width difference is therefore $w(0,t) - w(\gamma,t) \propto u_c(\gamma) - u_c^{\text{diff}}$. If the assumption in Eq. (322) that hydrodynamic and diffusive coarsening speeds add linearly is true, then the width difference is proportional to the hydrodynamic coarsening speed:

$$w(0,t) - w(\gamma,t) \propto u_c(\gamma) - u_c^{\text{diff}} = u_c^{\text{diff}} + u_c^{\text{hyd}} - u_c^{\text{diff}} = u_c^{\text{hyd}} \propto \gamma \,, \tag{324}$$

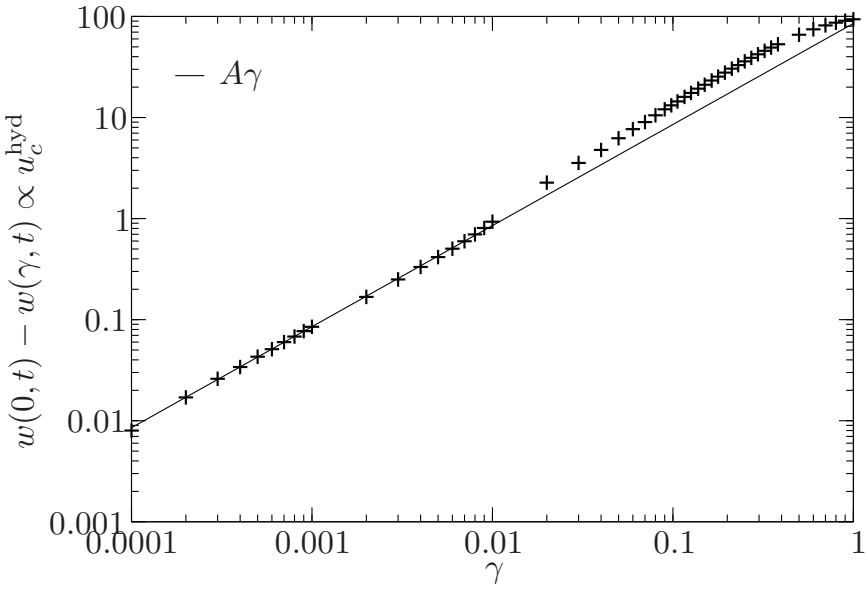

Figure F.3: A number of coarsened width comparisons at different values of the hydrodynamic driving parameter γ, shown as $+$. The line is fitted to the data for $10^{-4} \ll \gamma \ll 10^{-3}$ with the parameter $A \sim 85$.

and the width difference should be directly proportional to γ.

A large number of coarsening simulations for a wide range of γ values were run, and the results are shown in Figure F.3. The fitted line shows that the linear combination of hydrodynamic and diffusive coarsening described by Eq. (322) is a good approximation for $\gamma < 0.01$.

F.5. Orthogonal Stripe Formation by Phase Separation Fronts in a Binary Fluid

The preceding results support the analysis shown in Figure F.1 which predicts that if a fluid is highly viscous, a phase separation front passing though a binary fluid system has the potential to form orthogonal stripe structures. Typically the presence of any hydrodynamics destroys order in phase-separation front formed structures [25]. In order to definitively verify whether or not patterned structures can be formed in this way, a number of LBM simulations for phase separation fronts in binary fluids were performed.

The simulations were all of fronts moving into symmetrically mixed viscous fluid. The simulations were $l_x = 1024$ by $l_y = 1024$ lattice sites with the front at $x_f = 832$. The phase-separating parameters were $-a_S = b_S = \kappa_S = 0.15$. The phase-mixing parameters were $a_M = \kappa_M = 0.15$, and $b_M = 0.0$. Relaxation times were $\tau_f = \tau_g = 1$ with corresponding diffusive mobility $m = 1/2$ and viscosity $\eta = 1/6$. The spinodal length and time were $\lambda_{sp} = 8.9$ and $t_{sp} = 53.33$.

The simulation results are shown in Figure F.4. One rather interesting result is that, although orthogonal stripes formed in the two simulations with the small gamma values $\gamma = 0.00251$ and $\gamma = 0.00398$, the stripes never stabilized. What is not apparent from these still images is the how the stripes are constantly moving lateral to the front and changing size. The smallest stripes attached to the front are continuously being compressed until the pinch off and detach from the front. The domain fingers coarsening away from the front behind the thin stripe domains gives evidence of the detaching stripes. At the same time the thin domains are being squeezed out from the front, the wide domains are increasing width as domain fingers coarsen into the front. The coarsening away from the front of small stripes, and the coarsening into the front of large stripes drives convection currents which reinforce the process. Although they are not as enlightening as full motion videos, the images in Figure F.5 help to elucidate the description of the stripe dynamics described above. A description of how to read these figures is given in the caption. Available at `http://earth.physics.ndsu.nodak.edu/thesis/2012/foard/` are videos from these simulations.

The presence of this large scale convective currents is a surprising and interesting result. As shown in Figure F.5c, the anomalous back current $U_x^{\text{an}} = -0.9$ is on the same order as the phase separation front speed, while the anomalous forward current $U_x^{\text{an}} = 2.7$ is almost triple. While clearly this deserves more study, the already large

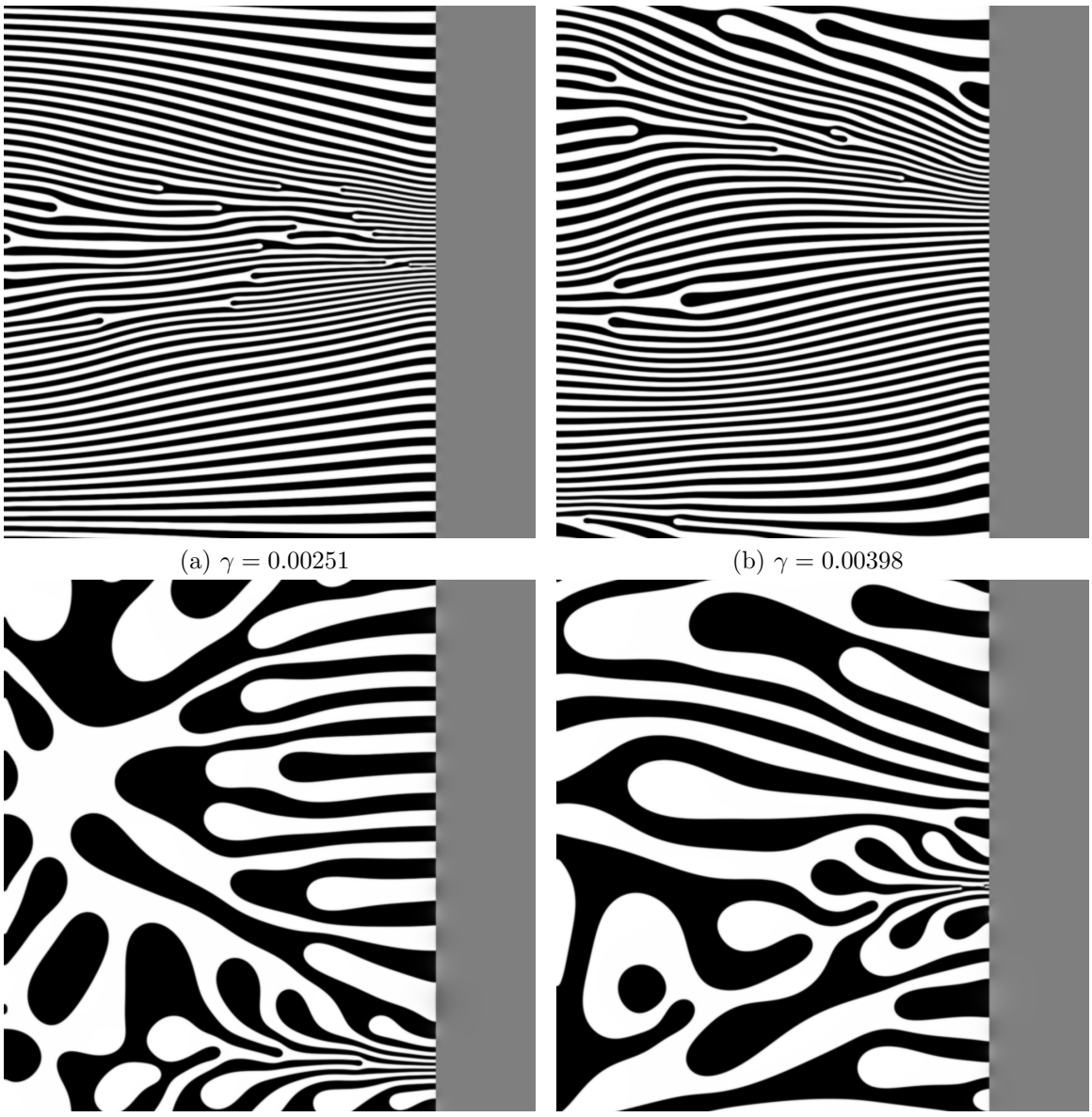

(a) $\gamma = 0.00251$ (b) $\gamma = 0.00398$

(c) $\gamma = 0.00631$ (d) $\gamma = 0.01000$

Figure F.4: Structures formed by LBM simulations of a phase separation front moving through a viscous binary fluid. The value of γ sets the crossover between the diffusive and viscous hydrodynamic scaling regimes. See Eq. (320), Figure F.1, and the text for more information.

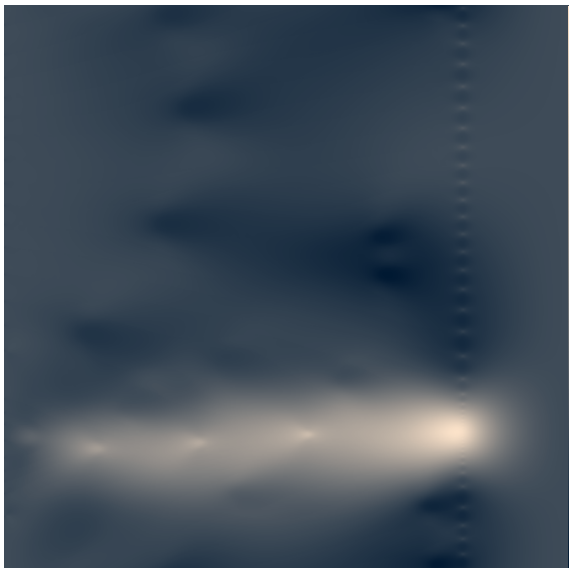

(a) $-0.5 < U_x^{\text{an}} < 1.5$ for $\gamma = 0.003981$

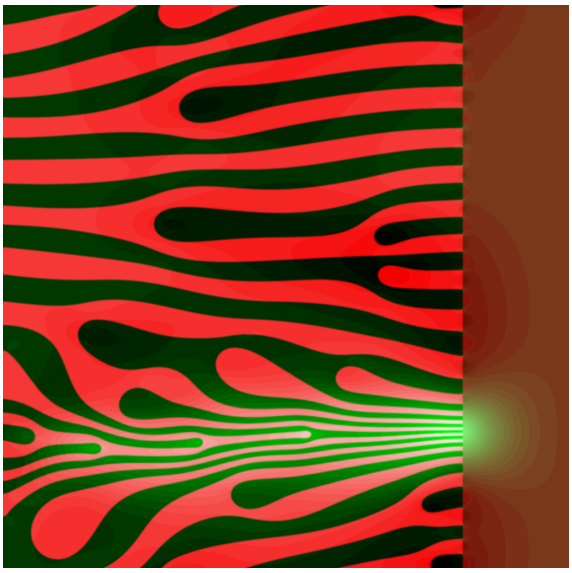

(b) ϕ and $-0.5 < U_x^{\text{an}} < 1.5$ for $\gamma = 0.003981$

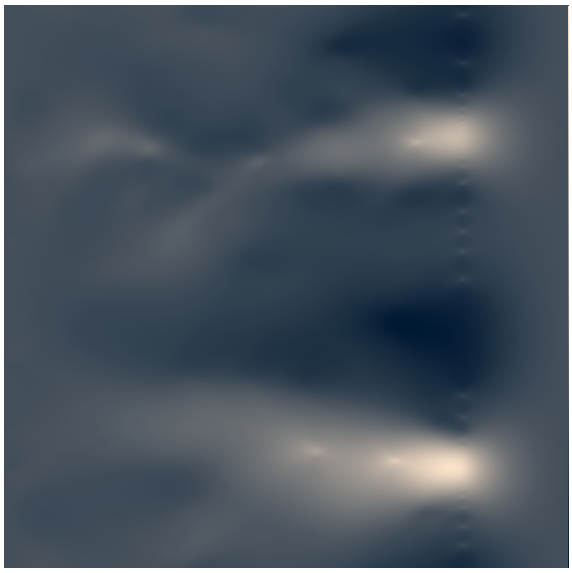

(c) $-0.9 < U_x^{\text{an}} < 2.7$ for $\gamma = 0.00631$

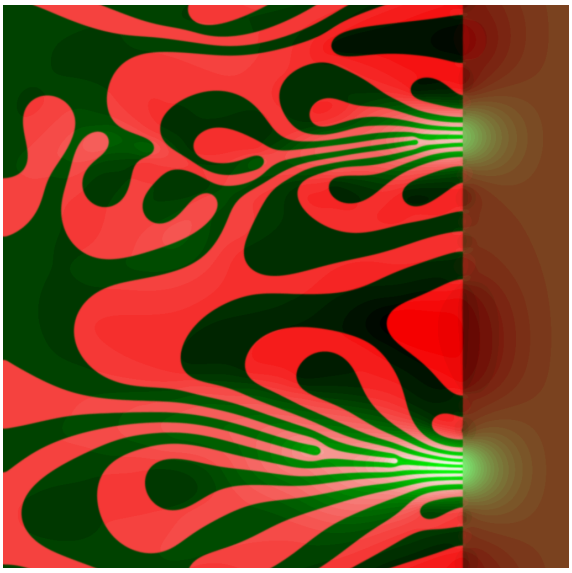

(d) ϕ and $-0.9 < U_x^{\text{an}} < 2.7$ for $\gamma = 0.00631$

Figure F.5: (Color online) Anomalous x-velocity field and morphologies two examples of phase separation front formed structure in a binary fluid. Images produced from the $\gamma = 0.003981$ and $\gamma = 0.00631$ simulations shown in Figure F.4, however after more than double the number of iterations. It is apparent by comparison to Figure F.4 that while these structures are not in a stationary state they have achieved a kind of steady state, as described in the text. On the left is plotted the anomalous x-velocity field $U_x^{\text{an}} = (u_x - u_x^{\text{front}})/u_x^{\text{front}}$. Flows faster than the front speed U_x^{front} are shaded lighter. The scale is given under each figure. On the right the anomalous flow is superimposed on the morphology.

simulation size may be too small for these numerical analyses. This issue is discussed further in the outlook below.

F.6. Outlook

It is apparent that more work needs to be done to test whether the predicted region of stability shown in Figure F.1 exists. Apart from the curious formation of large convective currents in the simulations attempted so far, doing this with the LBM simulation method given in Section 1.3 and Appendix E is challenging for the following reasons. To resolve the maximum stripe width, the simulation system size should be large by comparison $l_y \gg l_{\max}$. To show that the region itself exists, the maximum stripe width should be large compared to the minimum stripe width $l_{\max} \gg l_{\min}$. The theory presented above does not take into account the effects of a finite interface width, which Figure 31 shows becomes important when stripe wavelengths are on the order of the spinodal wavelength, therefore the minimum stripe width should be large by comparison $l_{\min} \gg \lambda_{sp}$. Additionally, in order to avoid lattice sticking and other Galilean invariance violations the spinodal wavelength should be large by comparison to the lattice spacing $\lambda_{sp} \gg \Delta x$ [54].

If a factor of ten is needed between scaling regimes, this would require simulations on the order of 10^5 lattice units in each spatial dimension. Simulations of this scale using the D2Q9 method given in Appendix E require 7.2×10^{11} bytes (670 Gb) of system memory for the (9×2) distribution functions alone. This is not currently feasible in a desktop or small cluster computer, and utilization of large clusters capable of these kinds of simulations would be prohibitively expensive. A more realistic upper memory requirement for simulations running on current desktop systems is ~ 1 Gb, which would result in scaling regimes which differ by a factor of ~ 5 and simulations with ~ 3000 lattice units on a side. Unfortunately, even such simulations are too

computationally intensive to perform a parameter space search like the one presented in Paper 3.

However, recently lattice Boltzmann method simulations have been ported to run on the extremely parallel graphics processing units (GPU). The performance increases over LBM simulations running central processing units (CPU) is reported to be significant [39]. Unfortunately, while GPU's with upwards of 3 Gb exist, they were not available in time to numerically examine the results shown here.

APPENDIX G. LBM OPEN BOUNDARY CONDITIONS FOR PHASE SEPARATION FRONTS

The LBM for simulation of phase-separation fronts given in Section 1.3 solves the drift-diffusion equation in the co-moving reference frame of the phase-separation front. The advantage to that approach is the ability of the simulation to follow along with and observe the phase-separation dynamics at the phase-separation front without the need to construct prohibitively large simulations. The trade-off for this significant advantage is the increased complexity of open inflow and outflow boundaries on one spatial axis. Mixed material flows into the simulation ahead of the front, and phase separated material flow out of the simulation behind the front. Here, different open boundary conditions (BCs) for lattice Boltzmann simulation of phase separation fronts are developed and evaluated.

The open boundary conditions will be developed and evaluated for the D2Q5 lattice Boltzmann method implementation outlined in Section 1.3. The illustration of the D2Q5 LBM scheme given in Figure 4 is a helpful reference, and is reproduced in Figure G.1.

A number of discrete lattice operators are presented below as part of the boundary condition definitions. To aid the readability of these operators, a stencil notation is used:

$$D\phi(x,y) = \begin{array}{c} y \\ \\ \\ \\ \\ \end{array} \begin{array}{c} \begin{array}{ccccc} & & x & & \\ & & \vdots & & \end{array} \\ \begin{bmatrix} & \ddots & w_{0,1} & \iddots & \\ \cdots & w_{-1,0} & w_{0,0} & w_{1,0} & \cdots \\ & \iddots & w_{0,-1} & \ddots & \end{bmatrix} \\ \begin{array}{ccccc} & & \vdots & & \end{array} \end{array} \phi = \sum_{i,j} w_{i,j}\phi(x+i, y+j)\ . \quad (325)$$

Here the discrete operator D is applied at position (x, y) to the field ϕ on a square

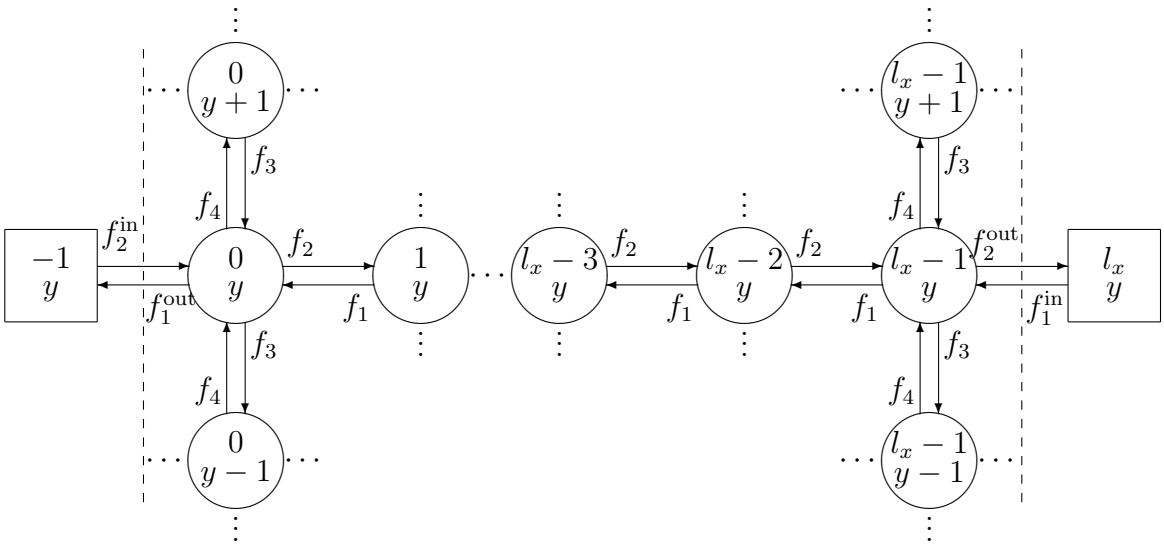

Figure G.1: Illustration of a D2Q5 LBM with open boundaries on the x-axis reproduced from Figure 4. Circles represent nodes inside the simulation. Outside the simulation boundary (represented by the dashed lines) are the off-simulation nodes represented by squares. The node's lattice position is given as a column vector inside the node symbol. Arrows are labeled with the streaming distributions they represent. Every time step $f_2^{\text{in}}(y)$ streams in from the left hand boundary, $f_1^{\text{in}}(y)$ from the right hand boundary, and $f_i(x, y)$ stream between the nodes. The distributions streaming into the simulation across the boundaries is determined by the boundary condition. Methods for calculating this distribution and evaluations of those methods are given in the text.

lattice. The column x and row y are labeled on the stencil to show where the operator is applied to the field. Weights $w_{i,j}$ are the multiplicative pre-factors of the field values at position $(x + i, y + j)$. The Laplace operator from Eq. (68) presented in stencil notation is:

$$\nabla^2\phi(x,y) = \begin{matrix} \\ y \end{matrix} \begin{matrix} \begin{matrix} \quad x \quad \end{matrix} \\ \begin{bmatrix} 0 & 1 & 0 \\ 1 & -4 & 1 \\ 0 & 1 & 0 \end{bmatrix} \end{matrix} \phi \,. \tag{326}$$

As shown in Figure G.1, and explained in Section 1.3, the LBM simulation has open boundaries on the x-dimension only. For sake of simplicity, except where needed only the boundary conditions for the right-hand, inflow boundary are presented. Each

simulated node at position (x, y) on the inflow x boundary receives a distribution f_1^{in} each time step streamed from a non-simulated node at $(x+1, y)$ across the boundary. In addition, the discrete Laplace operator used in the calculation of the chemical potential normally requires a value for the order parameter in the neighboring cells. However, since the boundary cells do not have off-simulation neighbors, the boundary condition must provide either an alternative Laplace operator on the boundary, or provide a way to determine an off-simulation value of the order parameter.

Two strategies are used to construct f_1^{in}. The first method is by determining the off-simulation values of ϕ and μ required to calculate the in-streaming distribution. This is referred to as the "imposed fields" boundary method. The second method is to calculate f_1^{in} from an imposed current flowing across the boundary to. This is called the "imposed current" method.

G.0.1. Imposed Fields Boundary Method

The imposed fields boundary method is straightforward: the in-streaming distribution is the equilibrium distribution

$$f_1^{\text{in}} = f_1^0(\phi, \mu) = \frac{1}{2}\left[\left(u_x^2 - u_x\right)\phi + \mu\right] \ , \ , \tag{327}$$

from some off-simulation ϕ and μ, and a constant speed u_x. The out-streaming distribution f_2^{out} is neglected. This method is widely used in LBM implementations of different models [54].

G.0.2. Imposed Currents Method

In the imposed current method, the out-streaming distribution is used to construct the in-streaming distribution by imposing a total flux j_x (current) across the boundary:

$$f_1^{\text{in}} = f_2^{\text{out}} - j_x^{\text{in}} \ , \tag{328}$$

for the right-hand boundary and

$$f_2^{\text{in}} = f_1^{\text{out}} - j_x^{\text{out}} \ , \tag{329}$$

for the right-hand boundary where the current j_x is assumed to flowing from right to left. This may seem like a strange definition for direction of the current, but it is consistent with defining the direction of travel of the phase-separation front to be in the positive x-direction.

G.1. Off-Simulation Order Parameter

As mentioned previously, both the imposed fields method and the imposed current method require either an alternative Laplace operator, or a way to determine an off-simulation ϕ. These requirements are effectively equivalent, and are discussed first.

In addition to be used in the discrete Laplace operator, the concentration field boundary values are used in the "imposed fields" boundary method to construct the in-streaming distribution from the equilibrium distribution. Here are four methods for determining the unknown off-simulation concentration field from known simulation parameters.

G.1.1. Constant Value: ϕ_{in}

For the inflow boundary the simplest choice for $\phi(x+1, y)$ is to set it equal to the concentration of the homogenous mixed material:

$$\phi(x+1, y) = \phi_{in} \ . \tag{330}$$

This is the correct concentration for boundaries which are far ahead of the front. For

boundaries behind the front, which must deal with on-lattice concentrations at the phase-separated equilibrium values, this approximation is obviously poor.

The concentration Laplacian in 2D is then:

$$\nabla^2\phi(x,y) = \begin{array}{c} \\ y \end{array} \begin{array}{c} \begin{array}{ccc} & x & \end{array} \\ \left[\begin{array}{cc|c} 0 & 1 & 0 \\ 1 & -4 & 0 \\ 0 & 1 & 0 \end{array}\right] \end{array} \phi + \phi_{in} \ , \tag{331}$$

where the vertical line in the stencil represents the inflow boundary. The concentration field to the right of vertical line is not available from the simulation, so all entries need to be zero.

G.1.2. Copy Boundary: $\phi 0^{\text{th}}$

As the concentration can vary significantly, an outflow boundary condition which takes into account the concentration of material at the boundary is desirable. A simple way to accomplish this is to copy the concentration of the boundary cell to the off-simulation cell:

$$\phi(x+1,y) = \phi(x,y) \ . \tag{332}$$

When used for the inflow, the mixed material near the boundary can more easily deviate from the homogeneous mixed material concentration. Since the dynamics of phase-separation at the front induces deviations in concentration ahead of the front, boundary conditions which allow such deviations may allow the boundary to be placed closer to the front, resulting in an overall smaller simulation. A concern with this approach is that allowing the boundary concentration too much deviation may alter dynamics at the front, possibly leading to more deviation and instability, or simply incorrect results.

The concentration Laplacian in 2D for this method is:

$$\nabla^2\phi(x,y) = \begin{matrix} \\ y \end{matrix} \left[\begin{array}{cc|c} & \overset{x}{} & \\ 0 & 1 & 0 \\ 1 & -4 & 0 \\ 0 & 1 & 0 \end{array}\right]\phi + \phi(x,y) = \begin{matrix} \\ y \end{matrix} \left[\begin{array}{cc|c} & \overset{x}{} & \\ 0 & 1 & 0 \\ 1 & -3 & 0 \\ 0 & 1 & 0 \end{array}\right]\phi \, . \tag{333}$$

G.1.3. Linear Extrapolation: $\phi 1^{\text{st}}$

The interior of domains of phase-separated material are of nearly constant concentration. However, the interfaces between domains have considerable changes in concentration. In order to account for this, a linear extrapolation of the concentration is used to find the off-simulation value:

$$\phi(x+1,y) = 2\phi(x,y) - \phi(x-1,y) \, . \tag{334}$$

This linear extrapolation assumes that the x-direction curvature of the order parameter is zero at the boundary node. It may be tempting to set the full Laplacian to zero, i.e. $\nabla\phi(x,y) = 0$, to attempt a more accurate extrapolation. However, it is worth noting that there is no specific reason to expect the curvature in any direction to be zero, or even small, and including additional dimensions in the extrapolation can actually make the accuracy worse.

The concentration Laplacian in 2D for the linear extrapolation method is:

$$\nabla^2\phi(x,y) = \begin{matrix} \\ y \end{matrix} \left[\begin{array}{cc|c} & \overset{x}{} & \\ 0 & 1 & 0 \\ 1 & -4 & 0 \\ 0 & 1 & 0 \end{array}\right]\phi + 2\phi(x,y) - \phi(x-1,y) = \begin{matrix} \\ y \end{matrix} \left[\begin{array}{cc|c} & \overset{x}{} & \\ 0 & 1 & 0 \\ 0 & -2 & 0 \\ 0 & 1 & 0 \end{array}\right]\phi \, . \tag{335}$$

G.1.4. Extrapolate Chemical Potential and Invert: $\mu^{-1}1^{\text{st}}$

Extrapolation of the order parameter ϕ using the previous two methods assumes ϕ varies slowly. This is obviously not the case for interfaces between phase-separated domains of different majority concentrations. In contrast to the sometimes sharply varying concentration, the chemical potential varies slowly. The off-simulation concentration $\phi(x+1, y)$ is the only unknown quantity in the calculation of the chemical potential $\mu(x, y)$ at the boundary node. In a stationary state, the Laplacian of the chemical potential is zero. Assuming a near-stationary state exists at the boundary, the unknown chemical potential at the boundary is well approximated by linear extrapolation:

$$\mu(x+1, y) - 2\mu(x, y) + \mu(x-1, y) = 0 \; . \tag{336}$$

The chemical potential at position (x, y) is

$$\mu(x, y) = \mu_{\text{bulk}}(x, y) - \kappa \left(\begin{array}{cc} & x \\ y & \begin{bmatrix} 0 & 1 & 0 \\ 1 & -4 & 1 \\ 0 & 1 & 0 \end{bmatrix} \phi \end{array} \right) \; , \tag{337}$$

where $\mu_{\text{bulk}}(x, y) = \phi(x, y) - \phi_{in}$ at the inflow, and $\mu_{\text{bulk}}(x, y) = \phi(x, y)^3 - \phi(x, y)$ at the outflow boundary. Combined and solved for the inflow off-simulation concentration, the above equations become:

$$\phi(x+1, y) = \begin{array}{cc} & x \\ y & \left[\begin{array}{cc|c} 0 & -1 & 0 \\ -1 & 4 + 1/\kappa & 0 \\ 0 & -1 & 0 \end{array}\right] \end{array} \phi + \frac{1}{\kappa} \left(\begin{array}{cc} & x \\ y & \left[\begin{array}{ccc|c} 0 & 0 & 0 & 0 \\ 1 & -2 & 0 & 0 \\ 0 & 0 & 0 & 0 \end{array}\right] \end{array} \mu - \phi_{in} \right) \; . \tag{338}$$

The expression for the outflow off-simulation concentration is:

$$\phi(x-1,y) = \begin{array}{c} \\ y \end{array} \left[\begin{array}{c|ccc} & x & \\ 0 & -1 & 0 \\ 0 & 4-1/\kappa & -1 \\ 0 & -1 & 0 \end{array}\right]\phi + \frac{1}{\kappa}\left(\begin{array}{c} \\ y \end{array} \left[\begin{array}{c|ccc} & x & \\ 0 & 0 & 0 & 0 \\ 0 & 0 & -2 & 1 \\ 0 & 0 & 0 & 0 \end{array}\right]\mu + \phi(x,y)^3\right) . \tag{339}$$

G.2. Defining Off-Simulation Chemical Potential Methods

As previously discussed, the "imposed field" method of constructing an open boundary condition requires determination of the off-simulation chemical potential field in order to construct the in-streaming LBM distributions

$$f_1^{\text{in}}(x,y) = \frac{1}{2}\left[\left(u_x^2 - u_x\right)\phi(x+1,y) + \mu(x+1,y)\right] , \tag{340}$$

at the inflow boundary, and

$$f_2^{\text{in}}(0,y) = \frac{1}{2}\left[\left(u_x^2 + u_x\right)\phi(-1,y) + \mu(-1,y)\right] , \tag{341}$$

at the outflow boundary. The schemes presented here are very similar to their off-simulation concentration counterparts previously presented in Section G.1.

G.2.1. Constant Value: μ_{in}

The simplest method to determine the off-simulation chemical is to impose it as a constant value

$$\mu(x+1,y) = \mu_{in} , \tag{342}$$

where μ_{in} is the chemical potential far away from the front. For this model of phase separation fronts, the chemical potential is designed to be zero in the mixed

material both far ahead of and behind the front. This method is similar to the method presented in Section G.1.1 for the constant value method to determine the off-simulation concentration, where there is no dependence of the method on the simulated nodes.

G.2.2. Copy Boundary: $\mu 0^{\text{th}}$

Similar to the way we developed methods for determining the off-simulation concentration in Section G.1, we try to refine the off-simulation chemical potential from information available in the simulation.

The first and simplest refinement, similar to Section G.1.1, is to copy the boundary node value of the chemical potential to the off-simulation position:

$$\mu(x+1,y) = \mu(x+1,y)\ . \tag{343}$$

Due to the fact that the chemical potential is continuous, and the chemical potential at the boundary may not be the equilibrium value, this method ought to produce a much more useful boundary condition than the previous one.

G.2.3. Linear Extrapolation: $\mu 1^{\text{st}}$

Like with the concentration, the complexity of the extrapolation method for finding the off-simulation chemical potential is increased with the hope of producing a better functioning boundary condition. There is some freedom in performing a linear extrapolation of the chemical potential to the off-simulation node. A simple method uses terms only in the x-direction:

$$\mu(x+1,y) = 2\mu(x,y) - \mu(x-1,y) = \begin{array}{c} \\ y \end{array} \begin{array}{c} \begin{array}{ccc} & & x \\ -1 & 2 & 0 \end{array} \\ \left[\begin{array}{cc|c} & & \\ & & \end{array}\right] \end{array} \mu\ . \tag{344}$$

Used in combination with the $\mu^{-1}1^{\text{st}}$ off-simulation concentration extrapolation method in Section G.1.4, where the boundary chemical potential is $\mu(x) = 2\mu(x-1) - \mu(x-2)$, the above linear extrapolation for the off-simulation chemical potential becomes $\mu(x+1) = 3\mu(x-1) - 2\mu(x-2)$. This extrapolation may result in an off-simulation chemical potential which overemphasizes the x-direction chemical potential gradient near the boundary.

An alternative extrapolation assumes the full discrete Laplacian of the chemical potential at the boundary node is zero:

$$\mu(x+1,y) = \begin{matrix} \\ y \end{matrix} \begin{matrix} \begin{matrix} x \end{matrix} \\ \left[\begin{array}{ccc|c} 0 & -1 & 0 & \\ -1 & 4 & 0 & \mu \\ 0 & -1 & 0 & \end{array}\right] \end{matrix} . \tag{345}$$

When used with the off-simulation concentration method in Section G.1.4, where the on-boundary chemical potential is derived from the nearby simulation nodes, the above becomes:

$$\mu(x+1,y) = \begin{matrix} \\ y \end{matrix} \begin{matrix} \begin{matrix} x \end{matrix} \\ \left[\begin{array}{ccc|c} 1 & -2 & 0 & \\ -4 & 7 & 0 & \mu \\ 1 & -2 & 0 & \end{array}\right] \end{matrix} . \tag{346}$$

These two linear extrapolation methods for the chemical potential, in combination with the concentration extrapolation method of Section G.1.4, will be evaluated as the separate boundary conditions D4a and D4b.

G.2.4. Alternate Extrapolation: μ_{alt}

The extrapolations presented in Section G.2.3 are not the only possibilities using the chemical potential from the near-boundary on-lattice nodes. There are an infinite number of consistent discrete extrapolations, each with different stencil

weights. This is a consequence of the freedom in choosing the weighting factors of the discrete gradient and Laplace operators [47]. Presented here is one such alternative extrapolation of the off-simulation chemical potential

$$\mu(x+1,y) = \begin{array}{c} \\ y \end{array} \left[\begin{array}{ccc|c} & & x & \\ 1 & -2 & 0 & 0 \\ -5 & 8 & 0 & 0 \\ 1 & -2 & 0 & 0 \end{array}\right] \mu \ , \tag{347}$$

which is used with the concentration extrapolation method presented in Section G.1.4 to create BC D5.

G.3. Defining Current Methods

Recall that in the current method, the in-streaming distribution is determined by the boundary flux $j_x = f_2^{\text{out}} - f_1^{\text{in}}$, and the out-streaming distribution f_2^{out}. Or as stated in Eq. (328): $f_1^{\text{in}} = f_2^{\text{out}} - j_x$. In some situations the current across the boundary may be known explicitly, or more easily calculated than the off-simulation chemical potential. In those cases, a boundary condition which guarantees a particular current has obvious benefits.

For the LBM simulations described in Section 1.3 of this model for front induced phase-separation, where the simulation is in the co-moving reference frame of the front, both the inflow and outflow current are

$$\langle \boldsymbol{j}^{\text{in}} \rangle_{\boldsymbol{x},t} = \langle \boldsymbol{j}^{\text{out}} \rangle_{\boldsymbol{x},t} = \begin{pmatrix} u_x \phi_{in} \\ 0 \end{pmatrix} \ , \tag{348}$$

provided the current across the boundary is averaged for a sufficiently long time.

G.3.1. Constant Current: j_{in}

Fulfilling the average boundary current requirement of Eq. (348) is most easily

done by simply specifying a constant boundary current:

$$j_x = u_x \phi_{in} \ . \tag{349}$$

The in-streaming distribution then becomes:

$$f_1^{\text{in}}(y) = f_2^{\text{out}}(y) - u_x \phi_{in} \ . \tag{350}$$

The average current is guaranteed to be correct by this boundary condition as the current at any node along the boundary at any given time is a constant value. However, this is an undesirable trait for an outflow boundary where domains containing different majority concentrations are far from the mixed-material equilibrium concentration ϕ_{in}.

G.3.2. Spatially Varying Current: $j(\phi)$

A current method boundary condition for phase separated material should take into account the concentration value at the boundary node. Two adjacent nodes in chemical equilibrium with each other with the same concentration $\phi(x, y) = \phi(x + 1, y)$, have a current $j_x = u_x \phi(x, y)$ flowing between them. Assuming the off-simulation node is in chemical equilibrium with the boundary node, the boundary current is

$$j_x(y) = u_x \phi(x, y) \ , \tag{351}$$

and the in-streaming distribution is:

$$f_1^{\text{in}}(x, y) = f_2^{\text{out}}(x, y) - u_x \phi(x, y) \ . \tag{352}$$

For the reasons discussed above, this boundary condition is more suitable for the outflow boundary at $x = 0$ on the left hand edge of the simulation. There the

in-streaming and out-streaming distribution are reversed, and the current across the boundary is from the flow out of the simulation space:

$$f_2^{\text{in}}(0,y) = f_1^{\text{out}}(0,y) + u_x\phi(0,y) \ . \tag{353}$$

G.3.3. Spatially Varying Current with Chemical Potential Gradient: $j(\phi,\mu)$

The boundary nodes may not be at equilibrium, in which case there is a gradient in the chemical potential at the boundary. As shown in Eq. (39) the total current includes a term for the chemical potential gradient in addition to the advection term:

$$j_x(y) = u_x\phi(x,y) - m(x,y)\nabla_x\mu(x,y) \ . \tag{354}$$

In contrast to the simulation bulk where the chemical potential gradient in Eq. (39) is calculated as a consequence of the LB method, this boundary method requires the explicit calculation of the gradient of the chemical potential at the boundary nodes. A biased gradient operator which does not include off-simulation nodes saves having to define the off-simulation chemical potential field. We use $\nabla_x\mu(x,y) = \mu(x,y) - \mu(x-1,y)$ at the inflow boundary on the right-hand side and $\nabla_x\mu(0,y) = \mu(1,y) - \mu(0,y)$ at the outflow boundary on the left-hand side.

With the above defined discrete gradient operators, the in-streaming distribution at the inflow boundary becomes

$$f_1^{\text{in}}(x,y) = f_2^{\text{out}}(x,y) - u_x\phi(x,y) + m(x,y)\left[\mu(x,y) - \mu(x-1,y)\right] \ , \tag{355}$$

and the in-streaming distribution at the outflow boundary is:

$$f_2^{\text{in}}(0,y) = f_1^{\text{out}}(0,y) + u_x\phi(0,y) - m(0,y)\left[\mu(1,y) - \mu(0,y)\right] \ . \tag{356}$$

G.3.4. Constant Average Spatially Varying Current: $\langle j(\phi,\mu)\rangle_y$

The current method outlined in Section G.3.3 does not guarantee the correct average current required by Eq. (348). This is remedied rather simply by requiring that the total current across the entire inflow boundary is constant:

$$\frac{1}{l_y}\sum_y \left[f_2^{\text{out}}(x,y) - f_1^{\text{in}}(x,y)\right] \equiv \langle j(\phi,\mu)\rangle_y = u_x\phi_{in}. \tag{357}$$

Implementing this boundary condition requires two passes over the boundary nodes. The first pass is constructs the same inflow distributions

$$\tilde{f}_1^{\text{in}}(x,y) = f_2^{\text{out}}(x,y) - u_x\phi(x,y) + m(x,y)\left[\mu(x,y) - \mu(x-1,y)\right] \ , \tag{358}$$

as those described Section G.3.3. Also during the first pass, the average would-be current $\tilde{j} = \sum_y \left[f_2^{\text{out}}(x,y) - \tilde{f}_1^{\text{in}}(x,y)\right]/l_y$ across the boundary is recoded, from which the average current error across the boundary is calculated:

$$\epsilon = u_x\phi_{in} - \tilde{j} \ . \tag{359}$$

During the second pass, each in-streaming inflow distribution is adjusted by the average current error:

$$f_1^{\text{in}}(x,y) = \tilde{f}_1^{\text{in}}(x,y) - \epsilon \ . \tag{360}$$

This method results in a boundary condition which allows for a spatially varying boundary current yet guarantees the average current across the boundary is constant. These are desirable properties for the inflow boundary. Since it allows for spatially varying current, it may be temping to use this method for the outflow boundary as well. This is problematic due to the fact that, while the spatiotemporal average is constant for this scenario of a moving phase-separation front, the spatial average of

Off-Simulation Order Parameter Method	Off-Simulation Chemical Potential Method				Boundary Current Method			
	μ_{in}	$\mu 0^{\text{th}}$	$\mu 1^{\text{st}}$	μ_{alt}	j_{in}	$j(\phi)$	$j(\phi,\mu)$	$\langle j(\phi,\mu)\rangle_y$
ϕ_{in}	D1				J1			
$\phi 0^{\text{th}}$		D2						
$\phi 1^{\text{st}}$			D3		J2	J3	J4	J5
$\mu^{-1}1^{\text{st}}$			D4	D5				

Table G.1: Boundary conditions constructed from the off-simulation concentration, off-simulation chemical potential, and imposed current methods. Each intersection of a row and column represents a possible boundary condition. Of the total 32 possible combinations, the ten named combinations were implemented and evaluated.

the outflow current can be wildly varying in time as different domains of different sizes and compositions are pushed across the outflow boundary. Even in the cases where stationary states are reached, the enrichment of majority-phase material at the front requires that the average current across the simulation space might be far from the average current for a considerable time before the stationary state stabilizes.

G.4. Method Combinations and Resulting Boundary Conditions

Each of the four off-simulation chemical potential and four boundary current methods can be paired with any of the four off-simulation concentration methods. From the methods presented so far there are 32 boundary conditions which can be constructed. Rather than performing an exhaustive analysis of all 32 possibilities, ten reasonable combinations are presented and tested. The boundary conditions selected for study are illustrated among the possible combinations in Table G.1. Five of the boundary conditions (D1-D5) use the imposed fields method, and the other five (J1-J5) use the imposed current method.

In constructing the distribution BCs we made a choice to pair off-simulation concentration and chemical potential methods of similar complexity. Method $\mu 1^{\text{st}}$ described in Section G.2.3 outlines two extrapolations. The first, given by Eq. (344),

contains only terms displaced from the boundary in the x-direction, and is the extrapolation used for D3 and D4a. The second, given by Eq. (345), includes terms from the y-direction neighboring nodes, and is used for D4b.

Except for J1 which sets the off-simulation concentration to a constant ϕ_{in}, the current method boundary conditions use the same linear extrapolation off-simulation concentration method $\phi 1^{\text{st}}$. The additional complexity of implementing $\mu^{-1}1^{\text{st}}$ over $\mu^{-1}1^{\text{st}}$ did not seem warranted, as the off-simulation concentration is only used for the Laplacian of the on-lattice boundary node. Interesting in it's own right, the effect of just changing the method of computing the near-boundary Laplacian should be studied, but will have to wait for future study.

A final notes regarding the difference between the distribution and current boundary condition methods: For the relaxation time $\tau = 1$ used in these simulations, the out-streaming distribution at the inflow boundary is given by the equilibrium distribution $f_2^{\text{out}}(y) = f_2^0[\phi(x,y), \mu(x,y)]$. The in-streaming distribution is constructed from the equilibrium distribution using off-simulation values $f_1^{\text{in}}(y) = f_1^0[\phi(x+1,y), \mu(x+1,y)]$. Therefore, the current flux across the boundary for a distribution method boundary condition is $j_x^{\text{in}}(y) = f_1^{\text{in}}(y) - f_2^{\text{out}}(y)$, and the distribution method BCs can be easily compared to current methods. For example, with BC D3 the off-simulation concentration give in Eq. (332) and chemical potential given in Eq. (343) are copies of the on-lattice values:

$$\begin{aligned} j_x^{\text{in}}(y) &= f_1^{\text{in}}(y) - f_2^{\text{out}}(y) \\ &= \frac{1}{2}\left[\left(u_x^2 - u_x\right)\phi(x,y) + \mu(x,y) - \left(u_x^2 + u_x\right)\phi(x,y) - \mu(x,y)\right] \\ &= u_x\phi(x,y)\ , \end{aligned} \tag{361}$$

which is the same inflow current defined by Eq. (351) for boundary condition J3.

Although they result in the same inflowing current, D2 and J3 use different methods to calculate the boundary Laplacian and therefore are not identical boundary conditions. This is most strikingly demonstrated by the circular domain test results shown below in Figures G.5 & G.6.

G.5. Boundary Evaluation

A boundary condition can only be evaluated as appropriate in the context of a particular system. For the model of co-moving phase separation front, there are very different desirable properties for the inflow versus the outflow boundary conditions. In the co-moving reference frame of the simulation, an inflowing current $j_x = u_x\phi_{in}$ matches the rate of material overtaken by a front moving at speed u_x passing through material of mixed concentration ϕ_{in}. The inflow boundary condition should ensure the correct average current $\langle j(x,y)\rangle_{\boldsymbol{x},t} = u_x\phi_{in}$ flowing into the simulation space. This is the subject of the first test of the boundary conditions.

Inflow boundary conditions, in addition to producing the correct average current, should have the minimal possible effect on the concentration and chemical potential fields in the simulation space. That is, a desirable inflow boundary is one that produces the same concentration and chemical potential fields when placed close to the phase-separation front as when placed far from the phase-separation front. This property is tested by comparing fields produced by different boundary conditions placed a different distances ahead of a front.

Similarly, the fields behind the phase-separation front should be minimally affected by the proximity of the outflow boundary. That is, any domain in contact with an outflow boundary should behave as if it were entirely within the simulation bulk. The third set of tests compare the fields produced by different outflow boundaries placed at decreasing distance behind the phase-separation front to the fields produced by a simulation with the outflow boundary very far behind the front.

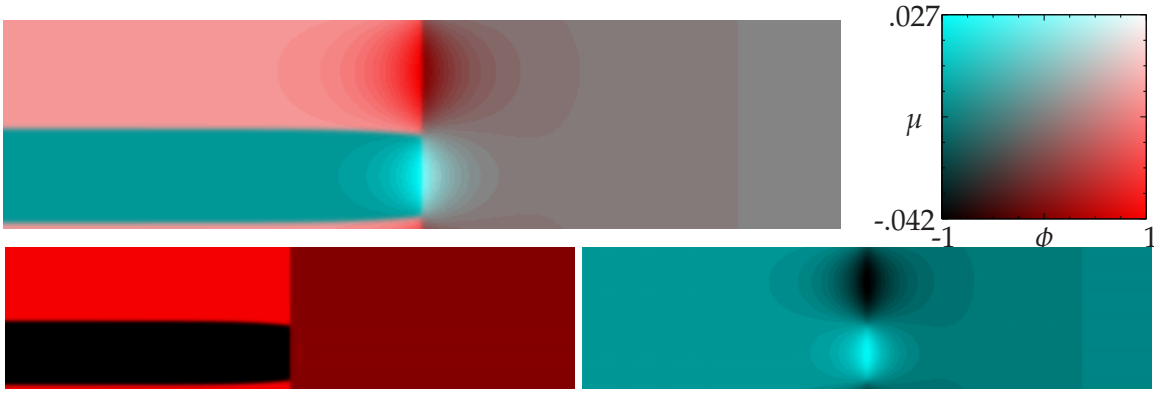

Figure G.2: (Color online) Example of stationary stripe example morphology formed by a phase separation front used for boundary condition evaluation. For the color version of this plot the range of values are shaded in the additive color model red $= (\phi - \phi_{\min})/(\phi_{\max} - \phi_{\min})$, cyan $= (\mu - \mu_{\min})/(\mu_{\max} - \mu_{\min})$. The separate channels are shown below the main figure, and may be viewed separately online with red/cyan anaglyph glasses. The simulation parameters for this example are $u_x = -0.001546$, $\kappa = 2$, and $\phi_{in} = 0.2$. Simulation size is $l_x = 2304$ by $l_y = 128$, however only the region from $x = 0$ to $x = 511$ is shown. The front is at $x_f = 256$. The inflow and outflow boundary conditions are respectively J1 and J4, which function reasonably well in this scenario, as shown in Figure G.4c and Figure G.6d.

The first three tests all deal with fields which reach a stationary state. Stationary states make good benchmarks because convergence is an easy criteria to test for numerically. An example and description of a stationary state similar to those used in the first three tests is given in Figure G.2.

As discussed in Paper 3, and shown in Figure 24, fields which become stationary in the co-moving reference frame of the front are only one possible resulting morphology. The final test evaluates outflow boundary conditions for their ability to deal with the notoriously difficult problem of advecting a circular domain across an open boundary.

G.5.1. Inflow Current

This first benchmark tests the ability of the inflow BCs to provide the correct material current $j_{in} = u_x \phi_{in}$ for the simulation. Using J4 as the outflow BC, each BC is tested as an inflow boundary in a series of simulations (similar to the one shown

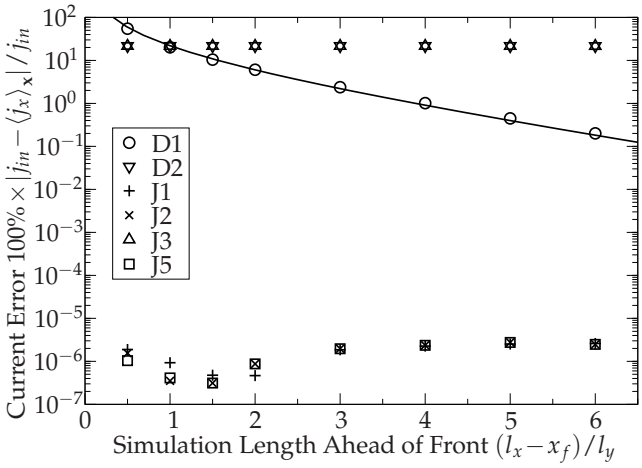

Figure G.3: Stationary state current errors of inflow boundary conditions placed various distances ahead of the phase separation front. Smaller values are better. Each simulation is initialized with mixed material $\phi(x > x_f, y) = \phi_{in} = 0.1$ ahead of the front and two phase-separated stripes such that $\langle \phi(x < x_f, y) \rangle_{\boldsymbol{x}} = \phi_{in} = 0.1$ behind the front. The simulation is run until the deviation of the spatially averaged x-direction current $|\langle j_x \rangle_y|$ either converges to a very small value $|\langle j_x \rangle_y| < 10^{-10}$, or diverges to a very large value $|\langle j_x \rangle_y| > 10^{10}$. Stationary states with converging currents appear similar to Figure G.2. Not included are BCs with diverging current simulations. Simulation size in the y-dimension is $l_y = 32$, outflow BC is J4, the front is placed at $x_f = 64$, inflow BCs are placed at $l_x = \{80,\ 96,\ 112,\ 128,\ 160,\ 192,\ 224,\ 256\}$. The front speed is $u_x = -0.0123697$, and the theoretical current is $j_{in} = u_x \phi_{in} = -0.00123697$. As shown in Section G.5.3, at $x_f = 64$ ($x_f/l_y = 2$) the phase-separation front is far enough ahead of the outflow BC J4 so as to not grossly influence the final stationary state of the simulation. Results are discussed further in the text.

in Figure G.2) which places the inflow boundary at increasing distances ahead of the phase-separation front. Results from simulations which reach a stationary state are compared in Figure G.3.

Some inflow BCs do not result in a stationary state in this test and are excluded from the results. This effect is due to positive feedback of any non-zero current present at the inflow boundary. Highly symmetric mixed inflow material $\phi_{in} = 0$ has zero net inflow current $j_x^{\text{in}} = 0$, and can mask this feedback mechanism if no fluctuations are present to break the symmetry. For this reason, a non-symmetric inflow mixture $\phi_{in} = 0.1$ is used. Interestingly, except for that highly symmetric case, the current

percent errors shown in Figure G.3 do not change as a function of the mixed material concentration. Simulations (not shown) with the same dimensions, front position, and front speed had the same current percent error for a given boundary condition with mixed material concentrations that varied from $\phi_{in} = 0.0001$ to $\phi_{in} = 0.3$, however not all BC shown in Figure G.3 were tested over the entire range. See Figure G.3 for further details of the simulation method.

The best results in this benchmark are obtained from the equally effective inflow BCs J1, J2, and J5, which were explicitly constructed to produce the correct inflow current. The current percent error for these methods can be reduced to machine accuracy (not shown) by reducing the allowable deviation of the average current and running the simulations for more iterations.

At larger simulation lengths, the current error for the simplest boundary condition D1 decays exponentially. However, the current error grows inversely with smaller simulation lengths. Shown in Figure G.3, the function $y = 40\exp(3x/2)/x$ (where $x = l_x/l_y$ and y is the percent difference) is included as an aid to the eye to show the trend. If the convergence continues on this trend, boundary condition D1 must be placed a distance $(l_x - x_f)/l_y = 22.5$ ($l_x - x_f = 720$ in lattice units) ahead of the front in order to have similar current percent error as the results for boundary conditions J1, J2, and J5. However, recall that the percent error for J1, J2, and J5 can be further reduced by several orders of magnitude simply by running the simulation longer.

Boundary conditions D2 and J3 result in the same current percent error, which remains constant regardless of how far ahead of the front the boundary is placed. Perhaps a surprising result given their apparently dissimilar formulations, the analysis in Section G.4 of the current produced by D2 shows that a given concentration field at the boundary $\phi(x, y)$ produces the same in-streaming current $j_x^{\text{in}}(y) = u_x\phi(x, y)$ as BC J3.

G.5.2. Inflow Fields

In addition to producing the correct overall current, the choice of inflow boundary should produce the correct concentration and chemical potential fields. In this test, the inflow boundary conditions with non-diverging currents in the previous test have their concentration and chemical potential fields compared to reference fields from a very large simulation. The results and details of the testing procedure are shown in Figure G.4.

A boundary condition performs well in this test if small simulations result in profiles which closely match the reference. Inflow BCs D2 and J3 do not converge to the correct stationary solution even at large simulation sizes. D1 converges correctly but slowly and shows significant deviation at small sizes. The current conserving BCs J1, J2, and J5 show correct convergence even for small simulations, with J2 and J5 showing the best performance. These results are consistent with those shown in Figure G.3. The reference profile is the stationary state ($|\langle j_x \rangle_y| < 10^{-12}$) result of a numerical simulation of a stripe pair similar to Figure G.2 with parameters $l_x = 768$, $x_f = 256$, $l_y = 32$, $u_x = -0.01234$, $\kappa = 2$, and $\Phi_{in} = 0.1$, and with inflow and outflow BCs J5 and D4b respectively. The comparison simulations are initialized with a copy of the reference simulation which is shortened in the x-dimension with a front position $x_f = 64$ and an overall length from the set $l_x = \{80,\ 96,\ 112,\ 128,\ 160,\ 192,\ 224,\ 256\}$. Simulations are halted once the average current deviation becomes small $|\langle j_x \rangle_y| < 10^{-10}$, indicating a stationary state.

The reason for the incomplete convergence of the current for BCs D2 and J3 is now apparent. The interface between phase-separated material has a preferred contact angle with the front which depends on the mixed-material concentration. This results in the interface curving in toward the minority phase stripe. The interface curvature results in a Laplace pressure, manifested as an overall deviation of the chemical

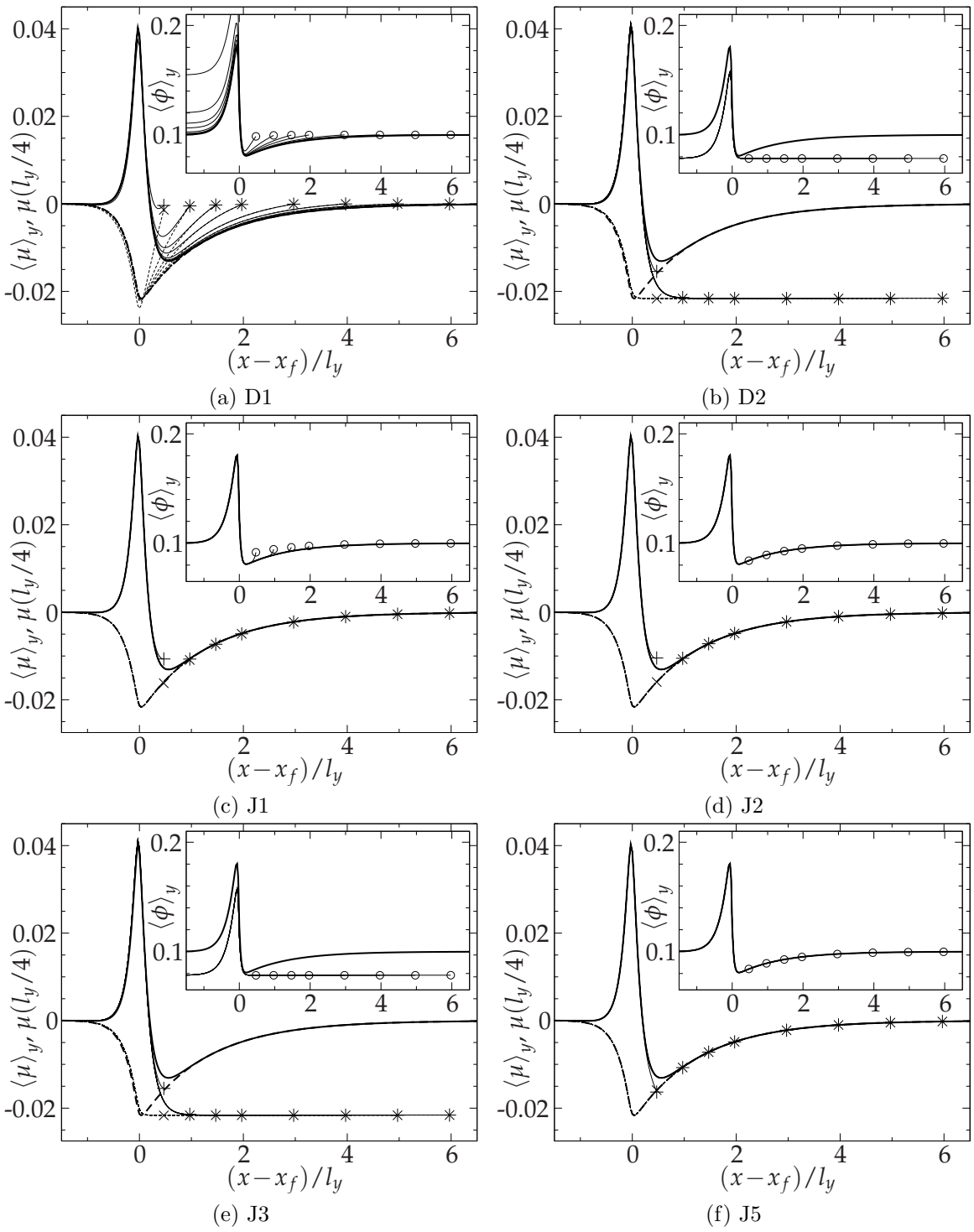

Figure G.4: Comparison of different inflow boundary conditions placed at varying distances ahead of the phase separation front compared with a reference stationary profile (bold). Outset: μ along stripe center (solid with $\times$) and $\langle\mu\rangle_y$ (dashed with $+$). Inset: $\langle\phi\rangle_y$ (with $\circ$). Symbols only mark the curve endpoints to show the inflow boundary value of each profile. Testing procedure and simulation parameters are described in the text.

potential at the front. This was observed and noted in our previous publication [20], and is discussed in more depth in Appendix A. An example of the effect can be seen in Figure G.2. Due to BCs D2 and J3 not specifying specific values for the fields or current at the boundary, the deviation of the average chemical potential and concentration fields at the front can extend to the boundary.

Also apparent from Figure G.4a is that using D1 for the inflow boundary produces acceptable fields for the largest of the trial simulations, even though (as shown in Figure G.3) the current percent error is several orders greater than the current conserving boundary conditions J1, J2, and J5. The BC J1 also produces acceptable fields for simulations larger than $(l_x - x_f)/l_y = 5$, however the static value of ϕ_{in} for the off-simulation concentration field causes deviations of the concentration field for smaller simulations.

Boundary conditions J2 and J5 give equally good results at all tested simulation sizes. As shown in Figure G.4d and Figure G.4f, the average chemical potential and average concentration fields for both BCs are indistinguishable from each other and from the reference fields. Both methods show a slight deviation in the cross-sectional chemical potential field for the smallest simulations; J2 undershoots, whereas J5 overshoots the proper value.

According to these results, the most appropriate boundary condition for use as an inflow boundary for this system is J5. As shown in Section G.5.1, both J1 and J2 produce the same correct average inflow current as J5. However, unlike J1 and J2 which fix the inflow current at each cell, J5 can produce a constant average inflow current which is not spatially constant. Hypothetically, this should allow the inflow boundary to be placed closer to the phase-separation front, but in practice the advantage is small and not worth the increased complexity.

G.5.3. Outflow Fields

This evaluation of the outflow boundary conditions tests the ability of the BC to reproduce the correct stationary-state concentration and chemical potential fields for phase-separated material behind the front. The smallest set of simulations are so close to the front that there is a significant Laplace pressure and subsequent chemical potential offset present in the minority phase stripe at the outflow boundary, which is a challenging situation for open boundary conditions. As mentioned in the previous section, the source of the Laplace pressure is the curved domain interface present at the front due to a preferential wetting angle.

A comparison of the resulting stationary state profiles for the outflow boundary conditions is shown in Figure G.5 and Figure G.6. These profiles are presented similarly to the inflow BC profile comparison shown in Figure G.4. In contrast to the inflow results where D1 performed well at large distances ahead of the front, even the largest simulations with D1 as an outflow produce profiles which poorly match the references. The remaining BCs show excellent performance for large simulations, and roughly equally good performance for small simulations. Like the inflow profile results, each test case is initialized as a cutout copy from the reference simulation, and the simulation halted when the stationary-state criteria ($|\langle j_x \rangle_y| < 10^{-10}$) is reached. The set of simulation lengths are $l_x = \{144,\ 160,\ 176,\ 192\}$, and the front positions $x_f = l_x - 128$ vary with the overall simulation length. Each simulation uses the inflow BC J5 which, as shown in Figure G.4, has excellent performance for the chosen simulation length $(x - x_f)/l_y = 4$ ahead of the phase separation front. All other parameters are the same as the inflow profile tests.

From Figures G.5 & G.6 it is apparent that the y-averaged concentration and chemical potential field are the most difficult to reproduce accurately. On this benchmark, D4a gives the best result, with D2 and D5 performing worse than all

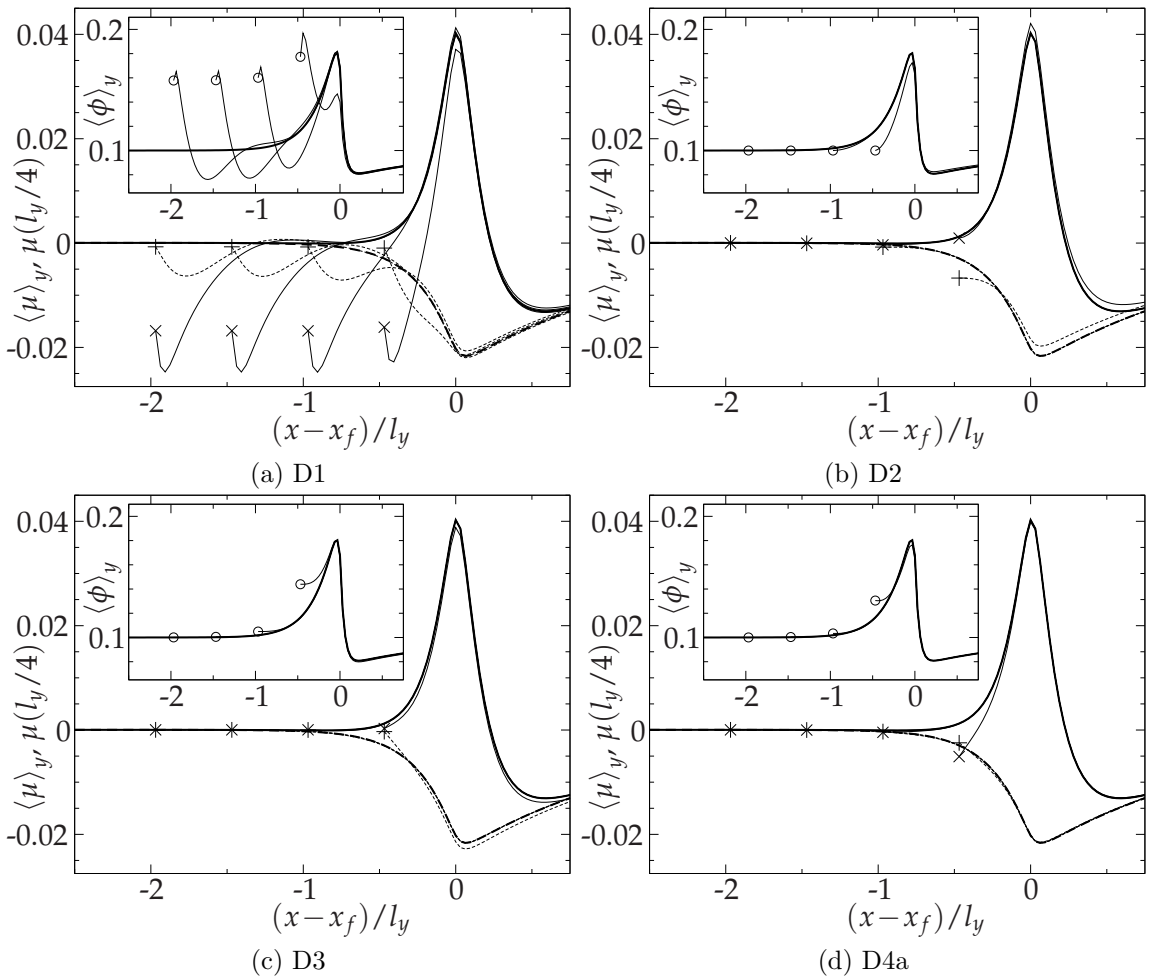

(a) D1 (b) D2

(c) D3 (d) D4a

Figure G.5: Comparison of D1, D2, D3, and D4a outflow boundary conditions placed at varying distances behind the phase separation front compared with a reference stationary profile (bold). Outset: μ along stripe center (solid with $\times$) and $\langle\mu\rangle_y$ (dashed with $+$). Inset: $\langle\phi\rangle_y$ (with $\circ$). Symbols only mark the curve endpoints to show the outflow boundary value of each profile. Testing procedure and simulation parameters are described in the text. Results continue in Figure G.6.

but the terribly performing D1. However, D2 and D5 best reproduced the chemical potential cross-section (solid line), whereas D4a was worse than all but D1. Placed appropriately far ($x_f/l_y \geq 1.5$) from the phase separation front, all outflow boundary conditions except D1 perform equally well at reproducing the correct concentration and chemical potential fields for this stationary system.

An important point not shown in these results is that orthogonal stripe morphologies

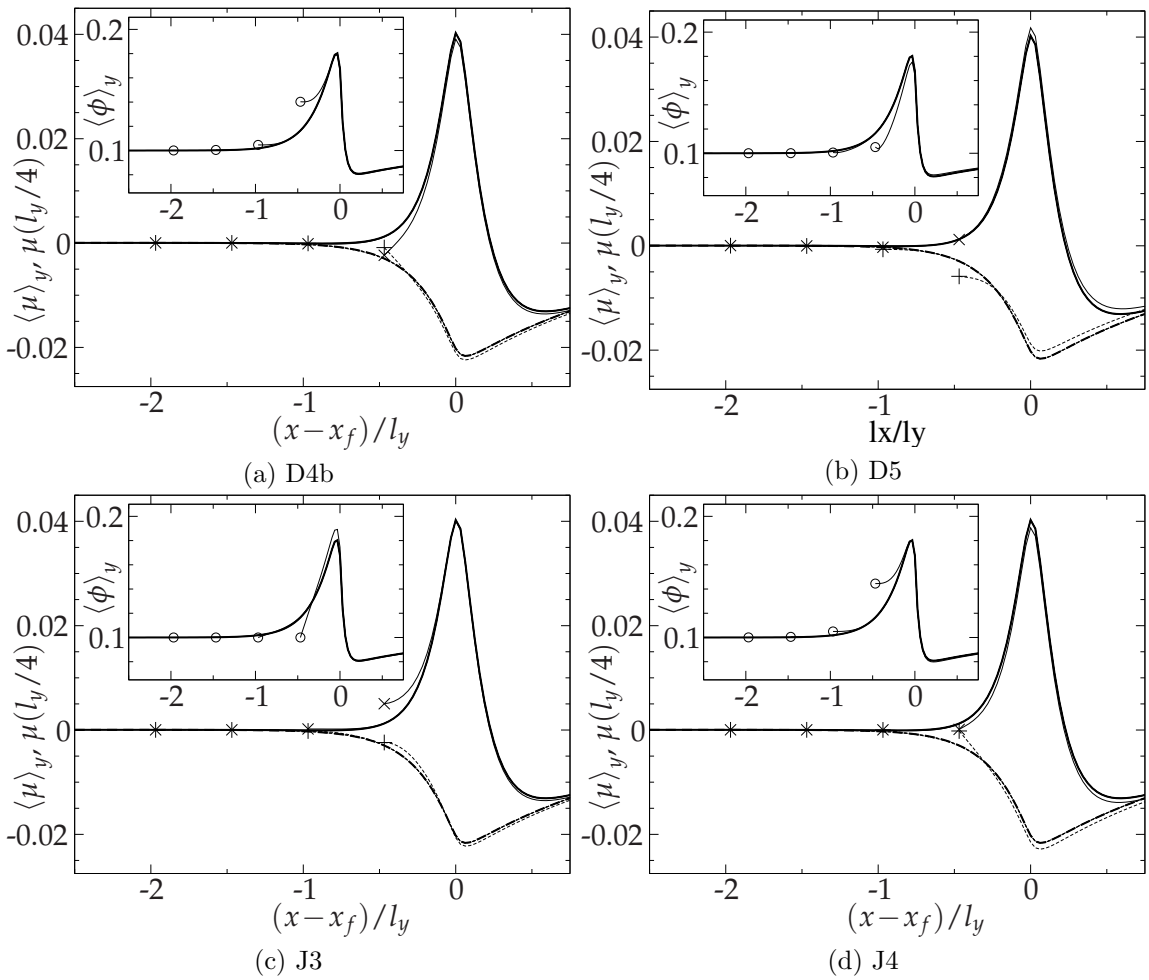

(a) D4b (b) D5

(c) J3 (d) J4

Figure G.6: Continuation of Figure G.5. Comparison of D4b, D5, J3, and J4 outflow boundary conditions placed at varying distances behind the phase separation front compared with a reference stationary profile (bold). Outset: μ along stripe center (solid with $\times$) and $\langle\mu\rangle_y$ (dashed with $+$). Inset: $\langle\phi\rangle_y$ (with $\circ$). Symbols only mark the curve endpoints to show the outflow boundary value of each profile. Testing procedure and simulation parameters are described in the text.

formed by phase separation fronts moving into asymmetrically mixed material need an increasing amount of distance between the front and the outflow boundary for increasingly asymmetric mixtures. That is, the further $\Phi_i n$ deviates from $\Phi_i n = 0$, the further ahead of the outflow boundary the front needs to be placed. This is due to the increased wetting and subsequently increased Laplace pressure. See Appendix A for more details.

G.5.4. Outflow of a Circular Domain

The final test of the outflow BCs is the advection of a single circular domain of phase-separated material out of a simulation at constant speed. This gauges the ability of the outflow BC to handle non-steady-state systems. Specifically, the outflow BC must deal with the following features: Between the domain and it's surroundings is an interface where the order parameter changes from the positive to negative equilibrium values. The position of where the interface crosses the boundary changes with time. The angle the interface relative to the outflow boundary changes with time. The curvature of the interface around the domain creates a Laplace pressure which causes the chemical potential to be higher inside, meaning the chemical potential at the boundary changes with time and position. The current at the boundary changes with space and time. Given these challenges, it is surprising that any of the relatively simple outflow boundary conditions formulated here performed at all well at this benchmark. Remarkably, BC D4b performed very well, and amazingly BC D5 performs nearly perfectly, as Figure G.8 shows.

Each BC was evaluated at a fast $u_x = -0.0785398$ advection speed and a slow $u_x = -7.85398$ advection speed. All outflow BCs had equally excellent performance in the fast advection speed test, and there were no noticeable differences between the test and reference domains. For this reason, the results of the fast advection test are not shown, but for reference they are nearly identical to the results in Figure G.8b for all tested outflow BCs. The results of the tests are shown as a time sequence of a simulation advecting the test circle across an outflow boundary. The test circle is overlaid on a time sequence of a reference simulation where the same boundary condition as the test simulation has been placed two circle diameters further away. The frames in each sequence are taken when 0%, 25%, 50%, 75%, and 100% of the reference circle has passed the position of the outflow boundary. Using a shading

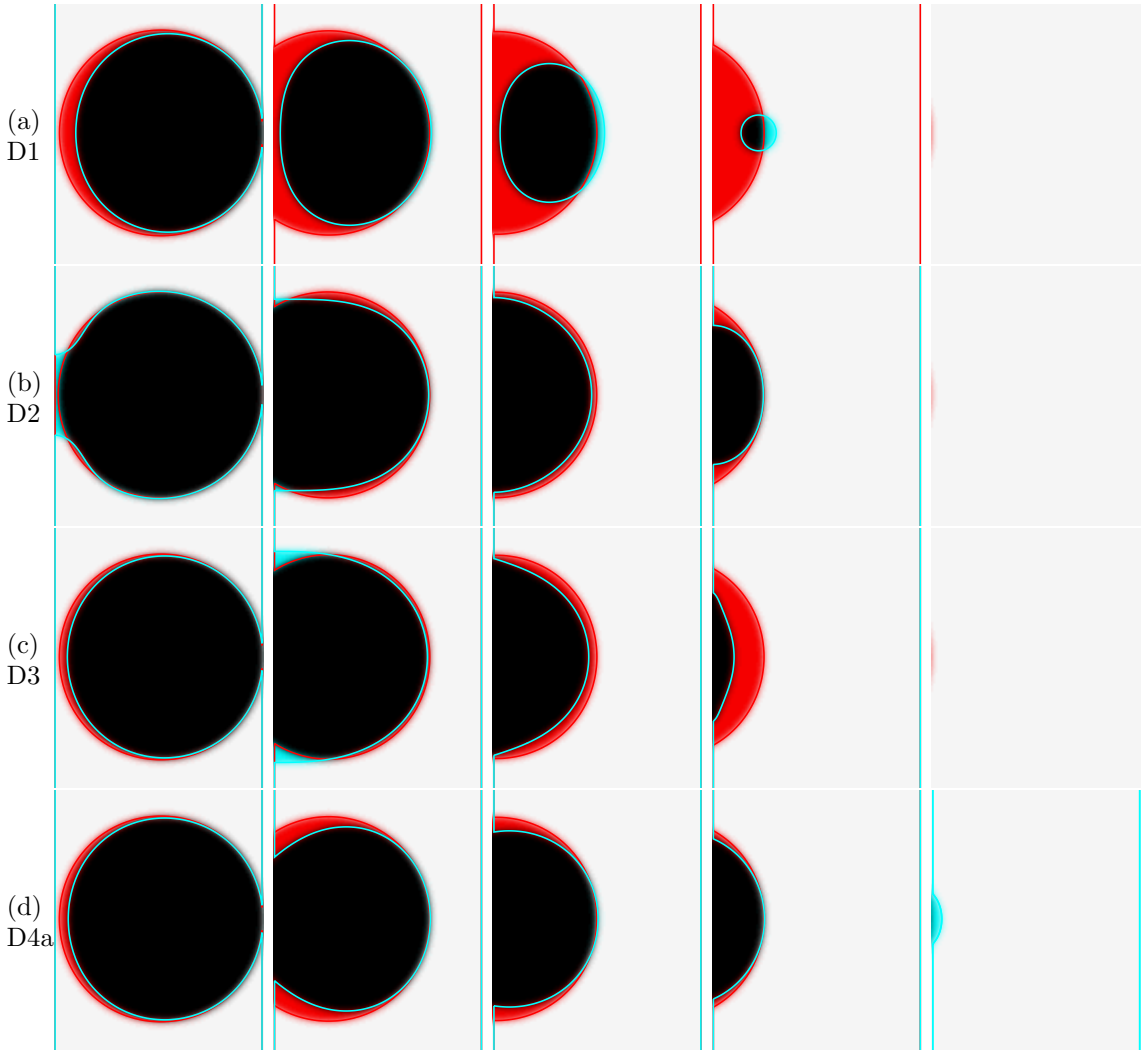

Figure G.7: Time sequence of simulations advecting a circular test domain across outflow boundary conditions D1, D2, D3, and D4a, compared to advection of a reference circular domain through the bulk of a larger simulation. Procedure, parameters, and results are described in the text. Results continue in Figure G.8.

method similar to Figure G.2, the test circle occupies the red color channel and the reference circle occupies the cyan color channel. Viewed online, the color channels can be separated with the use of red/cyan anaglyph glasses. The figure is black where the two domains overlap, cyan where the test domain extends beyond the reference circle, red where the reference circle extends beyond the test domain, and white where both domains are absent. To make the results more easily comparable when printed,

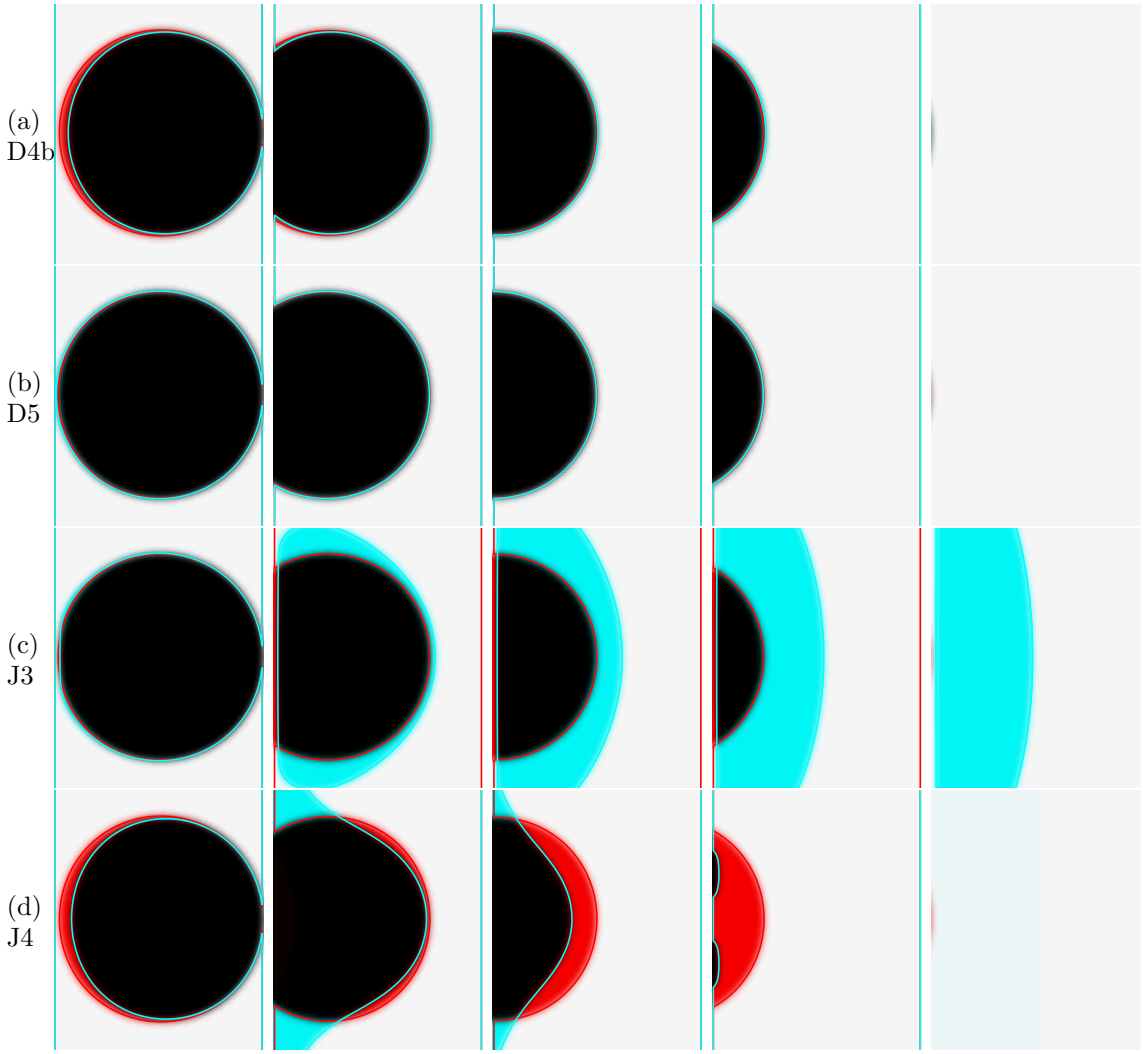

Figure G.8: Continuation of Figure G.7. Time sequence of simulations advecting a circular test domain across outflow boundary conditions D4b, D5, J3, and J4, compared to advection of a reference circular domain through the bulk of a larger simulation. Procedure, parameters, and results are described in the text.

the interface marking the edge of the test and reference domains are traced. Test simulations are 200×200 lattice nodes. The initial circle has a diameter of 100 lattice nodes and is placed at $x = 100$ in the center of the simulation. The front is at $x_f = 195$, the inflow BC is J5, and periodic boundaries are used the y-direction. The reference simulation is twice as wide $l_x = 400$, with the front at $x_f = 395$, and the circle is initially centered at $x = 300$, placing it the same distance from the inflow

boundary as the test simulation.

The results of the slow speed $u_x =$ tests, shown in Figures G.7 & G.8, are discussed in order. For the outflow D1 shown in Figure G.7a, the circular domain evaporates before it touches the outflow boundary. The evaporation begins quite far ahead of the boundary, and the test domain is significantly affected. Boundary D2 performs much better, as shown in Figure G.7b. Here the boundary induces a very strongly preferred orthogonal contact angle for the domain interface. The effect is strong at short ranges, but the relatively small curvature of the test interface means the bulk of the test domain remains mostly unaffected. In Figure G.7c the test domain reveals that D3 appears to have a slight problem with domain evaporation in addition to some issue maintaining a arbitrary interface contact angle. Although better than D1, D3 does not perform as well as D2. Similar to D3, minor evaporation problems are shown in Figure G.7d for D4a. However, here the interface contact angle does not appear as strongly affected. Although the domain has not been fully advected out by the last frame in the series, D4a performs somewhat reasonably well as an outflow BC in this test. Evaporation of the test domain is also an issue for D4b, however Figure G.8a shows none of the interface contact problems observed for D4a. The off-simulation chemical potential for D4a, given in Eq. (344), is the result of a linear extrapolation in the x-direction, whereas D4b uses the extrapolation given in Eq. (345) which includes neighboring cells in the y-direction. Clearly the best performing outflow BC in this test is D5, as can be seen in Figure G.8b. Only very close inspection reveals any deviation of the test domain form the reference circle. The results in Figure G.8c for J3—where the test domain never quite touches the outflow boundary and utterly fails to advect out of the simulation—is especially surprising considering how drastically different this result is from that for D2. As explained in Section G.4 and shown in Eq. (361), these boundary conditions are identical except

for the Laplacian of the concentration field, yet their behavior as an outflow BC in this test is vastly different. Lastly are the results for J4 shown in Figure G.8d. Here it appears that J4 has an evaporation problem nearly as bad as D1, and the inclusion of the chemical potential gradient in the outflowing current results in the test domain being strongly pulled across the outflow boundary.

G.6. Conclusion & Outlook

The results shown here indicate that a mix of boundary conditions perform best. At the inflow, a current conserving boundary condition such as J1, J2, or J5, should be used. The best performing inflow boundary is J5, which imposes a constant total inflow current, yet allows the current to vary spatially and temporally across the boundary. However, boundary condition J2 performs nearly as well at the given tests, and is much simpler to implement as it imposes a constant total current by imposing the same current everywhere across the boundary at all times. The best performing outflow boundary condition in these benchmarks is D5, and by a considerable margin. The ability to advect out a circular domain with no apparent distortion (see Figure G.8b) is worth the increased complexity and minor increase computational costs to ensure that boundary influences on domain structure is minimized.

Additional benchmarks should be developed, especially for the outflow boundary conditions. However, and perhaps more importantly, open boundary conditions for hydrodynamic multiphase flows need to be developed and tested. The boundary conditions presented here are specific to open boundaries for phase-separation fronts moving through a diffusive material. They can be applied to the drift-diffusion part of the coupled two-component hydrodynamic implementation (see Appendix E for more information), but open boundaries for the Navier-Stokes part of the implementation should be developed and evaluated. In the future, the technique presented here

whereby boundary conditions are generated by definition of off-simulation fields and boundary fluxes should be applied to the LBM for solving the Navier-Stokes equation coupled to the drift diffusion equation. Furthermore, evaluating these boundary conditions will require the development of new benchmarks.